Thèse n° 9024

Extension, validation, and optimization of Serpent/DYN3D/ATHLET code system for SFR applications

Présentée le 18 décembre 2023

Faculté des sciences de base
Laboratoire de physique des réacteurs et de comportement des systèmes
Programme doctoral en énergie

pour l'obtention du grade de Docteur ès Sciences

par

Vincenzo Anthony DI NORA

Acceptée sur proposition du jury

Prof. S. Haussener, présidente du jury
Dr K. Mikityuk, Dr E. Fridman, directeurs de thèse
Prof. E. Shwageraus , rapporteur
Dr E. Bubelis , rapporteuse
Prof. A. Manera, rapporteuse

École
polytechnique
fédérale
de Lausanne

2023

Zusammenfassung

Das Helmholtz-Zentrum Dresden-Rossendorf (HZDR) entwickelt und wendet eine Rechenplattform zur statischen und transienten Kernanalyse von Natrium-gekühlten schnellen Reaktoren (SFRs) an. Die Plattform basiert auf dem vom Technical Research Institute of Finland (VTT) entwickelten Monte-Carlo-Code Serpent und dem HZDR-eigenen dreidimensionalen Kernkernsimulator DYN3D. Die erfolgreiche Anwendung von Serpent/DYN3D auf SFRs wurde dank mehrerer neuerer Entwicklungsaktivitäten ermöglicht. Diese Aktivitäten umfassten Modifikationen von DYN3D zur Berücksichtigung von Wärmeausdehnungseffekten im Kern und die Entwicklung einer Serpent-basierten Methodik für die Generierung von Multigruppen-Wirkungsquerschnitten (XSs). Trotz der jüngsten Entwicklungen weist die Serpent/DYN3D-Sequenz noch einige Einschränkungen auf. Diese Analysen sind auf die Kernebene beschränkt und ein erheblicher Rechenaufwand ist erforderlich, um sowohl XS-Datenbanken für transiente Anwendungen zu generieren als auch damit verbundene Berechnungen durchzuführen. Diese Dissertation zielte darauf ab, solche Einschränkungen zu überwinden durch: die Erweiterung der Modellierung ausgehend vom Reaktorkern auf ganze SFR-Systeme, die Validierung des neuen erweiterten Berechnungswerkzeugs und die Optimierung der Genauigkeit von Lösungen in Bezug auf den Berechnungsaufwand.

Die Erweiterung des Analysebereichs auf SFR-Systeme wird durch die Kopplung der Sequenz mit dem Thermohydraulik-Code ATHLET erreicht, der in der Lage ist, die Strömung von flüssigem Natrium zu modellieren. Letzteres beinhaltet auch ATHLET-basierte Modellierungsmethoden, um die thermischen Ausdehnungen von Strukturen außerhalb des Kerns zu berücksichtigen, die die Reaktorneutronik stark beeinflussen können. Verifizierungs- und Validierungsaktivitäten, die Bestandteil der Erweiterung des gekoppelten Werkzeugs sind, werden anhand von numerischen und experimentellen Benchmarks auf der Grundlage Messdaten an den Reaktoren Phénix und Superphénix durchgeführt. Weiterhin werden Vereinfachungsoptionen von XS-Datenbanken untersucht, um die Rechenzeiten zu optimieren und gleichzeitig die Genauigkeit der Lösungen zu erhalten. Diese Optionen umfassen die Auswahl der optimalen kondensierten Energiegruppenstruktur für SFR-Analysen und die Darstellung von parametrisierten XSs über Ableitungen erster Ordnung.

Die im Rahmen dieser Doktorarbeit durchgeführten Forschungsaktivitäten führten zur erfolgreichen Entwicklung und Validierung eines neuen gekoppelten Berechnungswerkzeugs für stationäre und transiente Analysen von SFR-Systemen. Das Tool ist derzeit auf die Analyse von Szenarien anwendbar, die kein Natriumsieden oder Kernschäden beinhalten. Die Optionen zur Vereinfachung von XS-Daten und Beschleunigung von Neutronik-Berechnungen wurden implementiert und

getestet, wobei große Möglichkeiten für eine signifikante Beschleunigung von Analysen bei praktisch vernachlässigbarem Genauigkeitsverlust aufgezeigt wurden.

Abstract

The Helmholtz-Zentrum Dresden-Rossendorf (HZDR) is developing and applying a computational platform for static and transient core analyses of sodium-cooled fast reactors (SFRs). The platform is based on the Monte Carlo (MC) code Serpent developed by the technical research institute of Finland (VTT) and the HZDR in-house three-dimensional nuclear core simulator DYN3D. The successful application of Serpent/DYN3D to SFRs was made possible thanks to several recent development activities. The activities included modifications of DYN3D to account for in-core thermal expansions effects and development of a Serpent-based methodology for the generation of multi-group cross-sections (XSs). Despite the recent developments, the Serpent/DYN3D platform presents still some limitations. That is, the domain of the platform analyses is restricted to core level and considerable computational efforts are required both to generate XS libraries for transient applications and perform related calculations. This thesis aims at overcoming such limitations through: The extension of the modeling domain of the platform from core to whole SFR systems, the validation of the newly extended platform, and the optimization of the accuracy of solutions against computational efforts.

The extension of the analysis domain to SFR systems is achieved by coupling the existing platform with the thermal hydraulics code ATHLET capable of modeling the liquid sodium flow. Included in the extension is the development of ATHLET-based modeling methodologies to account for the thermal expansions of out-of-core structures that may strongly affect the reactor neutronics. Verification and validation activities inherent to the extension of the platform are performed against numerical and experimental benchmarks based on the Phénix and Superphénix reactor data. Options focused on the simplification of XS libraries are considered to optimize computational times while preserving the accuracy of solutions. The options include the selection of optimal condensed energy groups structure for SFR analyses and the representation of parametrized XSs via first-order derivatives.

The research activities conducted in this doctoral thesis led to the successful development and validation of a new computational platform for steady-state and transient analyses of SFR systems. The platform is currently applicable to the analyses of scenarios that do not involve sodium boiling or core damage. The options for the simplification of XS libraries and acceleration of neutronics calculations were implemented and tested revealing wide margins for significant speedup of analyses with the introduction of practically negligible errors.

Keywords

SFR, Serpent, DYN3D, ATHLET, thermal expansion, cross-section parametrization, simulated annealing

Acknowledgements

I remember the day this adventure started like it was yesterday, but several years have actually passed since then. During this time, I was lucky to collect various experiences that enriched me in professional, but above all in personal terms. All this was possible also thanks to the multitude of people who supported me during this journey and who, in doing so, kept the flame of my motivation alive.

In this regard, I think it is more than right to thank my family for having always believed in me, probably much more than I did it myself. To all of you "here" with me and to you who are no longer here: Thank you very much for having supported me in every way, for having offered advice in the moments of disorientation, and for the toughness with which you managed to get a smile out of me even in the darkest moments of these years. But especially, thanks for teaching me not to settle, and to fight to become a better and better version of myself every day.

It is my duty and pleasure to thank my advisors Prof. Mikityuk and Dr. Fridman for their patience and precious guidance offered over the years. Thank you for sharing with me your scientific vision which I hope to make more and more mine for the times to come. A special thank goes to Dr. Kliem, who welcomed me into his department at the Helmholtz-Zentrum Dresden-Rossendorf, and to the trust he placed in me. Thank you for having always supported me in my work as well as in my professional training. I also wish to express my gratitude to Dr. Ponomarev for his consistent encouragement and scientific support throughout my studies.

Thanks to all my colleagues of the Helmholtz-Zentrum Dresden-Rossendorf. In particular, thanks to Ms. Kurde without whom I would have been lost in the "sea" of the administrative issues. Thanks to Dr. Nikitin for his excellent support on neutronics matters. My infinite gratitude goes also to Dr. Bilodid who always helped me in overcoming most of the challenges, of both scientific and technical nature, that have arisen along my journey. Thank you, Mr. Berger, for the prompt IT support and for our chats in Italian. Thank you, Mr. Gommlich, for your kind and patient technical support.

Last but not least, Thank you friends from Catania, Turin, Dresden, and you others around the world. Thank you for your smiles and for your time. You have made and make still now my days joyful.

Table of contents

Abbreviations

0D : Zero-dimensional

1D : Mono-dimensional

2D : Two-dimensional

3D : Three-dimensional

AOO : Anticipated operation occurence

BC : Boundary condition

BOC : Beginning of cycle

BOL : Beginning-of-life

CR : Control rod

CRDL : Control rod drive-line

CSD : Control and shutdown devices

DBA : Design basis accident

DEC-A : Desing extension condition without significant fuel degradation

DEC-B : Desing extension condition with core melt

DHRS : Decay heat removal system

DiD : Defense-in-depth

EGS : Energy group structure

DOTE : Dispositif d'Origine de Transfert d'Expérience

DSD : Diverse shutdown device

EOC : End of cycle

EOL : End-of-life

ESFR : European sodium fast reactor

FOD : First-order derivative

GFR : Gas-cooled fast reactor

GIF : Generation-IV international forum

HZDR : Helmholtz-Zentrum Dresden-Rossendorf

IHX : Intermediate heat exchanger

LFR : Lead-cooled fast reactor

LWR : Light water reactor

MC : Monte Carlo

MDT : Multi-dimensional table

MOFC: Measurement of feedback coefficients

MSR : Molten salt reactor

NC : Natural circulation

NK : Neutron kinetics

NPP : Nuclear power plant

pcm : Percent mille

PFS: Primary flow step

PK : Point kinetics

PLOOP : Protected loss of off-site power

PSBO : Protected station black-out

PWR : Pressurized water reactor

RS : Reactivity step

SA : Simulated annealing

SCWR : Super critical water reactor

SD : Standard deviation

SFR : Sodium-cooled fast reactor

SG : Steam generator

SPH : Super-homogenization

SPX : Superphénix

SST : Self-stabilization test

TE : Thermal expansion

TH : Thernal-hydraulic

TM : Thermal-mechanic

ULOF : Unprotected loss of flow

ULOOP : Unprotected loss of off-site power

V&V : Verification and validation

VHTR : Very high-temperature reactor

VTT : Technical research institute of Finland

XS : Cross section

Notations

b : Burnup

C_b : Boron concentration

g : Genereic energy group in the multi-group approximation of diffusion equations

i : Generic reactor core node

j : Axial node j for the structure of control rod drive-line or vessel

$L|_{Tref}$: Axial length of a generic out-of-core structure at room temperature

$L_j|_{Tref}$: Axial length at room temperature of the node j of control rod drive-line or vessel

T : Average temperature of a generic out-of-core structure

t : Generic simulation time

t_0 : Beginning of the actual transient calculations after zero-transient

T_c : Coolant temperature

T_f : Fuel temperature

T_j : Average temperature of the axial node j for control rod drive-line or vessel

x : Generic nuclear reaction

α : Axial linear thermal expansion coefficient

$\alpha_{ave.}$: Average axial linear thermal expansion coefficient

ΔL : Absolute axial thermal expansion of a generic out-of-core structure

ΔL_{CRDL} : Absolute axial thermal expansion of control-rod drive-line

ΔL_{sk} : Absolute axial thermal expansion of strongback

ΔL_{tot} : Absolute total axial thermal expansion

ΔL_{vl} : Absolute axial thermal expansion of vessel

Δt_{CRDL} : Time delay for the effects of CRDL thermal expansions

Δt_{sk} : Time delay for the effects of strongback thermal expansions

Δt_{vl} : Time delay for the effects of vessel thermal expansions

ε_a : Relative clad- or fuel-driven axial expansion of fuel elements

ε_c : Relative cumulative axial relative elongation

ε_r : Relative average radial expansion of the diagrid

ρ_c : Coolant density

List of Figures

List of Tables

Chapter 1 Introduction

This chapter provides an overview of the background and objectives of this doctoral research, which is centered on the analyses of sodium-cooled fast reactors (SFRs). In particular, the background on SFR technology is covered in Section 1.1, which includes: Operational experiences collected on SFRs, characteristics of sodium coolant, main system designs, and a focus on the importance of thermal expansion effects for this technology. Section 1.2 presents the most established state-of-the-art computational tools dedicated to the analyses of SFRs. Section 1.3 introduces the computational platform Serpent/DYN3D, i.e., the subject of extension in this doctoral research, and the system code ATHLET, considered for such extension purposes. Section 1.4 presents considerations on potential improvements in the modeling and computational performance of SFR analyses. Specific objectives of this thesis and thesis structure are respectively outlined in Section 1.5 and Section 1.6.

1.1 Overview of SFRs

The generation-IV international forum (GIF) is a cooperative international effort that aims to establish the feasibility and performance of the next-generation nuclear power plants (NPPs) (GIF, 2021). This new generation of reactors is expected to fulfill specific goals outlined by the GIF, namely sustainable energy production, proliferation resistance, higher levels of fuel utilization, minimization and management of nuclear waste, long-term availability of systems, and excellence in safety operations and plant reliability.

In this regard, international collaborations have selected six different reactor concepts that align with the GIF goals, namely, the super-critical water reactor (SCWR), the very high-temperature reactor (VHTR), the molten salt reactor (MSR), the gas-cooled fast reactor (GFR), the lead-cooled fast reactor (LFR), and the SFR. Among these selected concepts, the GFR, LFR, and SFR concepts are designed to operate with a fast neutron spectrum, which makes such reactor concepts particularly prone to cope with the GIF's goals of high fuel utilization and nuclear waste minimization. In fact, reactor operations in a fast neutron spectrum generally allow for an increased rate of fission reactions compared to capture reactions, thereby enabling better utilization of uranium resources.

Each fast reactor concept has its own set of advantages and disadvantages. For instance, the GFR concept distinguishes itself with its expected high operating temperature and plant efficiency, which is designed to be approximately 48%. An added advantage of the GFR is its utilization of a transparent and inert gas coolant, such as e.g., helium, facilitating maintenance activities and reducing activation phenomena in the system. The GFR, however, faces challenges related to limited coolant heat

transfer, and raises safety concerns in depressurization scenarios as these involve with high probability the core meltdown. Furthermore, there are technological issues associated with the development and assessment of GFR fuel, making it problematic to demonstrate the technology effectively (Meyer, et al., 2007).

The LFR, whether cooled by lead or lead-bismuth eutectic, can rely on coolants that demonstrate excellent chemical compatibility with water and air. Additionally, the LFR boasts a high volumetric heat capacity that allows for efficient absorption and transfer of significant amounts of heat. However, one significant drawback of the LFR lies in the highly corrosive nature of lead, which can cause the corrosion of the fuel rod cladding. To overcome this challenge, the LFR typically limits the coolant velocity into the core to a few meters per second. Moreover, ongoing LFR research focuses on developing corrosion-resistant materials to effectively mitigate this issue (Alemberti, et al., 2020a).

The utilization of sodium as a coolant offers multiple advantages to the SFR concept. These advantages include, e.g., inexpensive coolant production, high heat conductivity, and high volumetric heat capacity like in the case of lead or lead-bismuth. The coolant allows SFRs to achieve a broad operating temperature range, from approximately 400°C to 550°C, with benefits for plant efficiency. In addition, sodium, unlike lead, is not corrosive. The most limiting drawback of the SFR lies in its chemical incompatibility with air and water. Sodium, in fact, can burn in air and react with water to produce hydrogen. This necessitates research and developments of suitable technologies and safety measure to prevent such reactions under all circumstances (Waltar, et al., 2012).

Among all previously introduced concepts, the SFR concept distinguishes itself as the most promising fast reactor concept, boasting significant technological maturity and potential for industrial deployment. The SFR has a distinct advantage due to its extensive operational experience, spanning several hundred reactor-years. In contrast, the LFR has less than a hundred reactor-years of operational experience (Alemberti, et al., 2020b), and the GFR is still in the design phase. Furthermore, the SFR has already achieved the commercial-scale stage (Guidez & Prêle, 2016; WNN, 2015), setting it apart from the LFR and GFR, which still require substantial development to attain similar commercial milestones.

Such operational experience gathered from past and present SFRs, from the 1950s to nowadays, is briefly summarized in the following section.

1.1.1 Operational experience and future perspectives

Over the past decades, SFRs have accumulated a wealth of operational experience worldwide, totaling roughly 400 reactor-years, see Table 1.

Table 1. Main SFR types and configurations of past, present and planned reactors based on (IAEA, 2006) and (WNA, 2021)

Reactor	Country	Configuration	Type	1st criticality	Status
EBR-I	USA	Pool	Experimental	1951	Shutdown in 1963
EBR-II	USA	Pool	Experimental	1963	Shutdown in 1994
Fermi-I	USA	Loop	Experimental	1963	Shutdown in 1975
FFTF	USA	Loop	Experimental	1980	Shutdown in 1996
Rapsodie	France	Loop	Experimental	1967	Shutdown in 1983
KNK-II	Germany	Loop	Experimental	1972	Shutdown in 1991
BOR-60	USSR	Loop	Experimental	1968	Shutdown in 2020
BN-350	USSR	Loop	Experimental	1972	Shutdown in 1999
JOYO	Japan	Loop	Experimental	1977	Shutdown in 2007
FBTR	India	Loop	Experimental	1985	In operation
CEFR	China	Pool	Experimental	2010	In operation
Phénix	France	Pool	Demonstrator	1973	Shutdown in 2009
PFR	UK	Pool	Demonstrator	1974	Shutdown in 1994
MONJU	Japan	Loop	Demonstrator	1994	Shutdown in 2010
BN-600	USSR	Pool	Demonstrator	1980	In operation
Superphénix	France	Pool	Commercial-size	1985	Shutdown in 1998
BN-800	USSR	Pool	Commercial-size	2014	In operation
BN-1200	Russia	Pool	Commercial-size	-	Project
CDFR-600	China	Pool	Demonstrator	-	In construction
CDFR-1000	China	Pool	Demonstrator	-	Project
MBIR	Russia	Loop	Experimental	-	In construction
PFBR	India	Pool	Demonstrator	-	Commissioning: 2024

The history of SFRs began with the construction of the experimental EBR-I by the Argonne National Laboratory (ANL). In a historic milestone, this reactor achieved the first criticality in 1951, marking the world's first utilization of nuclear power for electricity production purposes (INL, 2019).

Buildingon the success of EBR-I, the USA further developed and operated two other experimental SFRs in the early 1960s: EBR-II (Westfall, 2004) and Fermi-I (U.S.NRC, 2021), as well as another experimental SFR in the early 1980s, the FFTF (Newland & Krupar, 1984). During the 1960s to the 1980s, Europe also ventured into experimental SFRs, with notable examples being the French Rapsodie (Zaleski & Vautrey, 1962) and the German KNK-II (Marth, 1983). Meanwhile, the USSR, Japan, and India each contributed to the development of SFR technology by building and operating the experimental SFRs: The BOR-60 and BN-350 in the Soviet Union (ROSATOM, 2021); the JOYO in Japan (Matsuba, et al., 2006); and the FBTR, which is operational in India (Anandapadmanaban, et al., 2013). More recently, China joined the ranks of countries with experimental SFRs with the construction of the Chinese CEFR, which has been in service since 2010 (IPFM, 2021). The increasing knowledge and interest in SFR technology from the 1970s to the 1990s led to the development of various reactor demonstrators. These include the French Phénix (CEA Marcoule, 2010), the British PFR (Jensen & Olgaard, 1995), the Japanese MONJU (Akebi, 1991), and the Russian BN-600, which has been in operation since 1980 (Poplavsky, et al., 2004). Additionally, commercial-scale SFRs have contributed to the growing experience in this field. Notably, the French Superphénix (SPX) was connected to the national grid in 1986 (Guidez & Prêle, 2016), while the Russian BN-800 reached its first criticality in 2014 and has been in service since then (WNN, 2015).

Looking ahead, several SFR projects are either under construction or planned construction. Russia is in the process of building the experimental SFR MBIR (Dragunov, et al., 2015) and has plans for the BN-1200, scheduled to begin construction in 2030 (IPFM, 2019). China has already commenced construction of the CDFR-600 demonstrator (WNN, 2020) and is planning the development of the commercial-scale CDFR-1000 (WNA, 2021). Meanwhile, India is eagerly anticipating the commissioning of the PFBR demonstrator, expected to be operational by 2024 (Ramana, 2023). In Europe, several projects were also proposed to demonstrate the industrial relevance of SFRs, qualify innovative safety designs, and assess safety measures and plant reliability, let us consider, for instance, CP-ESFR (Fiorini & Vasile, 2012), ESNII Plus (Vasile, et al., 2015), and ESFR-SMART (Mikityuk, et al., 2017) projects.

The SFR technology exhibits distinct characteristics that relate to sodium coolant, design options, and specific challenges arising from the wide ranges of SFR operating temperature. Such peculiar features are described in more detail in the following to provide a comprehensive background of the technology.

1.1.2 Coolant characteristics

Sodium exhibits unique characteristics that have attracted substantial interest in both scientific and industrial frames over the years. These distinctive characteristics influence the SFR system design and give rise to specific challenges that need to be addressed.

The sodium coolant characteristics in term of neutronic, thermal-hydraulic, and chemical properties are outlined below:

- Neutronic properties: SFRs rely on a fast neutron spectrum to sustain the nuclear chain reaction, utilizing fission events within the high-energy range of neutrons. This characteristic necessitates minimizing neutron moderation effects caused by the coolant, while ensuring efficient core heat removal. In this context, selecting sodium as the coolant represents a suitable option from a neutronics standpoint. Sodium boasts, in fact, limited neutron moderation and absorption capabilities, which are essential for minimizing both neutrons slowing down and coolant activation.

  A crucial neutronic aspect to consider in SFRs, also related to safety concerns, pertains to the effects arising from the reduction of sodium density, which may result from sodium overheating. On core neutronics, these effects are of dual nature and opposite. On one hand, the reduction in coolant density is responsible for the reduction of neutron slowing down and absorption phenomena, which result in the insertion of positive reactivity. On the other hand, the reduction in sodium density causes an increase in neutron leakage, resulting in the insertion of negative reactivity. Net local effects on neutronics depend on the position and volume of the affected coolant spot within the core. In general, net positive effects occur in the internal regions of the core where the former effects prevail. Contrarily, net negative effects occur at the core boundaries where leakage effects are dominant.

- Thermal-hydraulic properties: Liquid sodium exhibits advantageous thermal-hydraulic properties that make it well-suited for nuclear reactor designs. One notable feature of sodium is its high boiling temperature of 883°C, at atmospheric pressure, see Table 2. This characteristic allows the coolant to retain a substantial amount of heat in its liquid state despite its low volumetric heat capacity. Given the sodium high boiling point, SFRs can operate at high temperatures, typically ranging from 400°C to 550°C, with consequent benefits for system thermodynamic efficiencies. It is worth noting that these benefits are achieved without the necessity of pressurizing the coolant.

This aspect holds significant safety-related implications as it mitigates the risk of a rapid and violent release of the coolant from the cooling systems in the event of any system integrity loss.

An aspect related to the wide difference in operating temperatures between the hot and cold regions of SFRs is the resulting enhanced coolant density difference between hot and cold sodium. Such a difference in density promotes an efficient and vigorous natural circulation. This is particularly important in accidental scenarios where natural circulation plays a dominant role in removing core heat from the primary circuit. Last but not least, sodium also has a high thermal conductivity, roughly 100 times higher than that of water, which favors heat exchange and heat removal phenomena. This is beneficial for heat exchange processes occurring within fuel rods and bundles of the heat exchangers. In addition, the high heat removal capability helps to reduce the probability of formation of local hot spots even in stagnant conditions.

- Chemical properties: Unlike lead, sodium presents limited corrosion capabilities. However, a significant drawback of sodium is its tendency to undergo exothermic reactions when facing air or water. To address these potential hazards, advanced safety measures have been incorporated into the design of SFR systems. For instance, one of the key solutions involves the use of inert argon to fill all the environments that confine with sodium, effectively minimizing the risk of sodium-air reactions. Whereas, intermediate sodium-cooled circuits between the primary circuit and steam generator loops are considered by design to reduce the risk of interactions between the active sodium of the primary system and water.

Table 2. Properties of sodium and water (most-conventional coolant), respectively, in typical SFRs and PWRs.

Parameter	Sodium	Water
State in operation	Liquid	Liquid
Thermal conductivity, W/m K	64.0[a]	0.57[b]
Heat capacity, Cp, J/kg K	1270	5463[b]
Density, ρ, kg/m3	825[a]	733[b]
Melting point, ◦C	98	–
Boiling point, ◦C	883	345[b]
Volumetric heat capacity, ρ·Cp, kJ/ m3 K	1048	3985[b]
Chemical reactivity w/ water and air	Severe	None
Optical transparency	Opaque	Transparent

a Value at a temperature of 530 ◦C.; b Value at average operational condition

1.1.3 System design

Based on the past, existing, and innovative SFR designs, this section presents the characteristics of the two main SFR layout types: The pool-type and loop-type designs. Fig. 1 illustrates the respective schematics of these designs. For both the design concepts, the figure allows one to identify three main circuits: The primary, secondary (or intermediate), and tertiary circuits.

In pool-type SFRs, the primary circuit consists of a large sodium pool confined within a metallic vessel, see Fig. 2. This large sodium pool is subdivided by an inner vessel, or redan, into two sub-pools, i.e., the hot and the cold pools, collecting hot and cold sodium in the primary circuit, respectively. Beyond the core, the primary circuit hosts essential components such as primary pumps, intermediate heat exchangers (IHXs), optional decay heat removal system (DHRS), and other reactor internals. Relevant reactor internals are, for instance, the strongback and diagrid, located beneath the core, and the control rod drive-lines (CRDLs), located in correspondence of the above-core structure region. In a pool-type SFR, the sodium flows along the core channels, removing the heat generated within the core. The heated coolant reaches the hot pool and accesses the IHXs via dedicated windows. In the IHXs, the sodium heat is yielded to the secondary circuits. Subsequently, the coolant flows into the cold pool, where it is drawn in by primary pumps and pumped back into the reactor core, passing through the structures of the strongback and diagrid. Some of the coolant is diverted from the strongback, via vessel cooling pipes, to the vessel cooling system, which serves to cool the vessel walls. From there, the sodium is directed back to the cold pool, completing the primary circuit flow. The primary heat generated in the core is transferred, through the IHXs, to the secondary circuits which consist of sodium-cooled loops. These secondary loops allow for the exchange of heat with the tertiary water-cooled circuits that include the steam generators (SGs) and turbine units, see Fig. 1.

In loop-type SFRs, the working principle of three cooling systems is similar to the one described for pool-type SFRs, but with a key distinction, i.e., the placement of pumps and IHXs outside the primary pool. This design introduces an additional potential safety risk for the plant, as the primary sodium exits the main reactor vessel to reach the IHXs.

Both designs share a distinct feature: The intermediate circuit positioned between the primary and steam generator loops. This circuit serves two essential purposes. Firstly, it effectively mitigates the risk of chemical interaction between water and sodium in the primary circuit. Secondly, it effectively isolates activated sodium of the primary circuit, ensuring its separation from the power conversion unit.

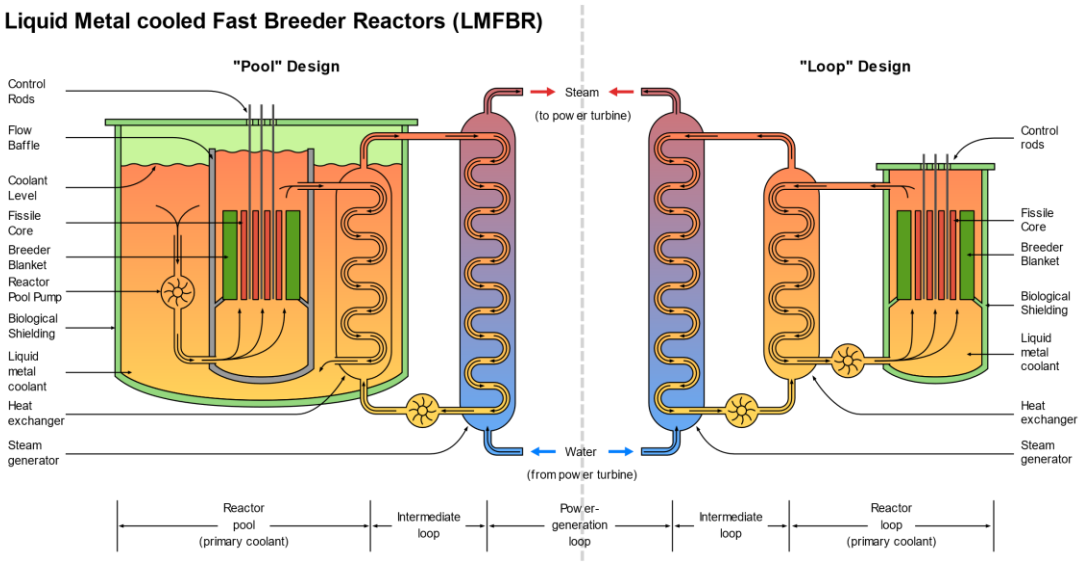

Fig. 1. Schemes of SFR designs (Wikipedia, 2021): Pool and loop configurations

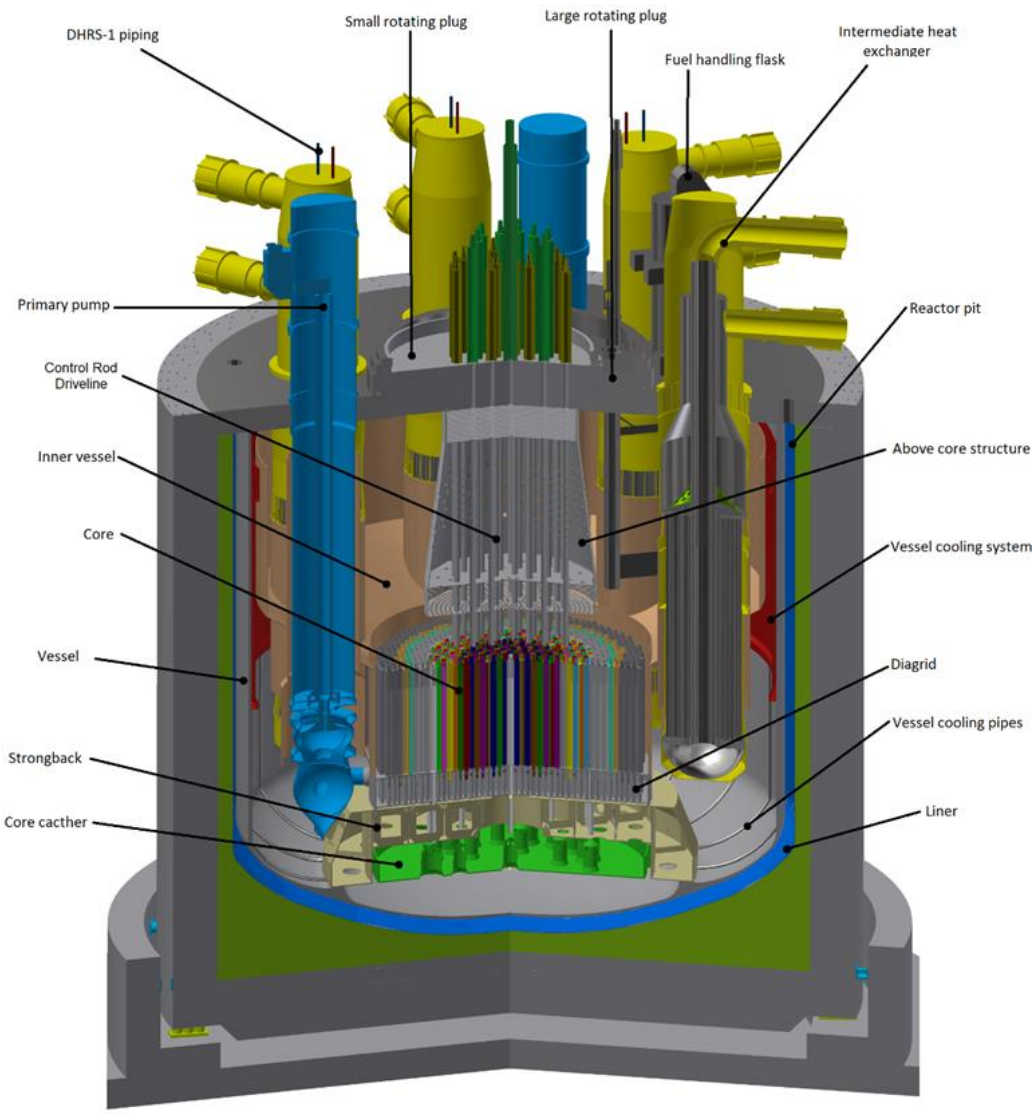

Fig. 2. Cut view of the pool-type ESFR (Guidez, et al., 2021)

Considering the design choices presented in Table 1 for demonstrational, commercial-size, and planned SFRs, it is evident that most of the designs are of the pool type. This suggests that a substantial emphasis has likely been placed on prioritizing safety aspects, which are better addressed by the pool-type SFR design.

1.1.4 Thermal expansion effects

A critical issue specific to SFRs is the impact of thermal expansion effects on core neutronics.

In SFRs, thermal expansions and related reactivity effects are notably more pronounced compared, e.g., to most conventional reactors such as, for instance, PWRs. The primary reason for that lies in the larger margin to boiling for sodium in SFRs, around ~300°C, as opposed to the margin for water in typical PWRs, which is only ~20°C. In PWRs, the drop in water density after the boiling onset results in voiding coolant effects becoming dominant over thermal expansion effects, making thermal expansions negligible in PWRs. On the other hand, in SFRs, the substantial margin to boiling can result in considerable thermal expansion effects. These effects not only impact on the relative volume fractions of fuel, cladding, sodium, and absorber materials within the core, but they also influence the positioning of control rods (CR) in relation to the core, and impact on core dimensions. It should be stressed that, as pointed out in (Waltar, et al., 2012), given the large mean free paths of neutrons in the fast spectrum, any of the effects outline above can have a profound impact on the neutron balance.

Some of the most relevant thermal expansion and related reactivity effects are listed in the following. The effects were categorized into in-core and out-of-core effects based on location of occurrence of the thermal expansion phenomena.

Relevant in-core thermal expansion effects include:

- Fuel expansion: As the temperature rises, the fuel expands axially and radially. Axial fuel expansions induce the reduction of the mass ratio between the fuel and coolant, absorber, and structural materials with consequent softening of the neutron spectrum and increase of neutron absorption. The axial and radial fuel expansion also contribute to the increase of neutron leakage from the fuel. Overall, the reactivity effects related to fuel expansion are negative. It should be mentioned that depending on the occurrence of pellet-clad contacts, the fuel axial expansion can be assumed to be driven by either the axial expansion of the clad or the fuel temperature.

- Clad expansion: The clad axial expansion reduces the clad density, altering the mass ratio between fuel and structural materials, and decreasing the occurrence of neutron parasitic captures in the

clad. Simultaneously, the radial expansion of the clad pushes out the sodium from the subassembly channels, resulting in a slight hardening of the spectrum due to the reduction of neutron slowing-down and parasitic absorption phenomena in the sodium. Overall, the reactivity effects related to clad expansion are positive.

- Wrapper expansion: Similarly to clad expansion, it reduces parasitic captures, promoting positive feedback effects on the neutron balance.

- Core radial expansion: It is affected by a complex interplay of thermal-mechanical effects, which becomes even more complex in the presence of a radial constraining structure, the so-called "core restraint system", used to limit core radial expansions. In designs without a core restraint system, two primary effects impact on core radial expansion. The first is diagrid expansion, which is driven by an increase in the inlet core coolant temperature. Diagrid expansion causes the pitch of fuel subassemblies and the sizes of inter-assembly gaps within the core to expand. The second effect is core flowering, which is driven by axial temperature distributions within the core. Core flowering denotes the non-uniform radial expansion of the core along the axial axis. Should a core restraint system be foreseen by design, the mechanical constraint effects of the restraint system and the contact of the pads add to the effects mentioned above. As an overall result of the outlined effects, the core radial expansion can influence the amount of sodium in the inter-assembly gaps, leading to softening or hardening of the neutron spectrum, depending on the considered axial position and reactor design. Additionally, the core radial expansion broadens the core boundaries, resulting in increased neutron leakage. Overall, the neutronics feedback effects associated with core radial expansions are negative.

Relevant out-of-core thermal expansion effects include:

- Axial strongback expansion: This effect is driven by the rising inlet core sodium temperature. As the sodium temperature increases, the strongback expands, pushing the core upward and causing the insertion of CRs into the core. This insertion of CRs negatively impacts the overall neutron balance, leading to negative reactivity feedback.

- Axial vessel expansion: The axial vessel expansion is driven by the increasing temperature of the sodium flowing in the vessel cooling system. This temperature rise is correlated with the temperature of the sodium flow diverted from the core inlet to the vessel cooling system, although with a certain delay. When the strongback sits at the vessel bottom as per the design, vessel expansions or contractions can affect the core position with respect to CRs. Similar considerations also apply

to situations where the strongback sits on an inner reactor vessel. In both cases, the vessels are assumed to be suspended from above and may expand downward, leading to CR withdrawing from the core, resulting in positive neutronics feedback.

- Axial CRDL expansion: This effect is caused by CRDLs, immersed in the sodium hot pool above the reactor core. The expansion of CRDLs is directly influenced by the sodium temperature in the hot pool. As the temperature of the hot pool rises, CRDLs expand causing a downward shift of the CRs into the core. This insertion of CRs provides negative neutronic feedback.

1.2 Analyses of SFRs: State-of-the-art

Operational safety and plant reliability of SFRs rely on computational analyses. These analyses demand sophisticated modeling capabilities for various physical fields, including core neutronics, system thermal hydraulics, heat conduction, thermal mechanics, and more.

To achieve the highest level of analysis coverage across the entire SFR multiphysics domain, numerous research organizations have dedicated efforts to develop advanced multiphysics computational tools. Examples of some of the most well-established and cutting-edge computational platforms available in the field are introduced in the following paragraphs:

- At the Argonne National Laboratory (ANL) in the United States, SFR steady-state neutron transport calculations are conducted using the DIF3D code, which embeds both the finite difference diffusion solver from the original DIF3D version (Derstine, 1984) and the variational nodal transport method VARIANT (Palmiotti, et al., 1996). Necessary multi-group cross-sections (XSs) for DIF3D calculations are evaluated instead by the in-house MC code MC^2-3 (Lee & Yang, 2017), specifically designed for fast reactor analyses. For perturbation and sensitivity analyses, ANL employs two codes: VARI3D and PERSENT (Smith, 1980). The former is based on the neutron flux solution of the finite difference diffusion solver, while the latter utilizes the neutron flux solution of the VARIANT solver. Complex structural analyses involving core restraint systems are performed by means of structural analysis code NUBOW-3D (Brunett, et al., 2017).

  ANL's transient simulation tool for SFR system analyses is the SAS4A/SASSYS-1 code. The code enables the analysis of operational transients as well as of design and beyond-design basis accidents, with and without core degradation (Brunett, et al., 2017). The system code is equipped with a built-in point kinetics model and has also been coupled with spatial neutron kinetics versions of DIF3D, i.e., DIF3D-K and VARIANT-K (Cahalan, et al., 2000). SAS4A/SASSYS-1 has gained global recognition and has been adopted by prominent organizations, including the

China Institute of Atomic Energy (CIAE) and TerraPower (IAEA, 2017). Moreover, an alternative version of SAS4A based on an older version of 1986, known as SAS-SFR (Imke, et al., 1994), is being co-developed and applied by the Commissariat à l'Energie Atomique (CEA), French Radioprotection and Nuclear Safety Institute (IRSN), Japan Atomic Energy Agency (JAEA), and Karlsruhe Institute of Technology (KIT).

- The SIMMER code is the result of a collaborative effort among several research organizations. SIMMER (Tobita, et al., 2002), originally SIMMER-II, was developed as first practical tool of its kind by Los Alamos National Laboratory (LANL), United States. A newer version of the code, i.e., SIMMER-III, emerged in late 1988, through the collaboration between LANL, and the Power Reactor and Nuclear Fuel Development Cooperation (PNC, now JAEA). The project was definitively handed over to PNC after a two-year joint study, re-gaining international interests. Since 1992, in fact, European research organizations such as Kernforschungszentrum Karlsruhe (now KIT) of Germany, and CEA have taken part to its development (Buckel, et al., 1999). Initial SIMMER-III limitations related to two-dimensionality flow modeling capability, have been addressed in a three-dimensional (3D) version, i.e., SIMMER-IV (Yamano, et al., 2008).

  So far, the tool has served as an advanced safety analysis computer code for core disruptive accidents of various reactor types with different neutron spectra and coolants. The SIMMER code covers three main modeling aspects: neutronics, structural (fuel-pin) modeling, and fluid-dynamics. The neutronics model generates nuclear heat sources using time-dependent neutron flux distributions. Related calculations are performed by an SN transport model via the TWODANT solver for space-dependent neutron flux and an improved quasi-static method for dynamics (Buckel, et al., 1999). Alternatively, the code can also employ its built-in point kinetics model (Poumerouly, et al., 2016). The evaluation of shielded macroscopic cross-section for the neutron transport equation solver can be carried out within the code. Structure modeling capabilities allow for the simulation of immobile fuel pins and cladding walls, interfaced with the fluid-dynamics model for heat and mass transfer. SIMMER can model up to five core materials: fuel, steel, sodium, control rods, and fission gas in solid, liquid, and vapor states.

- At CEA the neutronic analyses for fast reactors have been until recently performed by the ERANOS code (Rimpault, et al., 2002) which encompasses two main solvers for steady-state full core calculations: The BISTRO code (Palmiotti, et al., 1987) based on the SN method, and the TGV/VARIAN based on the variational nodal method. XSs for ERANOS full core calculations were generated by its submodule ECCO, which is a cell and lattice code (Rimpault, et al., 1989).

The ERANOS code is being replaced by the APOLLO-3 and TRIPOLI-4 codes, respectively, deterministic and stochastic codes (Schneider, et al., 2016). CEA can also rely on the GERMINAL code (Lainet, et al., 2019) for the performance of detailed fuel rod behavior analyses.

The CEA's main system analysis tool is CATHARE (Geffraye, et al., 2011), co-developed by AREVA, CEA, EDF, and IRSN and initially applied to the safety analyses of PWRs. CATHARE has been recently extended and thoroughly validated for SFRs (Tenchine, et al., 2012). In the transient analyses of SFRs, the system code employes a built-in point kinetics model with reactivity coefficients and kinetic parameters, provided, e.g., by APOLLO-3 (Sciora, et al., 2021).

- In Switzerland, the Paul Scherrer Institut (PSI) has developed the computational platform FAST (Mikityuk, et al., 2005) for the static and transient analysis of fast reactors including SFRs. The computational platform can rely on the American spatial reactor kinetics code PARCS based on nodal methods (Downar, et al., 2004). Nuclear XSs used in PARCS can be generated by ECCO, or alternatively, by the MC code Serpent (Leppänen, et al., 2015), capable of performing cell, lattice, and full-core static neutronic. Realistic fuel rod behavior analyses are carried out by the fuel performance code FRED (Mikityuk & Shestopalov, 2011).

  The system code of FAST is the best-estimate system code TRACE (Bajorek, 2008) developed by U.S. Nuclear Regulatory Commission (NRC). TRACE is currently capable of conducting static and transient thermal-hydraulic analyses of reactor systems using either sodium, water, helium, or lead-bismuth eutectic as a coolant. Within the FAST platform, the system code TRACE can account for the modeling of neutron kinetics either by its built-in point kinetics model, or by spatial kinetics models via an implemented coupling with PARCS (Mikityuk, et al., 2005).

- The computational platform GeN-Foam (Fiorina, et al., 2015), developed in Switzerland at the École Polytechnique Fédérale de Lausanne (EPFL), is based on OpenFOAM and represents a rather new multiphysics computational tool still under validation. GeN-Foam is currently able to simulate the multiphysics problem of SFRs by exploiting finite-volume methods for mostly all the physical fields of the problem. In particular, by applying finite-volume methods, the GeN-Foam can account for multi-scale mesh solvers for the modeling of thermal hydraulics at core and system levels, and spatial neutron kinetics solvers. As an alternative to spatial kinetics models, GeN-Foam offers also an embedded point-kinetics model for neutron kinetics simulation purposes. Necessary nuclear data required by the neutronic analyses are generated by Serpent. The

platform also offers finite-volume models for thermal-mechanical analyses of structures, which were already applied to the analyses of core flowering effects (Fiorina, et al., 2019).

GeN-Foam is certainly a promising and thorough computational platform. However, the application of finite volume methods for handling most of the physical fields of the problem presents still nowadays major limitations in terms of computational times, which are extremely time-demanding. This holds particularly true for those analyses that provide for modeling of large domains of the SFR systems, such as for instance, SFR primary pools. In such cases, the calculations can become excessively time-consuming, rendering the usage of the computational platform impractical.

All the computational platforms introduced above have the capabilities to perform quite complete and detailed system analyses while covering several aspects of the multiphysics domain, including core neutronics which is simulated either via point or spatial neutron kinetics models. Both modeling approaches entail specific advantages and disadvantages.

The point kinetics typically allows for faster calculations and the prediction of global changes in reactor power and reactivity. However, the approach does not allow one to predict spatial variations in the power shape within the reactor core. Studies such as (Lázaro, et al., 2014a; 2014b; Kruessmann, et al., 2015; Ponomarev, et al., 2021b) have shown the applicability and reliability of this approach for SFR transient analyses in scenarios where no strong perturbations of the core power shape are expected. Conversely, to simulate realistic variations of the core power shape, including those originated by an asymmetric core behavior, spatial kinetics models should be applied and coupled to system codes while performing system analyses. For instance, as done for SAS4A\SYS1 and DIF3D-K (Cahalan, et al., 2000), TRACE and PARCS (Mikityuk, et al., 2005), and, recently, SAS-SFR and PARCS (Ponomarev, 2017). Such an approach requires, naturally, longer computational times as compared to the previous one.

In line with the need to cover as much as possible the analysis domain of SFR transient scenarios, including those involving asymmetric core behavior, the Helmholtz-Zentrum Dresden-Rossendorf (HZDR) is developing its computational platform for the analyses of SFR systems. Such platform should be based on DYN3D (Rohde, et al., 2016), a reactor core simulator based on nodal diffusion methods which is being actively developed by HZDR. Currently, the reactor core simulator and the MC code Serpent (Leppänen, et al., 2015), used for XS generation, are jointly applied by the HZDR as a computational platform dedicated to the analyses of SFR cores. Such platform is planned to be further extended to the analyses of SFR system via coupling with the system code ATHLET

(Austregesilo, et al., 2016). Such an extension aims at providing the platform with the necessary computational capabilities to conduct SFR system analyses with DYN3D applied as a spatial neutron kinetic solver.

1.3 A DYN3D-based platform for SFR system analyses

The DYN3D code is a nodal diffusion reactor core simulator initially developed for LWRs, and also a well-established tool in the framework of the European scene for the analyses of LWRs (Kliem, et al., 2017; Chauliac, et al., 2010). Recently the code has undergone significant and continuous development to gain the capability of performing analyses of SFR cores. As a standalone core simulator, DYN3D allows for the static and transient core analyses while accounting for spatial neutron kinetics, and core thermal hydraulics. In addition, the code is capable of performing space-dependent decay heat power calculations and burnup calculations, allowing for the simulation of fuel cycle and subassembly shuffling operations.

The DYN3D neutronics model relies on the solution of 3D neutron diffusion equations in a multi-group approximation by nodal expansion methods (Rohde, et al., 2016; Bilodid, et al., 2018b). Namely, the neutronics problem is spatially handled by discretizing the reactor core into several axial layers. These layers are further subdivided into several prismatic nodes with trigonal, squared, or hexagonal bases. Multi-group neutron diffusion equations are solved over the nodes by making use of nodal expansion methods. For each energy group, the equations are solved by expanding the neutron flux into polynomials and exponential functions.

Core thermal hydraulics and heat conduction models have been developed in a dedicated module called "FLOCAL" (Manera, et al., 2005). The module is capable of modeling the coolant behavior along simulated core mono-dimensional (1D) channels through thermal-hydraulic balance equations of mass, moment, and energy. FLOCAL also includes 1D radial heat conduction models dedicated to the simulations of fuel rods (Rohde, 2001). The models allow one to set user-defined values of gap conductance or, alternatively, for the evaluation realistic gap conductance values through the URGAP model (Lassmann & Hohlefeld, 1987).

In addition, in the framework of LWR analyses, DYN3D has been coupled with system codes such as ATHLET (Grundmann, et al., 1995; Kozmenkov, et al., 2007; Kozmenkov, et al., 2015), and RELAP5 (Kozmenkov, et al., 2001; Kliem, et al., 2006), the sub-channel code SUBCHANFLOW (Gomez-Torres, et al., 2012), the computational fluid dynamics tool ANSYS CFX (Grahn, et al., 2015), and the fuel performance code TRANSURANUS (Holt, et al., 2014).

1.3.1 Serpent/DYN3D for SFR core analyses

The application of DYN3D to the analyses of SFRs was made possible by several recent extension and development activities carried out at the HZDR. These included, first of all, the upgrade of DYN3D coolant database properties with the thermal-physical properties of the liquid sodium. Subsequently, a sequence of development activities which were conducted in the framework of the previous doctoral dissertation in (Nikitin, 2019a). Namely:

- The development of a methodology for the generation of multi-group XSs, based on the MC code Serpent.
- The implementation of a thermal-mechanical module that could account for fuel axial and diagrid radial thermal expansions.

A Serpent-based methodology for the generation of few-group XSs to be used in SFR analyses was developed and validated in (Nikitin, et al., 2015a; 2015b). The methodology foresees, the generation of homogenized XSs via Serpent cell and lattice calculations for multiplying and non-multiplying regions. The methodology also foresees the eventual corrections, via the super-homogenization method (SPH), of those XSs representing non-multiplying materials facing fuel or absorber regions. The homogenized few-group XSs are generated over a 24-group energy structure as recommended in (Fridman & Shwageraus, 2013). The integration and validation of DYN3D with the thermal-mechanical module capable of simulating in-core thermal expansions was carried out in (Nikitin & Fridman, 2018a; 2018b; 2018c). In particular, the thermal-mechanical module allows DYN3D to take into account, dynamically, the uniform radial thermal expansion of the diagrid and the non-uniform axial thermal expansion of fuel.

The developments previously introduced, have enabled the joint application of DYN3D and Serpent in a computational platform dedicated to static and transient analyses of SFR cores. Since then, the platform has been applied to several benchmarks. Let us consider, for instance: The Phénix benchmark tests on the CRs withdrawal and unprotected stage natural circulation (IAEA, 2013; IAEA, 2014b), the static SPX benchmark (Ponomarev, et al., 2021a), and the FFTF benchmark (Nikitin & Fridman, 2019).

1.3.2 Extension to system analyses via ATHLET

The next milestone set in the development of the Serpent/DYN3D platform consists of the extension of the platform analyses domain from SFR cores to SFR systems. As previously mentioned, such objective can be achieved, e.g., through a coupling of DYN3D with a system code. Considering long

strategical cooperations between the HZDR and the Gesellschaft für Anlagen- und Reaktorsicherheit (GRS), developing the system code ATHLET (Austregesilo, et al., 2016), as well as previous existing and well-trusted coupling options between DYN3D and ATHLET for LWRs, the choice of the system code to be used for extending the analyses domain of the HZDR platform fell on ATHLET.

ATHLET is a system code originally conceived and designed for the analysis of LWRs. The code was developed with the purpose of simulating the behavior of LWR systems under different operational conditions, including steady-state and transient scenarios. The continuous extension of the system code and the update of the thermal-hydraulic database for coolant properties made it recently applicable to various generation-IV reactor concepts, including SFRs.

ATHLET is a comprehensive system code comprising multiple modules, each dedicated to the modeling a specific physical field. The system code comprises, in particular:

- The "TFD" module: It allows for modeling thermo-fluid-dynamics in systems through the creation of network representations for thermal-hydraulic systems. This is achieved by combining elementary objects to simulate the system flow paths. The primary elementary thermo-fluid-dynamic objects used are "pipes" and "branches". Pipes are 1D objects that simulate the behavior of coolant using 1D conservation equations governing mass, energy, and momentum. Branches are zero-dimensional (0D) control volumes used for merging branching pipes. Additionally, ATHLET supports the modeling of "cross-connection" objects. These objects enable transversal connections of parallel pipes, allowing for the modeling of 3D flow paths of systems.

- The "HECU" module: It comprehends models for the simulation of heat conduction and heat transfer within the solid structures of the systems, including fuel rods, heat exchanger pipes, and other reactor internals. Heat conduction models have been developed for simplified geometries, such as plates, hollow and full cylinders, and spheres. The module also includes heat transfer correlations, regulating the wall-to-fluid heat transfer.

- The "NEUKIN" module: The module includes built-in point kinetics model. It can consider reactivity effects due to fuel temperature, moderator temperature, etc., and other flexibly user-defined reactivity effects. Alternatively, NEUKIN allows for coupling with neutron spatial kinetics codes, such as DYN3D.

- The "GCSM" module: It serves as the control logic unit for the simulated systems. Through the definition of signals, it can monitor system variables, simulates hardware control, and initiates

protection actions, such as, e.g., control rod insertion. Control circuits, fluid systems, and balance-of-plant can be easily modeled by combining various signal options such as adders, delays, function simulators, switches, etc. These signals can be fed by variables of any ATHLET module. In addition, GCSM signals can be used also to simulate pressure, mass flows, power, and heat flux boundary conditions.

As well-established system code for LWRs, ATHLET has undergone continuous and systematic validation tests. These validation tests cover international standard problems and transient scenarios of real plants (Hollands, et al., 2021). Early stages validation and benchmarking activities have been recently conducted also for SFRs: Let us consider, for instance (Zhou, et al., 2013; Di Nora, et al., 2019; Ponomarev, et al., 2021b).

1.4 Knowledge gap in SFR modeling

As evident from Section 1.2, analyses of SFR systems can nowadays be conducted with quite a high degree of detail with modeling capabilities allowing for static and transient simulation of SFR systems while providing capabilities for spatial kinetics modeling (Cahalan, et al., 2000; Mikityuk, et al., 2005; Ponomarev, 2017), fuel rod performance (Lainet, et al., 2019; Mikityuk & Shestopalov, 2011), and structural mechanics (Brunett & Fanning, 2017; Fiorina, et al., 2019; Nikitin & Fridman, 2018a). Existing computational platforms can cover the analyses of SFRs for normal operation, anticipated occurrences, design, and beyond-design basis accidents, even including in some cases the core degradation (Brunett & Fanning, 2017; Tobita, et al., 2002).

However, further improvements in modeling capabilities can still be considered, for instance, in modeling effects that structural mechanics of out-of-core structures, such as CRDLs, strongback, and vessel, might have on core neutronics. The thermal expansion effects of such out-of-core structures have been revealed to be of crucial importance in analyses of SFRs because they directly affect the position of control rods within the core, thus, the reactor dynamic, see e.g., (Mikityuk & Schikorr, 2013). In the context of system analyses, these effects have been so far only accounted for, for calibration purposes, through simplified lumped heat structure models provided of tuned parameters such as, e.g., axial lengths and time-delay constants to simulate the thermal inertia of structures. The lumped heat structure models have been suitably coupled with point kinetics models via assumed reactivity coefficients (Mikityuk & Schikorr, 2013; Di Nora, et al., 2019) or pre-evaluated differential control rod worths (Ponomarev, et al., 2021b).

More realistic modeling of the effects outlined above can potentially be achieved in system analyses performed with spatial kinetics codes. Spatial kinetics codes might, in fact, allow one to account for the impact that thermal expansions of the out-of-core structures have on reactor dynamics via the direct adjustment of instantaneous control rod positions without requiring major approximations or preliminary calculations. Furthermore, modeling capabilities of such out-of-core effects can be significantly improved by adopting more realistic modeling approaches for out-of-core structures, e.g., considering their actual geometries and thermal inertia, along with realistic sodium flow paths within the system.

System analyses carried out by system codes coupled with spatial kinetics models offer competitive computational times especially when compared to more detailed analyses involving finite volume elements, as in OpenFOAM for instance. Nonetheless, there is still considerable room for optimizing the computational times required to perform spatial neutron kinetics calculations. One of the challenges lies in selecting an appropriate number of energy groups used for the discretization of the neutron flux that can ensure accurate predictive capabilities. Numerous studies have delved into this complex optimization problem, employing various methods such as the particle swarm optimization (Yi & Sjoden, 2013; Fleming, et al., 2016), the genetic algorithms (Massone, et al., 2017), and the simulated annealing (Di Nora, et al., 2021a; 2021b). While the previously outlined research has demonstrated that quality static solutions can be obtained using as few as half to one dozen energy groups in terms of multiplication factor and radial power distribution, the current state-of-the-art still employs 2 to 3 dozen energy groups in transient analyses of SFRs to ensure high-quality solutions.

There is significant value in exploring the possibility of using fewer energy groups to substantially speed up the times of transient analyses, without sacrificing solution quality. Investigating this within the framework of analysis performance of SFR is essential.

1.5 Thesis objectives

In line with the developments planned by HZDR to extend its SFR-dedicated platform from the analyses of SFR cores to SFR systems, see Section1.3, and in the light of the potential improvements in modeling and in analysis performance outlined in Section 1.4, this thesis has set the following high-level objectives:

- Extending the platform modeling domain from SFR cores to SFR systems, while including neutronic feedback rising from relevant out-of-core structures;
- Verifying and validating the new extended platform, and formulating its area of applicability;

- Optimizing the platform computation times against the accuracy of solutions through the optimization of XSs.

1. The extension of the modeling domain of the platform to SFR systems is achieved via the coupling with the system code ATHLET, capable of modeling the liquid sodium. The choice of ATHLET for coupling purposes allows one to exploit the existing LWR-version of the DYN3D/ATHLET as the starting point of the extension activity. This first thesis objective is achieved by implementing targeted modifications to the existing coupling routines to make these last applicable to SFR analyses. In particular, the modifications aim at allowing DYN3D/ATHLET to exploit the DYN3D models developed in (Nikitin, et al., 2018a; 2018b; 2018c) to catch in-core feedback effects, i.e., non-uniform fuel, clad- or fuel-driven, axial thermal expansions, and uniform diagrid radial thermal expansions. In addition, the objective requires the development of ATHLET-based modeling approaches to model relevant out-of-core structures and related effects on CR positions, see Section 1.1.4.

2. The extended computational platform and the developed ATHLET-based modeling approaches accounting for thermal expansions of out-of-core structures are extensively verified and validated against experimental benchmarks performed on Phénix and Superphénix (SPX). These benchmarks are, namely, the Phénix end-of-life (EOL) natural circulation (NC) test (IAEA, 2013) and SPX start-up tests (Ponomarev, et al., 2021b).

3. The optimization of the computational times of the platform against the accuracy of transient solutions is based on the application of condensed and optimized energy group structures (EGSs) used in the modeling of XSs. Such condensed and optimized EGSs were selected by a procedure involving the meta-heuristic simulated annealing algorithm, developed and applied in the framework of this doctoral thesis. The algorithm and the identified optimized EGSs are presented and then applied to transient analyses for optimization purposes. In this same optics, two main existing options for XS parametrization are presented and compared for the purposes of computational time reduction.

By accomplishing the high-level objectives outlined above, this thesis concretely aims, among others, at extending, validating, and optimizing a new computational platform for SFR applications. In the context of this dissertation, for SFR applications one means static and transient analyses of SFR systems, excluding scenarios that encompass sodium boiling or core degradation phenomena.

1.6 Dissertation structure

Beyond this introductory chapter, the dissertation consists of other four chapters. In particular, Chapter 2 presents a detailed description of the existing DYN3D/ATHLET coupling routines and

their extensions to SFR analyses. The chapter also presents ATHLET-based methodologies applied in this thesis for modeling the relevant out-of-core structures. Chapter 3 introduces the validation and verification (V&V) of the new computational platform, along with an overview of the reactors and related benchmarks used for the V&V exercises. Chapter 4 focuses on the optimization of few-group XSs. The chapter describes the simulated annealing algorithm, used for selecting optimal condensed energy groups to be used in SFR analyses. In addition, for optimization purposes, two main XS parametrization approaches are presented and compared in the chapter. Finally, Chapter 5 concludes the dissertation by providing a concise summary of the accomplishments of the doctoral research and offering suggestions for future research investigations.

Chapter 2 Code extension and modeling of out-of-core structures

This chapter describes the steps performed to achieve the objective of extending the modeling domain of the HZDR computational platform from SFR cores to SFR systems. To reach such objective, the capability of modeling reactor systems beyond the core should be provided to the computational platform, e.g., via a coupling with a system code. The ATHLET code system, capable of modeling the liquid sodium, was selected for this purpose. The choice of the GRS's code, ATHLET, was dictated by two main strategic reasons:

- First, a "DYN3D/ATHLET" coupling version existed already for LWRs and could be efficiently employed as a starting point for the platform extension, see Section 1.3.2.
- Second, in view of the extension, eventually required modifications of ATHLET could be promptly implemented by GRS with which the HZDR can boast a long historical cooperation.

The platform extension, described in detail in this chapter, comprised:

- Modifications of the existing DYN3D/ATHLET coupling routines to account for in-core reactivity feedback specific to SFRs. Such effects were already considered in Serpent/DYN3D and should be considered also in the extended platform.
- Development of ATHLET-based modeling approaches to account for relevant out-of-core TE effects on core neutronics. Specifically, the out-of-core structures considered were CRDLs, strongback, and reactor vessel.

Steps of the platform extension are presented in this chapter as follows. Section 2.1 presents the modifications of the DYN3D/ATHLET coupling routines. Section 2.2 describes ATHLET approaches used in this thesis for modeling of out-of-core structures and related reactivity feedback effects. In particular, first, a detailed approach involving the explicit modeling of primary systems is introduced in Section 2.2.1; the approach was developed in the frame of this thesis. Then, a simplified approach involving the modeling of primary systems by BCs is described in Section 2.2.2; this latter approach, already applied for ATHLET in (Ponomarev, et al., 2021b), was adapted to facilitate its application to DYN3D/ATHLET.

2.1 Modification of DYN3D/ATHLET coupling routines

In DYN3D, the neutron kinetics (NK) problem is spatially handled by expanding the reactor core into several prismatic nodes onto which nodal diffusion equations are solved. For each node, homogenized XSs are produced according to the composition of materials and values of specific state variables within the nodal volume, e.g., fuel and coolant temperatures, coolant density, etc. In standalone neutronic calculations, XSs are generated for fixed values of state variables and do not change during the entire calculations. In coupled neutronic and thermal-hydraulic calculations, the values of nodal XS should be updated according to actual nodal distributions of the state variables they depend on.

DYN3D accounts for XS dependencies on state variables by applying the so-called multi-dimensional table (MDT) parametrization approach (Rohde, et al., 2016). In particular, in the MDT approach, several values of the different state variables are selected within user-defined ranges. Then nodal XSs are generated, e.g., by Serpent, for all the combinations of values of the state variables previously selected. Finally, XS are stored in a suitable tabular format. During calculations, the nodal XSs are actualized on the run according to actualized nodal values of the state variables by accessing corresponding tabular data and performing multi-dimensional interpolations when needed. Fig. 3 shows a conceptual representation of an MDT XS table for three generic variables X_1, X_2, and X_3.

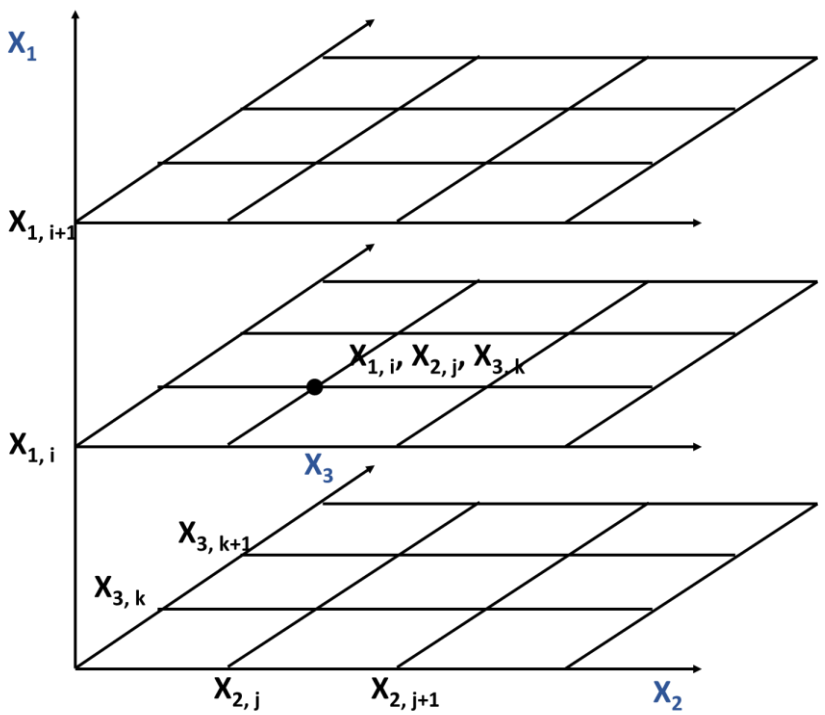

Fig. 3. MDT XS table: Example of multidimensional grid involving three generic variables X_1, X_2, and X_3

In the current XS parametrization approach used for LWR analyses, DYN3D considers the following state variables: Fuel and coolant temperatures, T_f and T_c, coolant density, ρ_c, and boron concentration, C_b. In addition, one might also account for the dependency of the fuel burnup, b. The dependency on state variables of XSs for a generic nuclear reaction "x" within the reactor core node "i", and related to the energy group (EG) "g" is then expressed in Eq. 2.1. If calculations with fixed burnup are to be performed, then $\Sigma_x^g|_i$ can be expressed by Eq. 2.2.

$$\Sigma_x^g|_i = \Sigma_x^g(b, T_f, T_c, \rho_c, C_b)|_i \qquad \text{Eq. 2.1}$$

$$\Sigma_x^g|_i = \Sigma_x^g(T_f, T_c, \rho_c, C_b)|_i \qquad \text{Eq. 2.2}$$

Instantaneous values of state variables appearing in Eq. 2.1 and Eq. 2.2 are evaluated, per node, by the FLOCAL module and then provided to the NK module of DYN3D that actualizes the XS values. In relation LWRs, a simplified scheme of variable exchanges between FLOCAL and the DYN3D NK module is presented in Fig. 4a.

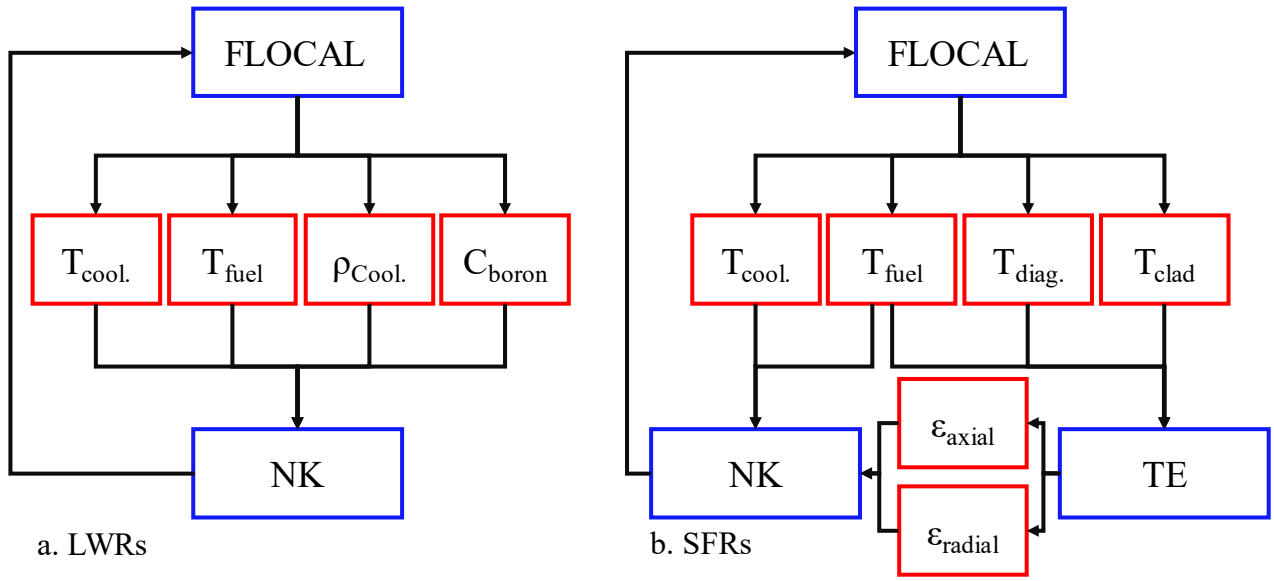

Fig. 4. a) LWR scheme: Variables exchange between the FLOCAL and NK modules. b) SFR scheme: Variables exchange among the FLOCAL, TE, and NK modules.

The XS parametrization employed by DYN3D for SFR analyses is rather different, see Table 3. To account for SFR specifics, XSs are parametrized by fuel and coolant temperatures, T_f and T_c, axial thermal expansions of the fuel elements driven by either clad or fuel, ε_a, and average radial expansion of the diagrid, ε_r.

Table 3. XS dependencies in DYN3D for LWRs and SFRs

XS parameter	LWRs	SFRs
Fuel temperature	✓	✓
Coolant temperature	✓	✓
Coolant density	✓	*
Boron Concentration	✓	
Fuel axial expansion (clad- or fuel-driven)		✓
Diagrid radial expansion		✓

* implicitly considered: $\rho_c(T_c)$

For SFRs, the dependency on state variables of XSs is then expressed by Eq. 2.3, or by Eq. 2.4 if calculations are performed with fixed burnup. At the current stage of DYN3D development, the effect of the coolant density on XSs is implicitly considered through its correlation with coolant temperature. That is, the sodium density is considered as a function of the coolant temperature in the process of XS generation.

$$\Sigma_x^g|_i = \Sigma_x^g\left(b, T_f, T_c, \varepsilon_a, \varepsilon_r\right)|_i \qquad \text{Eq. 2.3}$$

$$\Sigma_x^g|_i = \Sigma_x^g\left(T_f, T_c, \varepsilon_a, \varepsilon_r\right)|_i \qquad \text{Eq. 2.4}$$

In Eq. 2.3, and Eq. 2.4, the T_f and T_c are evaluated by FLOCAL as done for LWRs, while ε_a and ε_r are provided by the DYN3D TE module, recently implemented (Nikitin & Fridman, 2018a). Fig. 4b shows a simplified scheme of the exchange of variables among the FLOCAL, TE, and NK modules.

It is worth mentioning that core nodal distributions of the state variables, such as the fuel, clad, and coolant temperatures, are evaluated and collected by FLOCAL for all core nodes, e.g., nodes of fuel subassemblies, radial blanket, shielding regions, etc. All the axial regions of the subassemblies are considered, e.g., fissile and fertile regions, axial reflectors, gas and sodium plena, etc. Core nodal state variables related to the coolant, e.g., coolant temperature, density, etc., are averaged quantities evaluated within each volume of the core nodes. Whereas, core nodal state variables related to fuel rods, or solid structures in general, are averaged (within each core node) over the radial nodes of 1D heat conduction models, fuel rods are modeled with. The evaluation of the average diagrid temperature is instead carried out via a dedicated heat structure model implemented in (Nikitin & Fridman, 2018a). In principle, the modeling approach and capabilities described above enable, with a sufficient degree of detail, the collection of all TH variables required for each node by the XS models.

Beyond the schemes previously shown in Fig. 4a and Fig. 4b, which were presented as implemented in DYN3D, a variable exchange scheme for DYN3D/ATHLET was also developed for LWRs (Kozmenkov, et al., 2015). The developed DYN3D/ATHLET scheme was practically identical to the one shown in Fig. 4a, with the difference that FLOCAL was replaced by ATHLET. The current extension activity required the implementation of the SFR-dedicated scheme of Fig. 4b in DYN3D/ATHLET, starting from the existing LWR-version of the coupling.

In the existing LWR-version of DYN3D/ATHLET, the coupling routines were already able to collect from ATHLET the nodal distributions of T_f, T_c, ρ_c, and C_b. The distributions were then provided to DYN3D through dedicated data-acquisition and data-transfer blocks. In this regard, the following observations can be made in view of the DYN3D/ATHLET extension to SFRs:

- First, existing DYN3D/ATHLET data-acquisition and data-transfer blocks of T_f and T_c nodal distributions can be exploited without any modifications.
- Second, existing DYN3D/ATHLET data-acquisition and data-transfer blocks of nodal distribution of ρ_c, and C_b should not be accounted for. In fact, as Table 3 shows, ρ_c, and C_b are not directly exploited in DYN3D for SFRs applications.
- Finally, missing data-acquisition and data-transfer blocks for nodal clad temperature distribution and diagrid average temperature, required for the evaluation in DYN3D of the nodal state variables ε_a and ε_r, have to be implemented within the coupling routines.

The extension of the DYN3D/ATHLET from LWR to SFR applications was performed considering the observations listed above. Further details on the modifications of the coupling routines are reported in Appendix A. Related V&V tests of the extended routines are presented in the next chapter.

2.2 Modeling of out-of-core structures

As outlined in Section 1.1.4, axially expanding out-of-core structures such as CRDL, strongback, and vessel can alter the effective position of CRs with respect to the core and introduce non-negligible reactivity effects. Conceptually, expansions of such out-of-core structures can already be modeled in ATHLET by heat structures, and signals. This section shows how such out-of-core TE effects can be actually modeled in ATHLET for evaluating the changes in CR positions, which are subsequently dynamically transferred to DYN3D. In this regard, two possible ATHLET-based modeling approaches are presented in the following. The modeling approaches differ in the degree of detail with which both the primary system and out-of-core heat structures are represented, specifically:

- The first is a more realistic modeling approach applicable when a comprehensive modeling of the primary circuit can be conducted. In this case, the comprehensive representation of the primary loop allows for more detailed and realistic modeling of the out-of-core structures and their placement within the primary system. This method is described in Section 2.2.1 and constitutes a more systematic approach developed and applied in the frame of this doctoral thesis for the modeling of relevant out-of-core structures.

- The second is a simplified modeling approach applicable when the primary system is modeled through BCs defined at the inlet and outlet of the core. In this case, the out-of-core structures can be still modeled with simplified heat structures located close to the model boundaries. This approach is described in Section 2.2.2 and, it should be emphasized, represents an adaptation to ATHLET of existing models proposed for TRACE in (Ponomarev, et al., 2021b).

Both the aforementioned approaches are meant for the modeling of pool-type SFRs.

2.2.1 Detailed approach

The method described in this section is to be applied when the comprehensive modeling of the primary circuit is possible. In this case, more realistic representations of CRDLs, strongback, and vessel structures, as well as their axial TE effects can be accounted for. The method requires:

- The acquisition of data for the system under analysis, especially of those data related to the out-of-core structures, e.g., geometrical data, thermophysical properties of materials etc.

- The thermal-hydraulic modeling of all relevant parts of the primary system, e.g., primary hot and cold pools, below-core regions, vessel cooling system, redan, IHXs, primary pumps, DHRS, out-of-core structures, etc.

Before describing the approach for modeling out-of-core structures, this section provides an overview of a generic modeling approach for creating a coarse mesh to model an SFR primary system with ATHLET, using a porous medium approach.

According to this approach, the primary system is represented by using a very coarse 3D cylindrical mesh with azimuthal sectors defined in correspondence of azimuthal positions of IHXs, primary pumps, and DHRSs (if any). The radii of the mesh are defined by the radial dimensions of the core regions, redan, vessel cooling system and vessel walls. Fig. 5.a shows an example of azimuthal and radial discretization of the primary circuit.

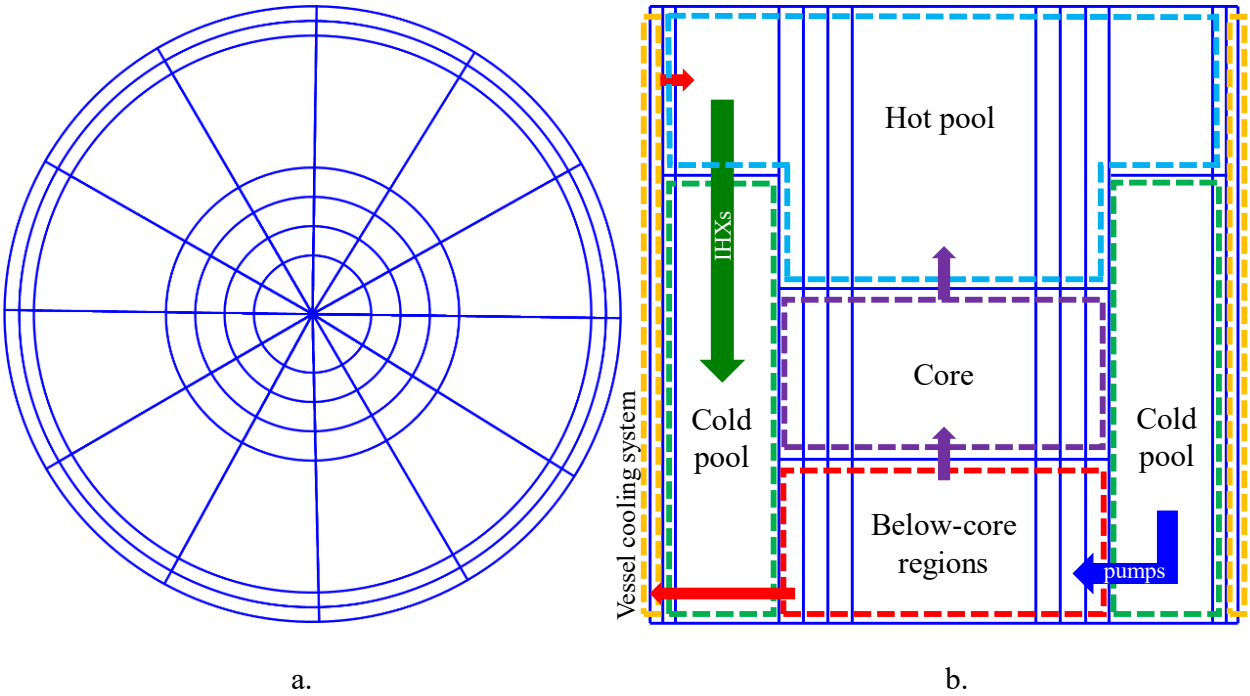

Fig. 5. SFR ATHLET primary system modeling scheme: a) azimuthal and radial discretization of the primary system, b) vertical view of the primary regions

Radial segments of the primary circuit are modeled by one or more vertical 1D thermo-fluid-dynamic objects, represented in Fig. 5.b by the blue rectangles in continuous lines. The thermo-fluid-dynamic objects are radially and azimuthally cross-connected in such a way as to define the various regions of the primary system. Actual 3D cylindrical or annular geometries are considered by dedicated ATHLET options. In particular, cylindrical geometries are used to model the hot pool and regions located below the core, whereas annular geometries are used for the modeling of the cold pool and vessel cooling system. For the core regions, the 3D option is not accounted for: The core is rather modeled through 1D channels as shown more in detail later in Section 2.2.2. Fig. 5.b shows a simple scheme of the primary system regions and their connections. In the figure, the 3D regions are marked by dashed lines, and connections by arrows. The below-core and hot pool regions are connected by the core channels. The IHXs and primary pumps, modeled by 1D thermo-fluid-dynamic objects, connect, respectively, the hot pool with the cold pool, and the cold pool with the below-core region. Connections from the below-core region to the vessel cooling system and from the latter to the hot pool are also modeled.

Heat exchanges are modeled between hot and cold pools, through the heat structure of the redan, and between primary and secondary circuits, through the heat structures of IHXs, see Fig. 6. The secondary circuits may be either modeled explicitly or simulated by heat-flux BCs.

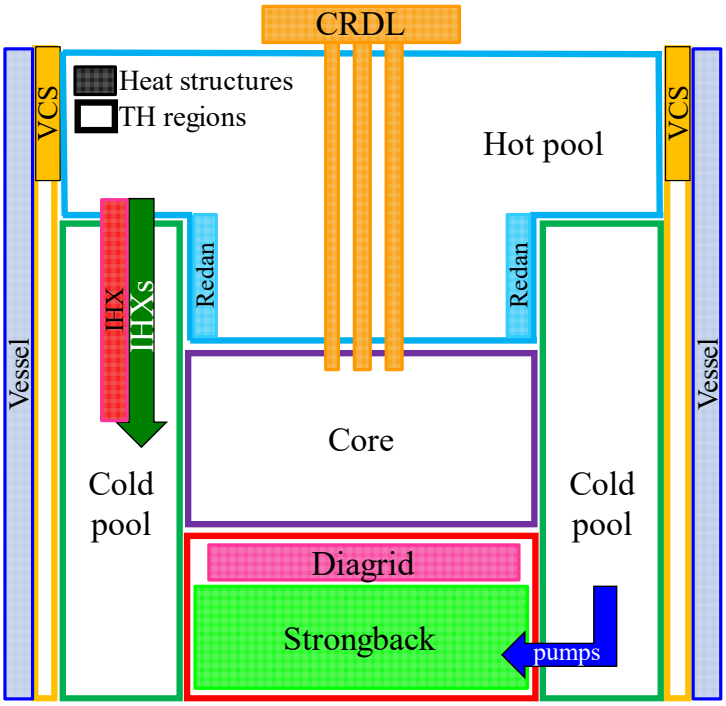

Fig. 6. Position-scheme of relevant heat structures within the primary circuit

According to this detailed approach, the heat structures of the CRDL, strongback, and vessel are represented as follows:

- The vessel wall, see Fig. 7a, is modeled as a hollow cylindrical structure split according to the azimuthal discretization of the system. In addition to the azimuthal discretization, the vessel heat structure presents an axial nodalization which is coherent with the nodalization of the thermo-fluid-dynamic objects to which the vessel is thermally coupled. The vessel structure is placed at the boundaries of the systems. Beyond the vessel walls, one might assume adiabatic conditions: Such assumption is especially applicable when simulating short-time transients, where the heat removal at the vessel boundary has negligible impact compared to other heat transfer pathways, such as heat exchanges between primary and secondary systems. Alternatively, more realistic vessel boundary conditions might be modeled, e.g., by imposing fixed or time-dependent heat fluxes on the external vessel walls or through more realistic modeling of the environment outside the vessel walls.

- The CRDLs, see Fig. 7b, are modeled by full cylindrical heat structures immersed inside the hot pool regions and partially within the core channels. The heat structures are axially nodalized in accordance with the nodalization of the thermo-fluid-dynamic objects constituting the hot pool.

- The strongback, see green structure in Fig. 7c, is modeled by multiple hollow cylindrical structures located across the radial segments of the model in the below-core regions. Furthermore, the structure is subdivided azimuthally upon the azimuthal sectors of the system.

The modeling of the diagrid, located on top of the strongback, is relevant to track dynamically the average temperature of such component and to feed the corresponding DYN3D radial diagrid TE model. In the modeling approach, the diagrid is modeled similarly to the strongback, see Fig. 7c.

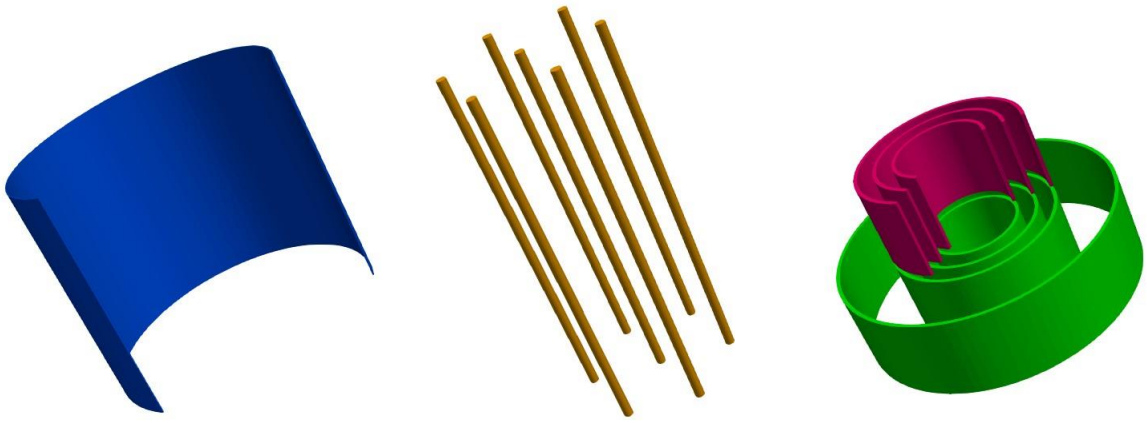

a. b. c.

Fig. 7. Schematic 3D view of heat structures models: a) Vessel walls. b) CRDL. c) Diagrid and strongback.

These models proposed for the modeling of out-of-core heat structures do not claim to recreate the exact geometry of the components. They rather aim at catching realistically enough the temperature trends within the thicknesses of the heat structures. Crucial for this purpose is the correct modeling of the thicknesses and thermophysical properties of the structural materials.

Absolute axial TEs of the out-of-core structures are evaluated through models accounting for (room temperature) axial lengths, and linear TE coefficients, respectively designated, "$L|_{Tref}$", and "α". For a generic structure of length "L", the axial elongation, "ΔL", induced by TEs at a generic time, "t", can be evaluated as shown in Eq. 2.5.

$$\Delta L(t) = L\big(T(t)\big) - L\big(T(t_0)\big) = L|_{T_{ref.}} \cdot \left[\int_{T_{ref.}}^{T(t)} \alpha\,(T)dT - \int_{T_{ref.}}^{T(t_0)} \alpha\,(T)dT\right] \qquad \text{Eq. 2.5}$$

In Eq. 2.5, T(t) and $T(t_0)$, are respectively the average temperature of the structure at generic times t and t_0, with t_0 assumed as the time at the beginning of the transient.

Exploiting the equivalence of Eq. 2.6, Eq. 2.5 can be rearranged in the form of Eq. 2.7.

$$\varepsilon_c\big(T(t)\big) = \int_{T_{ref.}}^{T(t)} \alpha\,(T)dT \qquad \text{Eq. 2.6}$$

$$\Delta L(t) = L|_{T_{ref.}} \cdot \left[\varepsilon_c\big(T(t)\big) - \varepsilon_c\big(T(t_0)\big)\right] \qquad \text{Eq. 2.7}$$

From a modeling perspective, the model formulation proposed in Eq. 2.7, is more convenient than that in Eq. 2.5. In fact, values of ε_c, can be pre-evaluated and stored as a function of the temperature in ATHLET and then used to compute ΔL without performing integral calculations. The general equation, Eq. 2.7, can applied to evaluate the axial TEs of the strongback, vessel, and CRDL through the procedures described below.

For the evaluation of the axial TE of the strongback, the ATHLET's GCSM module collects the temperature values all over the radial rings of the heat structure and averages them into a single value. The corresponding strongback axial TE, "ΔL_{sk}" is evaluated by applying the generic Eq. 2.7 exactly as in the form presented previously. The ΔL_{sk} is evaluated by replacing generic lengths and TE properties in Eq. 2.7 with specific lengths and TE properties of the strongback.

For the evaluation of the CRDL and vessel TEs, Eq. 2.7 has to be applied to calculate the axial TE of each axial node of the corresponding heat structures as shown in Eq. 2.8. The "T_j" shown in the equation is the average temperature of the axial node "j" of the heat structure, whereas $L_j|_{Tref.}$ is the axial length of the axial node j. The total axial expansion of the considered heat structures is then given by the sum of all the TEs of the nodes, see Eq. 2.9.

$$\Delta L_j(t) = L_j\big|_{T_{ref.}} \cdot \left[\varepsilon_c\left(T_j(t)\right) - \varepsilon_c\left(T_j(t_0)\right)\right] \qquad \text{Eq. 2.8}$$

$$\Delta L(t) = \sum_j \Delta L_j\,(t) \qquad \text{Eq. 2.9}$$

Eq. 2.8 and Eq. 2.9, are applied with the actual length and TE properties of out-of-core structures, to evaluate the axial TEs of CRDL and vessel, respectively, ΔL_{CRDL} and $\Delta L_{vl.}$

The total change in CR positions induced by the TEs of out-of-core strutures, ΔL_{tot}, at time t is then evaluated by summing up the contributions $\Delta L_{sk,}$ ΔL_{CRDL}, and ΔL_{vl} as shown in Eq. 2.10.

$$\Delta L_{tot}(t) = \Delta L_{vl}(t) - \Delta L_{CRDL}(t) - \Delta L_{sk}(t) \qquad \text{Eq. 2.10}$$

Fig. 8 provides more details on the working principle of Eq. 2.10, which describes, in fact, the effects that out-of-core TEs have on the CR position as seen by an observer placed at the core bottom.

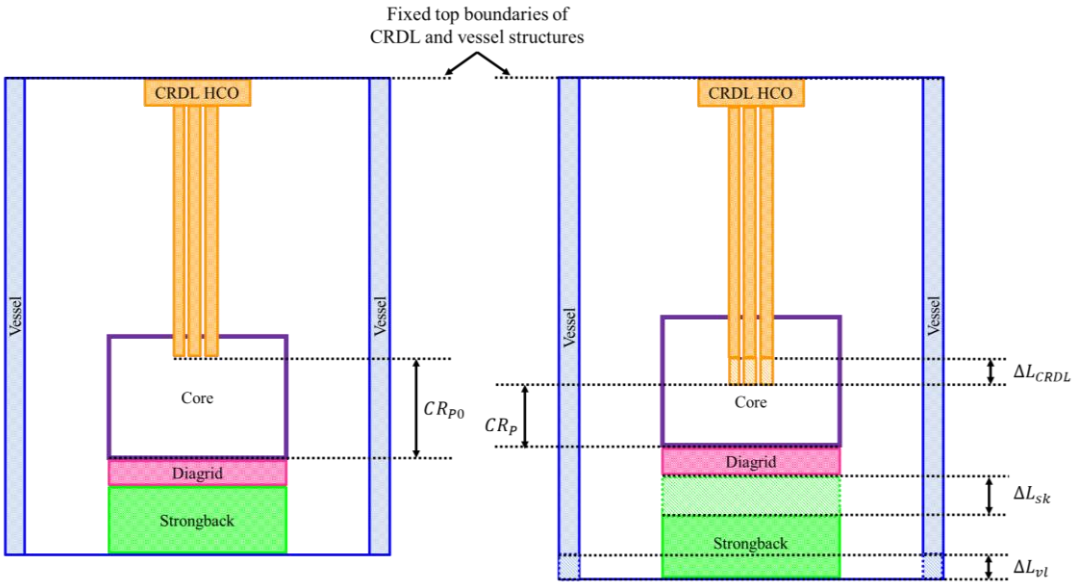

$\Delta L_{tot} = CR_p - CR_{p0}$
CR_{p0} = CR bottom position with respect to core bottom at time t_0
CR_p = CR bottom position with respect to core bottom at time t

Fig. 8. Schematic view of the TE contributions

With reference to Fig. 8 and considering that the upper extremes of both CRDL and vessel are assumed as fixed, the following can be stated:

- The expansion of the CRDLs brings CRs closer to the core bottom and reduces the distance of the former with respect to the latter. This aspect is considered by applying a negative sign ahead of ΔL_{CRDL} in Eq. 2.10.

- The expansion of the strongback pushes the core bottom in the direction of the CRs, leading to similar effects previously described for the expansion of CRDLs. This aspect is also considered by applying a negative sign ahead of ΔL_{sk}, see Eq. 2.10.

- The vessel expansion causes instead the downshift of the strongback, diagrid, and core, leading thus to an effective withdrawal of CRs. This aspect is accounted for by Eq. 2.10 through considering a positive sign for the contribution ΔL_{vl}.

It should be emphasized that ΔL_{tot} represents the correction factor to be dynamically applied to CR positions in DYN3D. It should be emphasized that ΔL_{tot} is evaluated by ATHLET and should be transferred through dedicated signals to DYN3D for the actualization of CR positions. Details of how

Eq. 2.10 is technically implemented by ATHLET signals, and of how such signals should be defined in ATHLET are shown in Appendix A, specifically, in Sections 2 and 3.

This detailed modeling approach was employed in the thesis for analyzing the initial stage of the natural circulation test performed on the Phénix reactor. Related V&V activities are presented in Section 3.1.

2.2.2 Simplified approach

The modeling approach described in this section is based on (Ponomarev, et al., 2021b) and it is to be applied when, beyond the core, the system is simulated through BCs. Fig. 9 shows, for clarity, the generic ATHLET modeling scheme involved by the approach.

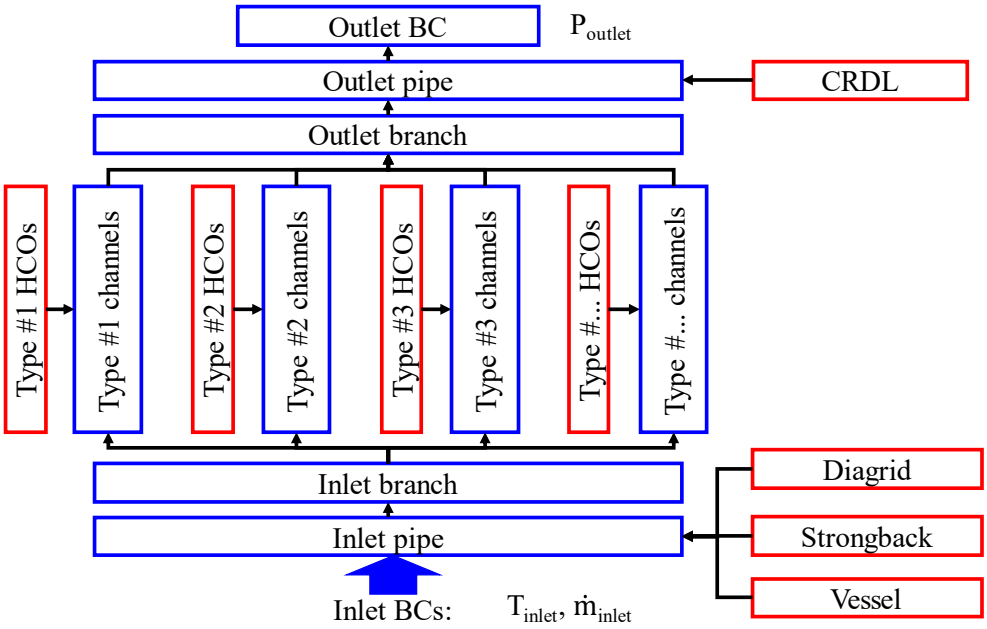

Fig. 9. SFR ATHLET modeling scheme with primary circuit response to the core simulated by BCs[1].

Fig. 9 shows in blue the thermo-fluid-dynamic objects of the model. Inlet mass flow and temperature fluid conditions are imposed through the inlet BCs represented by the blue arrow at the bottom of the figure. The coolant flows into the "Inlet pipe" and is branched through the "Inlet branch" into the core channels. The fluid merges again into the "Outlet branch" and flows through the "Outlet pipe" towards the exit of the system where a pressure BC is imposed on the branch "Outlet BC". This modeling scheme allows for the modeling of several types of core channels, each characterized by different geometries, friction loss coefficients, etc. Multiple channels of the same type can be grouped and represented by one channel with correspondingly increased flow and heat exchange areas. In the

[1] Where T_{inlet} and $\dot{m}_{inlet}$ are inlet temperature and mass flow rate of the coolant and P_{outlet} its outlet pressure.

scheme, core channels, and inlet and outlet channels are modeled as pipes. Cylindrical-shaped heat structures, marked in red in Fig. 9, are in addition linked to the core hydraulic channels. Such in-core heat structures are devoted to the modeling of fuel elements and other in-core solid structures.

In this simplified approach, out-of-core structures are modeled through representative heat structures attached either to the "Inlet pipe" (in the case of strongback and vessel) or to the "Outlet pipe" (in the case of the CRDL), as shown in Fig. 9. In more details, strongback and vessel are represented through hollow-cylinder-shaped heat structures, whereas the CRDLs are simulated by a cylindrical heat structure. In addition, the approach allows for the modeling of the diagrid, represented through a hollow-cylinder-shaped heat structure. In general, no axial discretization of the out-of-core structures and diagrid is accounted for.

To model each heat structure, approximate geometrical data such as equivalent thickness, equivalent axial length, and thermophysical material properties are required. Moreover, Eq. 2.7 is still applicable for the evaluation of the axial TEs of each out-of-core structure. However, further simplification of the model can be considered, e.g., using average values of the TE coefficients, "$\alpha_{ave.}$", instead of "ε_c". This simplification results in Eq. 2.11.

$$\Delta L(t) = L|_{T_{ref.}} \cdot \alpha_{ave.} \cdot [T(t) - T(t_0)] \qquad \text{Eq. 2.11}$$

Eventually, either the generic Eq. 2.7 or alternatively Eq. 2.11, have to be applied for the evaluation of the axial TEs of CRDL, strongback, and vessel, respectively, ΔL_{CRDL}, ΔL_{sk}, and ΔL_{vl}.

For the evaluation of ΔL_{tot}, one has to consider that the sodium flow paths from the core inlet to the structures and the thermal inertia of the latter are not directly modeled by the simplified approach. Clearly, both the sodium paths from the inlet core to the structures and the thermal inertia impact on the times with which the absolute TEs of out-of-core components effectively contribute to ΔL_{tot}. In this modeling approach, this aspect is tackled by considering representative time delays for the TE effects of CRDLs, strongback, and vessel, respectively, "Δt_{CRDL}", "Δt_{sk}", and "Δt_{vl}", see Eq. 2.12.

$$\Delta L_{tot}(t) = \Delta L_{vl}(t - \Delta t_{vl}) - \Delta L_{CRDL}(t - \Delta t_{CRDL}) - \Delta L_{sk}(t - \Delta t_{sk}) \qquad \text{Eq. 2.12}$$

It should be mentioned that the time delay related to CRDLs effect is much smaller compared to those of the vessel and strongback and can be neglected in most of the cases. A detailed overview of how Eq. 2.12 is implemented in ATHLET GCSM module is shown in Appendix A.2.

This simplified modeling approach was employed in the thesis for analyzing the SPX transient start-up tests. Related V&V activities are presented in Section 3.2.

2.2.3 Considerations on out-of-core structure models

In conclusion of the chapter, a few considerations on the pros and cons of the approaches used for modeling out-of-core structures can be drawn:

- The detailed approach represents a more realistic method and requires no major approximations or assumptions in the modeling of geometrical configurations and material properties of the out-of-core structures. That is, the structures are modeled as closely as possible in connection with the ATHLET modeling capabilities. In addition, sodium flow paths from the core inlet/outlet to the out-of-core structure surfaces are directly accounted for by modeling procedure. The aspects described above make unnecessary the usage of time delays to account for effectiveness of TE effects on CR positions.

  The main drawback of the approach lies in the efforts required for the acquisition of necessary geometrical and material data of the primary system and out-of-core structures, which are not always available.

- The simplified approach represents an efficient approximated modeling method that does not require a large amount of data to perform SFR analyses. However, the method requires sufficiently good assumptions, and parametric studies, to identify suitable "lumped" parameters for the model, i.e., equivalent geometries of out-of-core structures and time delay constants, capable of realistically emulate the physical behavior of systems under analysis.

Both the out-of-core modeling approaches presented in the chapter are applied in the next chapter in view of the V&V activities of the new platform, performed on experimental benchmarks dedicated to the Phénix and SPX reactors. Details on the Phénix and SPX models, including details of out-of-core structure models, are presented in the next chapter.

Chapter 3 Verification and validation

The goal of this chapter is to present the V&V of the newly extended HZDR computational platform as applied for the first time to the transient analyses of SFR primary systems. The V&V activities of this chapter show that the area of applicability of the platform can now cover static and transient analyses of SFR systems, at least for scenarios not involving sodium boiling or core damage.

- In the frame of platform extension, V&V activities [2]are essential to ensure, respectively, that the new platform (1) performs as intended by development specifications and (2) qualitatively fulfills the expectations related to its prediction capabilities. In this regard, the V&V of the platform presented in this chapter aimed at:Verifying the correct functioning of both the modifications implemented on the existing DYN3D/ATHLET coupling routines, see Section 2.1, and the ATHLET-based approaches for modeling relevant out-of-core structures, see Section 2.2.

- Validating the prediction capabilities of the platform against experimental data.

In the light of the above, the Phénix NC benchmark (IAEA, 2013) was selected for the verification of the coupling routines at core level. The choice of this benchmark offered, in this specific case, the possibility of exploiting the existing DYN3D core model developed in (Nikitin & Fridman, 2018c) and corresponding available solutions for an effective and clear verification of the new platform against DYN3D standalone. Whereas, for the verification of the platform applied with the ATHLET-based modeling approaches for out-of-core structures both the EOL Phénix NC benchmark and SPX start-up test benchmark (Ponomarev, et al., 2021b) were chosen. In particular:

- The Phénix NC benchmark was, once again, chosen to test the platform and the detailed modeling approach for out-of-core structures introduced in Section 2.2.1. This choice was driven by the availability of comprehensive and thorough data required to model the primary system and the out-of-core structures. The benchmark reports, in fact, several details of the primary TH system and of out-of-core structures, including structure geometries, as well as their material properties and positions within the primary circuit.

- The SPX start-up test benchmark presented in (Ponomarev, et al., 2021b) was chosen to test the platform and the simplified modeling approach for out-of-core structures, see Section

2.2.2. The choice of this benchmark was driven by the availability of lumped parameters required to apply the modeling approach of Section 2.2.2. Such parameters include, e.g., equivalent thickness and height of out-of-core structure, time delay constants, etc. It is worth noticing that the parameters were already identified in (Ponomarev, et al., 2021b) and applied for calibration purposes.

In terms of validation, the new platform prediction capabilities are assessed against experimental data provided by the benchmarks. This assessment is carried out in parallel with the verification activities.

This chapter is structured as follows: Section 3.1, presents the V&V of the platform carried out against the Phénix NC benchmark. The section also includes a description of the NC benchmark, and the Phénix models applied for V&V purposes. Section 3.2, presents the V&V of the platform carried out against the SPX start-up tests. The section also includes a brief description of the SPX benchmark, and the SPX models employed for the V&V. Section 3.3 closes the chapter with general considerations on the V&V.

3.1 V&V against Phénix NC test

In agreement with the chronological performance of the V&V tasks, the activities conducted on the Phénix NC benchmark are the first ones to be shown in this chapter. Brief descriptions of the Phénix reactor, NC benchmark, and Phénix models applied for the V&V are reported in the following.

3.1.1 Phénix reactor description

The Phénix reactor was a French pool-type SFR demonstrator. The reactor was operated until 1993 at a nominal power of 563 MW_{th} and after that at 350 MW_{th}. The reactor site was located in Marcoule, close to Orange. Fig. 10 shows a view of the NPP site. The construction of the Phénix started in November 1968. The reactor was brought into operation in 1973 and eventually shut down in 2009 after the performance of several EOL measurements and tests.

Fig. 10. View of the Phénix reactor site, Marcoule, France (https://www.irsn.fr/, 2021)

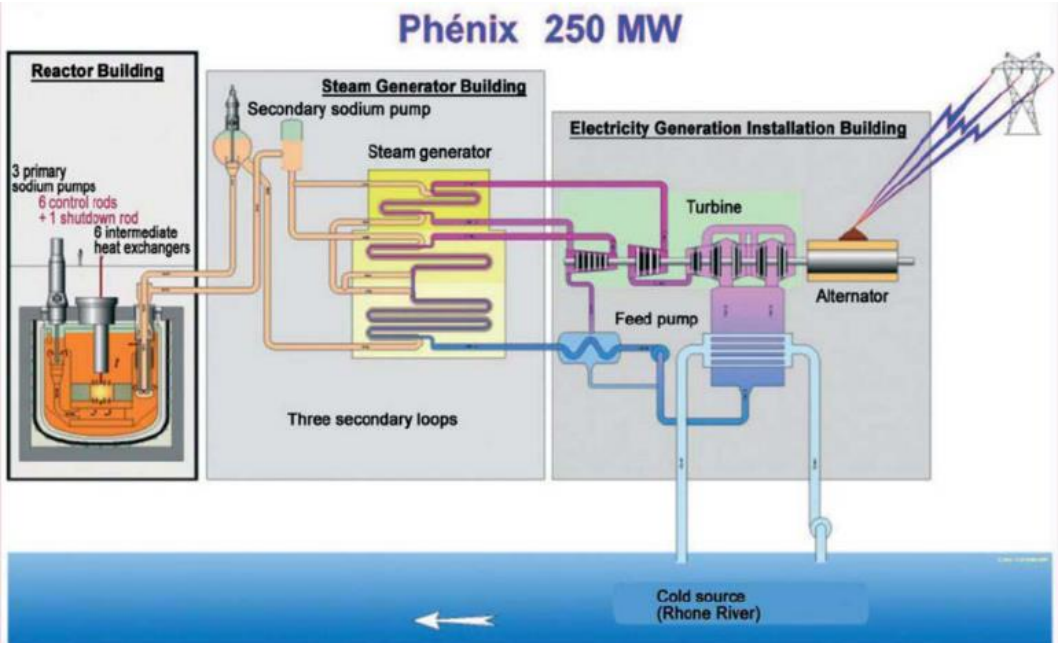

Fig. 11. Schematic view of the Phénix reactor (IAEA, 2013)

The reactor plant included the primary and secondary circuits, both sodium-cooled, and the circuit of the steam generators. As schematic view of the reactor system is shown in Fig. 11. The primary circuit was made up of a large sodium pool containing the core, six IHXs, three primary pumps, and other vessel internals. The reactor primary circuit hosted a sodium mass of about 800 tons within a double-envelope vessel conceived to retain potential sodium leaks and to provide thermal insulation capabilities. Three secondary loops, containing 140 tons of sodium each, were employed to evacuate the generated power from the primary circuit to the tertiary loops connected to the steam generators. The gross electrical power produced by the system turbine was about 250 MW_e until 1993 and 140 MW_e after (IAEA, 2013).

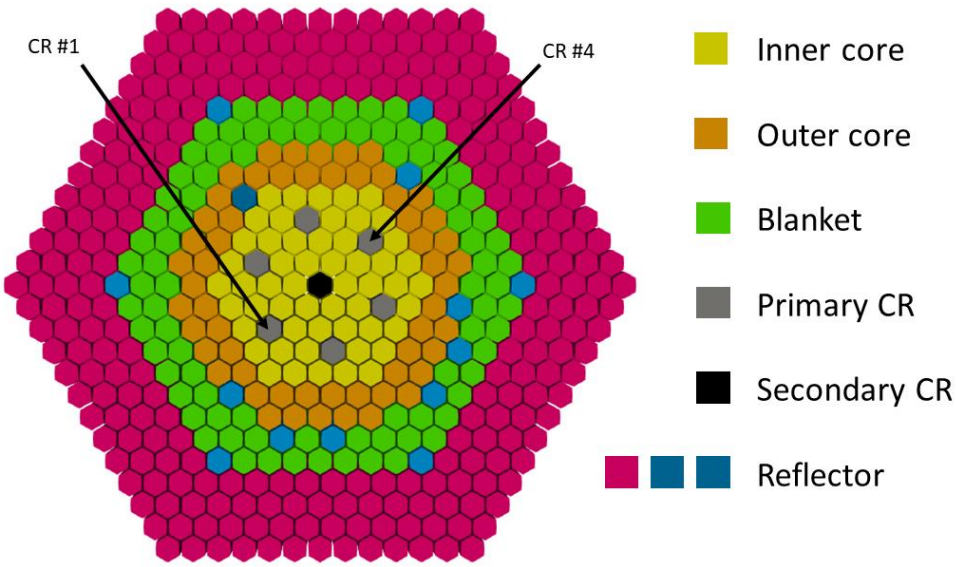

Fig. 12. Phénix core EOL configuration: Arrangement of subassemblies

At the EOL, the Phénix reactor core configuration consisted of inner core and outer core regions, made up of 54 and 56 fuel subassemblies loaded with mixed-oxide $(U,Pu)O_2$, see Fig. 12. In the configuration, the inner core was surrounded by the outer core which was in turn wrapped by surrounding radial blanket and steel reflector regions which include, respectively, 86 and 252 subassemblies. The core was also provided with 6 primary CRs, 1 secondary emergency CR, and 14 reflector-like subassemblies located both inside the core and blanket regions. Further details on core axial layout, geometries of subassemblies, core materials compositions, as well as modeling approach of TEs are provided in (IAEA, 2013).

3.1.2 NC test: Benchmark description

On the occasion of the Phénix reactor shut down in 2009, several measurement and transient tests were performed, including the NC and CR withdrawal tests. Both tests were used as a basis for two benchmark activities proposed by IAEA (IAEA, 2013; 2014). The benchmarking activities were aimed at:

- Improving the understanding of both neutronic and TH behavior of SFRs.
- Improving the modeling methodologies applied to the simulation of SFRs.
- Allowing for new V&V of modeling methodologies.

Both benchmarks are employed in the frame of this doctoral thesis. In particular, the NC benchmark is described already in the rest of this section as it is employed for the platform V&V. The CR withdrawal benchmark is instead described later on in Chapter 4, and is employed for optimization purposes related to the platform performance.

The Phénix NC test was carried out to study the onset of the sodium NC within the primary system and to investigate the effectiveness of natural convection effects within the primary system. For the experiment, the reactor was stabilized at 120 MW_{th}. The test was initiated by inducing the drying out of all the steam generators in operation, namely the steam generators 1 and 3 (steam generator 2 was out of service at the time of the experiment). The drying out of steam generators resulted in a heat sink loss scenario, prompting a reactor scram at 458 seconds, see Table 4.

Experimental data on power, reactivity, outlet and inlet core temperatures, as well as the inlet sodium mass flow were provided in (IAEA, 2013) with related uncertainties. The measurements covered 24000 s of the actual transient. The benchmark provided also details on the system geometries, secondary perturbations, and properties of materials. Specifications of the EOL core configuration, corresponding to the shutdown configuration, were available in the same document.

Table 4. Events occurred during the performance of the NC test (IAEA, 2013)

Time	Event
0 s	Dry out of steam generators #1 and #3. No change in pumps speed.
458 s	(1) Scram and (2) secondary pumps 1 and 3 automatically reduced to 110 rpm in 1 min
466 s	Stop of the 3 primary pumps, beginning of the 1st phase
4080 s	Secondary pumps speed reduced to 100 rpm (back-up motors)
10320 s	Steam generators cooled by air, beginning of the 2nd phase
24000 s	Closing of SG casings and end of the benchmark

It should be stressed that the Phénix NC benchmark was previously modeled and calculated by Serpent/DYN3D as a part of the validation of the fuel axial and diagrid radial TE models, implemented in (Nikitin & Fridman, 2018a; 2018c). The test was simulated only until the reactor scram, occurring at 458s. The benchmark and the corresponding Serpent/DYN3D solutions are employed in the next sections for:

- The verification of the new platform at core level, by employing a DYN3D/ATHLET core model of the Phénix reactor. The core model was developed preserving the equivalence with the Serpent/DYN3D model employed in (Nikitin & Fridman, 2018c). Out-of-core structures were not considered for this activity.
- The V&V of the new platform and the detailed TE models of the out-of-core structures at the system level, by employing a DYN3D/ATHLET model of the Phénix system. This DYN3D/ATHLET model was developed from scratch in the framework of this PhD project according to the detailed modeling approach of Section 2.2.1.

For the sake of completeness, the DYN3D/ATHLET core and system models used for V&V are briefly presented in the next Section.

3.1.3 Phénix model for V&V

The DYN3D/ATHLET model of Phénix core was developed while preserving the equivalence with the DYN3D model employed in (Nikitin & Fridman, 2018c) which was, in turn, modeled by following the specifications provided in (IAEA, 2013). The arrangement of the subassemblies was already presented in Fig. 12, while the number and type of subassemblies modeled are summarized in Table 5.

Table 5. Phénix: Number/Types of subassemblies

Channel type	# of channels
Inner core chan., Type # 1	54
Outer core chan., Type # 2	56
Radial blanket, Type # 3	86
Primary CRs, Type # 4	6
Secondary CR, Type # 5	1
Reflector 1, Type # 6	252
Reflector 2, Type # 7	13
Reflector 3, Type # 8	1

Fig. 13 shows the DYN3D/ATHLET TH scheme of the core model with TH channels simulating core subassemblies and heat structures simulating fuel rods of inner and outer core subassemblies, as well as the radial blanket. The actual number of subassemblies was considered in the modeling of the inner core, outer core, and radial blanket regions, i.e., in total 196 TH channels were modeled for these regions. Other 5 representative channels were considered for primary and secondary CR channels and reflector channels. For these last, the actual number of subassemblies was accounted by channel multiplication factors. Inlet sodium temperature and mass flow, and outlet sodium pressure were applied respectively on the TH components "Inlet pipe" and "Outlet BC ". More details on the BCs are presented in the next sections.

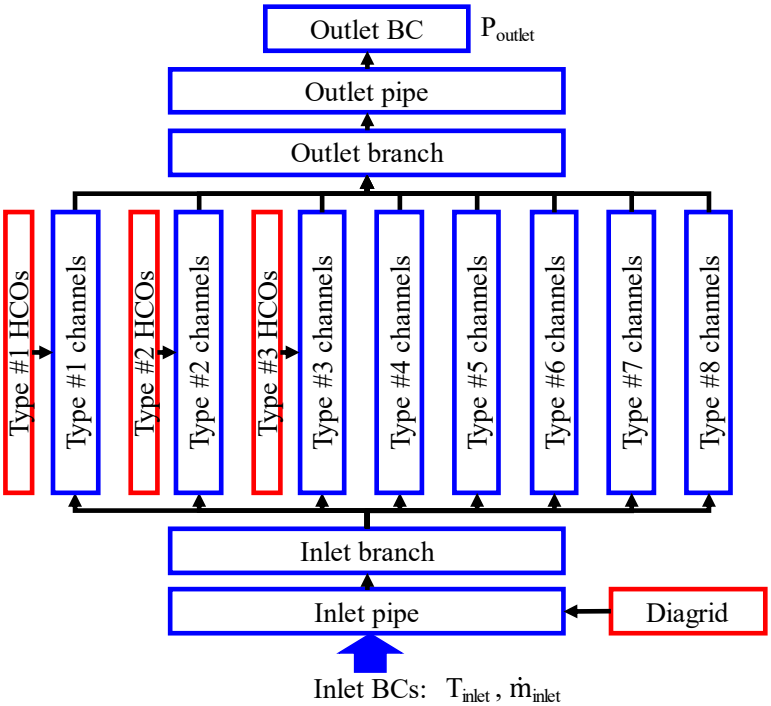

Fig. 13. Thermal-hydraulic scheme and heat structures of the Phénix core model

The DYN3D/ATHLET neutronic model and related XSs employed for the V&V exercise were adopted by the Serpent/DYN3D model developed in (Nikitin & Fridman, 2018c). The XSs were generated by following the existing Serpent-based methodology introduced in Section 1.3.1. For the sake of completeness, Appendix C.1 thoroughly reports the XS generation procedure adopted as initially described in (Nikitin, et al., 2015). The isotopic compositions of core materials used for XS generation were consistent with the specification of the NC benchmark. The XS parametrization accounted for the effects of, fuel and coolant temperatures, axial fuel expansion, and radial diagrid expansion. Assuming close-gap configurations of the fuel elements, representative of core EOL conditions, the axial fuel expansions were considered to be driven by the cladding.

Table 6. Phénix benchmarks: Values of state variables considered for the generation of XSs

T_f, K	T_c, K	ε_a	ε_r
523 900	523	ε_a(523K)	ε_r(523K)
1500 1800	900	ε_a(1200K)	ε_r(900K)

The XSs were parametrized according to the MDT approach. Values of the state variables selected for generating the XSs are presented in Table 6.

For the TH modeling of the Phénix system, one relied on specifications available in (IAEA, 2013). The model of the primary system was developed starting from the core model described in Fig. 13. In particular, the existing core model was extended by replacing the outlet TH components located beyond the core channels with a detailed primary circuit model. The Phénix primary system was modeled as an open system "cut" in correspondence with the core inlet. BCs were set on fluid inlet temperature and mass flow, and on the fluid outlet pressure.

The primary circuit was split into 12 azimuthal sectors: Fig. 14.a shows the top cut-view of the Phénix reactor, while Fig. 14.b the azimuthal and radial discretization of the primary circuit adopted in the development of the TH model. As Fig. 14.b shows, the 12 azimuthal boundaries defining the azimuthal sectors are placed such as to fully host the four IHXs, three primary pumps, three "empty" sectors, and two DOTE[3] components. Each azimuthal sector was split, in turn, into 7 radial segments with boundaries located in correspondence of different radial core regions, redan, vessel cooling system, and vessel walls. Fig. 15.a shows an axial cut-view of the Phénix, whereas Fig. 15.b presents the correspondent ATHLET nodalization scheme for two representative azimuthal sectors hosting, respectively, an IHX and a primary pump. Significant heat exchanges were modeled between hot and cold pools, through heat structures simulating the redan, and between primary and secondary circuits, through the heat structures of the IHXs, see Fig. 16.

The secondary circuit was modeled through 1D channels thermally coupled with the primary IHXs. The inlet mass flow and temperature, as well as the outlet pressure of the secondary coolant were imposed via BCs.

[3] Dummy IHXs connected to an out-of-service intermediate circuit.

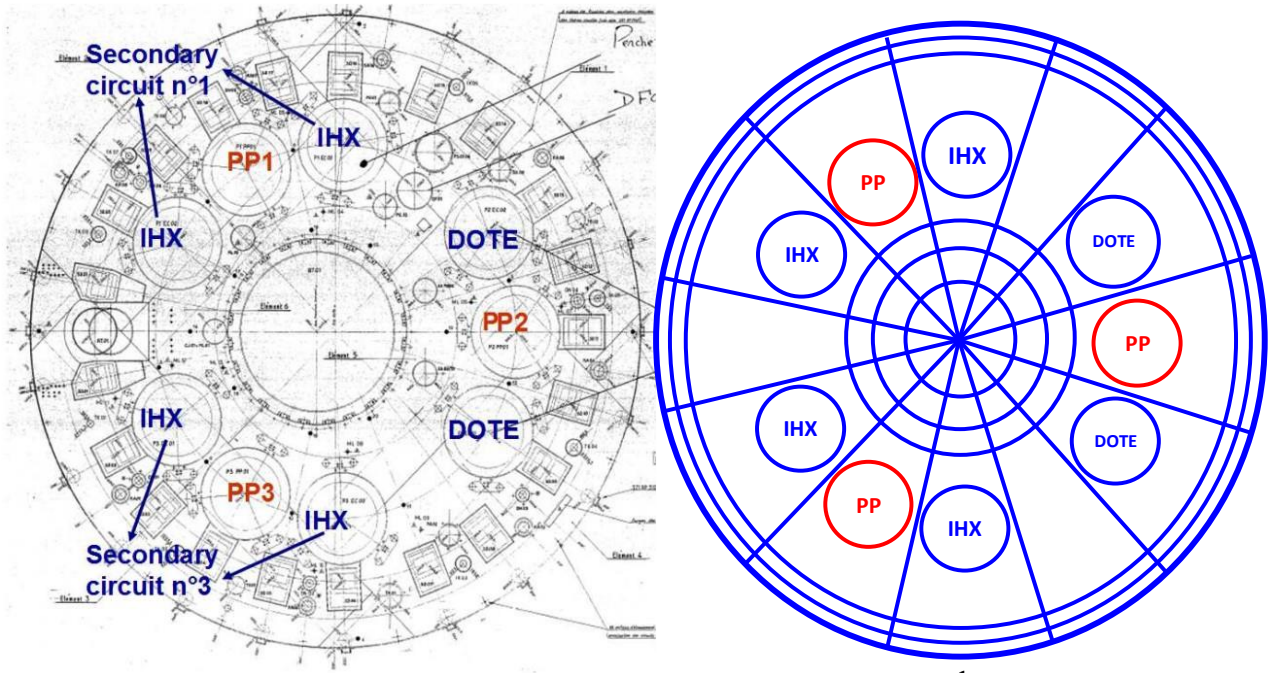

a. b.

Fig. 14. Phénix top cut-view: a) actual reactor top cut-view (IAEA, 2013), b) azimuthal and radial nodalization of the primary in ATHLET

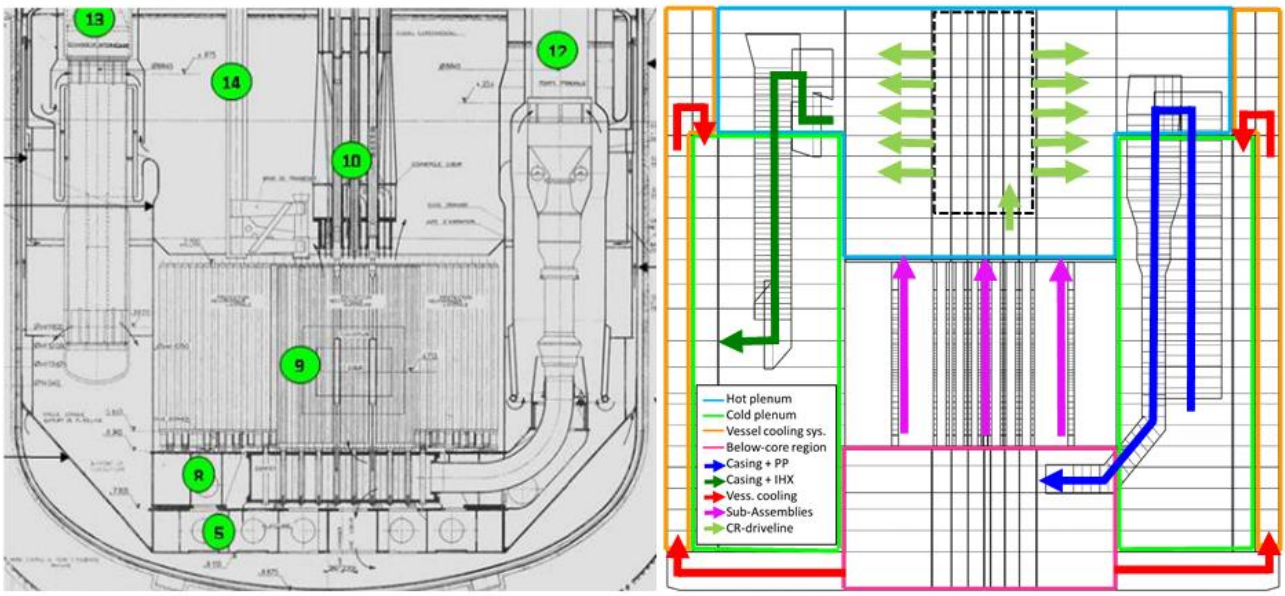

a. b.

Fig. 15. Phénix axial cut-view: a) actual reactor axial cut-view (IAEA, 2013), b) Radial and axial nodalization of the primary in ATHLET

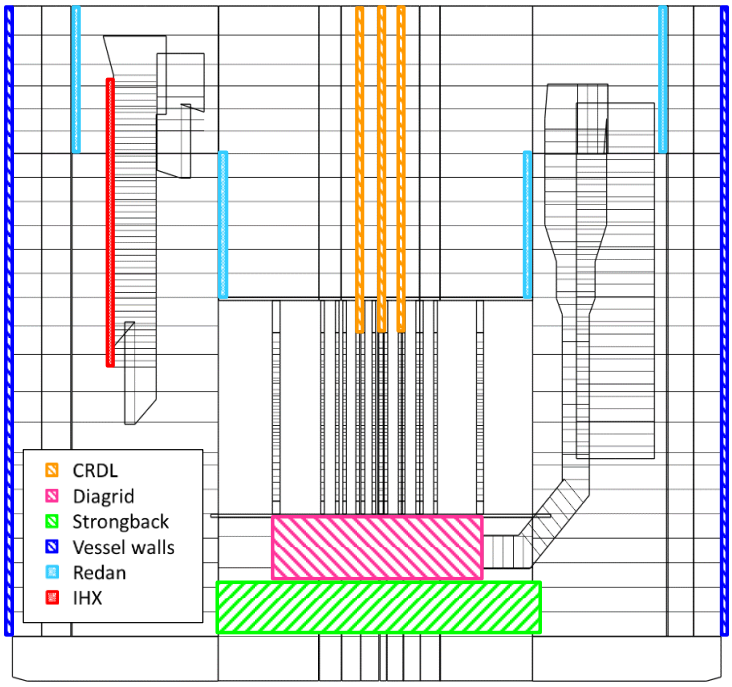

Fig. 16. Position scheme of most relevant heat structures within the primary circuit

The out-of-core heat structures of CRDLs, strongback, and vessel were modeled by applying the approach described in Section 2.2.1. The position of the latter within the primary system is shown in Fig. 16.

Details on geometrical data and material properties employed in the modeling of the out-of-core structures extracted from (IAEA, 2013) are presented in Table 7.

Table 7. Phénix: Geometrical and material data adopted for the modeling of the out-of-core structures

Parameter	Out-of-core component		
	CRDL	Strongback	Vessel
Material*	Stainless steel	Stainless steel	Stainless steel
Axial total length, m	5.3	2.6	10.1
Axial node number/, -	14	1	25
Geometry used for modelling, -	Cylinder	Hollow cylinder	Hollow cylinder
Component number, -	7	1	1
Radial ring number, -	-	4	1
Azimuthal sector number, -	-	12	12
Radius/thickness, m/cm	0.096/-	0.58-0.83-1.09-3.38/5.0	5.84/3.0

*Thermophysical properties of the austenitic stainless steel, including linear TE coefficients in polynomials were adopted from (Austregesilo, et al., 2016) and (Kim, 1975).

3.1.4 Verification of extended coupling routines at core level

The goal of the verification presented in this section is to prove the correct functioning of the extended coupling routines. This is verified in this section by demonstrating that equivalent solutions can be obtained, at core level, either by employing Serpent/DYN3D or the new platform.

In this regard, the platform was applied to the analysis of the Phénix NC test exploiting the DYN3D/ATHLET Phénix core model presented in the previous section. The model was developed to be equivalent to the Serpent/DYN3D model employed in (Nikitin & Fridman, 2018c) for validation purposes. In particular, the models have identical subassembly geometries, material properties, gap conductance values, and BCs. The solutions obtained with the new platform were compared against available Serpent/DYN3D solutions under static and transient conditions.

In relation to the static comparison, the platform was applied to evaluate a static configuration of the reactor core at 120 MW_{th}, which was representative of the initial condition of the NC test. The obtained core nodal static distributions of fuel, clad, and sodium temperatures were benchmarked against the Serpent/DYN3D distributions. Fig. 17 shows average deviations of the temperature distributions found for the inner core, outer core, and radial blanket regions.

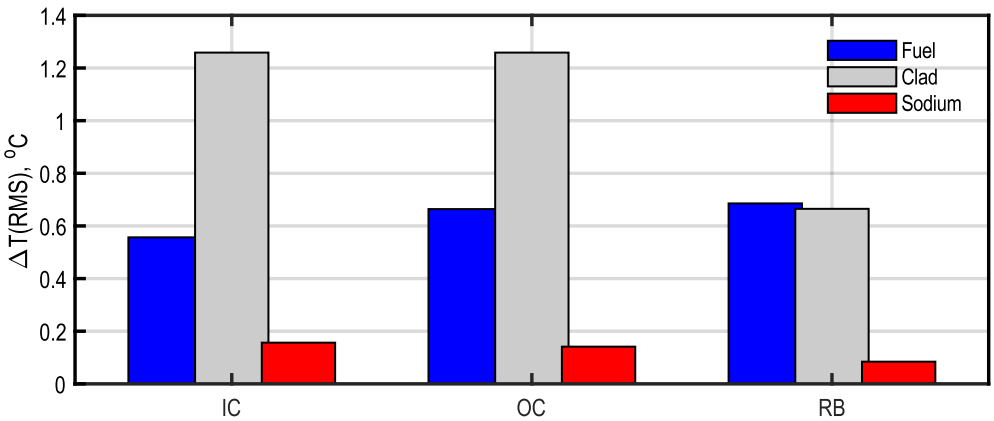

Fig. 17. Deviations in temperature distributions for inner core, outer core, and radial blanket regions

Fig. 17 shows globally good agreements among the temperature distributions. The best agreement was found between the temperature distributions of sodium for which root mean square (RMS) errors found are below 0.2 °C. Fuel temperature distributions are also close to each other for all the core regions and show errors below to 0.7 °C. Slightly larger deviations, up to 1.3 °C, are instead observed for the clad distributions. These should be attributed to the different models applied by the compared platforms for evaluating the wall-to-fluid heat transfer. However, such discrepancies represent variations that are below 1% of the clad temperature, therefore the agreement between the solutions can still be considered good. In general, one can state that no major deviations were encountered in

the static comparison between the temperature distributions evaluated with ATHLET and DYN3D's FLOCAL.

In relation to the transient comparison, analyses of the NC test were performed considering as a starting point the static configuration just analyzed. The scenario was simulated by imposing a time-dependent BC on the inlet core sodium temperature, see Fig. 18. The rising trend of the sodium inlet temperature shown in Fig. 18 is induced by the dry out of the steam generators. An inlet constant mass flow of 1284 kg/s was imposed during the whole simulated transient. In addition, a fixed pressure BC was set at the core outlet. The transient scenario was simulated until the reactor scram at 458 seconds.

Fig. 19 shows the comparison of the transient solutions evaluated with Serpent/DYN3D and the new computational platform. Quantities compared are the total reactor power, inner core sodium outlet, average core sodium at the outlet of all fissile channels, total reactivity, reactivities decomposed by components and clad average temperature in fissile and fertile core regions. In Fig. 19, the Serpent/DYN3D solutions are presented with dashed lines, whereas continuous lines are employed to identify DYN3D/ATHLET solutions. Experimental data are also shown, when available.

After the beginning of the transient, the inlet core temperature rises due to the reduction of the heat transfer from the primary system to the secondary circuits. The rise in sodium temperature at the core inlet causes the radial expansion of the diagrid, and consequently, the insertion of negative reactivity, see yellow curve in Fig. 19d. The hotter inlet sodium temperature causes also an average increase in the clad temperatures in the inner core and outer core subchannels, see Fig. 19f. As the fuel axial expansion is driven by the clad (a closed-gap configuration was assumed for the model), the increase of the average clad temperature leads to the axial expansion of the fuel, and ultimately to the insertion of negative reactivity. A positive Doppler effect counterbalances the negative reactivity contributions of the diagrid and fuel TEs. Sodium density effects play a marginal role during the whole transient. The trade-off of the reactivity components results in the insertion of net negative reactivity and in the decrease of power, see Fig. 19b and a. Sodium temperatures at the core outlet, see Fig. 19c and e, decrease following the reduction of the core power.

Overall, the agreement of the new solutions against the existing Serpent/DYN3D results is excellent: For all the quantities shown, the trends practically overlap. Remarkable are the agreement of the total power and reactivity, respectively shown in Fig. 19a and b. Negligible deviations are observed on the trends of sodium core outlet temperature, see Fig. 19c and e. The reactivity feedback of Doppler, sodium, axial fuel and radial diagrid expansions are almost identically predicted as Fig. 19d shows.

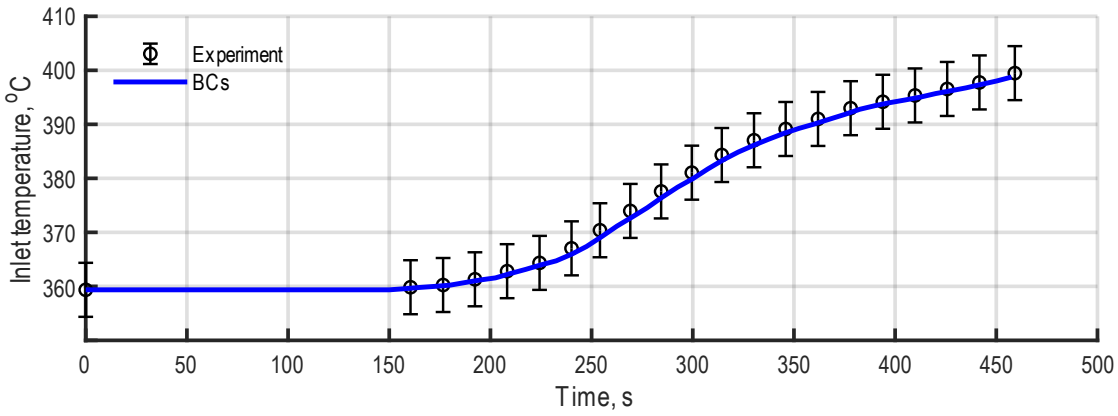

Fig. 18. Inlet core sodium temperature: Experimental trend and imposed time-dependent BC

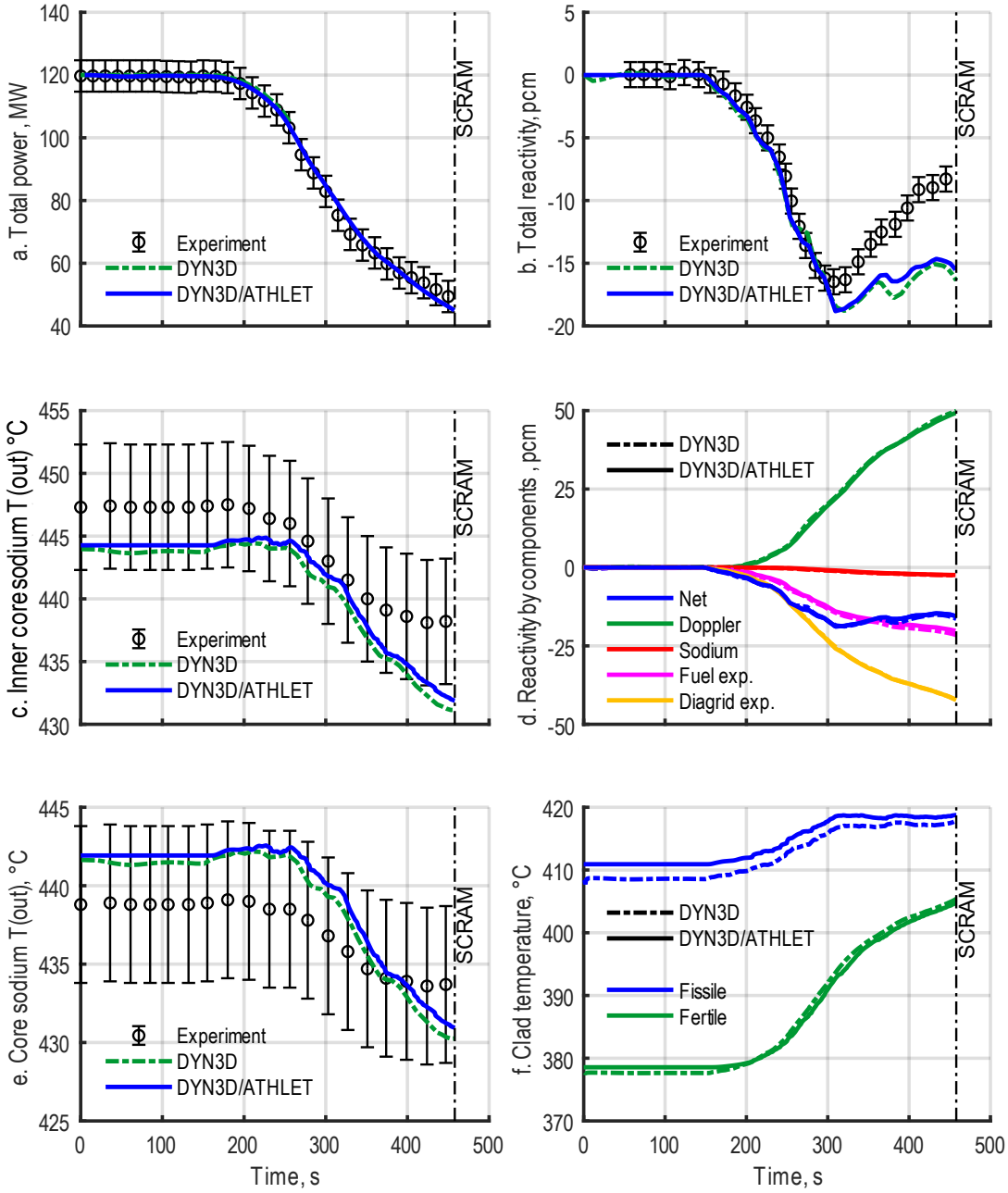

Fig. 19. Phénix core level V&V

The verification of the new coupling routines against the Phénix NC benchmark demonstrated successfully the equivalence of ATHLET and DYN3D's FLOCAL module both in static and transient comparisons. As a result, when compared with the experimental trends, the new platform is able to predict the transient behavior of the reactor core as accurately as Serpent/DYN3D does.

However, as also pointed out in (Nikitin & Fridman, 2018c), deviations of the Serpent/DYN3D solutions from experimental curves can be noted, especially in the evolution of net reactivity. Such discrepancies are likely due to missing models of out-of-core structures with related TEs, and in particular, to missing vessel effects which can insert positive reactivity as the sodium temperature at the core inlet increases. Improvements in the DYN3D/ATHLET solutions obtained can be thus achieved by considering suitable models accounting for out-of-core TE effects. In this regard, the detailed approach for modeling the out-of-core structures and their TEs, see Section 2.2.1, was applied to the analysis of the NC test in the next section.

3.1.5 V&V of platform and detailed models for out-of-core structures

The V&V of the platform and of the detailed models for out-of-core structures was conducted by applying the Phénix system model described in Section 3.1.3. On the primary side, the BCs imposed were a time-dependent inlet core sodium temperature, see Fig. 18, an inlet constant mass flow of roughly 1284 kg/s, and a pressure BC of 1.5 bar set at the argon/coolant interface on top of the sodium hot pool. On the secondary side, the BCs were imposed at the inlet and outlet sections of each IHX and they were namely: Time-dependent inlet sodium temperatures as shown in Fig. 20, constant mass flows of roughly 190 kg/s, and outlet sodium pressure BCs set to 1.5 bar. Such BCs were imposed in agreement with the benchmark specifications. Also for the current V&V activity, the transient calculations of the test covered the initial stage of the NC experiment until the reactor scram, i.e., the first 458 seconds of the test.

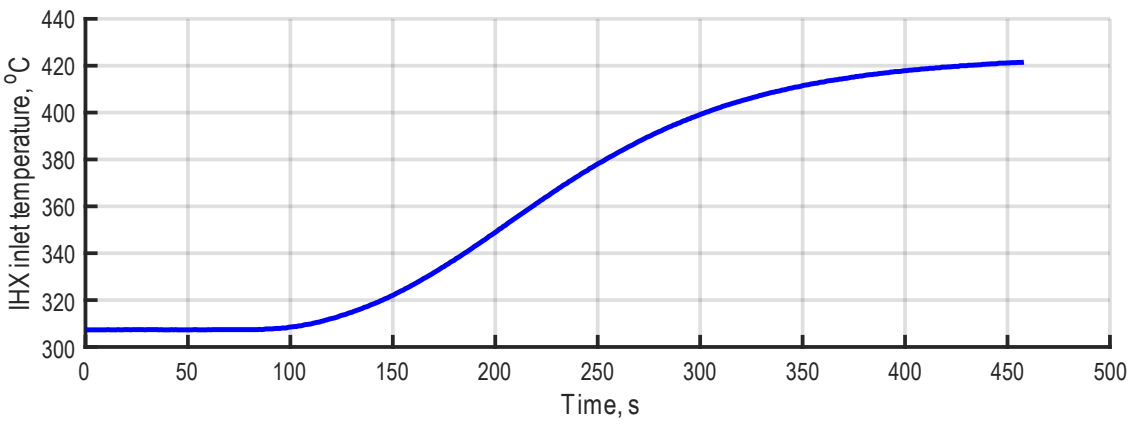

Fig. 20. IHX, secondary side: Sodium inlet temperature

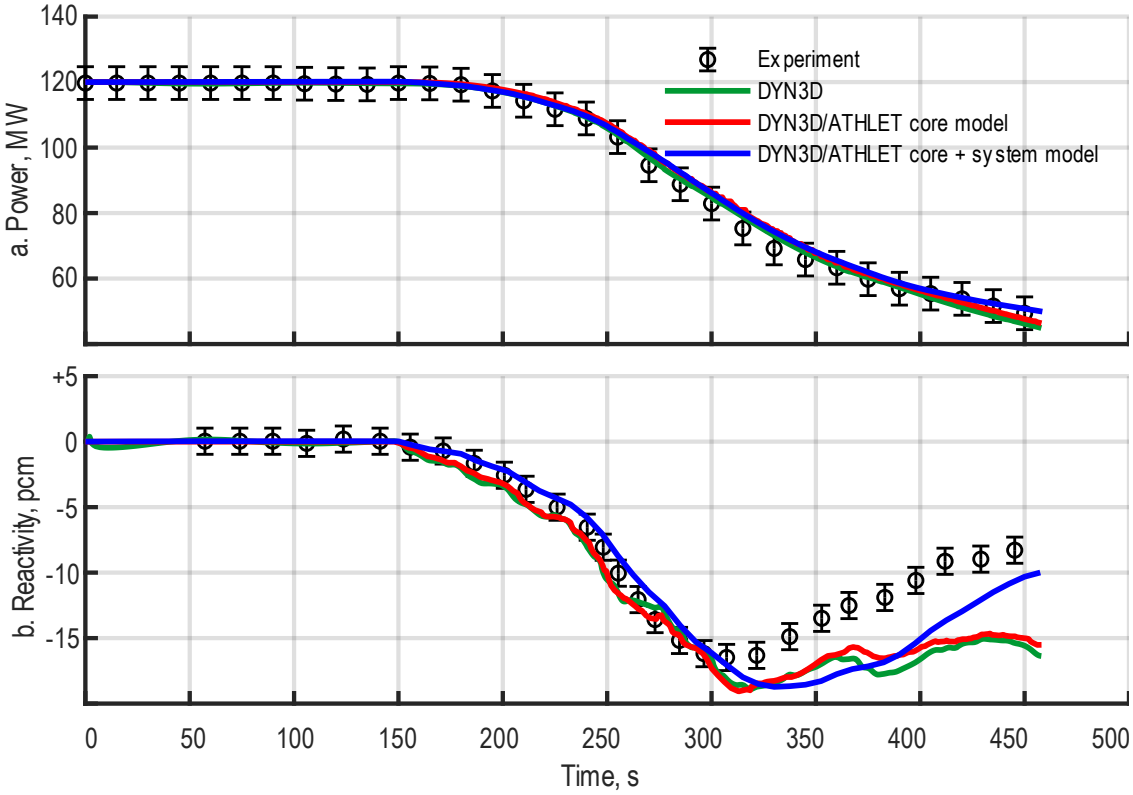

Fig. 21. Comparison of calculations vs experiment, a) power, b) reactivity, and c) inlet core coolant temperature

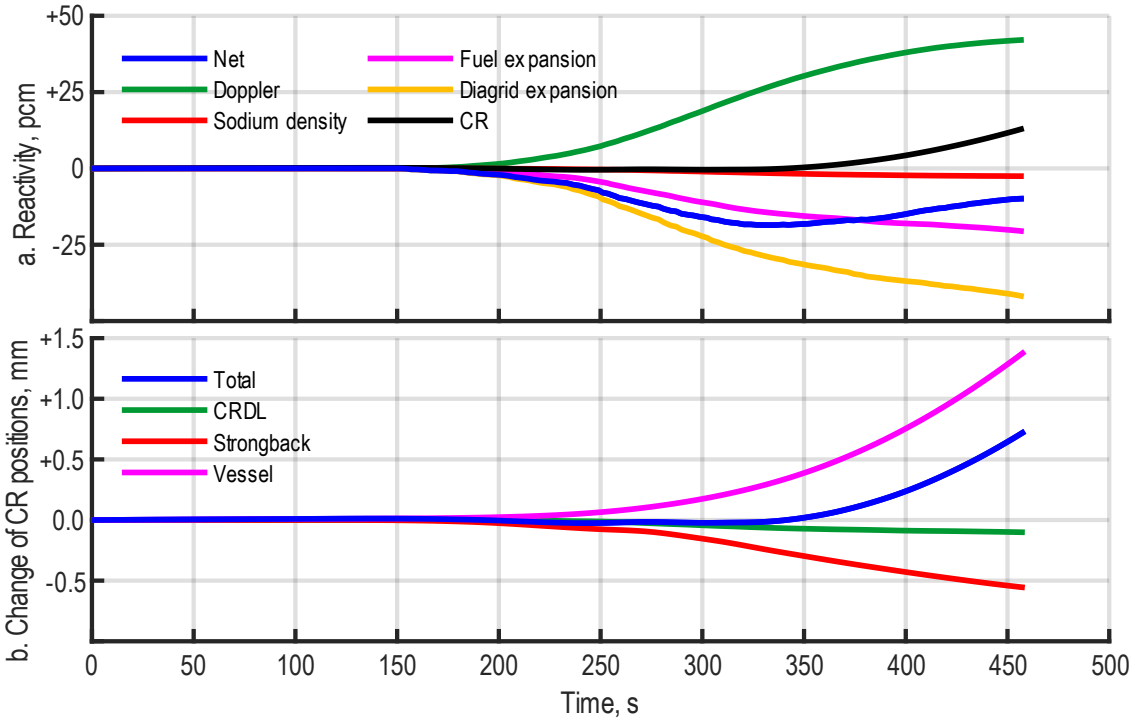

Fig. 22. NC test: a) reactivity components and b) out-of-core axial expansions of CRDL, strongback, and vessel

After an initial zero-transient, the inlet core temperature increases due to the deterioration of the heat transfer capabilities from the primary circuit to the secondary loops: The sodium at the inlet of the IHXs is hotter due to the drying out of steam generators. The increase in the core inlet temperature is responsible for radial diagrid and axial fuel expansions. Such expansion effects lead to a negative insertion of reactivity, see Fig. 21b and Fig. 22a, and consequently to the core power reduction, see Fig. 21a. The positive Doppler effect counterbalances the inserted negative reactivity. Sodium density effects play a marginal role during the whole transient. As Fig. 22 shows, at around 350 s, the reactivity effect of CRs induced by out-of-core TEs gradually inserts positive reactivity and causes a slight slowdown in the reactor power drop, see Fig. 21b and Fig. 22a. The main contribution responsible for the change in CR positions is the axial vessel expansion, see Fig. 22b[4]. A smaller contribution also rises from the axial expansion of the strongback. The contribution of the CRDLs to the change in CR positions remains instead negligible. This latter aspect correlates to the limited sodium mass flow, about 1.5% of the nominal one (IAEA, 2013), flowing through the CR plug-in where the CRDLs are located. With such a low mass flow, the temperature of the fluid within the CR plug-in and, ultimately, of the CRDLs can only be slowly perturbed.

The calculations performed with the new extended platform jointly applied with the detailed approach for modeling the TEs of out-of-core structures provided satisfactory outcomes. In particular, the applied detailed modeling approach reproduces in a physical-coherent way the TEs of out-of-core structures also in relation to perturbations applied to the system and allows for consistent prediction of TEs bias on the CR position. The calculations performed with the extended platform showed the capability of adequately predicting the power evolution against the experimental trend and improvements in the prediction capability of core reactivity.

3.2 V&V against SPX start-up tests

This section is dedicated to the V&V of the newly extended platform applied, this time, together with the simplified models of out-of-core structures. In this regard, a brief description of the SPX reactor, an overview of the SPX start-up tests, and the SPX model as applied to the V&V activities are also reported in the following.

[4] Please not that positive changes in the position of CRs with respect to their initial position, correspond to the withdrawal of CRs, whereas negative changes correspond to their insertion.

3.2.1 SPX reactor description

The SPX reactor was a French commercial-size SFR of the pool-type. The reactor was conceived to generate a nominal power of 2990 MW_{th} and still nowadays maintains the record of the largest ever built SFR for energy production purposes. The reactor was built close to the bank of the Rhone River in Creys-Malville next to the border with Switzerland, see Fig. 23. The construction activities began in 1976. After the commissioning phase, during which several measurements and start-up tests were performed, the NPP was connected to the French electrical grid in December 1986. The SPX is since 1997 in permanent closure.

Fig. 23. View of the SPX reactor site, Creys-Malville, France (Wikimedia, 2021)

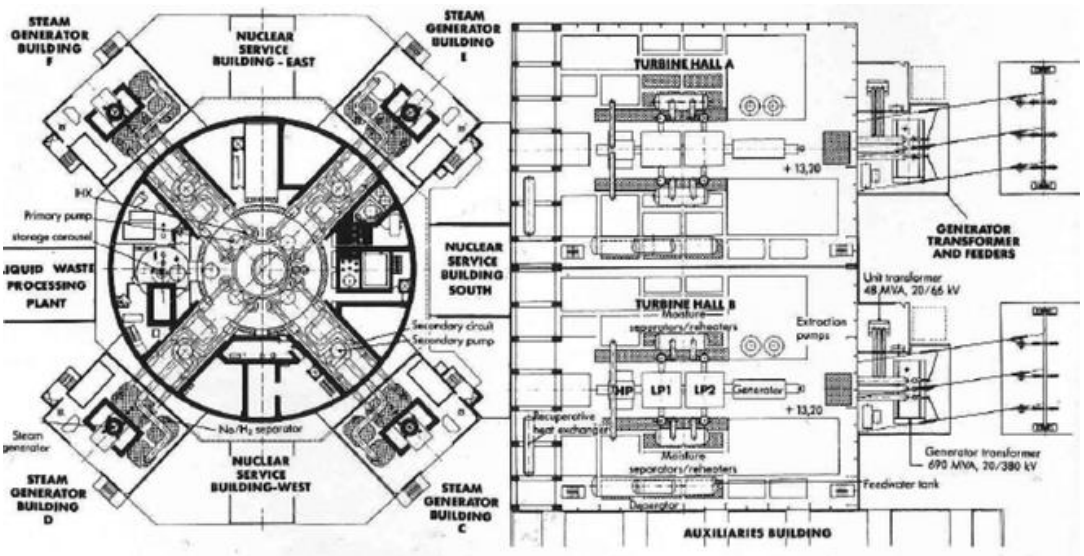

Fig. 24. Schematic top view of the SPX reactor and adjacent buildings (Guidez & Prêle, 2016)

The SPX reactor system consisted of three cooling circuits, i.e., the primary and secondary circuits, both sodium-cooled, and the circuit of the steam generators. The primary circuit was made up of a large sodium pool containing the core, IHXs, primary pumps, and vessel internals. The amount of sodium mass hosted in the circuit was about 3200 tons and, by design, a mass flow rate of 16.4 tons per second was conceived to flow through the core (Gourdon, et al., 1990). Four secondary loops were devoted to evacuating the produced heat from the primary circuit to the steam generators located in adjacent buildings, see Fig. 24. The steam generators were connected to two turbines producing 620 MW_e each (Guidez & Prêle, 2016).

At the beginning-of-life (BOL), the SPX core configuration consisted of inner core and outer core regions, made up of 190 and 168 fuel subassemblies loaded with mixed-oxide $(U,Pu)O_2$. The active core regions were peripherally surrounded by the radial blanket, loaded with depleted UO_2, and steel reflector regions, respectively including 222 and 297 subassemblies. The core was also provided with 21 primary control and shutdown devices (CSDs), 3 Diverse shutdown devices (DSD)s, and 18 diluent subassemblies located between inner and outer core regions, see Fig. 25. Further details on core axial layout, geometries of subassemblies, core materials compositions, as well as modeling approach of TEs are provided in (Ponomarev, et al., 2018).

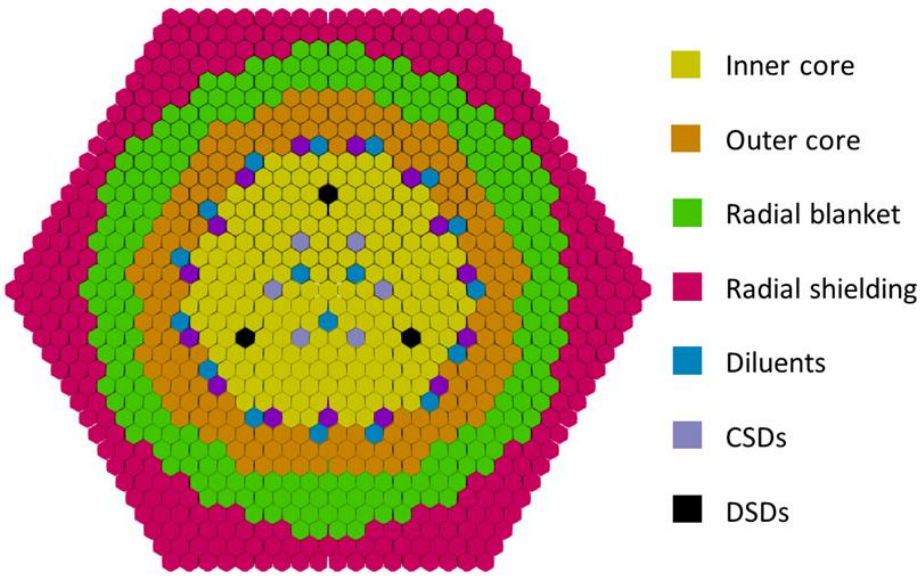

Fig. 25. Superphénix core beginning-of-life configuration: Arrangement of subassemblies

3.2.2 Start-up tests: Benchmark description

Profiting from available experimental data and actual measurements collected during the SPX commissioning and operational experiences, a new calculation benchmark was proposed in (Ponomarev, et al., 2018). The benchmark activities were launched in the framework of the ESFR-

SMART project (Mikityuk, et al., 2017). The goal of the benchmark was not only the validation of calculation tools used in the project but also a better comprehension of SFR modeling aspects under static and transient conditions. The benchmark included two parts:

- Static neutronics calculations.
- Transient coupled neutronics/thermal hydraulics calculations.

Both benchmark parts are employed in this doctoral thesis. The latter part is described already in the following paragraphs and is applied in this section for the V&V of the extended computational platform and the simplified model of out-of-core structures. The former benchmark part is instead described and applied later on in Chapter 4 in view of the optimization of the few-group XSs.

The second part of the SPX benchmark was dedicated to the analyses of transient tests performed on the occasion of the SPX start-up. During the SPX commissioning phase, numerous experiments and tests were carried out to assess the core TH and reactivity characteristics at different power levels. Among the performed tests, the benchmark proposed the analyses of six operational transients for which experimental data were available in the open literature.

In detail, the benchmark included three measurements of feedback coefficient (MOFC) tests respectively named MOFC1, MOFC2, and MOFC3 with experimental data available from (Vanier, et al., 1990). In addition, other three transients accompanied by experimental data were included in the benchmark considering as data source the report presented in (Bergeonneau, et al., 1990). Such transients are the reactivity step (RS) and primary flow step (PFS) tests performed at half of the nominal power, and the self-stabilization test (SST) carried out at zero power. The tests are summarized in Table 8.

Table 8. Set of start-up tests

Test designation	description	Initial power, MW_{th}
MOFC1	-50 pcm[5] reactivity insertion	692
MOFC2	10% secondary flow rate increase	633
MOFC3	10%primary flow rate reduction	663
PFS	10% primary flow rate reduction	1415
RS	-74 pcm stepwise reactivity insertion	1542
SST	+30 pcm reactivity insertion	≈0

[5] Per cent mille (pcm), i.e., reactivity unit expressed in one-thousandth of a percent.

In connection with this research, the six SPX start-up tests were modeled with DYN3D/ATHLET and related calculations performed to verify and validate the new platform and the ATHLET-based simplified approach for the modeling of out-of-core TEs. The parameters required for modeling the simplified out-of-core structures and related TEs were also available in the benchmark (Ponomarev, et al., 2021b) and were adopted from it.

For the sake of completeness, the SPX DYN3D/ATHLET model used for V&V purposes is presented in the next section.

3.2.3 SPX model for V&V

The DYN3D/ATHLET model of the SPX reactor was developed according to the specification provided in (Ponomarev, et al., 2021b). The model was developed considering the arrangement of the subassemblies presented in Fig. 25. Details on the number and types of subassemblies modeled are summarized in Table 9.

Table 9. Superphénix: Number/Types of subassemblies

Channel type	# of channels
Inner core, Type # 1	190
Outer core., Type # 2	168
Radial blanket, Type # 3	222
Shielding, Type # 4	297
CSDs, Type # 5	21
DSDs, Type # 6	3
Diluent, Type # 7	18

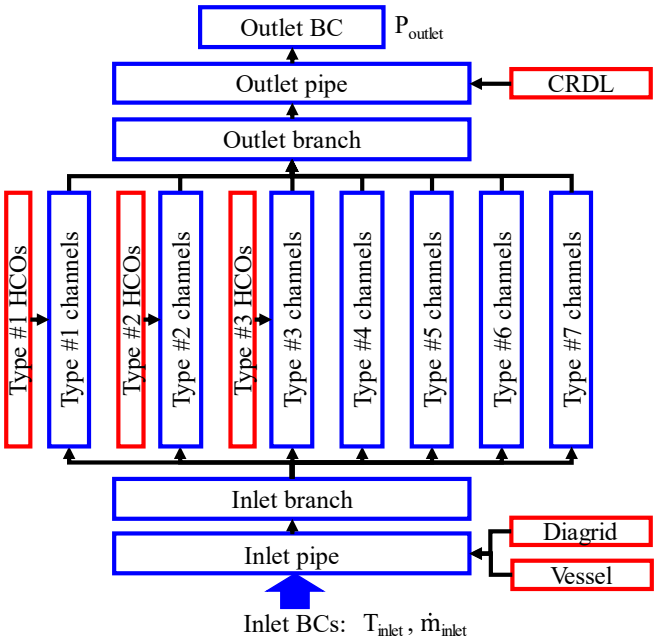

Fig. 26. Thermal-hydraulic scheme and heat structures of the SPX core model

The TH scheme of the SPX model with TH channels simulating the core subassemblies and heat structures simulating the fuel rods in inner and outer core subassemblies and assemblies of are shown in Fig. 26. The actual number of subassemblies was considered in the modeling of the inner core, outer core, and radial blanket regions, i.e., in total 580 TH channels were modeled for such regions. Other 4 representative channels were considered for the remaining TH channel types. For the latter, the actual number of subassemblies was accounted for by channel multiplication factors. Inlet sodium

temperature and mass flow, and outlet sodium pressure were applied as BCs, respectively, on the TH components "Inlet pipe" and "Outlet BC ". More details on the BCs are presented for each test in the next sections.

The SPX neutronic model and related XSs were developed by following the core specifications provided by (Ponomarev, et al., 2018). The XSs, parameterized according to the MDT approach, were generated by applying the Serpent-based methodology (Nikitin, et al., 2015) which is for the completeness reported in Appendix C.1. The isotopic compositions of core materials used for XS generation were consistent with the core specifications. State variables used for the XS parametrization were fuel and coolant temperatures, axial fuel expansion, and radial diagrid expansion. Values of the state variables selected for the XS generation are presented in Table 10.

Table 10. SPX benchmarks: Values of state variables considered for the generation of XS libraries

T_f, K	T_c, K	ε_a	ε_r
453	453	ε_a(453K)	ε_r(453K)
600	600		
900	900	ε_a(1500K)	ε_r(900K)
1500			

The model could account for the neutronics effects of non-uniform axial fuel expansion and uniform radial diagrid expansion via dedicated TE models implemented in DYN3D as described in (Nikitin & Fridman, 2018a). Axial fuel expansions were considered as driven by the fuel temperature by assuming an open-gap configuration of the fuel elements, which was representative of the core conditions at the BOL.

It should be emphasized that the XSs used for the V&V of the platform against the SPX start-up tests were generated in the framework of the current doctoral research. The verification of the parametrized XSs generated was conducted against existing Serpent/DYN3D solutions evaluated in (Ponomarev, et al., 2021a). The verification study is reported in Appendix B.1.

Details on geometrical configurations and material properties employed for the modeling of the out-of-core heat structures are reported in Table 11 as extracted from (Ponomarev, et al., 2021b). As one might notice, the heat structure of the strongback was not modeled: The TE of this component was rather considered to be driven by the core inlet temperature and delayed in time by applying a time constant delay of 100 s.

Table 11. SPX: Geometrical and material data adopted for the modeling of the out-of-core structures

Parameter	Out-of-core component		
	CRDL	Strongback	Vessel
Material*	Stainless steel	Stainless steel	Stainless steel
Average linear TE coefficient, K^{-1}	1.70E-05	1.73E-05	1.70E-05
Axial total length, m	6.0	4.0	13.5
Axial nodes' number, -	1	1	1
Geometry used for modelling, -	Cylinder	Hollow cylinder	Hollow cylinder
Components' number, -	1	1	1
Radial rings' number, -	-	1	1
Azimuthal sectors' number, -	-	-	-
Radius/thickness, m/cm	2.0/2.0	-/-**	10.0/3.0
Time delay (Δt), s	0	100.0	360.0

*Thermophysical properties of austenitic stainless steel and average linear TE coefficients were adopted from (Ponomarev, et al., 2021b).
**Heat structure not modeled for consistency with the specifications provided in (Ponomarev, et al., 2021b). TE of strongback directly driven by sodium core inlet temperature.

3.2.4 V&V of platform and simplified models for out-of-core structures

The six SPX start-up tests are employed in this section to perform the V&V of the extended platform and of the simplified approach for modeling the out-of-core structure and their TEs. In particular, the section shows the results of the transient analyses performed with the new computational platform while giving emphasis on the effects of out-of-core structures. Trends of power and sodium core heat-up evaluated by the platform are compared against the available experimental data.

MOFC1 test: -50 pcm reactivity insertion

Before the beginning of the transient test, the reactor power was stabilized at around 692 MW_{th}. The transient was initiated by the insertion of the CRs which led in turn to the insertion of negative reactivity of roughly -50 pcm. The test was reproduced both by simulating a down-shift of CRs and by applying a BC on the inlet core sodium temperature, corresponding to the inlet temperature recorded in the experiment, see Fig. 27. A fixed BC of 6300 kg/s was assumed as the inlet mass flow for the calculations, whereas a fixed BC on sodium outlet pressure was set to 1.5 bar. The transient simulation runs for 2750 s.

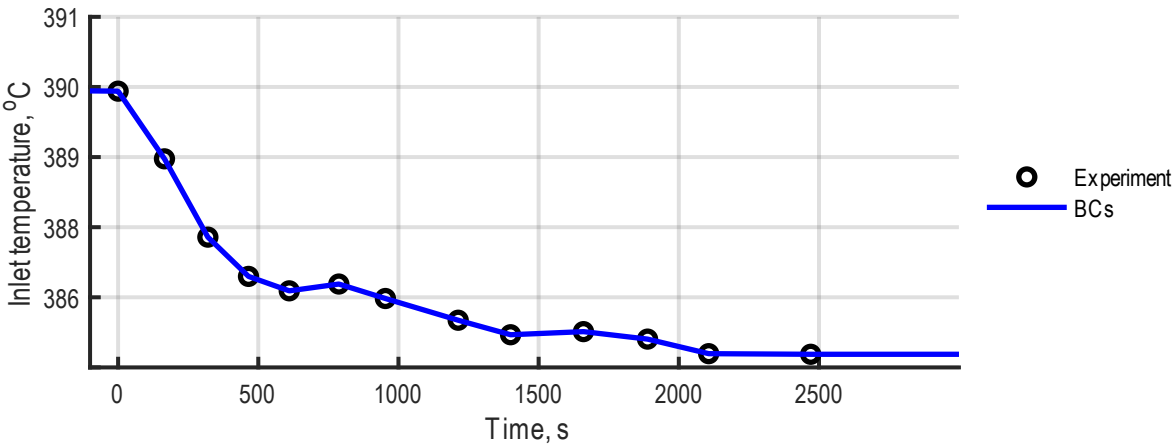

Fig. 27. MOFC1: Inlet core sodium temperature, experimental trend and imposed BC

Fig. 29a shows the insertion of the negative reactivity due to the insertion of CRs. The insertion of CRs causes a significant power drop, from roughly 692 to 600 MW_{th}, see Fig. 28a. The effect of the power drop is immediately counteracted by Doppler and fuel expansion feedback effects. During the first 500 s, the power grows. This is mainly due to reactivity effects introduced by the TEs of out-of-core structures, see Fig. 29a and b. In fact, as Fig. 29b shows, the axial contractions of CRDLs and strongback induced by the colder coolant temperature contribute to the withdrawal of CRs (up to 1 mm). Positive effects of the CRDLs and strongback are eventually compensated by the contraction of the vessel which results in the insertion of CRs, i.e., insertion of negative reactivity. Eventually, the power trend evolves towards a new steady state at lower power level, ca 640 MW_{th}.

The validation activity performed on the MOFC1 test provided satisfactory outcomes also in agreement with the results found by the benchmark participants in (Ponomarev, et al., 2021b). The extended platform and the simplified models adopted to capture the out-of-core TEs allowed for an accurate prediction of the total power and outlet core sodium temperature throughout the simulated interval of time, see Fig. 28a and b.

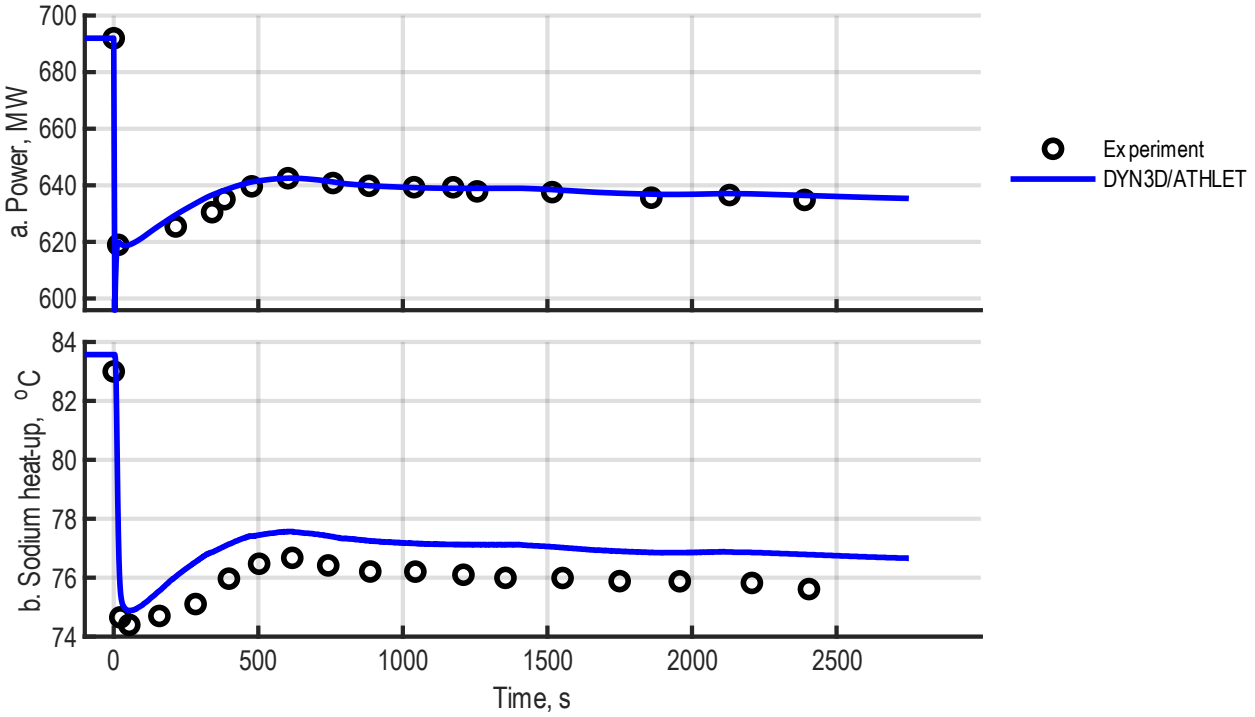

Fig. 28. MOFC1: Comparison of calculations vs experiment, a) power and b) inlet core coolant temperature

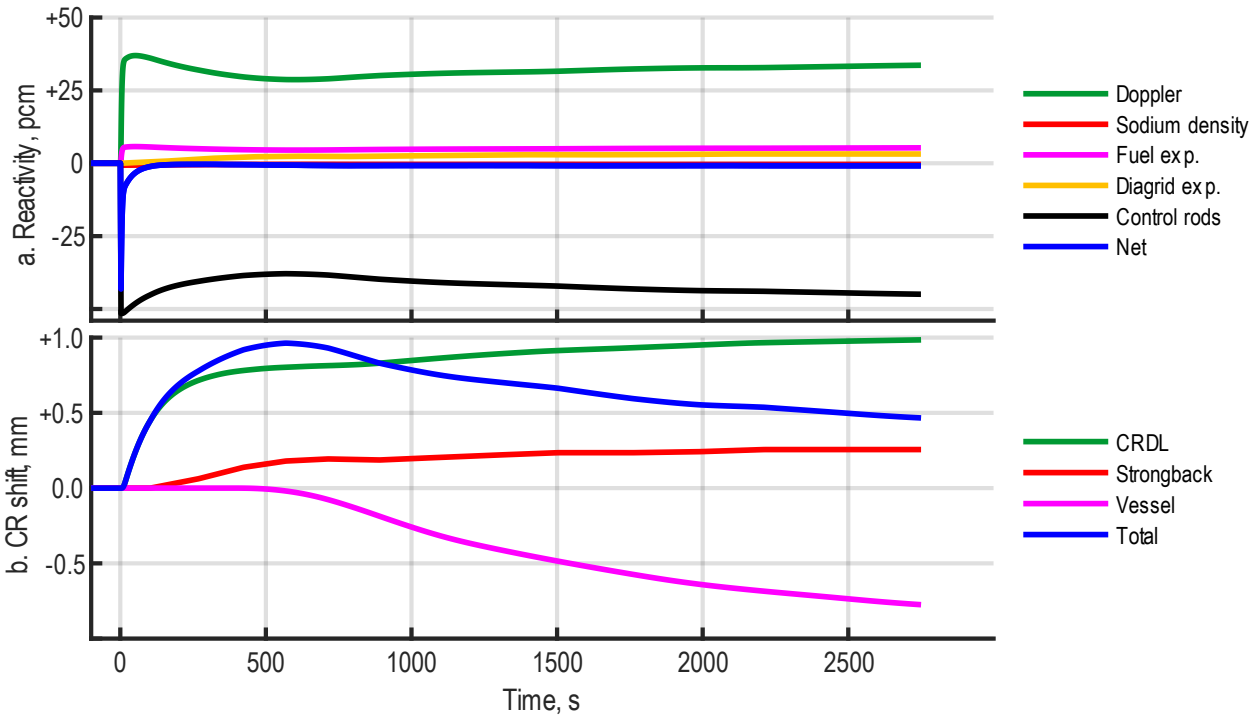

Fig. 29. MOFC1: a) reactivity and b) out-of-core axial expansions of CRDL, strongback, and vessel

MOFC2 test: 10 % increase in the secondary flow rate

The MOFC2 test was performed starting from steady state conditions with a power stabilized at 632 MW_{th}. The initiator event of the test was a 10% increase in secondary mass flow. The simulation of the experiment was performed by imposing a time-dependent core inlet BC on the sodium temperature in accordance with the experimental data, see Fig. 30. A constant sodium mass flowrate of 6360 kg/s was imposed at the inlet of the system. The outlet sodium pressure was set to 1.5 bar through an outlet BC.

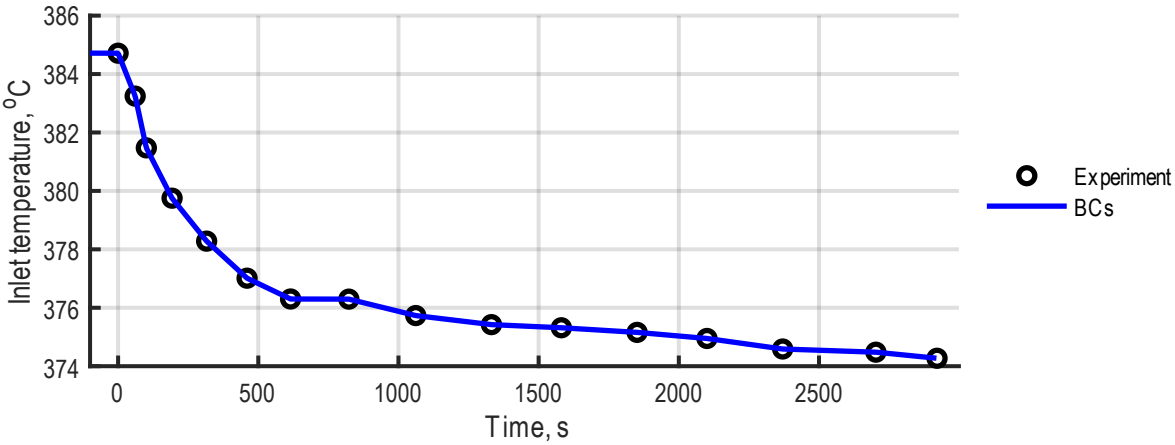

Fig. 30. MOFC2: Inlet core sodium temperature, experimental trend and imposed BC

Fig. 31a shows a power excursion up to 690 MW_{th} due to the insertion of positive reactivity induced by both the diagrid radial contraction and the withdrawal of CRs driven by axial contraction of CRDLs and strongback, see Fig. 32. In fact, both the CRDLs and strongback shrink as they are cooled down, respectively, by colder temperatures of the inlet and outlet sodium, see Fig. 30. The positive reactivity feedback are compensated by the negative Doppler and fuel expansion effects. As the vessel TE effects become effective, at around 500 s, the initial CR withdrawal effect is counterbalanced by the vessel shrinking which causes the insertion of CRs into the core. At the end of the test, the feedback effects balance each other, and the power tends to a new stationary level.

Despite the complex interplay among the TH and TE phenomena and their effects on the system neutronics, the validation outcomes are satisfactory. That is, in term of accuracy, the obtained results were in line with those reported by the benchmark participants in (Ponomarev, et al., 2021b). Minor relative deviations against experimental data, observed for the evaluated trends of power and sodium heat-up, remain below 2% as illustrated in Fig. 31a and b.

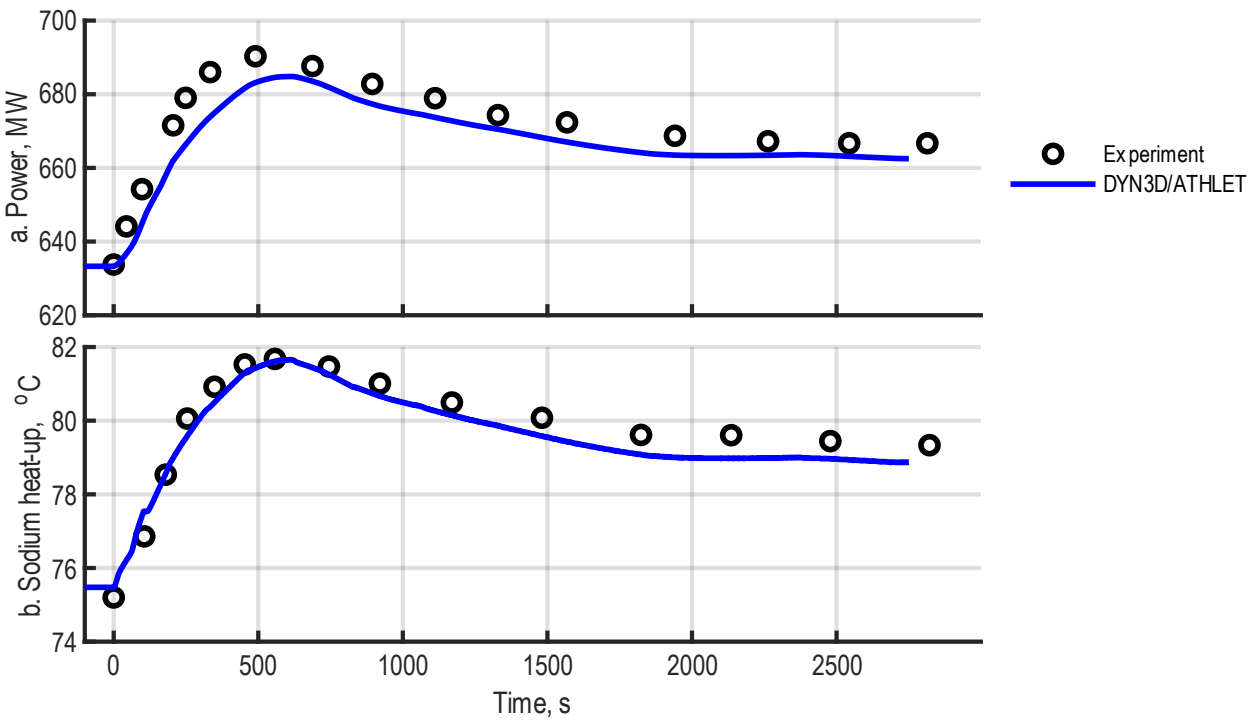

Fig. 31. MOFC2: Comparison of calculations vs experiment, a) power and b) inlet core coolant temperature

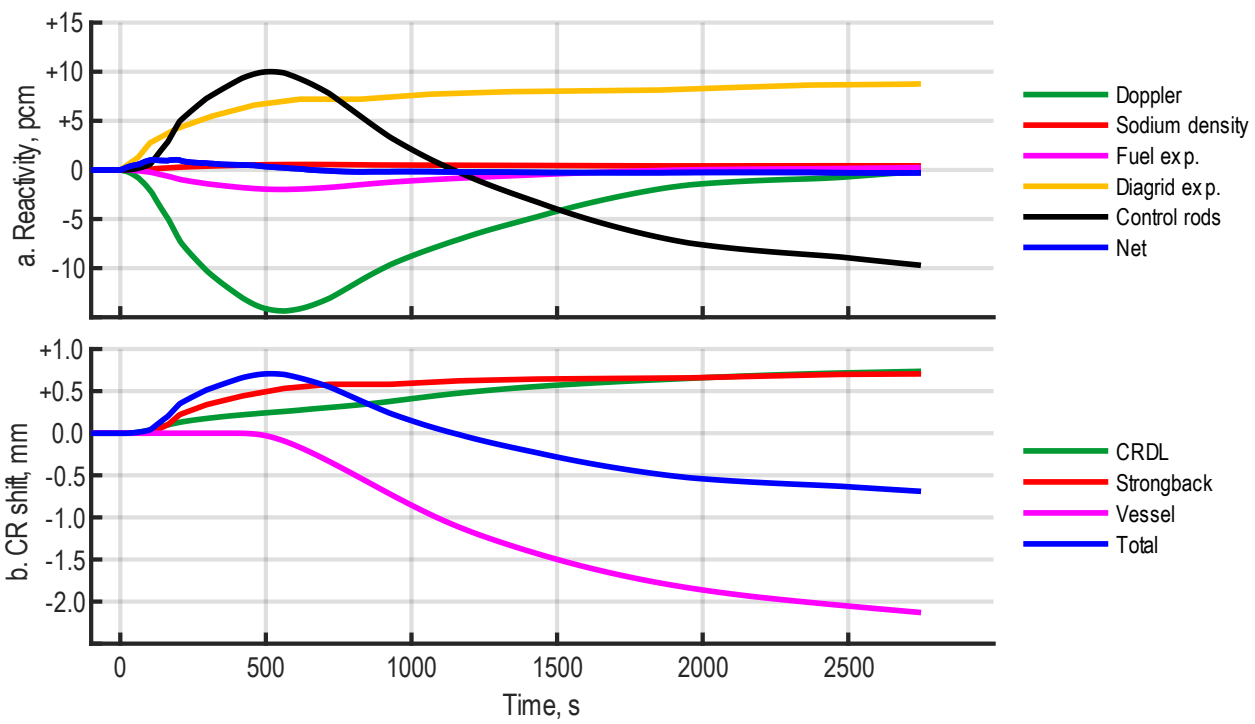

Fig. 32. MOFC2: a) reactivity and b) out-of-core axial expansions of CRDL, strongback, and vessel

MOFC3 test: 10 % primary flow reduction at 663 MW_{th}

The test was initiated from reactor steady conditions with a power level stabilized at 663 MW_{th}. At the test beginning, the initial primary system mass flow, roughly 6300 kg/s, was reduced by 10% in 75 s. For the simulation of the test, time-dependent BCs were set on the sodium temperature and mass flow at the inlet of the model in accordance with the experimental data shown in Fig. 33a and b.

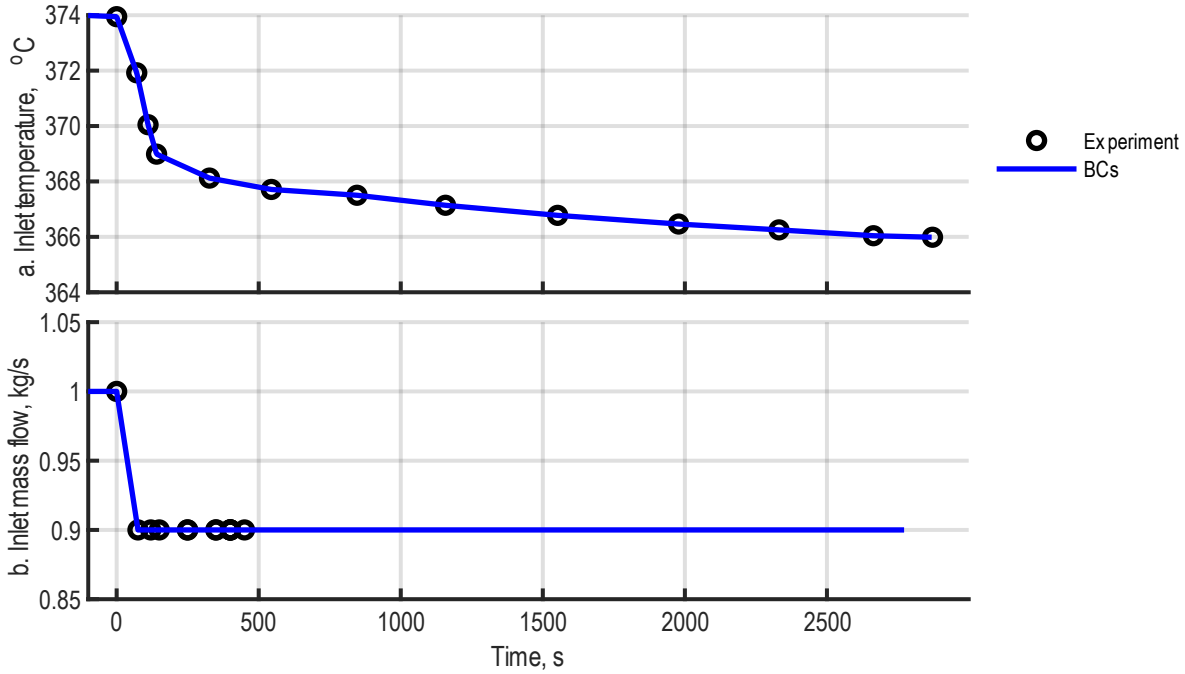

Fig. 33. MOFC3: Inlet core sodium temperature, experimental trend and imposed BC

As a response to the reduction of the inlet mass flow, the sodium temperatures at the core outlet, see Fig. 34b, increases causing the expansion of the CRDLs. The expansion of CRDLs pushes the CRs into the core inserting negative reactivity, see Fig. 35. The negative reactivity induces the power drop shown in Fig. 34a at around 90 s. The diagrid contraction, caused by the decrease of inlet coolant temperature, counteracts almost immediately the negative feedback effect of the CRDLs and leads to a power recovery. The axial shrinking of the strongback has an analogous effect which however becomes effective with a delay of roughly 100 s. At the end of the transient, the power level tends to restabilize also thanks to the negative reactivity insertion induced by the vessel contraction, which is driven by the inlet sodium temperature with a 360 s delay.

In the MOFC3 test, the reduction of 10% of the inlet mass flow rate added further complexity to the simulation of the experiment. The test is characterized by stronger a interplay of the reactivity components and axial expansion effects, especially during the first 1000 s of the transient. Although the platform realistically predicts the initial power drop, the power-recovery peak is not fully captured, and the power trend is slightly underestimated for most of the simulation time.

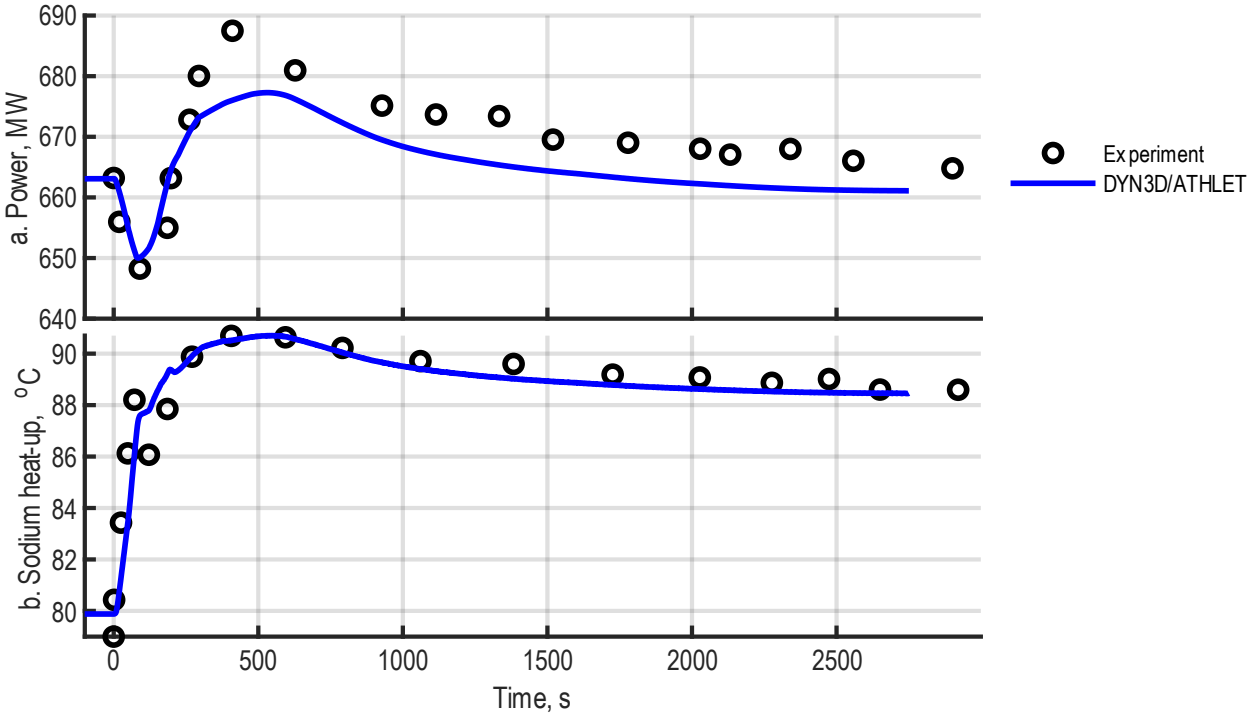

Fig. 34. MOFC3: Comparison of calculations vs experiment, a) power, b) inlet core coolant temperature, and c) inlet mass flow

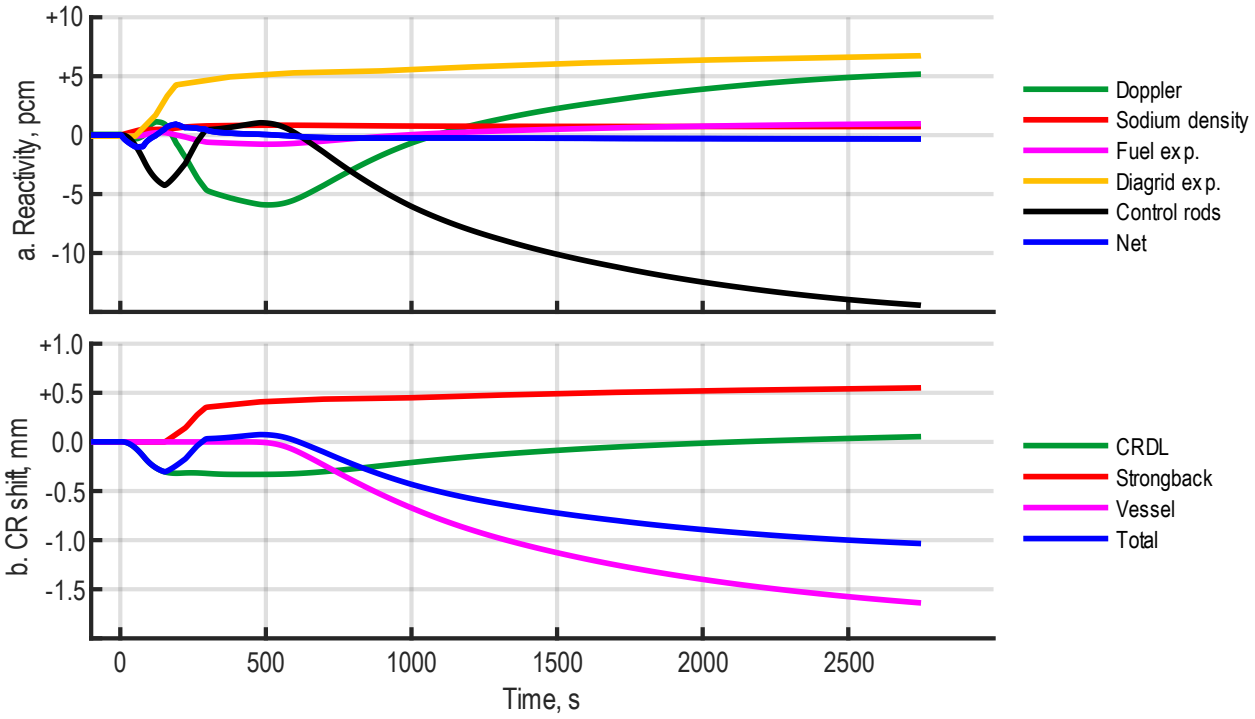

Fig. 35. MOFC3: a) reactivity and b) out-of-core axial expansions of CRDL, strongback, and vessel

Even though with minor discrepancies, the comparison of the evaluated solutions against the experimental trends of power and sodium heat-up show still good prediction capabilities of the platform, see Fig. 41a and b. The evaluated solutions, in fact, exhibit a level of accuracy that is consistent with that of the solutions identified in the SPX benchmark, see (Ponomarev, et al., 2021b).

PFS test: 10 % primary flow reduction at 1415 MW_{th}

This test was performed starting from stable power conditions at 1415 MW_{th}, i.e., roughly 50% of the nominal power. As in the case of MOFC3, the initiator of the transient scenario was the reduction of 10% in primary mass flow which was set initially to 10400 kg/s. Time-dependent BCs were imposed on the inlet sodium mass flow and temperature as shown in Fig. 36a and b, whereas an outlet BC of 1.5 bar was set for the sodium pressure. The calculations run for 2550 s.

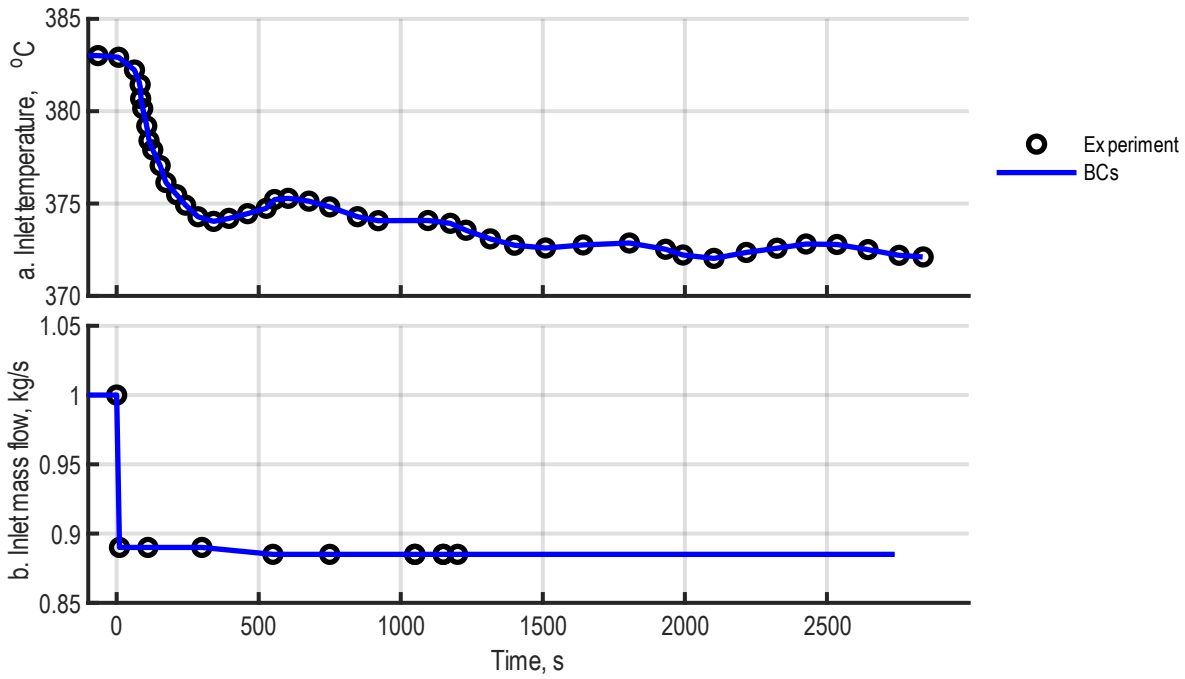

Fig. 36. PFS: Inlet core sodium temperature, experimental trend and imposed BC

The transient evolves according to similar mechanisms discussed for the MOFC3 test. In response to the primary flow reduction, the temperatures of both the core sodium outlet, see Fig. 37b, and CRDLs increase. While expanding, CRDLs push the CRs into the reactor core, inserting negative reactivity, see Fig. 38. As Fig. 37 shows, the initial CR insertion is responsible for the power drop occurring at around 50 s. The Doppler effect and the radial contraction of the diagrid, caused by the decrease of inlet sodium temperature, counteract almost immediately the negative reactivity effect of the CRDLs. Analogous effects are observed for the axial contraction of the strongback with a time delay of 100 s. The interplay of such effects induces a steep power rise, from roughly 1380 to 1460 MWth, between

50 and 300 s. As the vessel axial contraction, driven by the inlet coolant temperature, becomes effective (starting from 500 s), lower and lower power levels are reached.

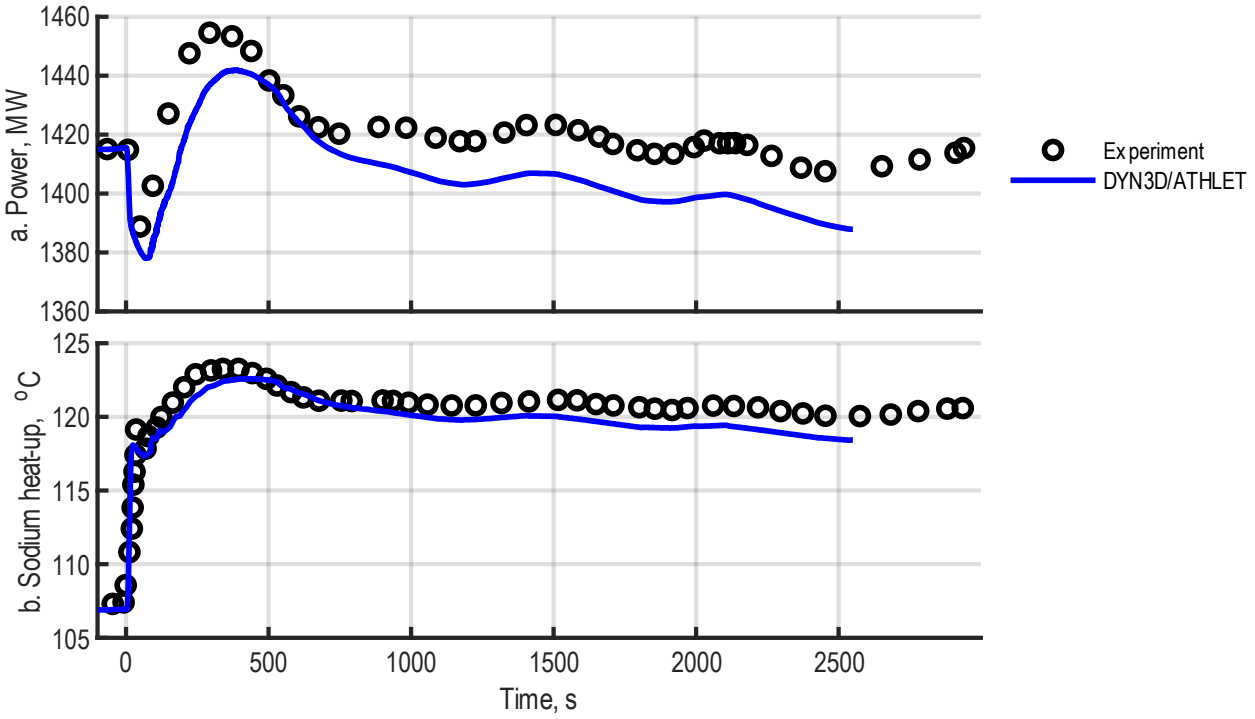

Fig. 37. PFS: Comparison of calculations vs experiment, a) power, b) inlet core coolant temperature, and c) inlet mass flow

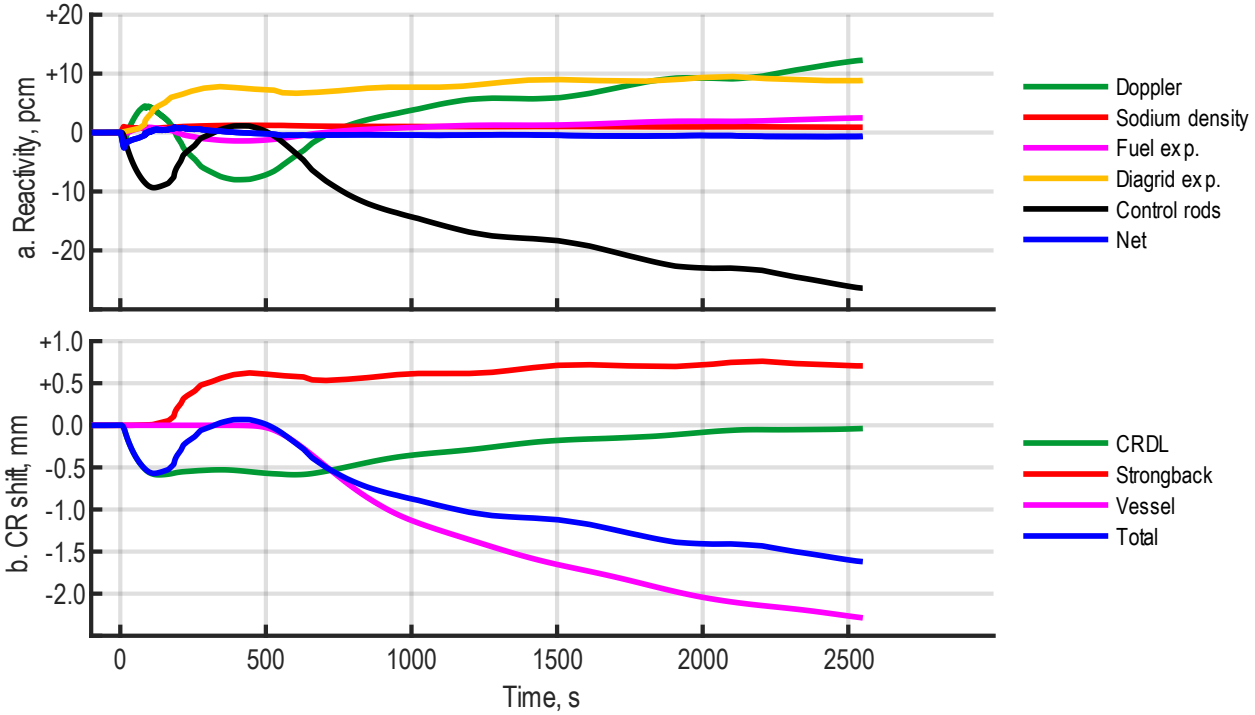

Fig. 38. PFS: a) reactivity and b) out-of-core axial expansions of CRDL, strongback, and vessel

At the end of the transient, the CRs are down-shifted of 1.5 mm into the core with respect to their steady-state position. The power fluctuations shown in Fig. 37a are induced by the fluctuating behavior of inlet sodium temperature, see Fig. 36a, and are representative of the full plant response to the primary flow step perturbation.

The considerations made on the validation of the MOFC3 test hold also for the PFS test. The tests are, in fact, both initiated by reducing by 10% the primary mass flow. The only difference between the tests is the initial power, which is higher in the case of the PFS test. The higher initial power makes the interplays of the reactivity components and axial expansion effects even stronger, and complex to capture. The platform appears to realistically predict the initial power drop, however, the predicted power-recovery occurring after 50 s is less steep than the experimental power. The calculated power evolution is slightly underestimated for most of the simulation time. Similar results were however obtained also by other benchmark participants as shown in (Ponomarev, et al., 2021b). Despite this aspect, the solutions obtained by the platform could still produce acceptable solutions also for the PFS scenario that involved higher power levels.

RS test: -74 pcm stepwise reactivity insertion

For the RS test the reactor model was stabilized at 1542 MWth. The test was driven by a stepwise insertion of CRs preceded by a soft decrease of the inlet sodium temperature. The CRs were inserted exactly at 400, 460, and 520 s leading to the insertions of, respectively, -25, - 25, and -24 pcm reactivity. The simulation of the test was carried out by imposing a CR motion scheme that consistently emulates the stepwise reactivity insertion, and by imposing the inlet core sodium temperature recorded during the experiment as BC, see Fig. 39. A constant sodium mass flow of 10400 kg/s was imposed at the model inlet, whereas an outlet BC of 1.5 bar was set for the sodium pressure. The calculations were run for the first 2800 s of the experiment.

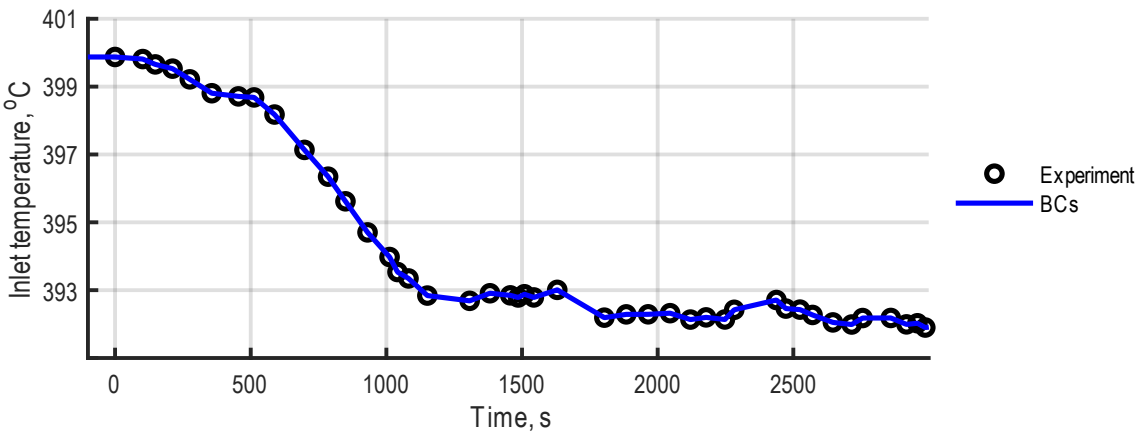

Fig. 39. RS: Inlet core sodium temperature, experimental trend and imposed BC

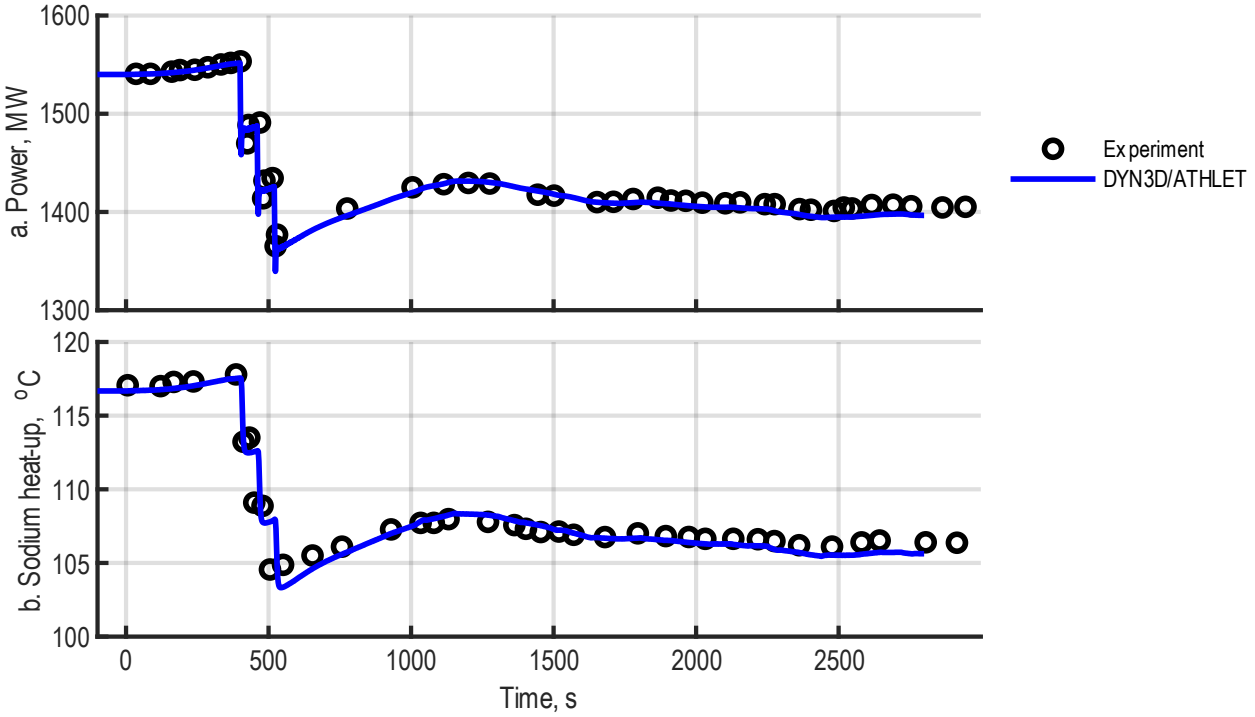

Fig. 40. RS: Comparison of calculations vs experiment, a) power and b) inlet core coolant temperature

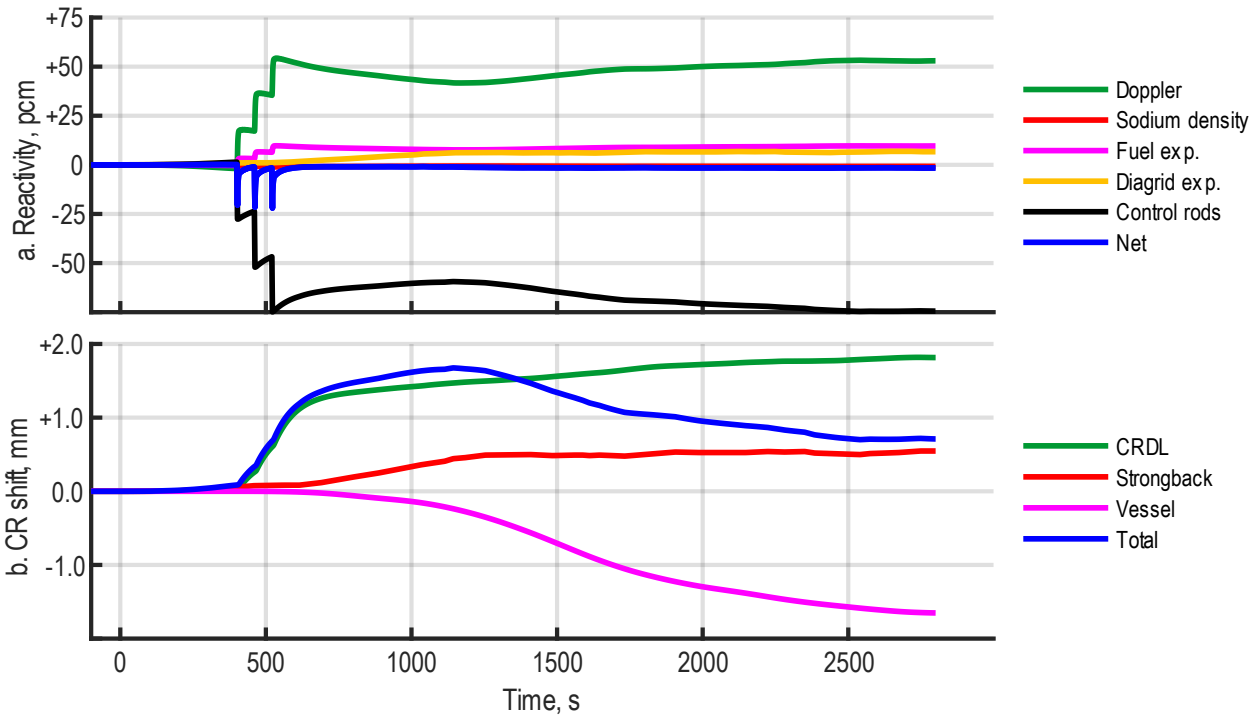

Fig. 41. RS: a) reactivity and b) out-of-core axial expansions of CRDL, strongback, and vessel

From 0 to 400 s, Fig. 40a shows an initial slight increase of the power due to a slight decrement in the inlet core sodium temperature, which results in a small insertion of positive reactivity. Between 400 and 520 s, the stepwise insertions of CRs are promptly counterbalanced by positive reactivity effects of Doppler, and fuel expansion, see Fig. 41a. As the power and, thus, the outlet sodium temperatures decrease, one can notice positive reactivity effects induced by the axial contraction of the CRDLs, see Fig. 41. The effect of CRDLs partially mitigates the negative stepwise reactivity insertion with gradual positive reactivity insertion. Such an offsetting of feedback causes a power dynamic response which is slightly underestimated at the beginning of the CR insertion steps and then followed by recoveries, see Fig. 40a. At the end of the transient, CR are withdrawn up to 2 mm with respect to their original position, and mainly because of the contraction of CRDLs. As in the previous tests, the vessel contraction eventually counteracts the CR withdrawal contributing to the stabilization of the power, see Fig. 41b.

The validation activity carried out on the RS test provided remarkable results. The new platform and the simplified models of the out-of-core structures allowed for an accurate prediction of the power and sodium heat-up during the whole simulation, see Fig. 40a and b. Both reactivity components and axial expansions of the out-of-core structures appear to be realistically estimated.

SST test: +30 pcm reactivity insertion at zero power level

The SST was conducted starting from critical, zero-power, and isothermal core conditions at 179 °C (453 K). The sodium heat-up through the core was practically close to zero. The test was initiated by the insertion of positive reactivity, roughly +30 pcm, through a mild imposed up-shift of CRs. The test was reproduced by both simulating the up-shift of CRs and by applying the experimental inlet sodium core temperature as an inlet BC, see Fig. 42. A fixed BC of 3200 kg/s was imposed as the inlet mass flow for this test. The calculations were run for the first 2500 s of the experiment.

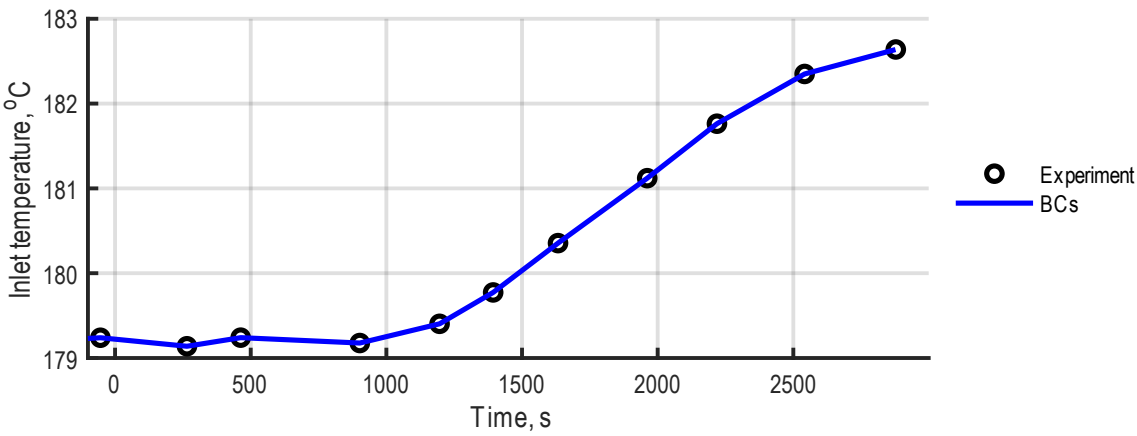

Fig. 42. SST: Inlet core sodium temperature, experimental trend and imposed BC

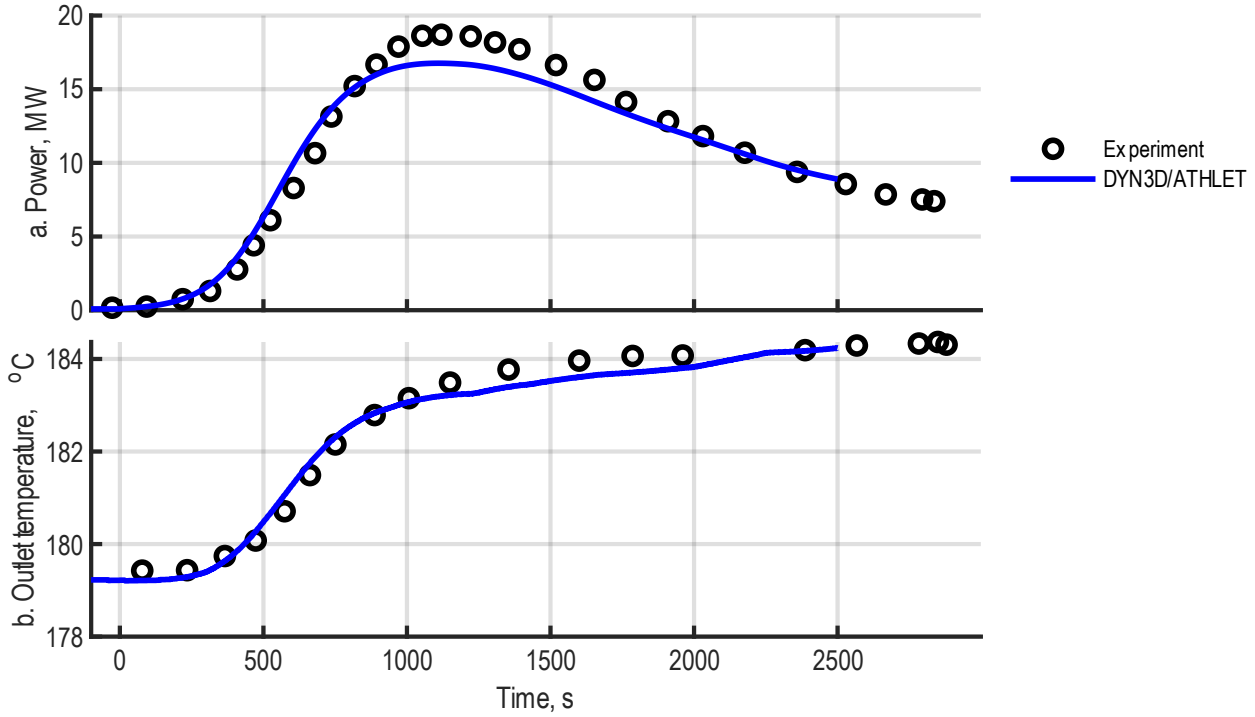

Fig. 43. SST: Comparison of calculations vs experiment, a) power and b) inlet core coolant temperature

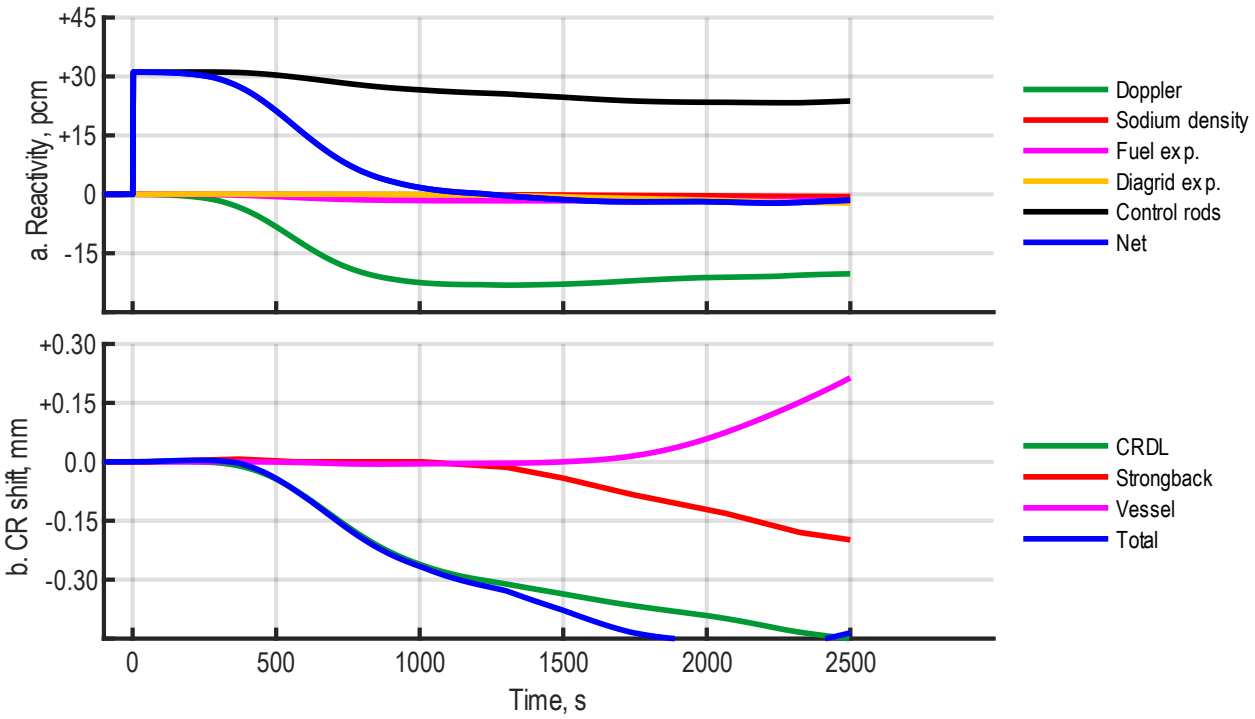

Fig. 44. SST: a) reactivity and b) out-of-core axial expansions of CRDL, strongback, and vessel

From Fig. 43 and Fig. 44, one can notice that the insertion of positive reactivity leads to an expected increase of the power, up to 20 MWth from the initial zero-power conditions. The only feedback that strongly counteracts the positive imposed reactivity insertion is a negative Doppler effect, see Fig. 44a. The effect of the out-of-core TEs on the position of CRs is quite limited in this transient and mainly induced by CRDLs which expand as the power and, thus, the sodium outlet temperature increase, see Fig. 43a and b.

For the considered scenario, the accurate assessment of the initial gap conductance values of fuel rods proved to be essential for a realistic prediction of the transient. For this purpose, the ATHLET dynamic gap model, which permitted the evaluation of more realistic initial gap conductance values, was employed in the test calculations. Related details on the application of the dynamic gap model are thoroughly reported in Appendix B.2.

The validation conducted on the SST test yielded highly satisfactory outcomes. The extended platform allowed for an accurate prediction of the total power and outlet core sodium temperature throughout the simulated interval of time, see Fig. 43a and b. The accuracy of the results obtained was in line with that of the solutions identified by the benchmark participants in (Ponomarev, et al., 2021b).

3.3 Summary and considerations

This chapter presented the V&V conducted on Serpent/DYN3D/ATHLET, as applied for the first time to the transient analyses of SFRs. Such activities were mainly focused on verifying and validating the extended DYN3D/ATHLET coupling routines, see Section 2.1, and the proposed ATHLET-based approaches for modeling relevant out-of-core structures, see Section 2.2. The V&V activities showed, on one hand, that the extended coupling routines and the approaches for modeling the out-of-core structures function as intended by the implementation specifics. On the other hand, they demonstrated that the new platform is capable of producing quality solutions reasonably close to the experimental trends. The activities conducted in this chapter are summarized in a V&V matrix in Table 12.

The verification of the extended coupling routines of the platform was conducted by demonstrating the equivalence between the new TH module of the platform, i.e., ATHLET, and the old one, i.e., FLOCAL, which was supposed to be replaced. The verification was conducted, at core level, against the Phénix NC test via comparison with existing Serpent/DYN3D solutions presented in (Nikitin & Fridman, 2018c). The verification demonstrated the equivalence between the TH modules both in

static and transient analyses: The new platform was able to predict the reactor core behavior as good as Serpent/DYN3D.

Table 12. V&V matrix

Test	Object modeled	Main object of verification/validation	Other models involved, and verified/validated	Perturbation involved	References
Phénix, NC (EOL), 120 MW_{th}	• Core	• DYN3D/ATHLET coupling routines	DYN3D: • 3D spatial kinetics • In-core TE models ATHLET: • Core thermal hydraulics	• Decrease in inlet core sodium temperature	• DYN3D* • Experiment
	• Core • Actual primary system • out-of-core structures	• DYN3D/ATHLET coupling routines • Detailed models of out-of-core structures	DYN3D: • 3D spatial kinetics • In-core TE models ATHLET: • System thermal hydraulics	• Decrease in inlet core sodium temperature	• DYN3D* • Experiment
SPX, MOFC1 (BOL), 692 MW_{th}	• Core • Primary system by BCs • out-of-core structures	• DYN3D/ATHLET coupling routines • Simplified models of out-of-core structures	DYN3D: • 3D spatial kinetics • XS models • In-core TE models ATHLET: • Core thermal hydraulics	• Decrease in inlet core sodium temperature • CR insertion (-50 pcm)	• Experiment
SPX, MOFC2 (BOL), 633 MW_{th}	• Core • Primary system by BCs • out-of-core structures	• DYN3D/ATHLET coupling routines • Simplified models of out-of-core structures	DYN3D: • 3D spatial kinetics • XS models • In-core TE models ATHLET: • Core thermal hydraulics	• Decrease in inlet core sodium temperature	• Experiment
SPX, MOFC3 (BOL), 663 MW_{th}	• Core • Primary system by BCs • out-of-core structures	• DYN3D/ATHLET coupling routines • Simplified models of out-of-core structures	DYN3D: • 3D spatial kinetics • XS models • In-core TE models ATHLET: • Core thermal hydraulics	• Decrease in inlet core sodium temperature • Decrease in core sodium flow rate (10% reduction)	• Experiment
SPX, PFS (BOL), 1415 MW_{th}	• Core • Primary system by BCs • out-of-core structures	• DYN3D/ATHLET coupling routines • Simplified models of out-of-core structures	DYN3D: • 3D spatial kinetics • XS models • In-core TE models ATHLET: • Core thermal hydraulics	• Decrease in inlet core sodium temperature • Decrease in core sodium flow rate (10% reduction)	• Experiment
SPX, RS (BOL), 1542 MW_{th}	• Core • Primary system by BCs • out-of-core structures	• DYN3D/ATHLET coupling routines • Simplified models of out-of-core structures	DYN3D: • 3D spatial kinetics • XS models • In-core TE models ATHLET: • Core thermal hydraulics	• Decrease in inlet core sodium temperature • Step-wise CR insertion (-74 pcm)	• Experiment
SPX, SST (BOL), ≈ 0 MW_{th}	• Core • Primary system by BCs • out-of-core structures	• DYN3D/ATHLET coupling routines • Simplified models of out-of-core structures	DYN3D: • 3D spatial kinetics • XS models • In-core TE models ATHLET: • Core thermal hydraulics • Dynamic gap model	• Increase in inlet core sodium temperature • CR withdrawal (+30 pcm)	• Experiment

*Available model and solutions from (Nikitin & Fridman, 2018c)

The V&V of the newly extended platform, jointly applied with detailed models of out-of-core structures, was also conducted against the Phénix NC test. This V&V exercise was carried out by comparing solutions obtained by the new platform against existing Serpent/DYN3D solutions, and experimental data. The applied detailed modeling methodology reproduced in a physical-coherent way the TEs of out-of-core structures and enabled the prediction of related changes in CR positions. The extended computational platform demonstrated the capability of adequately predicting the power evolution against the experimental trend, and satisfactory results were also found for the reactivity trend.

The V&V of the newly extended platform, jointly applied with simplified models of out-of-core structures, was conducted against the SPX start-up tests. For all the tests the simplified models of out-of-core structures appear to respond in a physical-coherent way to system perturbations and to adequately predict changes in CR positions induced by the out-of-core TEs. For all six SPX start-up tests, the computational platform demonstrated the capabilities to predict the evolutions of the power and sodium heat-up against experimental trends with acceptable discrepancies. All the solutions obtained were in good agreement with results originally found by the benchmark participants in (Ponomarev, et al., 2021b).

In parallel, to the main objects of V&V, other models were further verified and validated, in particular:

- The XS models generated to simulate the SPX startup tests were formerly tested against Serpent/DYN3D static benchmark solutions provided in (Ponomarev, et al., 2021a), see Section 1 of Appendix B, and validated under transient conditions in Section 3.2.4.
- The DYN3D in-core fuel TE models, previously validated only for closed gap configurations assumed at Phénix EOL conditions, were also applied and validated for open gap configurations assumed at SPX BOL conditions, see Section 3.2.4.
- The ATHLET dynamic gap conductance model, applied to the SPX SST test to evaluate more realistic values of the initial gap conductance, was validated in Section 3.2.4.

The set of the seven validation tests, presented in the V&V matrix of Table 12, allowed for an extensive preliminary V&V of the Serpent/DYN3D/ATHLET. The computational platform was tested against scenarios involving several core power levels, from kW to MW, and soft perturbations of different nature, such as, e.g., inlet core variations in coolant temperature and coolant mass flow, as well as CR insertion and withdrawal. The V&V activities demonstrated that the platform can well

predict the behavior of the selected SFR designs under the considered test scenarios. In principle, this achievement paves the way for further applications of the platform to analyses of other SFR designs and diverse transient scenarios, provided that the latter do not involve sodium boiling or core damage.

Chapter 4 Optimization

The V&V activities performed in Chapter 3 demonstrated good capabilities of the new HZDR platform in predicting the behavior of SFR systems under the selected scenarios. However, the corresponding transient analyses turned out to be extremely time-demanding[6]: In particular, as Fig. 45 shows, the analyses conducted on the Phénix NC test required 4 days for the simulation of 458 s of transient, whereas about 12 days were required to simulate, on average, 2700 s of each SPX start-up test. It must be stressed that the calculation times mentioned above did not include XSs' generation times. The need for such long computational times certainly represents a serious limitation of the platform capabilities. Potential solutions to accelerate the calculations had to be clearly considered.

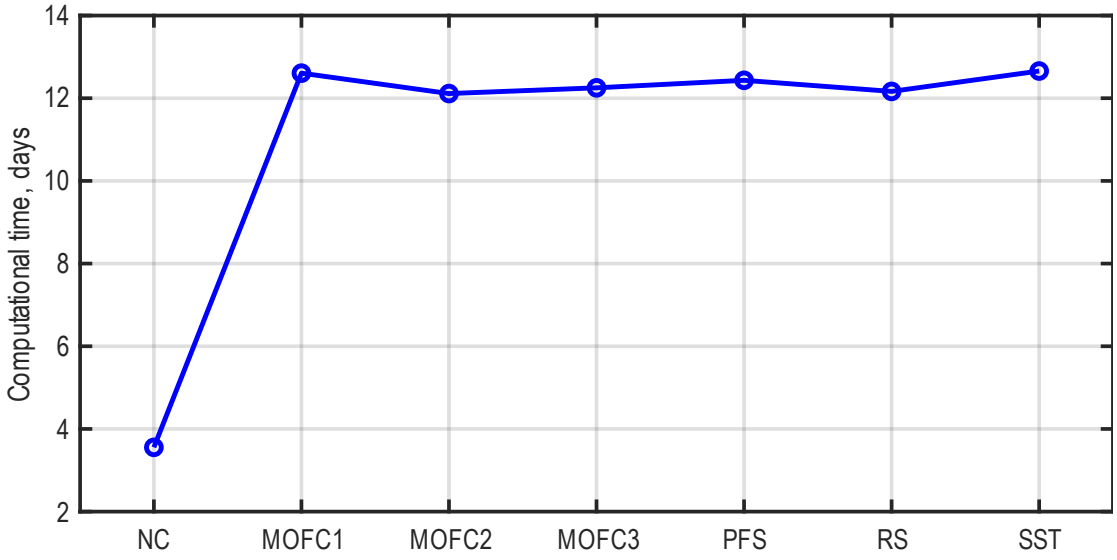

Fig. 45. Computational times required for analyses of the Phénix NC and SPX start-up tests

A main bottleneck of the analyses is constituted by neutronics calculations which, it should be recalled, were performed with XS libraries defined over a 24-group EGS proposed in (Fridman & Shwageraus, 2013) and parametrized via MDT approach.

In view of the above, two options were considered to optimize the computational times of the platform while preserving the accuracy of neutronics solutions. Both the options were related to the simplification of the XS library models and involved, specifically, the optimal condensation of the EGS, and the parametrization of XSs via FOD approach. In particular:

[6]Calculations were performed with the following setup: Intel Core i7 (2.90GHz), equipped with 8 cores and 16 logic units. For each run, 4 threads were dedicated to the calculations by exploiting available parallel capability options of DYN3D/ATHLET. Calculation times do not include XS generation times.

- The condensation of EGSs implied the reduction of the number of EGs used in the representation of XS libraries and, as a consequence, the reduction of computational times to perform neutronics calculations. The identification of condensed EGSs which can significantly accelerate calculations while preserving an acceptable quality of solutions is a challenging combinatorial problem. A new methodology for the selection of optimal EGSs to be used in the analyses of SFR designs was developed for this purpose. The developed methodology was assisted by the meta-heuristic "simulated annealing" (SA).

- The parametrization of XSs via the FOD approach, as applied in (Downar, et al., 2012), enabled one to avoid on-the-run multidimensional interpolations foreseen by the MDT approach to actualize the nodal XSs. The application of the FOD approach is not only beneficial for the acceleration of neutronics calculations but also for the simplification of the generation process of the XSs. The FOD approach, described in detail later on in this chapter, is an adaptation of the method used by the FAST code for the XS parametrization of SFRs (Mikityuk, et al., 2005).

This chapter aims at presenting in detail the XS modeling options described above through the following structure: Section 4.1 of this chapter provides a comprehensive overview of the methodology implemented for the optimization of EGSs assisted by the SA. Section 4.2 presents in detail the approach of XS parametrization via FOD and its main advantages. Section 4.3 presents the estimation of the benefits introduced by the proposed XS modeling options in terms of computational times and the assessment of the effect of the options on the quality of solutions.

4.1 Optimization of EGSs assisted by simulated annealing[7]

The solution of the multi-group diffusion equation requires multi-group macroscopic XSs which can be generated by high fidelity deterministic, or MC neutron transport codes. The choice of a number of energy groups and their structure affects the accuracy of the results and the computational time required to accomplish simulations. In LWR analyses, typically only few (2 to 4) energy groups are used[8]. However, as the neutron mean free path in SFRs is larger than in LWRs, the cell neutron spectrum of the lattice calculations and the actual core spectrum may significantly deviate from each other. This causes inconsistencies in the neutrons leakage treatment, especially at higher energies where capture and fission reaction rates strongly contribute to the SFRs neutron balance. To reduce

[7] The section summarizes and reports the content produced in (Di Nora, et al., 2021a; 2021b) which was developed in the framework of the present doctoral research.
[8] Therefore, very often a term “few-group” is used instead of “multi-group”.

the inconsistencies, a finer energy discretization is applied. For example, the well-known fast reactor analysis code ERANOS utilizes 33 energy groups for 3D full core calculations (Ruggieri, et al., 2006).

Thus far, DYN3D was successfully applied to steady-state analyses of various SFR cores. In all cases, the multi-group XS libraries were generated using the Serpent adopting an EGS comprised 24 groups shown in Table 13.

Table 13. Reference 24-group energy structure.

Group	Upper energy limit, MeV	Group	Upper energy limit, MeV	Group	Upper energy limit, MeV
1	1.9649E+01	9	3.0197E-01	17	5.5308E-03
2	1.0000E+01	10	1.8316E-01	18	3.3546E-03
3	6.0653E+00	11	1.1109E-01	19	2.0347E-03
4	3.6788E+00	12	6.7379E-02	20	1.2341E-03
5	2.2313E+00	13	4.0868E-02	21	7.4852E-04
6	1.3534E+00	14	2.4788E-02	22	4.5400E-04
7	8.2085E-01	15	1.5034E-02	23	3.0432E-04
8	4.9787E-01	16	9.1188E-03	24	1.4863E-04

This structure was formed by condensation of the last 10 EGs (from 24 to 33) of the ERANOS 33-group EGS into a single group as recommended in (Fridman & Shwageraus, 2013). The steady-state DYN3D diffusion calculations performed with 24 EGs are relatively cheap with the computational times on the order of minutes. However, the use of the same 24-group structure in transient calculations has a considerably higher computational footprint. For instance, Fig. 45 shows that the analyses of transient benchmarks required from 4 to 12 days to be accomplished. If a large number of transient calculations has to be performed, long-running times can become a serious bottleneck.

An obvious means to boost multi-group diffusion calculations is the reduction in number of EGs, which, however, can also compromise the quality of the results. Therefore, coarser EGSs should be judiciously selected as a trade-off between desired speedup and target accuracy. For this purpose, several methods were applied in the past, e.g., the particle swarm optimization (Yi & Sjoden, 2013; Fleming, et al., 2016), the genetic algorithms (Massone, et al., 2017), etc. This Section shows a new intuitive and alternative methodology for identifying optimized EGSs with a reduced number of EGs to be used in multi-group diffusion analyses of SFRs. The optimized structure should lead to considerable computational speedup without significant deterioration of the accuracy. The proposed methodology is based on two major steps. Firstly, the possible time-savings, resulting from the reduction in number of EGs from currently employed 24 groups downwards, are evaluated. Secondly,

for cases showing a significant speedup, best-performing configurations of the EGSs are derived from the reference 24-group structure.

It should be emphasized that, for a certain set of EGSs, step two represents a complex combinatorial optimization problem which cannot be directly solved through deterministic approaches due to a large number of possible combinations. For example, for an initial structure of 24 groups with the number of internal group boundaries n=23 and a condensed sub-structure of 12 groups with the number of internal group boundaries k=11, a number of possible combinations is provided by Newton's binomial formula Eq. 4.1, which in this case gives 1,352,078 possible combinations.

$$\binom{n}{k} = \frac{n!}{k!\,(n-k)!} \qquad \text{Eq. 4.1}$$

For this reason, impractical deterministic search techniques should be replaced by other more efficient and smart ways for exploring the combinatorial space. In the past, several methods such as the particle swarm optimization (Yi & Sjoden, 2013) and the genetic algorithms (Massone, et al., 2017) were applied to find optimum EGSs. In this study, the application of an alternative method was considered for the purpose, i.e., the SA method. The MC SA algorithm is a meta-heuristic, i.e., by definition: “an iterative generation process which guides a subordinate heuristic by combining intelligently different concepts for exploring and exploiting the search spaces using learning strategies to structure information in order to find efficiently near-optimal solutions” (Osman & Kelly, 1996). The procedure has already been successfully applied for solving complex combinatorial optimization problems (Scheff, et al., 2013; Kotlyar & Parks, 2016). The technique combines features of the more intuitive random walk and hill-climbing procedures, turning itself intuitive and relatively simple to implement.

The novel methodology for the selection of optimal EGSs with a reduced number of EGs to be used in multi-group diffusion analyses of SFRs was developed and tested in (Di Nora, et al., 2021a; 2021b). The following subsections summarize the procedure and the main outcomes obtained. In particular, Section 4.1.1 presents the general approach to EGS optimization. Section 4.1.2 introduces the SA procedure adapted to the EGS optimization process. Section 4.1.3 shows the outcomes of the methodology as applied to the SPX and Phénix cores.

4.1.1 Description of optimization methodology

The optimization methodology upgrades the Serpent/DYN3D XS generation procedure providing the possibility of selecting condensed EGS that accelerate calculations while preserving solutions'

accuracy. Given as a test case a generic SFR core design, the optimization procedure is performed by following the steps described below.

- The test case is statically analyzed with DYN3D standalone employing the Serpent/DYN3D XS generation procedure. Static solutions of the core configurations are derived. At this stage, the reference 24-group energy structure is used. The derived 24-group DYN3D solutions are considered as references.

- At the next stage, potential calculation speedups are quantified. The reference 24-group XSs are condensed arbitrarily into XS sets with a lower number of EGs. With the newly condensed XSs, the test cases are calculated again by DYN3D and the corresponding time savings, induced by the reduction in number of EGs, are estimated. At this stage, the accuracy of the results is not assessed.

- Then, by focusing only on those XS sets whose number of EGs allows for significant calculation speedups, condensed EGSs providing best quality of the solutions are identified. Depending on the number of possible configurations to explore, see Table 14, the optimization of the EGSs is conducted by either a deterministic direct search (brute-force) or applying the SA algorithm described in Section 4.1.2.

Table 14. EGSs, groups and # of possible configurations given by Newton's binomial formula

# of EGs	# of combinations	# of EGs	# of combinations	# of EGs	# of combinations
1	1	9	490,314	17	245,157
2	23	10	817,190	18	100,947
3	253	11	1,144,066	19	33,649
4	1,771	12	1,352,078	20	8,855
5	8,855	13	1,352,078	21	1,771
6	33,649	14	1,144,066	22	253
7	100,947	15	817,190	23	23
8	245,157	16	490,314	24	1

In the optimization analysis, the accuracy of a generic EGS should be measured by a cost function that evaluates the deviation of the condensed solutions from the reference 24-group solution.

Initially, the EGS optimization procedure was tested on Case number 1 of the static neutronic SPX benchmark. This corresponds to an isothermal unrodded core state. The optimization was driven by the cost function “h” defined as shown in Eq. 4.2.

$$h = |\Delta P_{RMS}| + w_\rho \cdot |\Delta\rho| \qquad \text{Eq. 4.2}$$

In Eq. 4.2, $\Delta\rho$ is the error in the core reactivity[9] and ΔP_{RMS} is the subassembly-wise RMS error in power distribution[10] between the results obtained with the reference and condensed EGSs. The contributions of $\Delta\rho$ and ΔP_{RMS} to h were balanced using the weighting factor w_ρ. Parametric studies showed that the setting of w_ρ equal to 0.002 allows one to identify solutions with optimal compromises between the components of the cost function. In particular, the factor 0.002 takes into account the difference in the order of magnitude of the quantities balanced, slightly giving priority to the power distribution component of the cost function.

However, when applied to more realistic problems, the cost function in Eq. 4.2 may be not sufficiently representative of all core states. Although, the cost function can be constructed to explicitly include a wide range of operating conditions, this approach is computationally too expensive. As an alternative, the cost function can be formed with a help of two bounding or “extreme” cases. The unrodded and rodded core states were considered as such extreme cases. A new cost function “H”, defined as Eq. 4.3 shows, was thus introduced.

$$H = h_{unrodded} + w_{Rod} \cdot h_{rodded} \qquad \text{Eq. 4.3}$$

In Eq. 4.3, w_{Rod} is a weighting factor used to balance the unrodded and rodded contributions while the $h_{unrodded}$ and h_{rodded} are calculated by Eq. 4.2, respectively considering the unrodded and rodded core configurations. Globally, acceptable compromises were found on the accuracy of the solutions by choosing w_{Rod} equal to 0.5 for the cost function H. Parametric studies performed for the selection of w_{Rod} are reported in Appendix D.1.

In the optimization process, combinations of $\Delta\rho$ and ΔP_{RMS} values were used for tracking the quality of the solution. Obviously, this combination can be either extended or replaced by other parameters of interest, e.g., certain reactivity coefficient, safety- relevant thermal-hydraulic parameters, etc.

---

[9] $\Delta\rho = \rho^{calculated} - \rho^{reference}$ where $\rho = \frac{k_{eff}-1}{k_{eff}}$

[10] $\Delta P_{RMS} = \sqrt{\frac{1}{N_{sub}} \sum_i \left(\frac{P_i^{calculated} - P_i^{reference}}{<P>} \right)^2}$

where "N_{sub}" is the number of fuel subassemblies, "P_i" is the power generated in subassembly "i", and $< P >$ is the average subassembly power.

4.1.2 The SA algorithm

The MC SA algorithm is a nature-inspired high-level procedure applied to solve combinatorial optimization problems (Elperin, 1988; Glover & Greenberg, 1989; Eliasi, et al., 2002; Kotlyar & Parks, 2016). With reference to (Elperin, 1988), the natural mechanism inspiring the SA algorithm is next shortly presented.

Given a generic system of n particles within the phase space of variables (x_1,...,x_n), the function H(x_1,...,x_n) of variables (x_1,...,x_n) is assumed as the internal energy of the system. The problem consists in finding an optimal configuration of the variables (x_1*,...,x_n*) that minimize H within the space of possible configuration **D**. In other words:

$$H(x_1^*, \dots, x_n^*) = min\{H(x_1, \dots, x_n)\}, \boldsymbol{x} \in \boldsymbol{D} \qquad \text{Eq. 4.4}$$

From thermodynamics, it is known that the probability of a generic configuration (x_1,...,x_n) to occur is given by the Boltzmann-Gibbs distribution described by:

$$p(x_1, \dots, x_n) = \frac{1}{Z} exp\left[-\frac{H(x_1, \dots, x_n)}{T}\right] \qquad \text{Eq. 4.5}$$

where T is a temperature and Z is the normalization constant equaling the statistical sum of the exponential term. In case of equilibrium of the system, H assumes its minimum value and p its maximum, i.e., both Equations Eq. 4.4 and Eq. 4.6 are valid.

$$p(x_1^*, \dots, x_n^*) = max\left\{\frac{1}{Z} exp\left[-\frac{H(x_1, \dots, x_n)}{T}\right]\right\}, \boldsymbol{x} \in \boldsymbol{D} \qquad \text{Eq. 4.6}$$

The actual problem can be thus solved by generating virtual configurations j of the system $(x_1,...,x_n)^j$, computing p, and accepting randomly its ever more probable states. In correspondence of the most probable state of the system, its minimum energy and optimum configuration (x_1*, ..., x_n*) are found. Eventually, local minima are skipped because of the randomness of the process which also leads to the acceptance of unlikely states of the system. As Equations Eq. 4.5 and Eq. 4.6 show, the stochastic process depends on the temperature T. With such random evolution, a system of n particles at temperature T reaches the equilibrium configuration while skipping the local minima thanks to the thermal fluctuation.

In the EGS optimization problem, static configurations of the core design under study play the role of the system. The discrete variables (x_1,...,x_n) are a sub-selection of the internal boundaries of the reference 24-group structure which should be removed to obtain a new condensed energy grid (B_1,...,B_n). Finally, the function H corresponds to the cost function defined in Eq. 4.3.

The SA algorithm is graphically presented in Fig. 46 and its steps are summarized hereafter:

1. Generation of a trial zero configuration of boundaries (B_1^0,...,B_n^0), the corresponding condensed XSs are generated and the cost function value $H(B_1^0,...,B_n^0)$ is calculated. The boundaries combination (B_1^0,...,B_n^0) and the value $H^0=H(B_1^0,...,B_n^0)$ are stored as first trial optimum, i.e., $(B_1^*,...,B_n^*)=(B_1^0,...,B_n^0)$ and $H^*=H^0$.

2. For each step k, starting from the optimum configuration (B1*,...,Bn*) a randomly picked boundary B_m^* is changed in B_m^k. The boundary substitution is made in agreement with the constraints of the adjacent boundaries.

3. The corresponding condensed XSs are generated, and the test case is recalculated.

4. The value H^k corresponding to (B_1^*,...,B_{m-1}^*,B_m^k,B_{m+1}^*,…,B_n^*) is computed.

    a. If $H^k \leq H^*$, jump to step 6.

    b. If $H^k > H^*$, go to step 5.

5. Evaluate the probability $P=\exp[-(H^k-H^*)/T_k]$ as given from the Boltzmann factor.

    a. With the probability P, go to step 6.

    b. Otherwise, go to step 7.

6. Accept (B_1^*,...,B_{m-1}^*,B_m^k,B_{m+1}^*,…,B_n^*) as the new optimum configuration, and H^k as the new H*.

7. If k is smaller than the total number of iterations N, go to step 2. Quit the process otherwise.

At the end of the procedure, an optimal configuration of the system's energy boundaries is found. The temperature T_k in step 5 is updated at each kth iteration according to cooling schedule in Eq. 4.7:

$$T_k = \frac{N-k}{N} \cdot T_0 \cdot e^{-\frac{k}{r}} \qquad \text{Eq. 4.7}$$

In Eq. 4.7, N is the total number of iterations, T_0 is the initial temperature and r is the cooling rate. The parameters N, T_0 and r affect the probability P in step 5 and, consequently the performance of the algorithm. The selection process of such parameters was conducted via parametric studies and is reported in Appendix D.2.

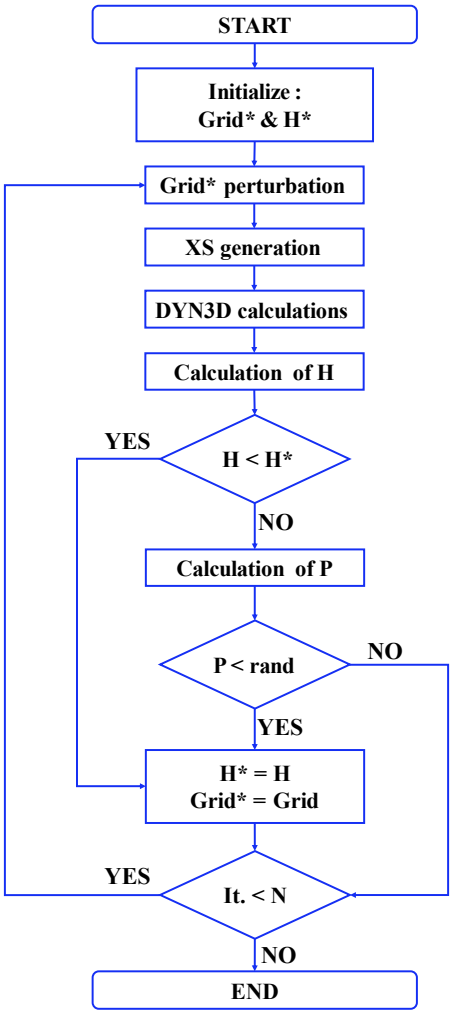

Fig. 46. SA-optimization scheme

4.1.3 Optimization of EGS for SPX and Phénix analyses

The optimization procedure assisted by the SA was applied to the SPX and Phénix cores to determine optimal condensed EGS to use for accelerating the neutronic calculations performed either with DYN3D standalone or DYN3D/ATHLET coupled.

The optimization was conducted by employing the cost function H in Eq. 4.3. In the case of the SPX calculations, Cases number 1 and 13 of the SPX neutronics benchmark are selected as the unrodded and rodded cases of the analysis. Both the cases represent isothermal BOL core states at 453K. For the Phénix calculations, unrodded and rodded contributions of the cost function were calculated

considering static unrodded and rodded isothermal EOL core configurations at 523K. Static 24-group DYN3D solutions of the unrodded and rodded configurations of both SPX and Phénix core designs were derived and considered as references.

To quantify potential accelerations of calculations, speedup tests were performed with DYN3D by calculating static and transient benchmark test cases employing XS sets with a reduced number of EGs (i.e., from 23 to 1). Case number 1of the SPX benchmark and the initial stage of the Phénix NC test were considered respectively for static and transient tests. At this stage, the condensed structures were arbitrarily derived from the reference 24-group grid. The speedup factors were obtained as the ratio of the DYN3D running times with the reference and collapsed EGs. The results of the speedup tests are summarized in Fig. 47.

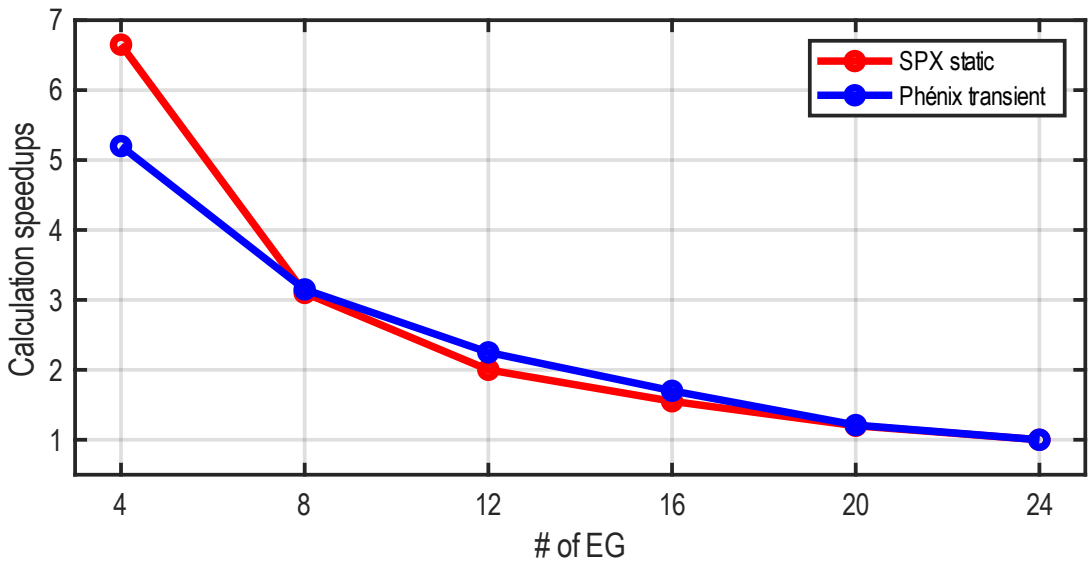

Fig. 47. Trends of speedup factors against the # of EGs

In static calculations, the diffusion solver implemented in DYN3D runs a loop over energy groups, so the calculation cost (i.e., calculation time) is roughly linearly proportional to the number of energy groups. The calculation speedup is defined as a ratio of calculation times applying reference 24-group EGs and the considered EGs. It can be roughly estimated with the expression shown in Eq. 4.8.

$$Speedup_{\#EGs} = \frac{time_{24}}{time_{EGs}} \cong \frac{24}{\#EGs} \qquad \text{Eq. 4.8}$$

Speedup tests performed on the Phénix natural circulation transient confirmed the possibility of significantly reducing computational times in transient calculations, see Fig. 47. Although these last lso include thermal hydraulics steps, the speedup curve of transient tests practically reproduces the static speedup trend since computational times are dominated by neutronics.

The research of best performing condensed EGS was conducted then to EGS exhibiting a speedup of 2 and above, which was considered as “substantial”. According to Fig. 47, this corresponds to EGS with up to 12 EGs. As shown in Table 14, for EGSs with EGs between 1 and 6, the number of the possible configurations to explore is reasonably low. This allows for a direct brute-force determination of best-performing grids. That means that for such EGSs, all possible combinations of the condensed structures can be tested and compared. For the EGSs with a number of energy bins between 7 and 12, the number of possible grids to explore goes respectively from 100,947 to 1,352,078 combinations. For these cases, a direct determination of the optimal configurations is neither computationally practical nor efficient. The identification of the best performing EGSs is thus conducted by applying the meta-heuristic SA algorithm.

As the performance of the SA are dependent on the cooling schedule and related parameters T_0, r, and N showed in Eq. 4.7, suitable values of the constants were determined through parametric analyses. Corresponding studies are shown in Appendix D.2. Eventually, the parameters T_0, r, and N were set to 1, 1000, and 1500, for the optimization of EGSs of the SPX, and to 1, 500, and 2000 for the optimization of EGSs of the Phénix.

The best performing optimal condensed EGS identified through the procedure for the SPX and Phénix are shown in Fig. 48 as subsets of the reference 24-group energy structure along with the neutron flux spectra. For each identified optimal condensed EGS, adjacent subsets are diversified in green and blue rectangles. The components of the cost function (i.e., $\Delta\rho$ and ΔP_{RMS} of the unrodded and rodded core states) for the optimal EGS are shown in Table 15 for both SPX and Phénix cores.

Table 15. Performance of the optimal EGSs

	SPX, Unrodded		SPX, Rodded			Phénix, Unrodded		Phénix, Rodded		
EG #	ΔP_{RMS}, %	$\Delta\rho$, pcm	ΔP_{RMS}, %	$\Delta\rho$, pcm	H	ΔP_{RMS}, %	$\Delta\rho$, pcm	ΔP_{RMS}, %	$\Delta\rho$, pcm	H
2	2.53	306	12.67	1932	11.41	0.99	232	1.46	201	2.38
3	1.84	21	3.57	618	4.29	0.49	40	0.59	497	1.36
4	1.57	49	1.82	147	2.73	0.49	2	0.75	138	1.01
5	0.74	50	1.58	234	1.86	0.25	14	0.40	165	0.64
6	0.50	39	0.98	140	1.21	0.20	1	0.44	34	0.45
7	0.46	28	0.69	30	0.89	0.16	2	0.38	8	0.36
8	0.24	7	0.60	96	0.65	0.08	4	0.19	100	0.29
9	0.22	6	0.45	12	0.47	0.06	6	0.15	72	0.22
10	0.18	13	0.31	11	0.37	0.07	6	0.14	21	0.17
11	0.14	2	0.31	2	0.30	0.06	1	0.10	27	0.14
12	0.12	0	0.18	1	0.21	0.04	2	0.13	9	0.12

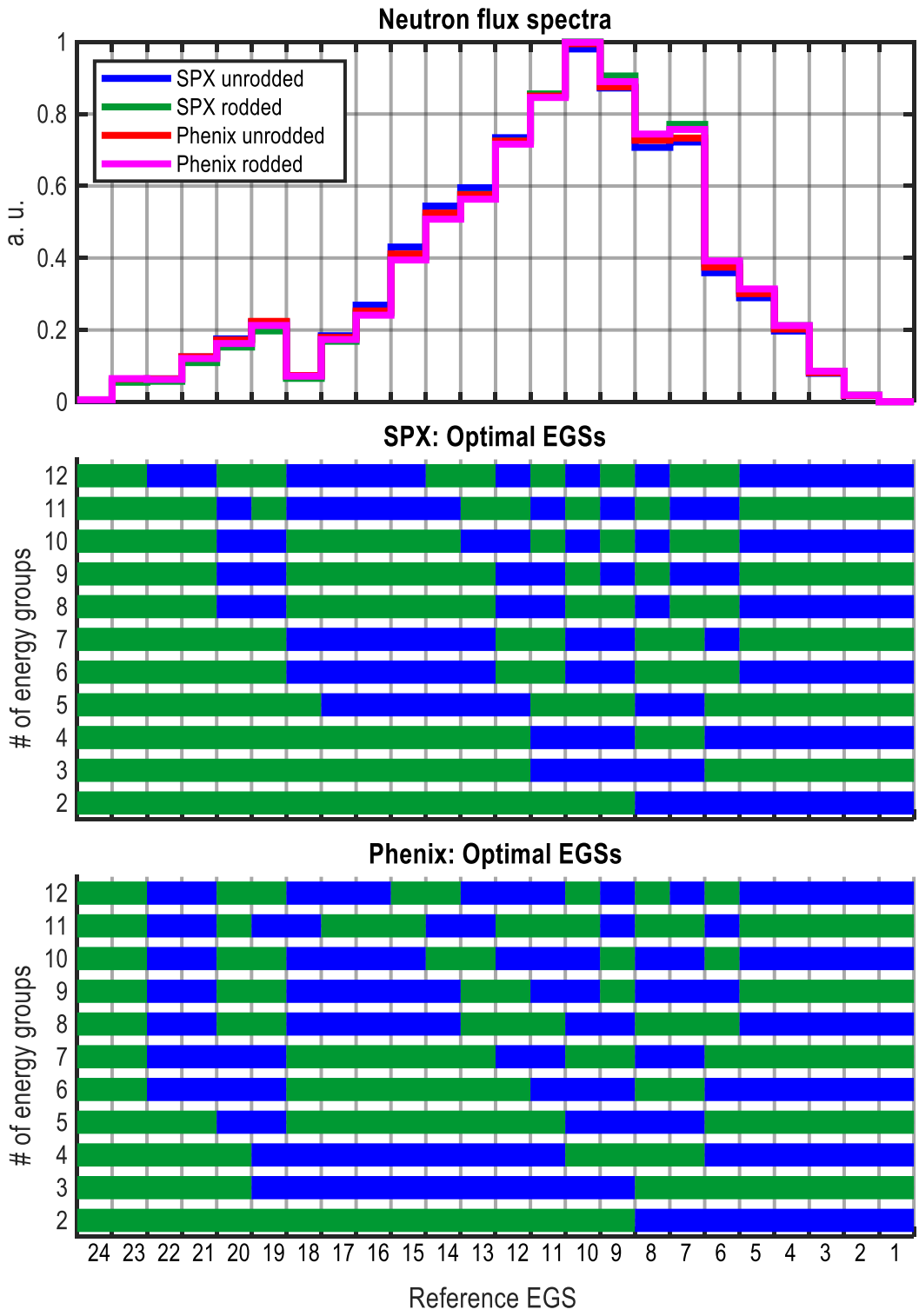

Fig. 48. Core average neutron flux spectra and optimal EGSs as subsets of the reference 24-group structure

The results of the optimization, presented in Fig. 48, and Table 15, lead to the following observations:

- As shown in the upper panel of Fig. 48, the neutron flux spectra in the unrodded and rodded SPX and Phénix cores are quite similar. However, the derived optimal EGS of SPX and Phénix, shown in the middle and lower panels of Fig. 48, noticeably differ. This observation

suggests that the optimal EGSs are design depended. Nevertheless, for both designs, there is a clear tendency to resolve more populated energy regions and to collapse less populated parts.

- Table 15 demonstrates that for both core designs, the results are improving with increasing number of EG.
- The results with 2 to 3 EG are noticeably diverging from the reference, particularly in the fully rodded cases.
- The solutions with 4 to 8 EG are closer to the references. In the SPX case, ΔP_{RMS} contributions are in general below 2% and specifically below 1% for 6- and 8-groups solutions. Values of $\Delta\rho$ are mostly below 150 pcm, except for the 5-groups structure where the fully rodded $\Delta\rho$ is equal to 234 pcm. As compared to the 4-group case, such an evident discrepancy in $\Delta\rho$ is compensated by a halved value of the unrodded ΔP_{RMS}. In the Phénix case, the $\Delta\rho$ and ΔP_{RMS} values do not exceed 165 pcm and 0.5%, respectively.
- Excellent agreements are observed for the solutions with 9 to 12 EG. For the SPX core, the $\Delta\rho$ values do not exceed 13 pcm and ΔP_{RMS} components are below 0.5%. For the Phénix core, the $\Delta\rho$ values are limited by 72 pcm and ΔP_{RMS} components are below 0.2%.

The EGSs found in the previous subsection were already successfully applied in (Di Nora, et al., 2021b) to evaluate DYN3D solutions of the static SPX benchmark and transient Phénix natural circulation test. The condensed EGSs are applied in Section 4.3 to perform new calculations of the reference solutions obtained in Chapter 3. Corresponding calculation speedup factors and errors introduced by applying the condensed optimized EGSs are later on estimated.

4.2 MDT and FOD approaches in comparison

For coupled calculations involving several multi-physics aspects, one has to account for neutronic feedback arising from XS dependencies of the most relevant state variables. In SFRs, state variables giving rise to corresponding neutronic feedback effects are, e.g., fuel and sodium temperatures, sodium density, axial fuel expansion, and radial diagrid expansions, respectively, T_f, T_c, ρ_c, ε_a and ε_r. As described in Section 2.1, the XS dependencies on state variables must be considered through adequate parametrization models as shown, e.g., in Eq. 2.4.

Currently, the XS dependencies presented in Eq. 2.4 are accounted for by DYN3D through MDT XS libraries (Rohde, et al., 2016). As already mentioned in Section 2.1, at this stage of the code

development, the effect of the coolant density is implicitly considered together with the coolant temperature effect.. It should be mentioned that Eq. 2.4. holds for multiplying core regions whereas for non-multiplying regions where the fuel is not present the expression simplifies in Eq. 4.9.

$$\Sigma_x^g|_i = \Sigma_x^g(T_c, \varepsilon_r)|_i \qquad \text{Eq. 4.9}$$

Beyond the MDT XS parametrization, another possible approach widely applied to account for XS dependencies is the FOD approach. Both the XS parametrization approaches MDT and FOD are described in detail in Section 4.2.1 together with their main advantages and disadvantages. Details on the XS generation processes for the Phénix and SPX analyses with emphasis on the FOD approach are provided in Section 4.2.2.

4.2.1 Description, advantages, and disadvantages

With the MDT approach, several values of the state variables, or "points", are selected within user-defined ranges, then, nodal XSs are generated for all combinations of points and stored in tables. The greater is the number of points selected for each state variable, the higher is the accuracy of the approach. Nodal XS values are actualized according to instantaneous nodal distributions of state variables through multi-dimensional interpolations of known table data. Multi-dimensional interpolations allow one to account for the mutual effects of the state variables on each other.

For each of the state variables considered, e.g., T_f, T_c, ε_a and ε_r, the user-defined number of points are addressed as, respectively, N_{T_f}, N_{T_c}, N_{ε_a}, and N_{ε_r}. The number of total states, N_{states}, to be evaluated for each core region to build the XS libraries is given by the formula Eq. 4.10.

$$N_{states} = \begin{cases} N_{T_f} \cdot N_{T_c} \cdot N_{\varepsilon_a} \cdot N_{\varepsilon_r}, & \text{for multiplying core regions} \\ N_{T_c} \cdot N_{\varepsilon_r}, & \text{for non-multiplying core regions} \end{cases} \qquad \text{Eq. 4.10}$$

This means that even with the coarsest multidimensional table, i.e., considering only the extremes of each XS parameter, the minimum output of Eq. 4.10 is 2^4 for multiplying regions and 2^2 for non-multiplying ones. The corresponding N_{states} configuration of each core region have to be previously evaluated and stored in XS libraries.

The MDT approach represents quite a realistic method to be applied for the modeling of XS dependencies in coupled calculations. However, the method presents disadvantages:

- It strongly affects the computational times of the analyses, especially transient ones, due to the multi-dimensional interpolations performed on-the-run.
- It requires a considerable number of calculations in the process of XS generation due to the large number of states to be considered for each core region.

In this regard, the XS parametrization via the FOD approach represents a valuable option to speed up both the simulation running times and XS generation processes.

With the FOD parametrization approach, the XS dependencies on state variables are accounted for by first-order XS derivatives. In general, the approach provides for the generation of nodal XSs in correspondence with specific "reference" conditions of state variables and evaluations of first-order XS derivatives with respect to such variables. The derivatives are evaluated between the reference state and extreme user-defined values of state variables. Nodal XSs are actualized according to instantaneous nodal distributions of state variables by summing up linear combinations of derivatives and related perturbations of variables within the node. Effects of the state variables are assumed to be linearly independent. The parametrization of Eq. 2.4 via FOD approach is expressed by Eq. 4.11.

$$\Sigma_x^g|_i = \Sigma_x^g\left(T_f, T_c, \varepsilon_a, \varepsilon_r\right)|_i = \{\Sigma_{x0}^g + \left[\frac{\Delta\Sigma_x^g}{\Delta lnT_f}\right]_{T_{f_1},T_{f_0}} \left(lnT_f - lnT_{f_0}\right) + \\ + \left[\frac{\Delta\Sigma_x^g}{\Delta T_c}\right]_{T_{c_1},T_{c_0}} \left(T_c - T_{c_0}\right) + \left[\frac{\Delta\Sigma_x^g}{\Delta\varepsilon_a}\right]_{\varepsilon_{a_1},\varepsilon_{a_0}} \left(\varepsilon_a - \varepsilon_{a_0}\right) + \left[\frac{\Delta\Sigma_x^g}{\Delta\varepsilon_r}\right]_{\varepsilon_{r_1},\varepsilon_{r_0}} \left(\varepsilon_r - \varepsilon_{r_0}\right)\}|_i \qquad \text{Eq. 4.11}$$

In Eq. 4.11, the component, $\Sigma_{x0}^g|_i$, is the value of the XSs at a reference user-defined state. That is, the XS value calculated in correspondence with reference states of parameters, or lower bounds, T_{f_0}, T_{c_0}, ε_{a_0}, and ε_{r_0} as presented in Eq. 4.12.

$$\Sigma_{x0}^g|_i = \Sigma_x^g\left(T_{f_0}, T_{c_0}, \varepsilon_{a_0}, \varepsilon_{r_0}\right)|_i \qquad \text{Eq. 4.12}$$

The components $\left[\frac{\Delta\Sigma_x^g}{\Delta lnT_f}\right]_{T_{f_1},T_{f_0}}$, $\left[\frac{\Delta\Sigma_x^g}{\Delta T_c}\right]_{T_{c_1},T_{c_0}}$, $\left[\frac{\Delta\Sigma_x^g}{\Delta\varepsilon_a}\right]_{\varepsilon_{a_1},\varepsilon_{a_0}}$, and $\left[\frac{\Delta\Sigma_x^g}{\Delta\varepsilon_r}\right]_{\varepsilon_{r_1},\varepsilon_{r_0}}$ are evaluated as shown in Eq. 4.13 to Eq. 4.16.

$$\left[\frac{\Delta\Sigma_x^g}{\Delta lnT_f}\right]_{T_{f_1},T_{f_0}} |_i = \frac{\Sigma_x^g\left(T_{f_1},T_{c_0},\varepsilon_{a_0},\varepsilon_{r_0}\right) - \Sigma_x^g\left(T_{f_0},T_{c_0},\varepsilon_{a_0},\varepsilon_{r_0}\right)}{lnT_{f_1} - lnT_{f_0}}|_i \qquad \text{Eq. 4.13}$$

$$\left[\frac{\Delta\Sigma_x^g}{\Delta T_c}\right]_{T_{c_1},T_{c_0}} |_i = \frac{\Sigma_x^g\left(T_{f_0},T_{c_1},\varepsilon_{a_0},\varepsilon_{r_0}\right) - \Sigma_x^g\left(T_{f_0},T_{c_0},\varepsilon_{a_0},\varepsilon_{r_0}\right)}{T_{c_1} - T_{c_0}}|_i \qquad \text{Eq. 4.14}$$

$$\left[\frac{\Delta\Sigma_x^g}{\Delta\varepsilon_a}\right]_{\varepsilon_{a_1},\varepsilon_{a_0}} |_i = \frac{\Sigma_x^g\left(T_{f_0},T_{c_0},\varepsilon_{a_1},\varepsilon_{r_0}\right) - \Sigma_x^g\left(T_{f_0},T_{c_0},\varepsilon_{a_0},\varepsilon_{r_0}\right)}{\varepsilon_{a_1} - \varepsilon_{a_0}}|_i \qquad \text{Eq. 4.15}$$

$$\left[\frac{\Delta\Sigma_x^g}{\Delta\varepsilon_r}\right]_{\varepsilon_{r_1},\varepsilon_{r_0}} |_i = \frac{\Sigma_x^g\left(T_{f_0},T_{c_0},\varepsilon_{a_0},\varepsilon_{r_1}\right) - \Sigma_x^g\left(T_{f_0},T_{c_0},\varepsilon_{a_0},\varepsilon_{r_0}\right)}{\varepsilon_{r_1} - \varepsilon_{r_0}}|_i \qquad \text{Eq. 4.16}$$

In equations from Eq. 4.11 to Eq. 4.16, the derivatives of the state variables are considered within an operational range that covers from the lower to upper extreme values of state variables defined by the user. Lower and upper extreme values of the variables are marked, respectively, with subscripts 0 and 1. Eq. 4.11 holds for multiplying core regions only, for non-multiplying regions the parametrization does not account for fuel temperature and its axial TE.

Considering the FOD approach, the number of total states, N_{states}, to be evaluated to build the XS libraries of each core region is given by Eq. 4.17.

$$N_{states} = 1 + N_{Variables} \qquad \text{Eq. 4.17}$$

In other words, the approach needs one calculation for the XS reference state, with all variables considered at the reference state "0", and additional "$N_{Variables}$" calculations, i.e., one per variable considered. The latter calculations are obtained starting from the reference state by perturbing individually each variable from the reference to the upper bounding values chosen.

Considering the state variables in use by DYN3D for the XS parametrization of multiplying and non-multiplying regions, i.e., 4 and 2, the N_{states} to evaluate according to Eq. 4.17 are 5 and 3, respectively.

The parametrization of XSs via the FOD approach presents two main advantages:

- It is beneficial for the acceleration of neutronics calculations. In fact, the complex multidimensional interpolations foreseen by the MDT approach to actualize nodal XSs are replaced by multiplications and summations.

- It simplifies the process of the preparation of XS libraries through reduction of Serpent calculations needed to construct the XS libraries.

On the other hand, assuming that XSs depend on state variables considered independent from each other may introduce significant errors in the prediction capabilities of neutronics models. In fact, prediction errors of the model might arise in the case eventual effects of covariance exist among the variables of the parametrization, such as, e.g., the effects of sodium voiding on fuel Doppler (Ponomarev, et al., 2010).

To evaluate the quality of the neutronics model outlined above, the option of the parametrization of XSs via FOD approach was implemented in DYN3D in the frame of this thesis. The evaluation of potential errors that the FOD approach may introduce in the solutions is proposed in Section 4.3.

4.2.2 Parametrized XSs for SPX and Phénix analyses

Sets of XSs parametrized via MDT approach were generated to perform V&V activities in Chapter 3. The values of state variables considered for the generation of MDT libraries for Phénix and SPX were presented in Table 6 and Table 10. To optimize computational times while preserving the accuracy of solutions of Chapter 3, the option of parametrization via FOD approach is also applied and tested. The parametrization of XSs via FOD approach was implemented by setting specific lower and upper bounds values of state variables for Phénix and SPX as shown in Table 16.

Table 16. FOD parametrization: Lower and upper bounds values of state variables for Phénix and SPX

	Phénix				SPX			
State variables	T_f, K	T_c, K	$\varepsilon_{a,}$ -	$\varepsilon_{r,}$ -	T_f, K	T_c, K	$\varepsilon_{a,}$ -	$\varepsilon_{r,}$ -
Lower bound “0”	523	523	ε_a(523K)	ε_r(523K)	453	453	ε_a(453K)	ε_r(453K)
Upper bound “1”	1500	900	ε_a(1200K)	ε_r(900K)	1500	900	ε_a(1500K)	ε_r(900K)

It should be mentioned that in the XS generation process the Phénix and SPX cores were divided into respectively 17 and 15 representative regions of which respectively 7 and 4 were multiplying regions, see Table 17.

Table 17. Total number of regions for Phénix and SPX cores and total # of Serpent calculations

	Phénix	SPX
# of representative core regions	17	15
# of Multiplying/Non-multiplying regions	7/10	4/11
MDT approach: N_{states} Multiplying/Non-multiplying	32/4	48/6
FOD approach: N_{states} Multiplying/Non-multiplying	5/3	5/3
MDT approach: # of Serpent lattice calculations	264	258
FOD approach: # of Serpent lattice calculations	65	53

In the case of parametrization via MDT approach, the numbers of N_{states} used for multiplying and non-multiplying regions were for Phénix 32 and 4, and for SPX 48 and 6. In this case, the number of Serpent lattice calculations required to build the MDT libraries are as result 264 and 258. By parametrizing XSs via FOD approach, the number of N_{states} used for multiplying and non-multiplying regions is for both cores 5 and 3 and the number of Serpent lattice calculations required to represent the XS libraries are 65 and 53.

In reference to the analyses conducted on the Phénix and SPX, computational efforts required for the XS generation processes are significantly reduced respectively by factors 4 and 5 by applying the FOD approach. The set XS parametrized according to the FOD approach are applied in Section 4.3 to evaluate new solutions of the reference benchmarks presented in Chapter 3. Corresponding calculation speedup factors and errors introduced by applying the approach are estimated.

4.3 Assessment of performances

Both the methodology for the selection of optimal EGS described in Section 4.1, and the alternative FOD XS parametrization approach described in Section 4.2, are applied and assessed in this section. The assessment activities are performed against static benchmarks conducted on the Phénix and SPX reactors, namely, the Phénix CR withdrawal benchmark as proposed in (IAEA, 2014) and the SPX static benchmark as proposed in (Ponomarev, et al., 2021a). In addition, assessment activities are also performed against the Phénix and SPX transient benchmarks introduced in Chapter 3. Reference solutions considered for the purpose of comparison in the assessment are:

- For the static benchmarks, DYN3D standalone solutions obtained by applying the 24-group EGS shown in Table 13. These solutions are presented next in this section and, it should be stressed, they were adopted by previously existing scientific work not conducted in the framework of this thesis.

- For the transient benchmarks, the DYN3D/ATHLET solutions evaluated in Chapter 3 for the V&V of the new platform and, also in the case, obtained by applying the 24-group EGS and XSs parametrized via the MDT option.

The benefits of the condensation methodology are evaluated by applying the optimal EGS found in Section 4.1.3 to both static and transient benchmarks. In this regard, new calculations of the benchmarks are conducted with the optimal 4, 6, 8, and 12 EGSs. Whereas, the comparison of the MDT and FOD XS parametrization approaches is only conducted considering the Phénix and SPX transient benchmarks introduced in Chapter 3. The benchmark solutions were newly calculated and potential deviations from reference solutions introduced by the methods evaluated.

4.3.1 Assessment on Phénix benchmarks

This section is dedicated to the assessment of the optimal EGS identified in Section 4.1 and of the alternative FOD parametrization approach. The assessment activities in question were conducted by exploiting the Phénix CR withdrawal and NC tests. In this regard, this section presents a brief description of the CR withdrawal benchmark and the corresponding existing DYN3D solutions (Nikitin & Fridman, 2018b), which were considered in this section as reference solutions for the CR withdrawal benchmark. Actual assessment activities conducted on both the Phénix static CR withdrawal and transient NC benchmarks are eventually reported afterward.

4.3.1.1 Phénix static CR withdrawal benchmark and reference solutions

The CR withdrawal test was carried out on the Phénix reactor at the EOL in 2009 during the decommissioning phase. The test was conducted to investigate the perturbation of the radial power distribution caused by axial non-symmetric CR positioning under several core configurations. A set of four core static configurations were considered in total for the test. For each configuration, experimental subassembly-wise power distributions were collected through the measurements of outlet sodium temperatures. The sodium temperatures were measured by thermocouples located at each subassembly outlet. Profiting of experimental data, the IAEA proposed a benchmark activity based on the test with the aim of improving the analytical capabilities of the participants in relation to the modeling of SFRs. More in detail, the scope of the benchmark was to improve simulation and design capabilities of the participants with respect to the prediction of SFRs' core temperature and power distributions. Specifications for the modeling of the test and experimental data were provided by the organization in (IAEA, 2014).

The core configuration assumed for the benchmark calculations corresponds to the Phénix EOL configuration already presented in Section 3.1.1. The set of investigated core states included a static

core state stabilized at 335 MW_{th} with the primary CRs positioned at identical insertion depths and other perturbed core configurations obtained by shifting CRs (see Fig. 12), as indicated in Table 18.

Table 18. Shift of CRs #1 and #4 from reference positions

Core config.	CR positions (mm)*					
	CR #1	CR #2	CR #3	CR #4	CR #5	CR #6
Ref. state	558.3	557.4	558.0	557.4	557.4	557.6
Step1	608.5	608.6	606.6	340.8	608.5	607.8
Step2	848.4	567.7	571.0	340.6	566.3	573.5
Step3	848.4	523.6	523.4	523.4	523.5	523.5

*With respect to the origin of Z-axis, i.e., 5mm below the fissile core

In 2018, the Phénix CR withdrawal benchmark was calculated by DYN3D to validate the fuel axial TE model implemented within the code in (Nikitin & Fridman, 2018a; 2018b). The calculations of the benchmark cases were performed with in 24-group XSs parametrized by using the MDT approach. The XSs correspond to the XSs employed for V&V purposes in Section 3.1. More details on the XS generation procedure can be found in Appendix C.1.

The existing 24-group DYN3D solutions obtained in (Nikitin & Fridman, 2018b) are used as reference solutions for optimization purposes in the next section.

4.3.1.2 Optimized solutions of Phénix static CR withdrawal benchmark

The effectiveness of the methodology for the selection of optimal condensed EGS described in Section 4.1.1 was tested on the static Phénix CR withdrawal benchmark. The core configurations proposed in the benchmark were calculated by using the optimal condensed 4-, 6-, 8-, and 12-group EGS found for the Phénix reactor in Section 4.1.3. Fig. 49 presents the deviations in radial power distribution and core reactivity with respect to the reference 24-group solutions, see (Nikitin & Fridman, 2018b), respectively, ΔP_{RMS} and $\Delta\rho$.

As Fig. 49 shows, the results obtained with the condensed EGS are globally in good agreement with the references. The distribution of ΔP_{RMS} and $\Delta\rho$ errors are typically flat, i.e., the introduction of a condensed EGS adds a constant flat bias to the solutions. Maximum errors of 0.5% are found for ΔP_{RMS} in 4-group solutions and are observed to be even below 0.21% for finer optimal EGS. The values of $\Delta\rho$ are in any case limited to 55 pcm for all the solutions. Very good agreements are found for 6- and 12-group solutions for which a $\Delta\rho$ below 22 pcm are estimated. As one might notice in Fig. 49, $\Delta\rho$ values obtained with the 8-group EGS case are worse than those obtained with the 6-group EGS. However, in terms of the cost function, the 8-group solutions are improved in comparison

with 6-group ones, since the goal of the analysis is the optimization of the cost function as a whole rather than its single components.

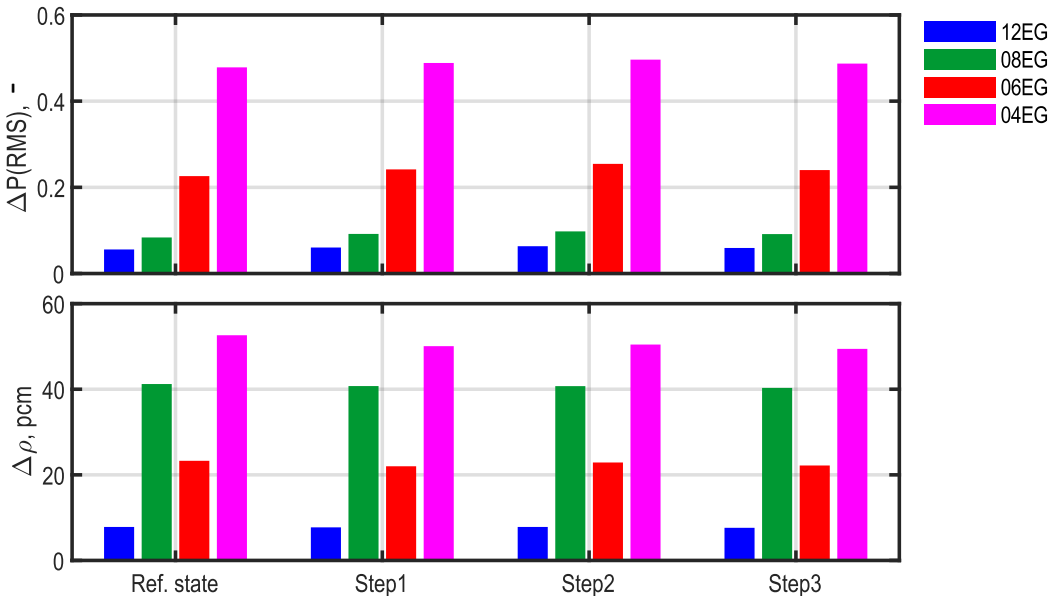

Fig. 49. Phénix CR withdrawal test solutions: Error components ΔP_{RMS} and $\Delta\rho$

4.3.1.3 Optimized solutions of Phénix transient NC benchmark

The solution of transient analyses performed on the initial stage of the Phénix NC test was presented in Section 3.1.5. The calculations of the corresponding test were obtained by applying the 24-group MDT XS libraries and are assumed as the reference calculations in this section. To optimize computational times while preserving the accuracy of the solution, new simulations of the test are performed with including the options to accelerate the calculations. In particular, the new calculations are executed by employing the optimal EGSs with 4, 6, 8, and 12 EGs and parametrizing the related XS libraries via both MDT and FOD approaches. The 24-group FOD solutions are evaluated as well. The new solutions are benchmarked against the reference calculations in terms of power, sodium heat-up, total reactivity, Doppler reactivity, maximum clad, and fuel temperatures. For each of the quantities mentioned above, deviations on the transient trends are compared through the evaluation of mean errors and related SDs.

The simulations performed on the initial stage of the NC test scenario revealed generally a good agreement of the solutions with respect to the reference. In Fig. 50, most of the solutions derived by using the MDT XS libraries show a converging behavior to the reference. Namely, as the number of EGs used in calculations increases, mean errors become ever closer to zero and likewise the corresponding SDs. Analogous behaviors are observed also on the errors of solutions obtained with FOD XS libraries but with additional marginal biases. The usage of the FOD approach leads, in general, to a slight overestimation of all the quantities compared.

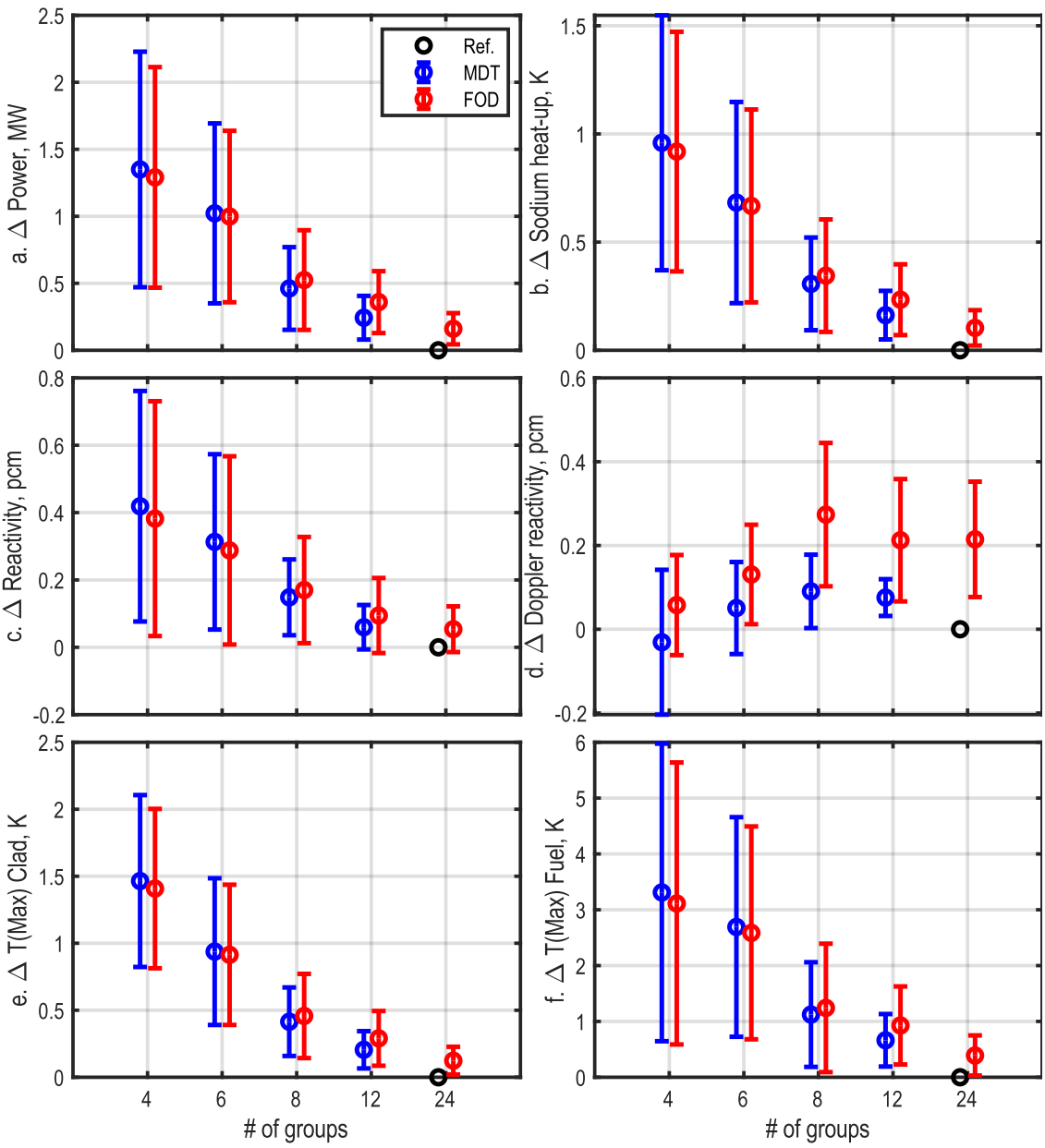

Fig. 50. Assessment of optimal condensed EGS and XS parametrization approaches on the NC test

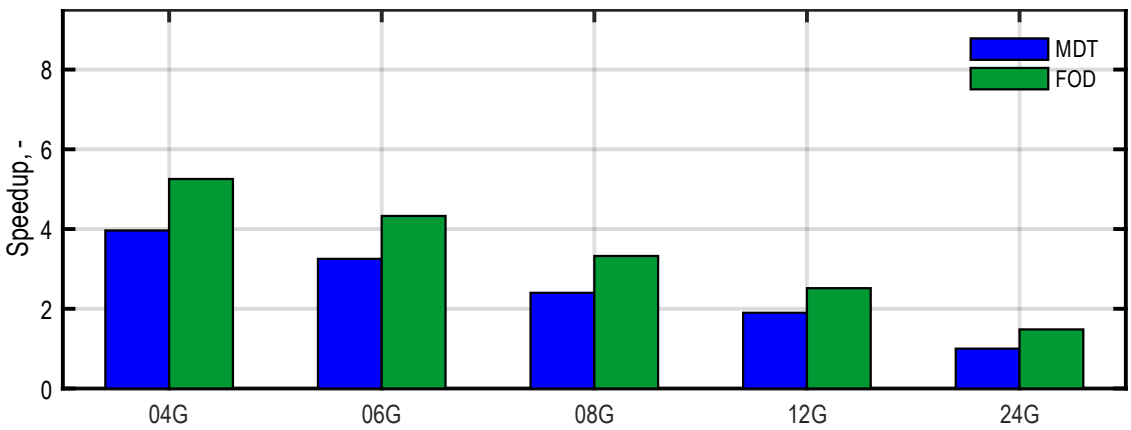

Fig. 51. Speedup of calculations for the NC test

Fig. 50a shows that the maximum mean error observed on the power trend is below 1.5 MW and is accompanied by a SD of ± 0.8 MW. Such error is estimated for the 4-group MDT solution. Errors found on the sodium heat-up trends closely follow the behavior of power errors. The mean error values are generally below 1 K with a SD of 0.6 K, see Fig. 50b. The worst values of mean errors found on the total reactivity and Doppler reactivity components are, respectively 0.4 and 0.3 pcm both accompanied with SDs of 0.2 pcm, see Fig. 50c and d. Fig. 50e and f present the largest mean errors on the trends of maximum clad and fuel temperatures, which are respectively 1.5 and 3.5 K with SDs of 0.6 and 3 K. The errors are found in the correspondence of 4-group solutions and significantly reduce for finer EGSs.

Fig. 51 shows the speedup in calculations obtained by applying the optimal condensed EGSs with both the parametrization approaches. Average speedup factors of values 2, 3, 4, and 5 are obtained by using respectively the 12, 8, 6, and 4 EGSs. With the application of FOD XS libraries, the calculations are accomplished on average 1.4 times faster with respect to calculations performed with MDT XS libraries.

4.3.2 Assessment on SPX benchmarks

This section is dedicated to the assessment of the optimal EGS identified in Section 4.1.3 and of the alternative FOD parametrization approach. The assessment activities in question were conducted by exploiting the SPX static neutronics benchmark, as proposed in (Ponomarev, et al., 2021a), and the SPX transient start-up benchmark. In this regard, this section presents a brief description of the SPX static neutronics benchmark and the corresponding existing DYN3D solutions presented also in (Ponomarev, et al., 2021a). The existing DYN3D solutions were considered in this section as reference solutions for the static benchmark. Actual assessment activities related to XSs' optimization and conducted on both the benchmarks mentioned above are eventually reported afterward.

4.3.2.1 SPX static benchmark and reference solutions

The SPX static neutronics benchmark, devoted to static standalone neutronics calculations, took the advantage of the measurements performed on the occasion of the reactor commissioning phase. The measurements were conducted after the loading of core subassemblies to measure core static characteristics, e.g., core criticality, neutron fluxes, power distributions, control rod worth, etc. The related experimental data sources were taken from (Flamenbaum, et al., 1990), and (Vanier, et al., 1990). In addition to the latter data sources, assumptions on the basis of (IAEA, 1996) and (Hunter, 1998) were made to provide benchmark specifications in (Ponomarev, et al., 2018).

The core configuration assumed for the benchmark calculations corresponds to the SPX start-up configuration already presented in Section 3.2.1. By exploiting the specifications in (Ponomarev, et al., 2018), the benchmark participants evaluated 13 core states of the SPX core start-up configuration differing by temperatures of the core materials/components, TE states, and CR insertion depths as shown in Table 19. The benchmark provided for the evaluation of core configurations by the neutronics computational tools of participants and the benchmarking of obtained solutions against Serpent MC solutions. The benchmark envisaged, in addition, the evaluation of reactivity effects, such as Doppler constants at different temperatures, isothermal reactivities, TE reactivities, control rods worth at different insertion depths. The formulations of corresponding derived reactivity effects, representative of core characteristics, are shown in Table 20.

Table 19. Static SPX neutronic benchmark: Summary of core states

Case #	Temperature for neutronics/geometry, K			CR insertion
	Fuel fissile	Fuel fertile	Other	Depths, cm
1	453/453	453/453	453/453	0
2	673/673	673/673	673/673	0
3	1500/1500	900/900	673/673	0
4	300/300	300/300	300/300	0
5	300/453	300/453	300/453	0
6	300/673	300/673	300/673	0
7	600/673	600/673	600/673	0
8	900/673	900/673	900/673	0
9	600/673	600/673	300/673	0
10	300/673	300/673	300/673	40
11	600/673	600/673	600/673	40
12	673/673	673/673	673/673	40
13	453/453	453/453	453/453	100

Table 20. Static SPX neutronic benchmark: Derived reactivity effects

Designation	Description	Formulation
Dopp1	Fuel and steel Doppler reactivity (ΔT=300 K)	$\rho_{case7} - \rho_{case6}$
Dopp2	Fuel and steel Doppler reactivity (ΔT=600 K)	$\rho_{case8} - \rho_{case6}$
Dopp3	Fuel Doppler reactivity (ΔT=300 K)	$\rho_{case9} - \rho_{case6}$
Dopp4	Fuel Doppler reactivity 40 cm CR insertion (ΔT=300 K)	$\rho_{case11} - \rho_{case10}$
IsoTh	Isothermal temperature reactivity (ΔT=220 K)	$\rho_{case2} - \rho_{case1}$
ThExp	Thermal expansion reactivity (ΔT=220 K)	$\rho_{case6} - \rho_{case5}$
H-to-Z	Hot-to-zero power reactivity defect	$\rho_{case1} - \rho_{case3}$
CRW-40	CR worth: 40 cm insertion	$\rho_{case10} - \rho_{case6}$
CRW-100	CR worth: 100 cm insertion	$\rho_{case13} - \rho_{case1}$

As a benchmark participant, the HZDR contributed to the benchmark calculations with the in-house DYN3D code. The corresponding results were published in (Ponomarev, et al., 2021a). The 24-group DYN3D solutions of the static benchmark cases were obtained with non-parametrized XSs, i.e., for each benchmark case, XSs were generated according to specific fixed values of state variables. The XSs used for the calculations were produced, also in this case, by applying the procedure described in Appendix C.1. The existing 24-group DYN3D solutions obtained in (Ponomarev, et al., 2021a) are used as reference solutions for optimization purposes in the next section.

4.3.2.2 Optimized solutions of SPX static benchmark

To test the effectiveness of the optimal EGSs identified in Section 4.1.3 over a wider sample of core states characterized by different operating conditions, the 13 cases of the static SPX static benchmark, described in the previous section, were recalculated by using the optimal energy grid. Fig. 52 presents the deviations in radial power distribution and core reactivity with respect to the reference 24-group solutions, respectively, ΔP_{RMS} and $\Delta\rho$.

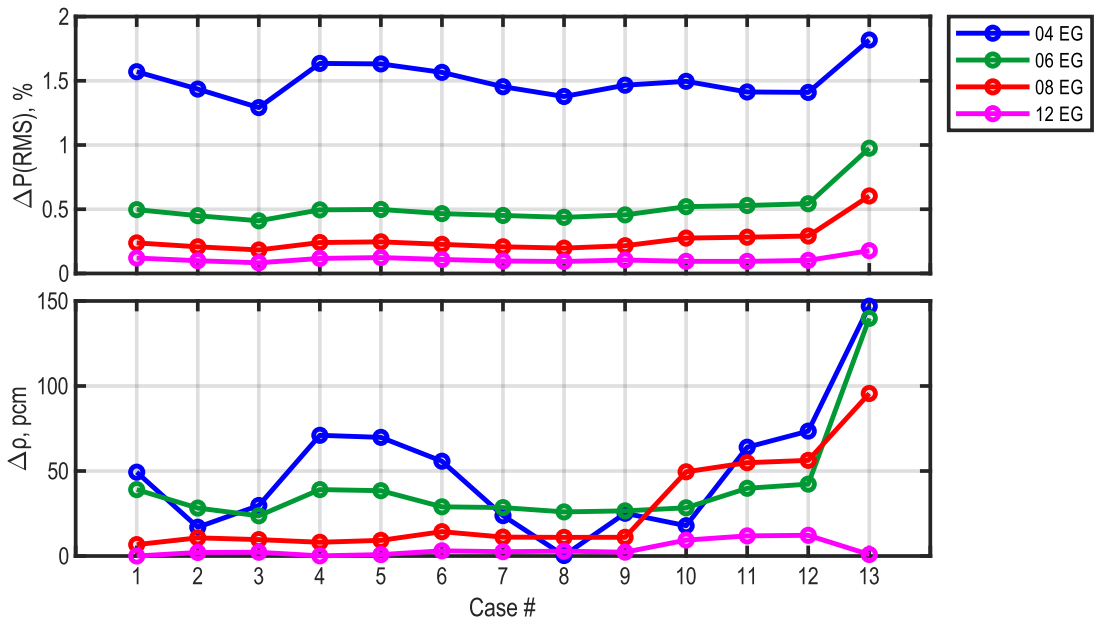

Fig. 52. SPX static benchmark solutions: Error components ΔP_{RMS} and $\Delta\rho$

As Fig. 52 shows, the majority of the results obtained with the condensed EGS are in good agreement with the references. For all EGSs with 6- to 12-group, ΔP_{RMS} is typically flat with error peaks occurring in fully rodded cases only. Maximum errors on ΔP_{RMS} are below 1% for the 6-group solutions and below 0.5% for the 8-group ones. Considerable deviations, up to 2%, are observed on the 4-group solutions. In the solutions obtained with 6- to 12-group EGS, the deviations in core reactivity are roughly limited to 50 pcm with a few exceptions for structures with 6 and 8 EG. For the latter, peak $\Delta\rho$ values of about 150 and 100 pcm are observed for the fully rodded core state (case

number 13 of the benchmark). More diverging behaviors are observed for the Δρ values found with the 4-group EGS, which in any case do not exceed 150 pcm. In general, the magnitudes of Δρ and ΔP_{RMS} decrease with the increasing number of EG used. In Fig. 52, one might notice that some of the Δρ values of the rodded 8 EG cases are worse than those of the 6 EG cases. However, it should be emphasized that the ΔP_{RMS} values of the 8 EG solutions are all significantly improved in comparison with 6 EG ones. That is, from a global perspective, the quality of the former solutions with respect to the latter remains still improved.

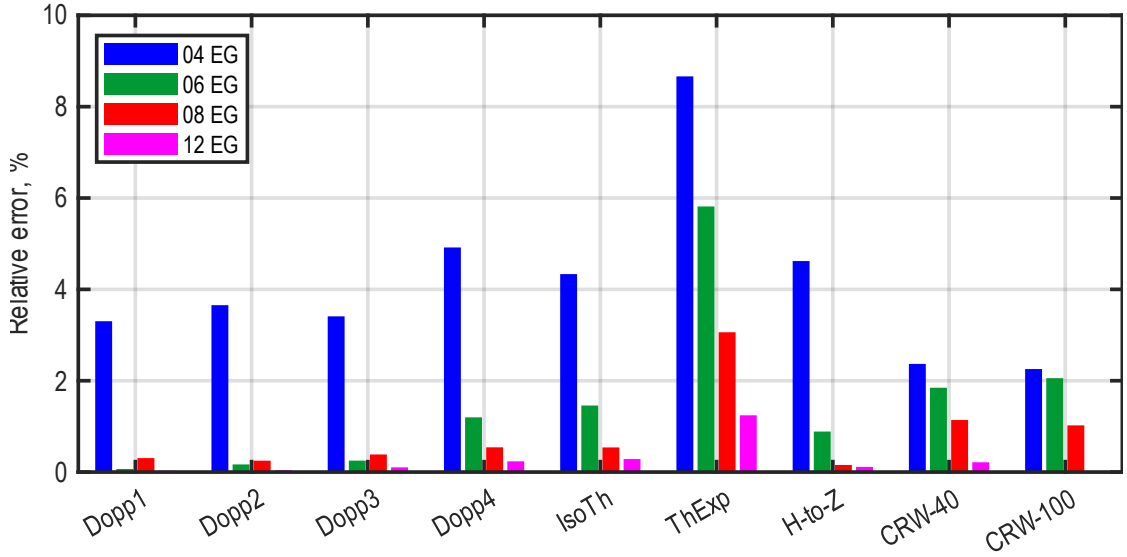

Fig. 53. SPX static benchmark solutions: Error calculations on reactivity coefficients

Fig. 53 shows the relative errors in reactivity effects with respect to the reference values. For 6- to 12-group solutions, the maximum errors are below 1.5% for Doppler (Dopp1-4), isothermal (IsoTh) and hot-to-zero power (H-to-Z) reactivity effects. Deviations in CR worth for 40 and 100 cm insertions do not exceed 2.1%. Greater errors can be noticed for 6 EG solutions on the thermal expansion reactivity effect (ThExp), with discrepancies of around 5.8%. It should be noted that the ThExp reactivity effect has the smallest absolute value, and 5.8% deviation corresponds to 9 pcm difference in core reactivity. Larger discrepancies from the references are registered for the 4-group solutions which mostly show errors above 3% and a peak relative error on the ThExp reactivity effect of 8.6%. Finally, the best agreements with the reactivity effect are observed for solutions with 8 and 12 EG characterized by errors below 1% with the only exception observed on the ThExp effect but, in any case, limited to 3%.

4.3.2.3 Optimized solutions of SPX transient benchmark

Calculations of the SPX start-up tests presented in Section 3.2.4 are performed again by employing the optimal condensed EGSs and exploiting both the MDT and FOD XS parametrization approaches.

The outcomes of the tests are presented in the following for each transient scenario considered. The quality of the results is assessed through comparison with the reference 24-group solutions obtained with MDT parametrized XSs. For each variable compared, errors from the reference trends are estimated at each time step and error mean values and standard deviations (SDs) are eventually evaluated. Error mean values and SDs are evaluated on the trends of total core power, sodium heat-up, total reactivity, Doppler reactivity component, and maximum clad and fuel temperatures. Calculations of the SPX transient benchmark are performed with optimal condensed 4, 6, 8, and 12 EGSs accounting for both the MDT and FOD XS parametrization approaches. The 24-group solutions with XS parameterized via the FOD approach are evaluated as well.

MOFC1 test at 692 MWth

Globally, Fig. 54 shows a converging behavior of the "MDT" solutions with respect to the reference solution. That is, as the number of groups considered in the calculations increases, mean errors on trends of MDT solutions and related SDs, represented by error bars in Fig. 54, tend to zero. Converging behaviors can be observed also for the FOD solutions. However, the introduction of the FOD approach makes FOD solutions slightly diverging from the reference and in general marginally overpredicted for most of the quantities shown in Fig. 54. As a result, even though the average error values of FOD solutions decrease, their SDs remain wider as compared to those of the MDT solutions.

It should be emphasized that for both approaches, MDT and FOD, the errors are acceptable in all of the cases except for 4-group solutions and specifically in the case of power. In fact, as shown in Fig. 54a, mean error values of 5 to 4 MW with SDs of respectively 0.3MW and 1.6MW, are observed for both MDT and FOD approaches. For the rest of the solutions, mean error values on the power are limited to 1.2 MW, in the case of the MDT approach, and to 2 MW in the case of the FOD approach. SDs are practically negligible for MDT solutions whereas they range on average to 0.6 MW for the FOD solutions. Similar consideration can be made for the sodium heat-up, Fig. 54b, for which mean error values are in any case found to be smaller than 0.5 K and with a SD of a maximum of 1.8 K in the worst case, i.e., for 4-group solutions. Errors on the total reactivity are in good agreement with the reference and converge for both the XS parametrization approaches, see Fig. 54c. The maximum value reached on mean errors and SDs is respectively of 0.05 and 0.08 pcm. Slightly more noticeable are the deviations of FOD solutions on the Doppler reactivity with the maximum mean value and SD of -0.5 and 0.2 pcm, see Fig. 54d. Discrepancies on the maximum clad and fuel temperatures are respectively below 2 and 4 K, for 4-group solutions and even below 0.5 and 2K for the other solutions regardless of the approach used for XS parametrization, see Fig. 54e and f.

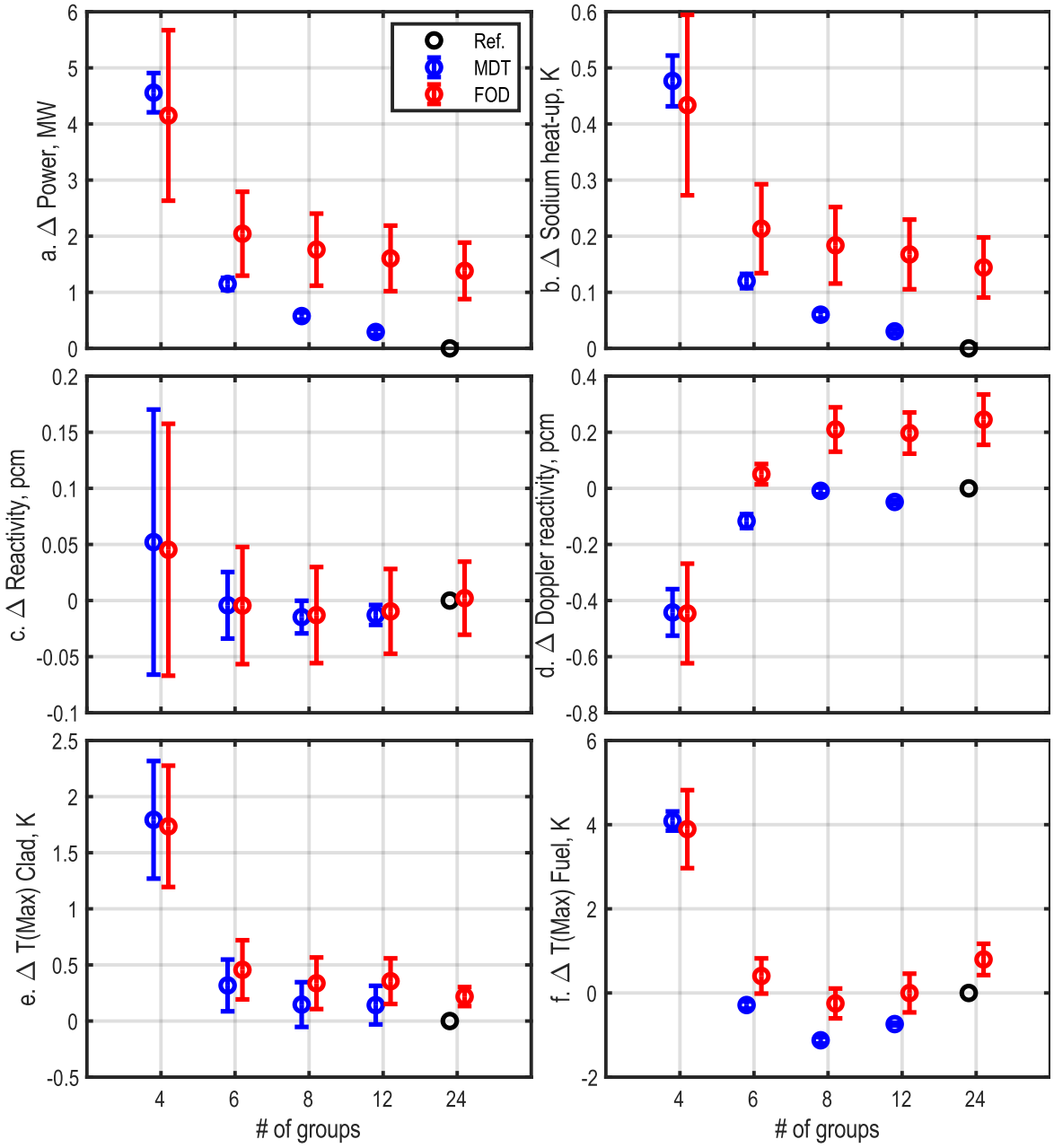

Fig. 54. Assessment of optimal condensed EGS and XS parametrization approaches on the MOFC1 test

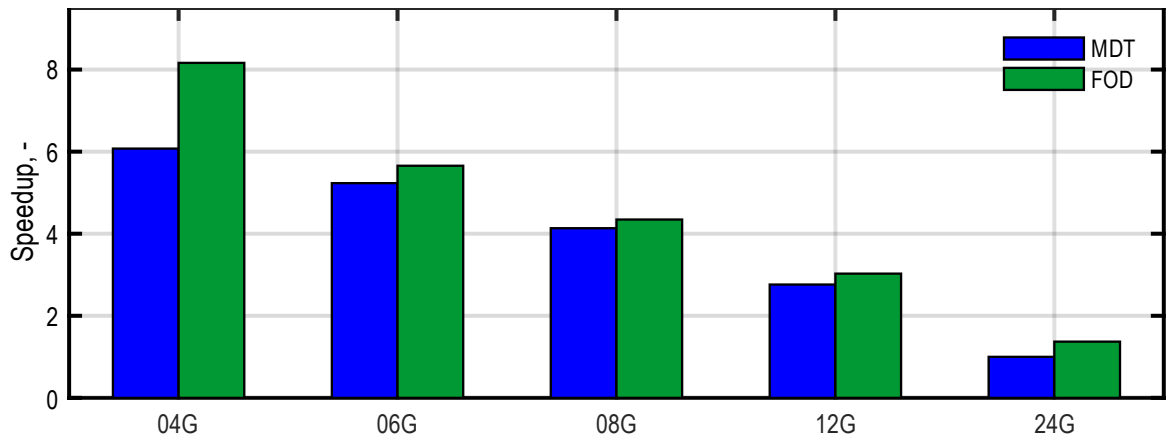

Fig. 55. Speedup of calculations for the MOFC1 test

Fig. 55 shows the speedup in calculations obtained by applying the optimal condensed EGSs with both the parametrization approaches. On average, significant speedup factors of 3, 4, and 5 are obtained by using the 12, 8, and 6 EGSs. Accelerations up to factors 6 and 8 are achieved by employing the 4-group EGS with respectively the MDT and FOD parametrized XSs. The calculations performed with the FOD approach are on average 1.2 times faster than their respective calculations executed by using the MDT approach.

MOFC2 test at 633 MWth

Tests executed on the MOFC2 transient lead overall to better solutions as compared to those obtained previously in the case of the MOFC1 scenario. As Fig. 56 shows the solutions obtained with the MDT parametrization approach present a converging behavior with respect to the reference. By increasing the number of groups employed in the calculations increases, the mean error values of MDT solutions converge to zero and similarly do the related SDs. The solutions obtained with the FOD XS parametrization approach closely replicate, at least in terms of mean values, the MDT solutions. For most of the quantities shown in Fig. 56, SDs of the FOD solutions do not significantly decrease with increasing the number of EG used in the calculations. This evidence is indicative of wider discrepancies between the FOD solutions, and the references as compared to those found by using the MDT parametrization approach. Nevertheless, it should be emphasized that the deviations observed are practically negligible over all the quantities presented.

In general, the largest mean error found on the power trend in Fig. 56a is limited to -0.7 MW with a SD of 0.7 MW. The errors on the prediction of sodium heat-up follow the trend of errors found for power, see Fig. 56b. Even in the worst case, i.e., for solutions obtained with 4-group EGS, both mean error and SDs are below 0.1 K for both MDT and FOD solutions. Discrepancies on the total reactivity from the reference are practically absent, that is, in any case below 0.01 pcm, see Fig. 56c. Slightly larger discrepancies are found for the Doppler reactivity shown in Fig. 56d with errors, however, below 0.15 pcm. Maximum clad and fuel temperatures are well predicted by the solutions. Mean errors are contained within ±2 K and are accompanied by limited SDs, see Fig. 56e and f.

Acceleration factors of calculations obtained by applying the optimal condensed EGSs with both the parametrization approaches are shown in Fig. 57. Similar considerations made for Fig. 55 hold also Fig. 57. That is, mean acceleration factors of 3, 4, and 6 are observed by performing calculations with the 12, 8, and 6 EGSs. Speedup factors of about 6 and 8 are obtained by using the 4-group EGS with XS parametrized via MDT and FOD approaches. Calculations performed with FOD parametrized XSs are on average 1.2 times faster than calculations performed with MDT parametrized XSs.

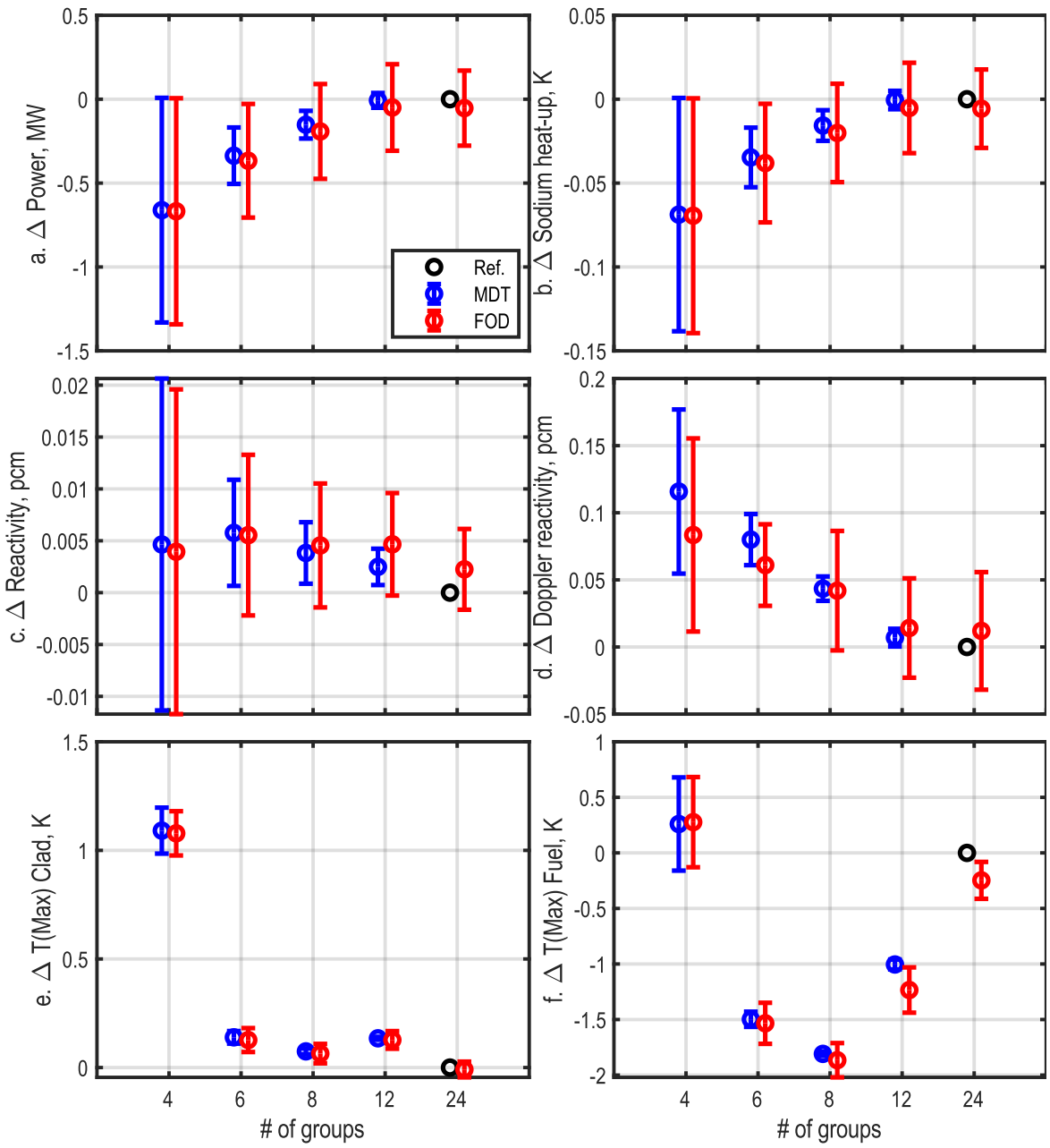

Fig. 56. Assessment of optimal condensed EGS and XS parametrization approaches on the MOFC2 test

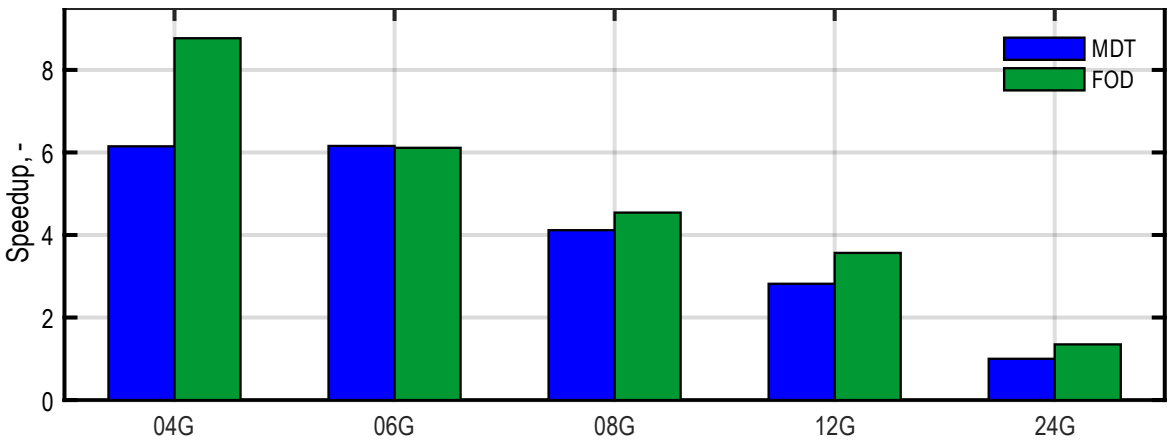

Fig. 57. Speedup of calculations for the MOFC2 test

MOFC3 test at 663 MWth

The simulations performed on the MOFC3 scenario revealed generally a good agreement of the new solutions against the reference. In Fig. 58, solutions obtained by applying the MDT parametrization approach show a converging trend to the reference. That is, as the number of EG used in simulations increases, the mean error values become ever closer to zero, and likewise do the related SDs. A similar converging behavior is observed also on the mean error values of the solutions obtained with the FOD parametrization approach. However, for errors on power, sodium heat-up, total reactivity, and Doppler reactivity components, the SDs of the FOD solutions do not significantly decrease with the increase of the number of EG used in the simulations, see Fig. 58. For the quantities mentioned above, the use of the alternative XS parametrization approach introduces a bias on the solutions. Such a bias is indicated by both slightly up-shifted mean error values and wider non-converging SDs. Better agreements of the FOD solutions were found for the maximum temperatures of clad and fuel.

As shown in Fig. 58a, the maximum mean error value observed on the power is negligible and close to -0.2 MW with a SD of ± 0.5 MW. These values are found for the 4-group solution obtained with the FOD parametrized XSs. Discrepancies on the prediction of sodium heat-up repeat similarly the trend of power errors. The average errors are practically null, i.e., even for the worst solution, the largest mean error and related SDs are below 0.02 and 0.06 K, see Fig. 58b. The total reactivity is predicted in excellent agreement with the reference for all the simulations. In Fig. 58c, both maximum mean error values and corresponding SDs are below 0.02 pcm. For the prediction of the Doppler reactivity component, the errors are somewhat larger, i.e., maximum mean error values and maximum SDs are respectively below 0.2 and 0.1 pcm, see Fig. 58d. Mean error values found on the maximum clad and fuel temperatures are, in the worst case, i.e., in 4-group solutions, 1.5 and 3 K. By increasing the number of EG such errors sensibly reduce assuming values below 0.3 and 1K, see Fig. 58e and f. Standards deviations are practically negligible in the case of the of clad temperature and slightly larger for the fuel temperature, especially in the case of FOD solutions. In Fig. 58e and f, the mean errors and SDs converge to zero for both the parametrization approaches used.

The acceleration factors shown in Fig. 59 present consistency with those ones previously found for the MOFC1 and MOFC2 tests. On average speedup factors of 3, 4, and 5 are found respectively for runs executed with 12, 8, and 6 EGSs. Wider acceleration margins, i.e., about 6 and 8, are found by performing the calculations in 4-group with XS parametrized via MDT and FOD approaches. The mean acceleration factor of runs performed with FOD XS libraries against corresponding runs executed with MDT libraries is about 1.2.

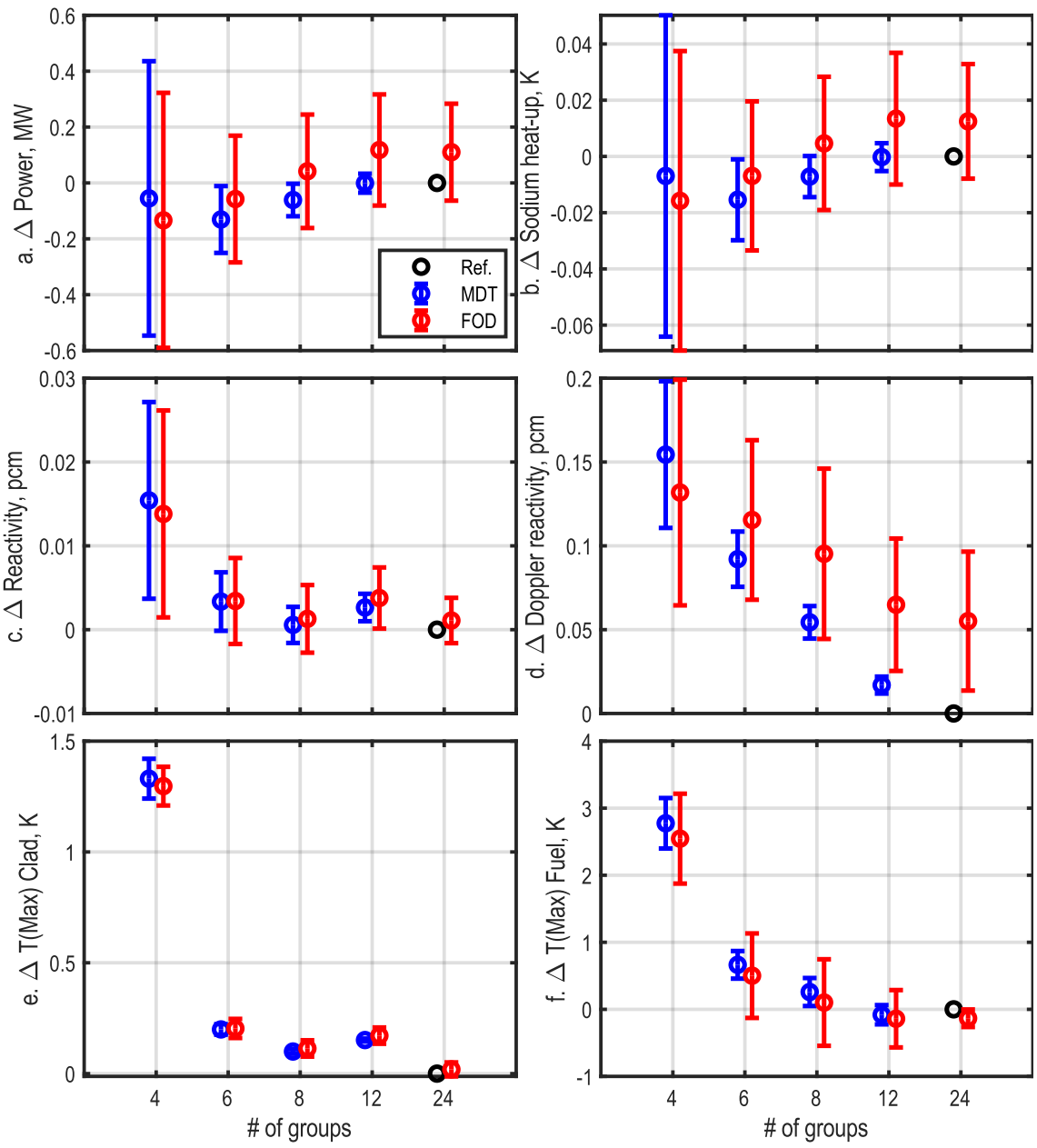

Fig. 58. Assessment of optimal condensed EGS and XS parametrization approaches on the MOFC3 test

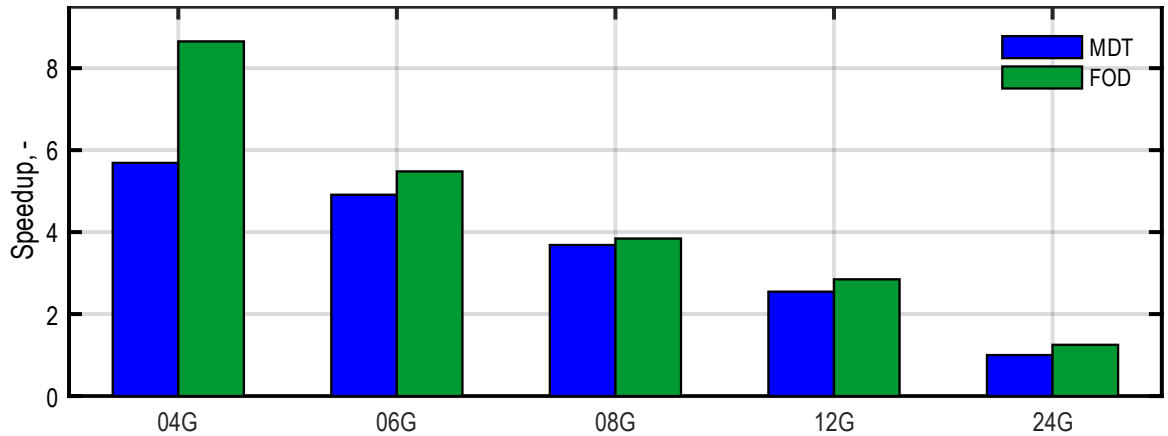

Fig. 59. Speedup of calculations for the MOFC3 test

PFS test at 1415 MWth

The tests carried out on the PFS transient show overall a close agreement of the newly calculated solutions against the reference, with a few exceptions for solutions obtained with the 4-group EGS. As the number of EG used in simulations increases, the solutions found by employing the MDT parametrization converge both in terms of mean error values and SDs, see Fig. 60. Similar trends are observed equally in the solutions computed with XS parametrized via FOD approach. In particular, the mean errors of FOD solutions replicate the errors of MDT solutions, especially in the cases of total reactivity, Doppler reactivity, and maximum clad and fuel temperatures. Small biases of solutions are recorded for the trends of power and sodium heat-up. Eventually, the SDs of FOD 24-group solutions converge for most of the trends shown in Fig. 60 other than power and sodium heat-up.

Fig. 60a shows that the power trends are on in general well predicted for all the recalculated solutions, in fact, estimated mean errors are generally below 1 MW. However, larger errors are observed in the cases of 4-group solutions, especially for the MDT solution which shows a SD of 3 MW. The errors found on the predicted sodium heat-up trends are marginal in all the cases, see Fig. 60b. Maximum values of error mean value and SD are indeed limited to 0.05 and 0.1 K. Fig. 60c shown that the total reactivity is predicted in excellent agreement with the reference for all the simulations except for the 4-group MDT solution. The Doppler reactivity components predicted by most of the solutions practically overlap the reference trend, see Fig. 60d. The 4-group MDT solution in Fig. 60d slightly distinguishes itself negatively among the others due to its larger SD which is anyway limited to 0.25 pcm. Mean errors found on maximum clad and fuel temperatures are, in the case of 4-group solutions, 1.5 and 4 K and fall over the threshold of 0.3 and 1K by increasing the number of EG, see Fig. 60e and f. Values of standards deviations tend to zero in the case of the clad temperature and eventually also for the fuel temperature.

Fig. 61 shows the speedup factors obtained by performing calculations of the PFS test. The calculations executed with FOD XS libraries result to be continuously accelerated by decreasing the number of EGs in use in calculations. The speedup factors increase until a maximum value of 5 is reached in correspondence of 4-group calculations. The speedup factors of calculations executed with MDT XS libraries reach the value of 4 in correspondence 8-group calculations and do not change significantly for calculation with lower EGs. The mean acceleration factor of runs performed with FOD XS libraries against corresponding runs executed with MDT libraries remains as for the other tests of about 1.3.

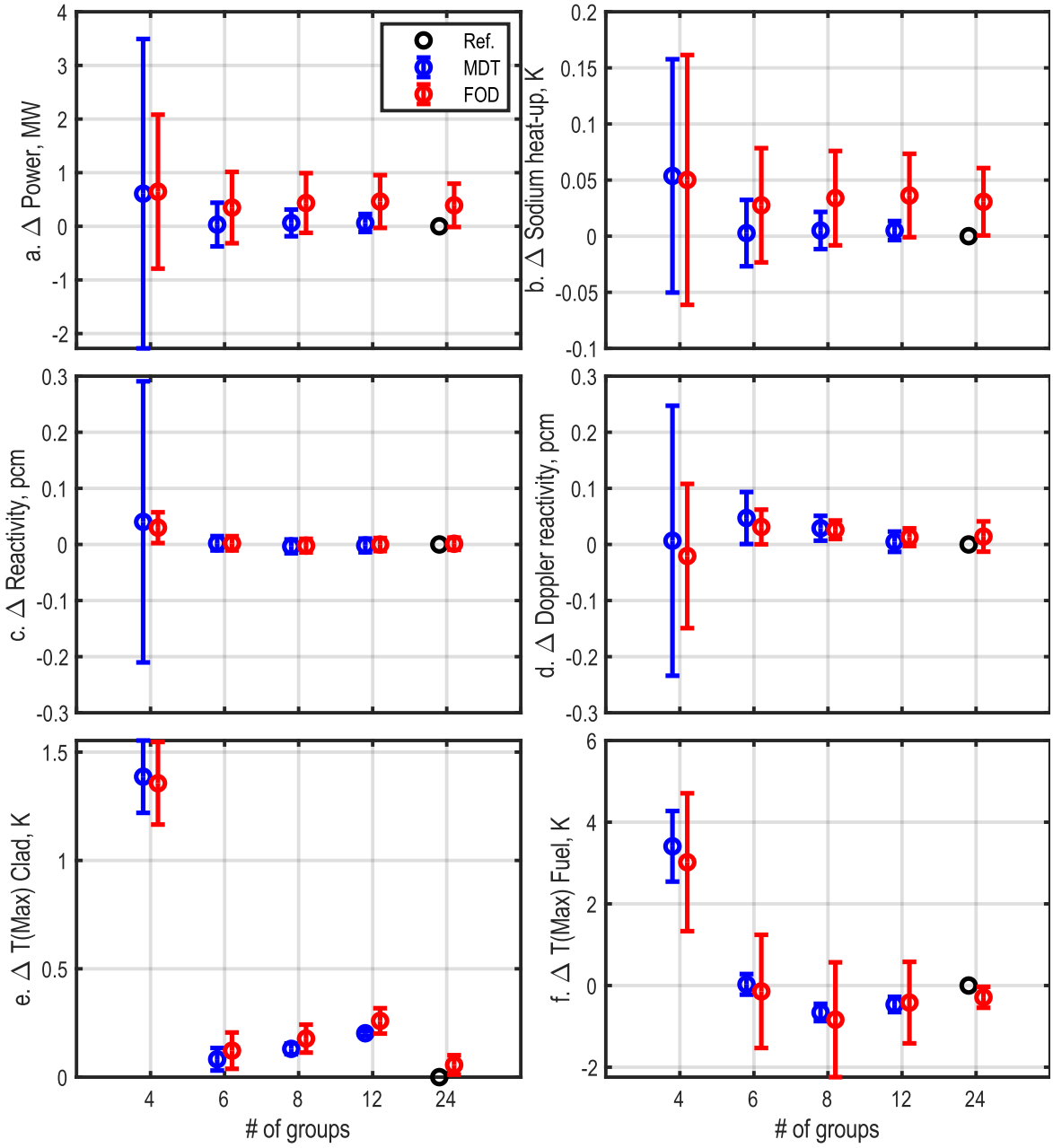

Fig. 60. Assessment of optimal condensed EGS and XS parametrization approaches on the PFS test

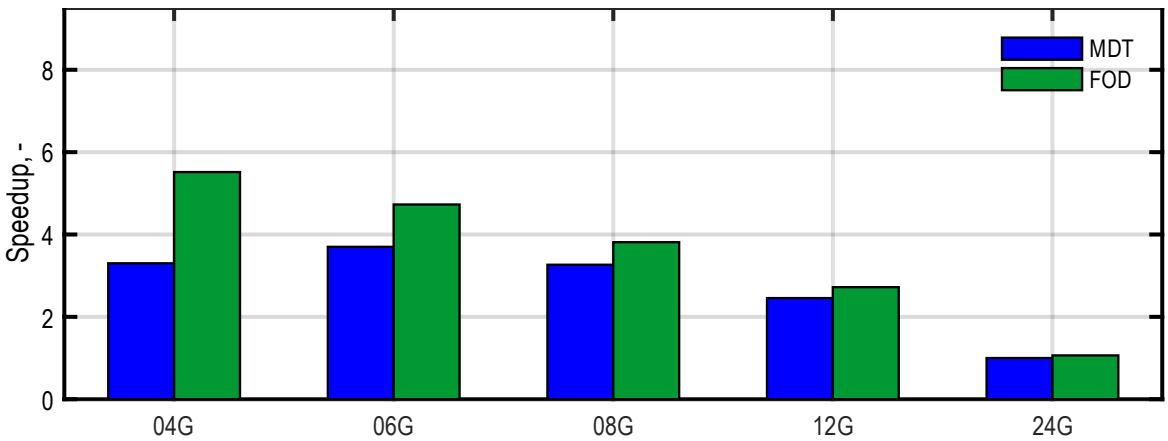

Fig. 61. Speedup of calculations for the PFS test

RS test at 1542 MWth

Apart from 4-group calculations, the simulations executed on the RS scenario lead to acceptable agreements of new solutions against the reference. As the number of EG increases, the quality of the MDT solutions improves in terms of mean errors and SDs, see Fig. 62. Even though with some bias, similar converging behavior is observed also for FOD solutions. However, for the latter, prominent discrepancies are found on trends of power and sodium heat-up trends. Other minor biases are noticed on the trends of Doppler reactivity and on maximum clad and fuel temperatures. The best agreement of FOD solutions against the reference is obtained for the total reactivity of which mean errors overlap the ones obtained by the MDT solutions. As the number of EGs increases, SDs of the FOD solutions become narrower for the total reactivity and maximum clad temperature. Similarly do the SDs of power, and sodium heat-up which, however, preserve larger error spreads as compared to the error bands of the MDT solutions. Fluctuating SDs are found on trends of Doppler reactivity and maximum fuel temperature. The application of FOD XS libraries leads to a global overestimation of solutions. Fig. 62a shows significant mean errors on power for 4-group solutions, i.e., up 10 MW with error spreads of ±5 MW. For the rest of the solutions, the mean error values were below 5 MW with a SD of ±2.5 MW. The maximum mean error estimated on the sodium heat-up trends is 0.8 K with an error spread of 0.4 K, see Fig. 62b. Fig. 62c shows that the total reactivity is predicted in excellent agreement with the reference for most of the simulations. An exception is found for the 4-group MDT solution characterized by a slightly larger average error and SD, that is, 0.1 pcm and 0.25 pcm. Doppler reactivity trends are well predicted for most of the simulations with peak average errors and SD of, respectively, 1 and 0.5 pcm estimated for 4-group solutions, see Fig. 62d. Fig. 62e and f show, in the case of 4-group solutions, mean errors up to 2.5 and 9 K for the trends of maximum clad and fuel temperatures. By increasing the number of EG such discrepancies significantly reduce assuming values below 0.7 and 3K. SDs decrease in the case of the clad temperature as the EG employed in the calculations increases for both the XS parametrization approaches in use. Similar considerations hold for the errors estimated on the trend of fuel temperature except for the 24-group FOD solution.

Fig. 63 presents the acceleration factors derived by the new calculations of the RS test. As for the PFS test, the calculations executed with FOD XS libraries result to be continuously accelerated by decreasing the number of EGs in use in calculations. A maximum speedup factor of 5 is reached in correspondence of 4-group calculations. The speedup factors of calculations executed with MDT XS libraries oscillate, starting from 8-group calculations, around a value of 3.6 without significantly changing for calculations with lower EGs. The calculations performed with FOD XS libraries are accelerated of a factor 1.2 against the corresponding runs performed with MDT libraries.

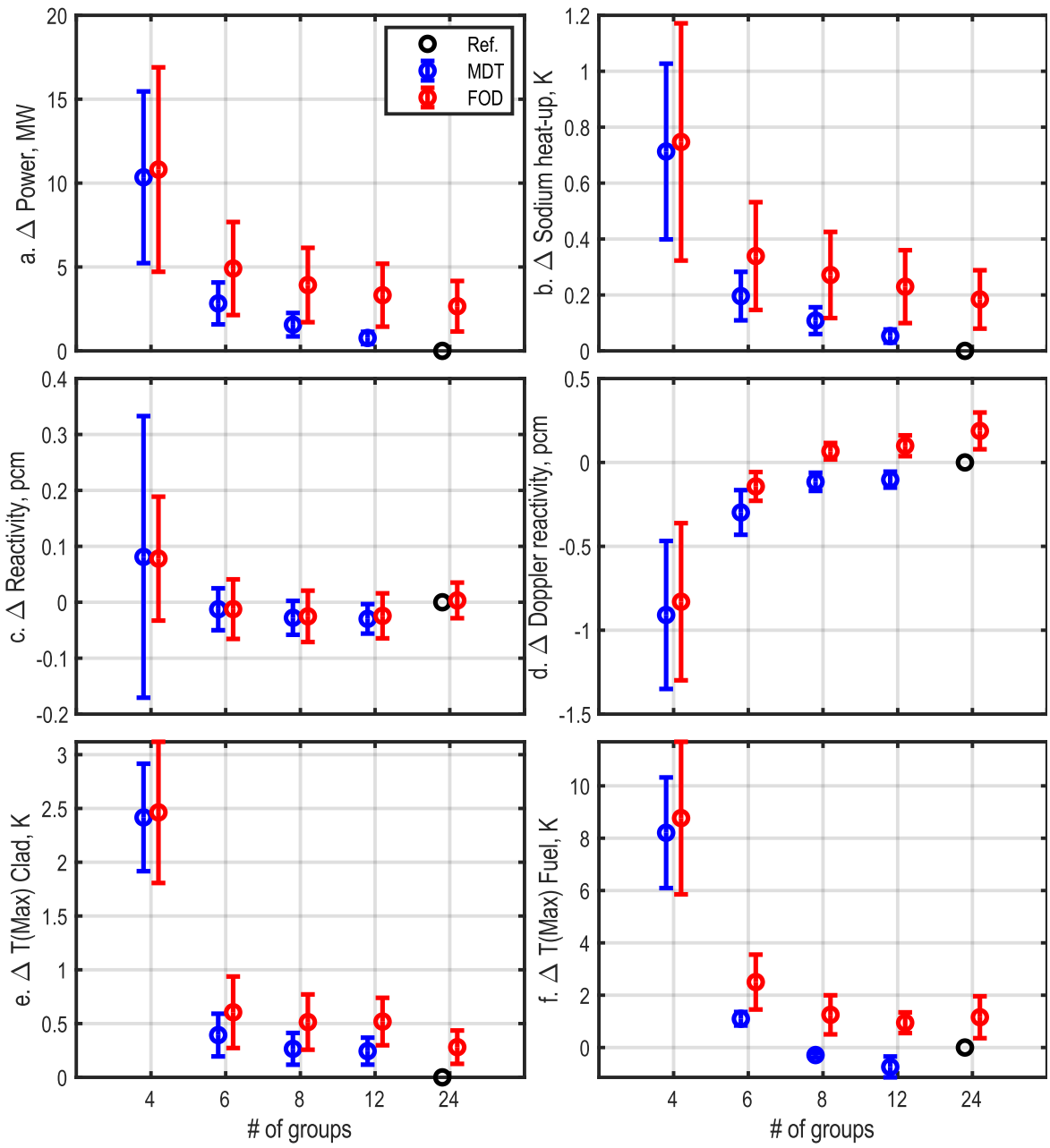

Fig. 62. Assessment of optimal condensed EGS and XS parametrization approaches on the RS test

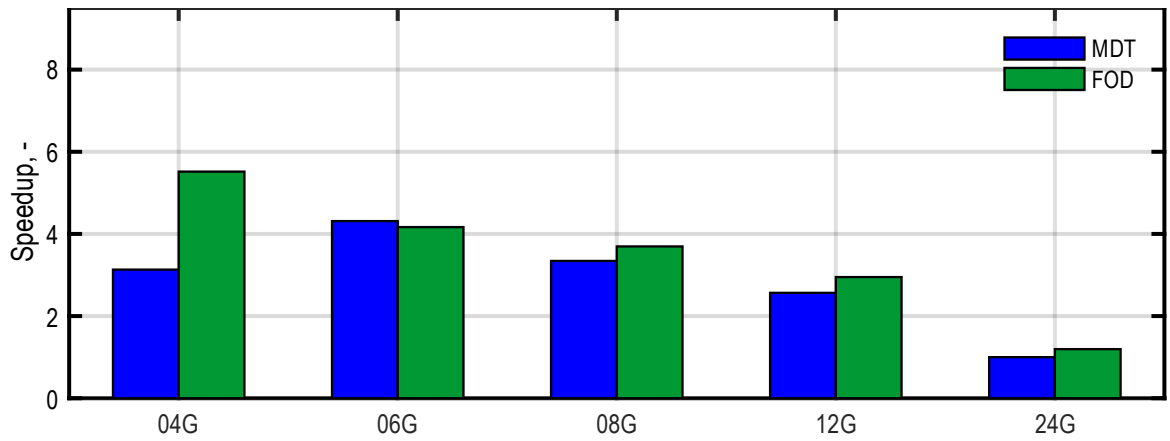

Fig. 63. Speedup of calculations for the RS test

SST test at hot zero-power

The calculations performed on the SST scenario reveal good agreements of the newly calculated solutions against the reference. With increasing the number of groups used in simulations, the MDT solutions perfectly converge both in terms of mean error values and SDs, see Fig. 64. Although the mean errors estimated on FOD solutions slightly diverge from reference, the trends prediction remains overall accurate enough. SDs of the FOD solutions, estimated on all quantities shown in Fig. 64 do not decrease as the number of EG used in calculations increases. Both mean errors and SDs estimated on solutions obtained with FOD libraries are indicative of a marginal underestimation of the trends.

Fig. 64a shows that the power trends are on average well predicted for all the recalculated solutions and especially for those obtained with MDT XS libraries. Average errors found on power trends are mostly below 0.3 MW within a SD of 0.24 MW. A negative exception is represented by the 4-group MDT solution for which the mean error is deviating of 0.8 MW from the reference with an error spread of 0.4 MW. Considering the maximum power reached in the transient, i.e., roughly 20 MW, the latter error is rather significant and thus unacceptable. The errors on the predicted sodium heat-up are marginal in all the cases. The largest mean error and SD are indeed limited to 0.15 and 0.05 K, see Fig. 64b. Fig. 64c shows that, apart from 4-group solutions, the total reactivity is predicted in excellent agreement against the reference with practically negligible mean errors and a SD of 0.1 pcm. Also the Doppler reactivity trends are well predicted for most of the simulations, and especially by MDT ones. Peak mean errors and SD of, respectively, 0.7 and 0.6 pcm are found for 4-group solutions, see Fig. 64d. Fig. 64e and f show that for the solutions other than 4-group ones mean error values found on the trends of maximum clad and fuel temperatures are below 0.1 and 0.5 K. In the case of the 4-group solutions the errors are somewhat larger but, in any case, below 0.25 and 1.2 K. In all the cases SDs on maximum clad and fuel temperature are negligible.

Fig. 65 shows the speedup in calculations obtained by applying the optimal condensed EGSs with both the parametrization approaches. On average, significant speedup factors of 3, 4, and 6 are obtained by using the 12, 8, and 6 EGSs. Accelerations up to factors 6 and 9 are achieved by employing the 4-group EGS with respectively the MDT and FOD parametrized XSs. The calculations performed with the FOD approach are on average 1.3 times faster than their respective calculations executed by using the MDT approach.

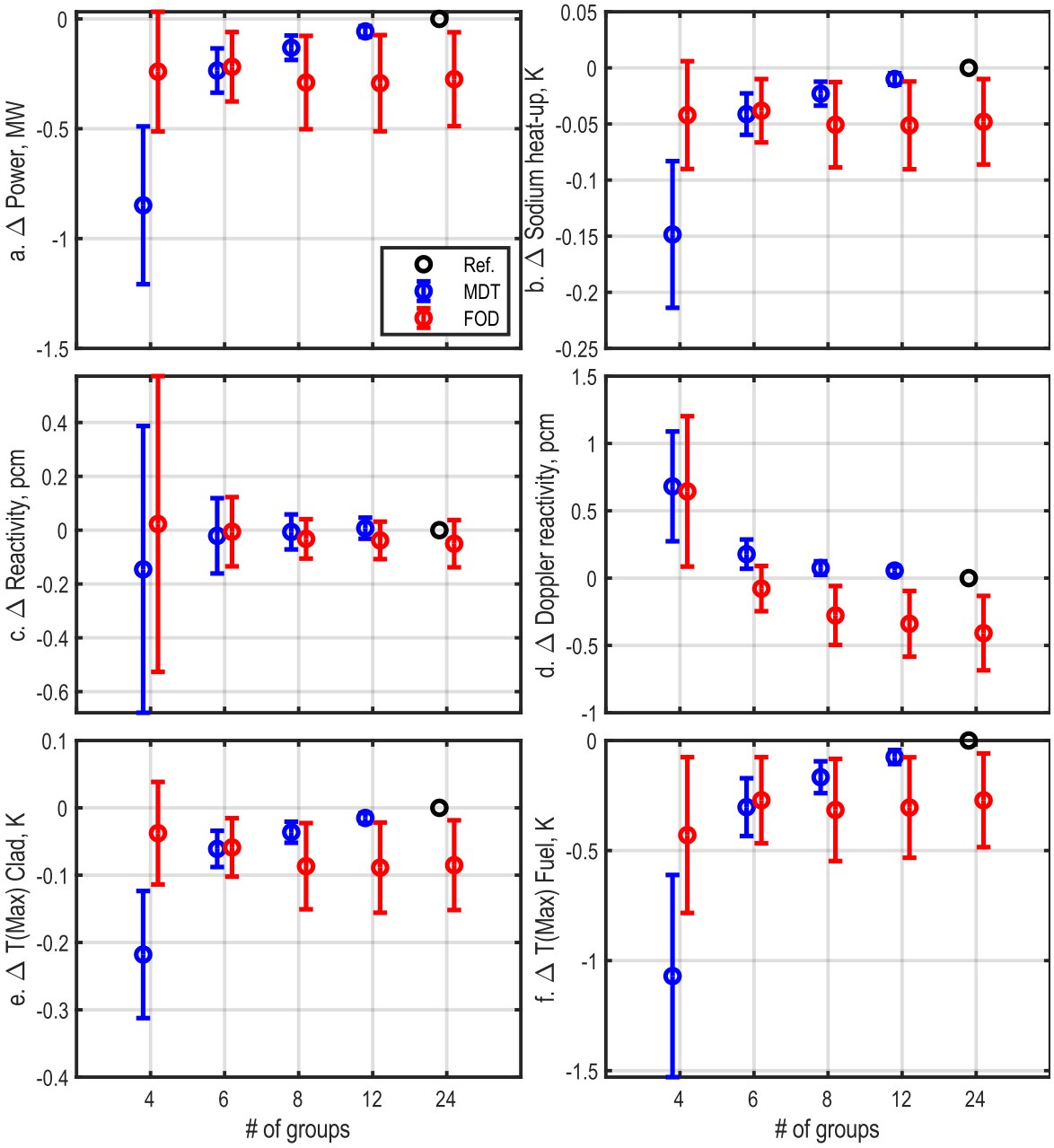

Fig. 64. Assessment of optimal condensed EGS and XS parametrization approaches on the SST test

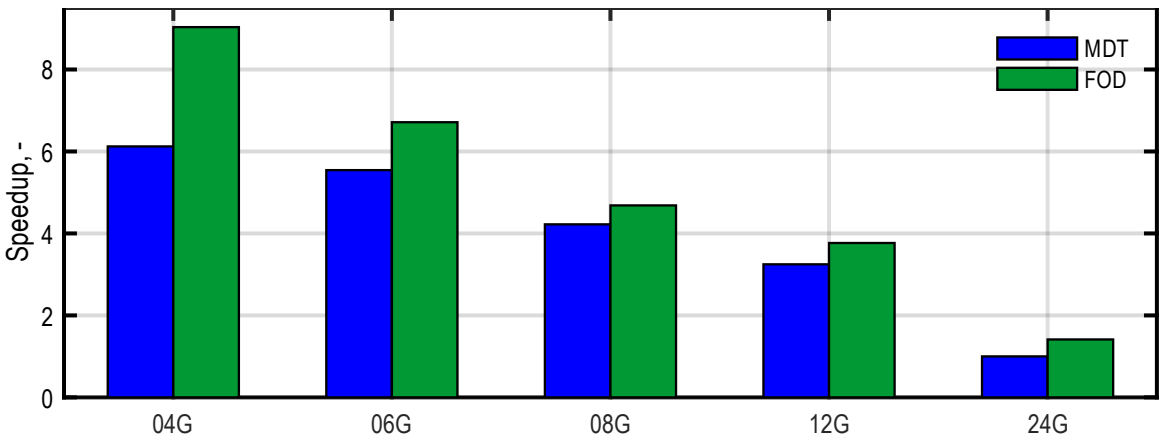

Fig. 65. Speedup of calculations for the SST test

4.4 Considerations on the optimization

Chapter 3 presented the V&V activities of the new HZDR computational platform as applied for the first time to static and transient analyses of SFR systems. Despite the activities showed good capabilities of the platform in predicting behaviors of SFR systems for the selected scenarios, transient analyses were time-demanding and required up to 12 days to be accomplished.

This chapter proposed and applied two potential options to reduce the computational times of the platform while preserving the accuracy of its solutions. Both the options were related to the simplification of the XS library models; they consisted of:

- The application of optimal condensed EGSs judiciously selected through a new optimization methodology assisted by the SA algorithm.
- The implementation of XS parametrization via the FOD approach.

The first option reduced the number of EGs, thus the number of multi-group equations, considered in neutronics models leading consequently to the global acceleration of calculations. The second option simplifies/accelerates the calculations required to update the nodal XSs to the current distributions of the state variables and reduces the number of calculations needed for the generation of XS libraries.

To show the benefits of the study, the static and transient benchmarks conducted on the Phénix and SPX reactor were recalculated with including the options mentioned above. In particular, recalculations with optimal condensed EGSs were performed on static and transient benchmarks. Whereas both the optimal condensed EGSs and FOD parametrized XS libraries were applied to the recalculations of transient benchmarks only.

Considering both the MDT and FOD parameterization approaches, the new calculations show that the accuracy of the solutions is well preserved by using optimal condensed EGSs down to 6-group. For the latter, in fact, errors on sodium heat-up, total reactivity, Doppler reactivity, maximum clad, and fuel temperatures are all practically negligible. Errors on power are in all cases limited to 1.5% in the worst case, i.e., the SST test. The application of optimal condensed 4-group EGSs is not recommended as it leads to somewhat deteriorated solutions, especially, in terms of power, i.e., errors up to 4% were observed in the SST solutions. All the solutions found with the application of FOD XS libraries do not significantly diverge from corresponding solutions obtained with the MDT libraries.

Wide margins for accelerating calculations were found for all the benchmark recalculations and maximum speedup factors up to 9 were observed in 4-group calculations run with FOD XS libraries, e.g., in MOFC2, MOFC3, and SST tests. It should be noted that in general, the calculations performed with FOD parametrized XSs are on average from 1.2 to 1.4 times faster than calculations performed with MDT parametrized XSs. Considering both the quality of solutions and reduction of computational times, best compromises are found for 6-group solutions obtained with FOD XS libraries exhibiting speedups from 4 to 7, see Fig. 66b. By employing the 6-group EGSs with the FOD parametrization approach, the calculations presented in Sections 3.1.5 and 3.2.4, previously executed in 12 days, were accomplished in 2 to 3 days maintaining the quality of solutions, see Fig. 66a.

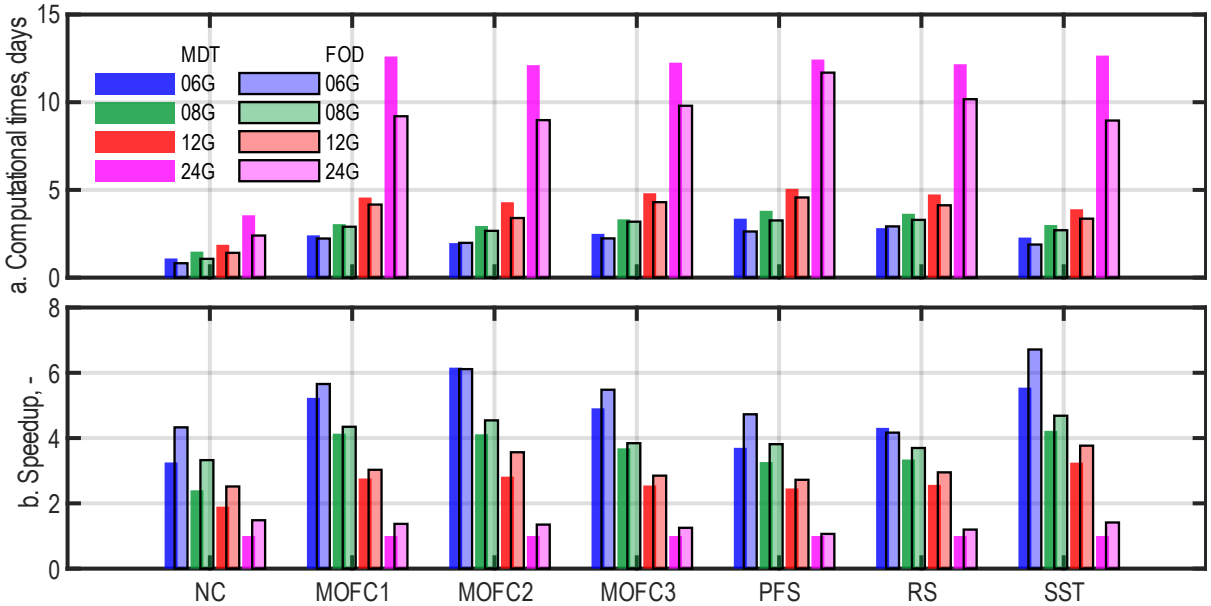

Fig. 66. Summary: Speedup and computational times of calculations

Chapter 5 Conclusions

The goals achieved by this doctoral thesis were:

1. Extension of the modeling domain of the computational platform of the HZDR from SFR cores to SFR systems. The extension included developments of ATHLET-based approaches for modeling relevant out-of-core structures and related thermal expansions.
2. Extensive verification and validation of the platform and formulation of its area of applicability.
3. Optimization of the computational times of the simulations against the accuracy of solutions and reduction of the computational burden required by the cross-section generation process for transient analyses of SFRs.

The verification and validation exercises conducted for the platform represented the first-of-a-kind transient application of DYN3D/ATHLET to SFR analyses. The analyses included the accountancy of most relevant reactivity feedback, in particular, fuel Doppler, sodium density, non-uniform axial expansions of core subassemblies, uniform core radial expansion driven by the diagrid expansion, and dynamic change of control rod positions induced by thermal expansions of the control rod drive-lines, strongback, and vessel.

The achieved goals of extension, verification, and validation extended, in principle, the applicability of the platform to the analyses of SFR systems that do not involve sodium boiling and core degradation. Options to optimize the computational times of calculations and processes of cross-section generation were proposed and tested against SFR numerical benchmarks and experimental tests. The evidence showed that the proposed options can significantly accelerate the simulations, making them at least three times faster, while practically preserving the accuracy of the solutions.

The following subsections summarize in more details the main achievements of the present dissertation and provide perspectives for future research.

5.1 Summary

The computational platform Serpent/DYN3D already applied to the analyses of SFR cores was extended to the analyses of SFR systems through the coupling with the ATHLET system code capable of modeling liquid-sodium-cooled systems. The extension was conducted by exploiting as starting point of the activity existing coupling routines of DYN3D/ATHLET, initially developed for LWR

analyses, and achieved by implementing targeted modifications to extend the coupling routines to the SFR analyses. The modifications enabled the coupling routines to use of SFR-specific in-core thermal expansion models already implemented in DYN3D standalone. The extension of the platform provided for the development of ATHLET-based methodologies for the modeling of relevant out-of-core thermal expansion effects, i.e., expansions of control rod drive-lines, strongback, and vessel. Such out-of-core effects can, in fact, dynamically affect the position of control rods with respect to the core, and thus significantly affect the core neutronics. A detailed modeling approach and a simplified one were presented.

The extended platform and the ATHLET-based modeling approaches outlined above were verified and validated against SFR transient tests. In particular, the platform was firstly applied to predict the initial stage of the Phénix natural circulation test and verified against existing solutions previously obtained by Serpent/DYN3D and validated against the data of the experiment. Secondly, the platform was also applied to predict six Superphénix transient tests conducted on the occasion of the reactor start-up and validated against available experimental data. At the current stage of development, the applicability of the platform can now be applied to the analyses of SFR systems and, specifically, to analyses of scenarios not involving sodium boiling or core damage.

The optimization of computational times related to transient calculations and cross-section generation was achieved through the optimization of the methodology used for cross-section generation. The step-one of the optimization regarded the development of a methodology, aided by the meta-heuristic "simulated annealing", for the selection of optimal condensed energy group structures. This step of the optimization led to the speedup of calculations through the reduction of the number of energy groups used in the multigroup diffusion equations. Testing activities on the optimization method and related condensed energy group structures found were successfully conducted both against static neutronics benchmarks and the Superphénix and Phénix transient tests. The evidence demonstrated the possibility of substantially accelerating the simulations, achieving a minimum threefold increase in speed while practically maintaining the accuracy of the solutions. The step-two of the optimization was focused on the investigation of a cross-section parametrization approach that could offer an alternative to the multidimensional table representation. The approach investigated was based on the representation of cross-section dependencies via first-order derivatives as already implemented in PARCS as a submodule of the FAST code. The application of such parametrization approach allowed one to drastically reduce the number of calculations required for the preparation of the cross-section libraries and further accelerating transient calculations. The investigation activities dedicated to the

alternative parametrization approach were conducted on the Superphénix and Phénix transient tests and revealed acceptable error margins of the obtained solutions with respect to the references.

5.2 Research outlook

The new HZDR computational platform can now enable one to perform safety analyses of entire SFR systems. However, to become a reference state-of-the-art tool for the safety analyses of SFRs, the platform has still to undergo further development and testing activities. In this regard, perspectives for possible future research are proposed hereafter.

For both ATHLET and DYN3D, the capabilities in modeling of the sodium coolant are limited to the liquid phase. This means that SFR analyses are currently restricted to the prediction of scenarios without coolant boiling. To perform comprehensive analyses of SFRs which may involve boiling phenomena, one has to provide to the code the capability of modeling the sodium vapor phase. In this respect, both ATHLET and DYN3D sodium thermal-hydraulic databases should be upgraded with thermal-physical properties of the sodium vapor and additional equations and closure relations for the vapor phase should be considered and solved.

The cross-section parametrization used by Serpent/DYN3D and the new computational platform implicitly accounts for sodium coolant density. Currently, the sodium density is determined implicitly from the sodium temperature. Within the set of validation transient tests performed in this thesis, such an approach represented an acceptable approximation, as sodium voiding effects were negligible. However, it is recommended to parameterize the cross-section while explicitly considering the dependence on sodium density. This can be especially beneficial in the analysis of scenarios involving coolant saturation conditions, where the fluid temperature remains constant, whereas the fluid density may change significantly.

Currently, the radial expansion of the core is uniformly modeled and assumed to be driven by the radial expansion of the diagrid. Core subassemblies maintain a fixed geometrical configuration along the axial layers of the subassemblies. Future platform extensions should grant the possibility of simulating non-uniform radial expansion of the core along the axial coordinate. Such an extension of the platform can, in principle, open up to the modeling of core flowering effects which, as shown in (Fontaine, et al., 2011), may play a significant role in transient scenarios of SFRs.

The actual version of the platform is based on the existing DYN3D/ATHLET "internal" coupling option initially developed to perform LWR analyses. Although such an option represents the most robust and validated option among the possibilities, the related calculations are computationally

demanding if numerous core channels have to be modeled. According to the experiences collected in performing LWR analyses with DYN3D/ATHLET, quicker executions of calculations are possible by applying the "external" and "parallel" coupling options. Explorations of these coupling options are, thus, recommended as they could potentially accelerate further the computational times.

At the moment, the transient tests employed for the validation of the new platform are the six Superphénix start-up transients and the initial stage of the Phénix natural circulation transient. Although the tests have been crucial in assessing the performance of the code, they were representative of scenarios initiated mostly by soft thermal-hydraulic perturbations, e.g., 10% primary flow rate reduction, 10% secondary flow rate increase, etc. In addition, most of the tests involved symmetric behaviors of the core. Beneficial for further verification and validation activities is thus the application of the platform in the prediction of scenarios driven by stronger perturbations and leading to asymmetric core responses (Jeong, et al., 2015). The test cases employed for the activities can be either "artificially" built benchmarks or actual experimental tests. The FFTF loss of flow without scram test (IAEA 2019) is an example of a transient test driven by a stronger perturbation that may contribute to the further verification and validation of the platform. Experimental data of the test were provided by the Pacific Northwest National Laboratory and the Argonne National Laboratory in the framework of a coordinated research project proposed by IAEA in 2017 and are accessible to the HZDR as a member organization of the project.

Last but not least, the platform can be further extended by considering the coupling with other computational tools dedicated to the detailed simulation of specific areas of nuclear modeling, e.g.: the modeling of fuel performance behavior, the behavior of sodium flow within the subassemblies and in the regions of the system where three-dimensional sodium flow effects are not negligible, etc. For instance, the coupling with a fuel performance code, such as TRANSURANUS (Lassmann, 1992), able to model the fuel rod thermal-mechanic behavior under irradiation conditions, can allow for a more precise estimation of the fuel temperature and heat transfer coefficients of the gap. The further platform extension via coupling with sub-channel codes, e.g., FLICA-4 (Toumi, et al., 2000), designed to describe the flow in rod bundles, can provide a more detailed description of the fluid behavior within subassemblies. Finally, the coupling with a computational fluid dynamic tool, like TrioCFD (Angeli, et al., 2015), may allow the platform to catch complex three-dimensional thermal-hydraulic effects occurring in the hot and cold pools of SFRs. Examples of such effects, hard to simulate by system codes, are e.g., the thermal stratification and mixing phenomena and are essential to predict precisely the fluid temperature and flow distributions within the primary system.

Bibliography

Schneider, D. et al., 2016. *APOLLO3 CEA/DEN deterministic multi-purpose code for reactor physics analysis.*. Unifying Theory and Experiments in the 21st Century, May 2016, Sun Valley, United States. ffcea-02509714, PHYSOR2016.

Akebi, M., 1991. *Overview of MONJU project.* Japan: Atomic Energy Society of Japan.

Alemberti, A. et al., 2020a. ALFRED reactor coolant system design. *Nuclear Engineering and Design*, 370(0029-5493), p. 110884.

Alemberti, A. et al., 2020b. *Lead-cooled Fast Reactor (LFR) System Safety Assessment,* s.l.: GIF Risk & Safety Working Group.

Anandapadmanaban, B., Thangamani, M., Sureshkumar, K. V. & Srinivasan, G., 2013. *26 Years of Operating Experience of FBTR and Feedback to Future Reactor Design.* s.l., IAEA.

Angeli, P., Bieder, U. & Fauchet, G., 2015. *OVERVIEW OF THE TRIOCFD CODE: MAIN FEATURES,V&V PROCEDURES AND TYPICAL APPLICATIONS TO NUCLEAR ENGINEERING.* Chicago, s.n.

Austregesilo, H. et al., 2016. *ATHLET 3.1A Models and Methods.* s.l.:s.n.

Bajorek, S., 2008. *TRACE V5. 0 Theory manual, field equations, solution methods and physical models.* s.l.:s.n.

Bergeonneau, P. et al., 1990. An Analysis of the Dynamic Behavior of the Core. *Nuclear Science and Engineering,* Volume 106, pp. 18-29.

Bilodid, Y., Fridman, E., Kotlyar, D. & Shwageraus, E., 2018a. Explicit decay heat calculation in the nodal diffusion code DYN3D. *Annals of Nuclear Energy,* 121(0306-4549), pp. 374 - 381.

Bilodid, Y., Grundmann, U. & Kliem, S., 2018b. The HEXNEM3 nodal flux expansion method for the hexagonal geometry in the code DYN3D. *Annals of Nuclear Energy.*

Bodi, J., 2017. *Development of a CAD model for the European Sodium.* Villigen, Switzerland: s.n.

Brunett, A. J. & Fanning, T. H., 2017. *U.S. Sodium Fast Reactor Codes and Methods: Current Capabilities and Path Forward.* Yekaterinburg, Russian Federation, ANL.

Buckel, G. et al., 1999. *A new SIMMER-1I1 Version with improved Neutronics Solution Aigorithms,* Karlsruhe: Forschungszentrum Karlsruhe.

Cahalan, J. et al., 2000. *Development of a coupled dynamics code with transport theory capability and application to accelerator-driven systems transients. In Int. Conf. on the Physics of Reactors (PHYSOR), Paper 197. May 7-12 2000.* s.l., s.n.

CEA Marcoule, 2010. *One day, Phenix.* Editions Paris Le Sud a cura di France: s.n.

Chauliac, C. et al., 2010. NURESIM – A European simulation platform for nuclear reactor safety: Multi-scale and multi-physics calculations, sensitivity and uncertainty analysis. *Nuclear Engineering and Design,* 241(ISSN 0029-5493), pp. 3416 - 3426.

DAE, 2021. *Government of India: Department of Atomic Energy, "Construction of PFBR".* India: s.n.

Derstine, K. L., 1984. *DIF3D: a code to solve one-, two-, and three-dimensional finite-difference diffusion theory problems. [LMFBR]. United States. https://doi.org/10.2172/7157044,* s.l.: s.n.

Di Nora, V. A., Fridman, E. & Mikityuk, K., 2019. *Benchmarking ATHLET against TRACE as applied to Superphénix start-up tests.* International Congress on Advances in Nuclear Power Plants - ICAPP2019, 12.-15.05.2019, Juan-les-Pins, France, s.n.

Di Nora, V. et al., 2021a. Optimization of multi-group energy structures for diffusion analyses of sodium-cooled fast reactors assisted by simulated annealing – Part I: Methodology demonstration. *Annals of Nuclear Energy,* Volume 155, p. 108183.

Di Nora, V. et al., 2021b. Optimization of multi-group energy structures for diffusion analyses of sodium-cooled fast reactors assisted by simulated annealing – Part II: Methodology application. *Annals of Nuclear Energy,* Volume 163, p. 108541.

Downar, T. J., Lee, D., Yunlin, X. & Kozlowski, T., 2004. *Theory manufal for the PARCS neutronics Core Simulator.* s.l.:s.n.

Downar, T., Xu, Y., V., S. & Hudson, N., 2012. *"PARCS v3.0 U.S. NRC Core Neutronics Simulator: Theory Manual.",* s.l.: " Ann Arbor..

Dragunov, Y. et al., 2015. *Experimental Potentialities of the MBIR Reactor.* Monti, S. (Ed.) a cura di s.l.:International Atomic Energy Agency (IAEA): IAEA.

Eliasi, R., Elperin, T. & Bar-Cohen, A., 2002. Monte Carlo thermal optimization of populated printed circuit board. *IEEE Transactions on Components, Hybrids, and Manufacturing Technology,* 13(4), pp. 953-960.

Elperin, T., 1988. Monte Carlo structural optimization in discrete variables with annealing algorithm. *International Journal for Numerical Methods in Engineering,* 26(4), pp. 815-821.

Fiorina, C., Clifford, I., Aufiero, M. & Mikityuk, K., 2015. GeN-Foam: a novel OpenFOAM® based multi-physics solver for 2D/3D transient analysis of nuclear reactors. *Nuclear Engineering and Design,* Volume 294, pp. 24-37.

Fiorina, C., Clifford, I., Aufiero, M. & Mikityuk, K., 2015. GeN-Foam: A novel OpenFOAM® based multi-physics solver for 2D/3D transient analysis of nuclear reactors. *Nuclear Engineering and Design,* Volume 294, pp. 24 - 37.

Fiorina, C., Radman, S., Koc, M. & Pautz, A., 2019. DETAILED MODELLING OF THE EXPANSION REACTIVITY FEEDBACK IN FAST REACTORS USING OpenFOAM..

Fiorini, G. L. & Vasile, A., 2012. European Commission – 7th Framework Programme The Collaborative Project on European Sodium Fast Reactor (CP ESFR). *Nuclear Engineering and Design,* 241(9), pp. 3461-3469.

Flamenbaum, G. et al., 1990. Superphenix Core-Loading Strategy Using the Checkerboard Pattern. *Nuclear Science and Engineering,* Volume 106, pp. 11-17.

Fleming, M. J., Morgan, L. W. G. & Shwageraus, E., 2016. Optimization Algorithms for Multigroup Energy Structures. *Nuclear Science and Engineering,* 183(2), pp. 173 - 184.

Fontaine, B. et al., 2011. Description and preliminary results of PHENIX core flowering test. *Nuclear Engineering and Design,* 241(10), pp. 4143-4151.

Fridman, E. & Shwageraus, E., 2013. Modeling of SFR cores with Serpent–DYN3D codes sequence. *Annals of Nuclear Energy,* Volume 53, pp. 354-363.

Garcia, E., Sciora, P. & Rimpault, G., 2019. *Analysis of the feedback coefficients of the Superphenix start-up core with APOLLO3. ICAPP 2019 - International Congress on Advances in Nuclear Power Plants, May 2019, Juan-Les-Pins, France..* s.l., s.n.

Geffraye, G. et al., 2011. CATHARE 2 V2.5-2: A single version for various applications. *Nuclear Engineering and Design,* 241(11), pp. 4456-4463.

GIF, 2021. *Generation IV Goals.* [Online] Available at: https://www.gen-4.org/gif/jcms/c_9502/generation-iv-goals

Glover, F. & Greenberg, H. J., 1989. New approaches for heuristic search: A bilateral linkage with artificial intelligence. *European Journal of Operational Research,* 39(2), pp. 119-130.

Gomez-Torres, A. M., Sanchez-Espinoza, V. H., Ivanov, K. & Macian-Juan, R., 2012. DYNSUB: A high fidelity coupled code system for the evaluation of local safety parameters – Part I: Development, implementation and verification,. *Annals of Nuclear Energy,* Volume 48, pp. 108-122.

Gourdon, J., Mesnage, B., Voitellier, J. L. & Suescun, M., 1990. An overview of Superphenix commissioning tests. *Nuclear Science and Engineering,* Volume 106:1, pp. 1-10.

Grahn, A., Kliem, S. & Rohde, U., 2015. Coupling of the 3D neutron kinetic core model DYN3D with the CFD software ANSYS-CFX,. *Annals of Nuclear Energy,,* Volume 84, pp. 197-203.

Grundmann, U., Lucas, D. & Rohde, U., 1995. *Coupling of the thermo-hydraulic code ATHLET with the neutron kinetic core model DYN3D. In: Proc. Int. Conf. On Mathematics and Computations, Reactor Physics, and Enviromental Analyses, Portland, Oregon, USA, April 30-May 4 1995.* s.l., s.n.

Grundmann, U., Rohde, U., Mittag, S. & Kliem, S., 2005. DYN3D version 3.2 - Code for calculation of transients in light water reactors (LWR) with hexagonal or quadratic fuel elements - description of models and methods. *Fzr-434,* p. 140.

Guidez, J. et al., 2021. New Reactor Safety Measures for the European Sodium Fast Reactor—Part I: Conceptual Design.. *Journal of Nuclear Engineering and Radiation Science,* 8(1).

Guidez, J. & Prêle, G., 2016. *Superphenix : les acquis techniques et scientifiques.* s.l.:s.n.

Hebert, A., 1993. A Consistent Technique for the Pin-by-Pin Homogenization of a Pressurized Water Reactor Assembly. *Nuclear Science and Engineering,* 113(3), pp. 227 - 238.

Hebert, A. & Mathonniere, G., 1993. Development of a third-generation superhomogeneisation method for the homogenization of a pressurized water reactor assembly. *Nuclear Science and Engineering1992,* 115(2).

Herman, M. & Trkov, A., 2009. *ENDF-6 Formats Manual,* s.l.: Report BNL-90365-2009.

Hollands, T. et al., 2021. *ATHLET 3.3: VALIDATION,* Garching bei München: GRS.

Holt, L. et al., 2014. *Two-Way Coupling Between the Reactor Dynamics Code DYN3D and the Fuel Performance Code TRANSURANUS at Assembly Level. 2014 22nd International Conference on Nuclear Engineering. ICONE22.* s.l., s.n.

Hunter, S. N., 1998. *Super-Phenix benchmark used for comparison of PNC and CEA calculation methods, and of JENDL-3.2 and CARNAVAL IV nuclear data,* Japan: s.n.

IAEA, 1996. *Fast Reactor Database, IAEA-TECDOC-866,* Vienna, Austria: IAEA.

IAEA, 2006. *Fast reactor database. IAEA-TECDOC-1531 ISBN 92-0-114206-4. IAEA, Vienna, Austria, 2006,* s.l.: s.n.

IAEA, 2013. *Benchmark Analyses on the Natural Circulation Test Performed during the PHENIX End-of-life Experiments,* s.l.: s.n.

IAEA, 2014a. *Defence-in-Depth and Its Role in Nuclear Safety.* [Online] Available at: https://www.iaea.org/newscenter/news/defence-depth-and-its-role-nuclear-safety

IAEA, 2014b. *Benchmark Analyses on the Control Rod Withdrawal Tests Performed during the PHENIX End-of-Life Experiments,* s.l.: s.n.

IAEA, 2014. *Benchmark Analyses on the Control Rod Withdrawal Tests Performed during the PHENIX End-of-Life Experiments,* s.l.: s.n.

IAEA, 2016. *Considerations on the Application of the IAEA Safety Requirements for the Design of Nuclear Power Plants,* s.l.: s.n.

IAEA, 2017. *Benchmark Analysis of EBR-II Shutdown Heat Removal Tests. INTERNATIONAL ATOMIC ENERGY AGENCY.* Vienna: s.n.

Imke, U., Sanchez, V. & Gomez, R., 2010. *SUBCHANFLOW: A new empirical knowledge based subchannel code. In: Proc. KTG Annual Meeting on Nuclear Technology 2010, Berlin, Germany, May 4-6.* s.l., s.n.

Imke, U. et al., 1994. *Status of the SAS4A code development for consequence analysis of core disruptive accidents. In Proceedings of an International Topical Meeting on Sodium Cooled Fast Reactor Safety.* Obninsk, Russia, s.n.

INL, 2019. *Idaho National Laboratory, "EBR-I lights up the history of nuclear energy development".* [Online] Available at: https://inl.gov/article/ebr-i-lights-up-the-history-of-nuclear-energy-development/

IPFM, 2019. *International Panel on Fissile Materials, "Construction of Russia's BN-1200 fast-neutron reactor delayed until 2030s".* [Online]
Available at: https://fissilematerials.org/blog/2019/08/the_construction_of_the_b.html

IPFM, 2021. *International Panel on Fissile Materials, "China's CEFR fast reactor begins "high-power operations"".* [Online]
Available at: https://fissilematerials.org/blog/2021/02/chinas_cefr_fast_reactor_.html

Jensen, S. E. & Olgaard, P. L., 1995. *Description of the Prototype Fast Reactor at Dounreay.* s.l.:s.n.

Jeong, H. Y., Ha, K. s., Choi, C. W. & Park, M. G., 2015. Analysis of Phenix End-of-Life asymmetry test with multi-dimensional pool modeling of MARS-LMR code. *Annals of Nuclear Energy,* Volume 75, pp. 443-451.

Kim, C. S., 1975. *Thermophysical properties of stainless steels,* United States: ANL.

Kliem, S. et al., 2017. Testing the NURESIM platform on a PWR main steam line break benchmark. *Nuclear Engineering and Design,* 321(ISSN 0029-5493), pp. 8-25.

Kliem, S., Kozmenkov, Y., Höhne, T. & Rohde, U., 2006. Analyses of the V1000CT-1 benchmark with the DYN3D/ATHLET and DYN3D/RELAP coupled code systems including a coolant mixing model validated against CFD calculations,. *Progress in Nuclear Energy,,* 48(8), pp. 830-848.

Koning, A., Forrest, R. & Kellett, M., 2006. *The JEFF-3.1.1 Nuclear Data Library,* s.l.: s.n.

Kotlyar, D. & Parks, G. T., 2016. Enhancing plutonium incineration in the thorium-based I2S-LWR design with loading pattern optimization. *Annals of Nuclear Energy,* Volume 96, pp. 401-411.

Kozmenkov, Y. et al., 2007. Calculation of the VVER-1000 coolant transient benchmark using the coupled code systems DYN3D/RELAP5 and DYN3D/ATHLET. *Nucl. Eng. Des.,* Volume 237, pp. 1938 - 1951.

Kozmenkov, Y., Kliem, S. & Rohde, U., 2015. Annals of Nuclear Energy Validation and verification of the coupled neutron kinetic / thermal hydraulic system code DYN3D / ATHLET. *Annals of Nuclear Energy,* Volume 84, pp. 153-165.

Kozmenkov, Y. et al., 2001. *Development and benchmarking of the DYN3D/RELAP5 code system, Germany: Inforum.* s.l., s.n.

Kruessmann, R. et al., 2015. Assessment of SFR reactor safety issues: Part II: Analysis results of ULOF transients imposed on a variety of different innovative core designs with SAS-SFR. *Nuclear Engineering and Design,* 285(0029-5493), pp. 263-283.

Lainet, M. et al., 2019. GERMINAL, a fuel performance code of the PLEIADES platform to simulate the in-pile behaviour of mixed oxide fuel pins for sodium-cooled fast reactors,. *Journal of Nuclear Materials,* 516(0022-3115), pp. 30-53.

Lassmann, K., 1992. TRANSURANUS: a fuel rod analysis code ready for use. *Journal of Nuclear Materials,* Volume 188, pp. 295-302.

Lassmann, K. & Hohlefeld, F., 1987. The revised URGAP model to describe the gap conductance between fuel and cladding. *Nuclear Engineering and Design,* 103(2), pp. 215-221.

Lázaro, A. et al., 2014a. Code assessment and modelling for Design Basis Accident Analysis of the European sodium fast reactor design. Part I: System description, modelling and benchmarking. *Nuclear Engineering and Design,* 266(ISSN 00295493.), pp. 1 - 16.

Lázaro, A. et al., 2014b. Code assessment and modelling for Design Basis Accident analysis of the European SodiumFast Reactor design. Part II: Optimised core and representative transients analysis. *Nuclear Engineering and Design,* 277(ISSN 00295493), pp. 265 - 276.

Lee, C. & Yang, W. S., 2017. MC2-3: Multigroup Cross Section Generation Code for Fast Reactor Analysis. *Nuclear Science and Engineering, 187(3):268–290, sep 2017. ISSN 0029-5639. doi:10.1080/00295639.2017.1320893..*

Leppänen, J., 2015. Serpent: a Continuous-energy Monte Carlo Reactor Physics Burnup Calculation Code. p. 164.

Leppänen, J., 2022. Methodology, applications and performance of the CAD-based geometry type in the serpent 2 Monte Carlo code. *Annals of Nuclear Energy,* 176(109259).

Leppänen, J. et al., 2015. The Serpent Monte Carlo code: Status, development and applications. *Annals of Nuclear Energy,* 82(ISSN 03064549), pp. 142-150.

Macfarlane, R. E., Muir, D., Boicourt, R. M. & Kahler, A. c., 2012. The NJOY Nuclear Data Processing System, Version 2012. *LA-UR-12-27079, Los Alamos National Laboratory.*

Malo, J. Y. et al., 2008. *Gas cooled fast reactor 2400 MWth, end of the preliminary viability phase.* United States: American Nuclear Society - ANS.

Manera, A., Rohde, U., Prasser, H.-M. & van der Hagen, T., 2005. Modeling of flashing-induced instabilities in the start-up phase of natural-circulation BWRs using the two-phase flow code FLOCAL. *Nuclear Engineering and Design,* 235(14), pp. 1517-1535.

Marth, M., 1983. *KNK II operating experience and fuel cycle activities.* s.l.:s.n.

Martin, L., 2009. *Phénix: 35 ans d'exploitation, 1974-2009.,* s.l.: Revue Générale Nucléaire, SFEN.

Massone, M., Gabrielli, F. & Rineiski, A., 2017. A genetic algorithm for multigroup energy structure search. *Annals of Nuclear Energy,* Volume 105, pp. 369-387.

Matsuba, K.-i., Kawahara, H. & Aoyama, T., 2006. *Introduction of the experimental fast reactor JOYO,* s.l.: s.n.

McCrosson, F. J., 2001. *ENDF/B Thermal Data Testing,* s.l.: United States, Web. doi:10.2172/787923.

Meyer, M. K., Fielding, R. & Gan, J., 2007. Fuel development for gas-cooled fast reactors. *Journal of Nuclear Materials,* Volume 371, pp. 281 - 287.

Mikityuk, K. et al., 2017. *ESFR-SMART: new Horizon-2020 project on SFR safety.* Yekaterinburg, Russian Federation, s.n.

Mikityuk, K. et al., 2005. FAST: An advanced code system for fast reactor transient analysis. *Annals of Nuclear Energy,* 32(15), pp. 1613-1631.

Mikityuk, K. & Schikorr, M., 2013. *New transient analysis of the Superphénix start-up tests.* s.l., IAEA FR2013,.

Mikityuk, K. & Shestopalov, A., 2011. FRED fuel behaviour code : Main models and analysis of Halden IFA-503 . 2 tests. *Nuclear Engineering and Design,* 241(7), pp. 2455-2461.

NEA, N. e. a., 2022. *Joint Evaluated Fission and Fusion (JEFF).* [Online] Available at: https://www.oecd-nea.org/dbdata/jeff/

Newland, D. J. & Krupar, J. J., 1984. *FFTF operational experience (HEDL-SA--3047-FP),* United States: s.n.

Nikitin, E., 2019a. *Extension of the nodal code DYN3D to SFR applications. PhD Thesis.* Lausanne: s.n.

Nikitin, E. & Fridman, E., 2018a. Extension of the reactor dynamics code DYN3D to SFR applications – Part I : Thermal expansion models. *Annals of Nuclear Energy,* Volume 119, pp. 382-389.

Nikitin, E. & Fridman, E., 2018b. Extension of the reactor dynamics code DYN3D to SFR applications – Part II : Validation against the Phenix EOL control rod withdrawal tests. *Annals of Nuclear Energy,* Volume 119, pp. 411-418.

Nikitin, E. & Fridman, E., 2018c. Extension of the reactor dynamics code DYN3D to SFR applications – Part III: Validation against the initial phase of the Phenix EOL natural convection test. *Annals of Nuclear Energy,* Volume 119, pp. 390-395.

Nikitin, E. & Fridman, E., 2019. Modeling of the FFTF isothermal physics tests with the Serpent and DYN3D codes. *Annals of Nuclear Energy,* Volume 132, pp. 679-685.

Nikitin, E., Fridman, E. & Mikityuk, K., 2015a. Solution of the OECD/NEA neutronic SFR benchmark with Serpent-DYN3D and Serpent-PARCS code systems. *Annals of Nuclear Energy,* Volume 75, pp. 492-497.

Nikitin, E., Fridman, E. & Mikityuk, K., 2015b. On the use of the SPH method in nodal diffusion analyses of SFR cores. *Annals of Nuclear Energy,* Volume 85, pp. 544-551.

Nikitin, E., Fridman, E. & Mikityuk, K., 2015. On the use of the SPH method in nodal diffusion analyses of SFR cores. *Annals of Nuclear Energy,* Volume 85, pp. 544-551.

Osman, I. H. & Kelly, J. P., 1996. *Meta-Heuristics: Theory & Applications.* Boston, MA: Springer US.

Palmiotti, G., Lewis, E. E. & Carrico, C. B., 1996. *VARIANT: VARIational Anisotropic Nodal Transport for Multidimensional Certesian and Hexagonal Geometry Calculation, oct 1996. URL https://inis.iaea.org/search/search.aspx?orig_qÆRN:27049245.,* s.l.: s.n.

Palmiotti, G., Rieunier, J., Gho, C. & Salvatores, M., 1987. *BISTRO Optimized Two Dimensional Sn Transport Code. In TopicalMeeting on Advances in Reactor Physics, Mathematics and Computation.* Paris, France, s.n.

Ponomarev, A., 2017. *Improved methodologies for evaluation of severe transient conditions of sodium-cooled fast systems.* s.l.:Karlsruher Institut für Technologie (KIT).

Ponomarev, A., Bednarova, A. & Mikityuk, K., 2018. *New sodium fast reactor neutronics.* Cancun, Mexico, s.n.

Ponomarev, A., Broeders, C. H. M., Dagan, R. & Becker, M., 2010. *Evaluation of Neutron Physics Parameters and Reactivity Coefficients for Sodium Cooled Fast Reactors - Proceedings of ICAPP '10, San Diego, CA, USA, June 13-17, 2010, Paper 10366.* s.l., s.n.

Ponomarev, A. et al., 2021a. Superphénix Benchmark Part I: Results of Static neutronics. *Journal of Nuclear Engineering and Radiation Science,* p. 8(1): 011320.

Ponomarev, A. et al., 2021b. Superphénix Benchmark Part II: Transient Results. *Journal of Nuclear Engineering and Radiation Science,* p. 8(1): 011321.

.

Poplavsky, V., Oshkanov, N., Vasiliev, B. & Ershov, V., 2004. *Operating experience of BN-600 fast neutron reactor and BN-800 reactor design (IAEA-CN--114),* s.l.: International Atomic Energy Agency (IAEA).

Poumerouly, S., Lemasson, D. & Girardi, E., 2016. Comparison of the point-kinetics and quasi-static methods with SIMMER-III -Application to a ULOF calculation..

Rachamin, R., Wemple, C. & Fridman, E., 2013. Neutronic analysis of SFR core with HELIOS-2, Serpent, and DYN3D codes. *Annals of Nuclear Energy,* Volume 55, pp. 194-204.

Ramana, M. V., 2023. *India's Prototype Fast Breeder Reactor delayed again.* [Online] Available at: https://fissilematerials.org/blog/2023/03/indias_prototype_fast_bre_1.html [Consultato il giorno 5 March 2023].

RELAP5, 1995. *RELAP5/MOD3 Code Manual.* Washington: Vol 2. NUREG/CR-5335-Vol II. Office for Nuclear Regulatory Research.

Rimpault, G. et al., 2002. *The ERANOS code and data system for fast reactor neutronic analyses. In Physor 2002.* Seoul, Korea, s.n.

Rimpault, G. et al., 1989. *Validation of new sub-group algorithms for resonance self-shielding in heterogeneous structures.* s.l.:s.n.

Rohde, U., 2001. The modeling of fuel rod behaviour under RIA conditions in the code DYN3D. *Annals of Nuclear Energy,* Volume 28, pp. 1343-1363.

Rohde, U. et al., 2016. The reactor dynamics code DYN3D - Models, validation and applications. *Progress in Nuclear Energy,* Volume 89, pp. 170-190.

ROSATOM, 2021. *ROSATOM, "Fast Reactor BOR-60".* [Online] Available at: http://www.niiar.ru/eng/node/224

Ruggieri, J. M. et al., 2006. ERANOS 2.1: International code system for GEN IV fast reactor analysis. *Proceedings of the 2006 International Congress on Advances in Nuclear Power Plants, ICAPP'06,* 2006(June 2015), pp. 2432-2439.

Scheff, J. D. et al., 2013. A multiscale modeling approach to inflammation: A case study in human endotoxemia. *Journal of Computational Physics,* Volume 244, pp. 279-289.

Schikorr, W. M., 2001. Assessment of the kinetic and dynamic transient behaviour of sub-critical systems (ADS) in comparison to critical reactor systems. *Nuclear Engineering and Design,* Volume 210, p. 95–123.

Sciora, P. et al., 2020. *ANALYSIS OF THE SUPERPHENIX START-UP TESTS WITH APOLLO-3: POWER TRANSIENT ANALYSIS.* EPJ Web of Conferences 247, 06044, PHYSOR2020.

Sciora, P. et al., 2021. *ANALYSIS OF THE SUPERPHENIX START-UP TESTS WITH APOLLO-3: FROM ZERO POWER ISOTHERMAL CONDITIONS TO DYNAMIC POWER TRANSIENT ANALYSIS.* EPJ Web Conf., PHYSOR2020 – International Conference on Physics of Reactors: Transition to a Scalable Nuclear Future.

Smith, K. S., 1980. *Spatial homogenization methods for light water reactor analysis. PhD thesis, Massachusetts Institute of Technology,* s.l.: s.n.

Tenchine, D. et al., 2012. Status of CATHARE code for sodium cooled fast. *Nuclear Engineering and Design,*, 245(ISSN 00295493.), p. 140–152.

Tobita, Y. et al., 2002. *The development of SIMMER-III, an advanced computer program for LMFR safety analysis. In Joint IAEA/NEA Tech. Mtg. on the Use of Computational Fluid Dynamics Codes for Safety Analysis of Reactor Systems (including Containment),* s.l.: s.n.

Toumi, I. et al., 2000. FLICA-4: a three-dimensional two-phase flow computer code with advanced numerical methods for nuclear applications. *Nuclear Engineering and Design,* 200(1–2), pp. 139-155.

U.S.NRC, 2021. *U.S.NRC, "Fermi – Unit 1".* [Online] Available at: https://www.nrc.gov/info-finder/decommissioning/power-reactor/enrico-fermi-atomic-power-plant-unit-1.html

Vanier, M. et al., 1990. Superphenix Reactivity Feedback And Coefficients. *Nuclear Science and Engineering,* Volume 106, pp. 30-36.

Vasile, A. et al., 2015. *The European project ESNII Plus. In Proceedings of 2015 international congress on advances in nuclear power plants (ICAPP 2015) (pp. 928-936).* s.l., s.n.

Waltar, A. E., Todd, D. R. & Tsvetkov, P. V., 2012. *Fast Spectrum Reactors.* s.l.:Springer.

Westfall, C., 2004. Vision and reality : The EBR-II story. *Nuclear News,* 1(February).

Wikimedia, 2021. *File:Superphenix reactor east closed up.jpg.* [Online] Available at: https://commons.wikimedia.org/wiki/File:Superphenix_reactor_east_closed_up.jpg

Wikipedia, 2021. *Wikipedia, "Sodium-cooled fast reactor".* [Online] Available at: https://en.wikipedia.org/wiki/Sodium-cooled_fast_reactor

WNA, 2021. *World Nuclear Association, "Fast Neutron Reactors".* [Online] Available at: https://world-nuclear.org/information-library/current-and-future-generation/fast-neutron-reactors.aspx

WNN, 2015. *World Nuclear News, "Russian FNR developments".* [Online] Available at: http://www.world-nuclear.org/information-library/current-and-future-generation/fast-neutron-reactors.aspx

WNN, 2020. *Worl Nuclear News, "China starts building second CFR-600 fast reactor".* [Online] Available at: https://www.world-nuclear-news.org/Articles/China-starts-building-second-CFR-600-fast-reactor

Yamaguchi, K., 1987. Flow pattern and dryout under sodium boiling conditions at decay power levels.. *Nucl. Eng. Des.,* Volume 99, pp. 247 - 263.

Yamano, H. et al., 2008. Development of a threedimensional CDA analysis-code: SIMMER-IV and its first application to reactor case. *Nucl. Eng. Des.,* Volume 238, p. 66 – 73.

Yi, C. & Sjoden, G., 2013. Energy group structure determination using particle swarm optimization. *Annals of Nuclear Energy,* Volume 56, pp. 53-56.

Zaleski, C. P. & Vautrey, L., 1962. *Le réacteur rapide surrégénérateur rapsodie,* s.l.: s.n.

Zhou, C., Huber, K. & Cheng, X., 2013. Validation of the modified ATHLET code with the natural convection test of the PHENIX reactor. *Annals of Nuclear Energy,* Volume 59, pp. 31-46.

Appendix A

1. Modifications of DYN3D/ATHLET coupling routines

In the framework of this doctoral thesis, an SFR-version of DYN3D/ATHLET was developed considering the scheme of Fig. 4.b. The existing LWR-version of DYN3D/ATHLET was considered as a starting point for the development activity and extended to SFR applications.

Considering the existing LWR-version of DYN3D/ATHLET, it has to be mentioned that the coupling routines of the platform collect from ATHLET the nodal distributions of T_f, T_c, ρ_c, and C_b. The distributions are then provided to DYN3D through dedicated data-acquisition and -transfer blocks. In this regard, the following observations can be made in view of the DYN3D/ATHLET extension to SFRs:

- First, existing DYN3D/ATHLET data-acquisition and -transfer blocks of T_f and T_c nodal distributions can be exploited without modifications.
- Second, existing DYN3D/ATHLET data-acquisition and -transfer blocks of nodal distribution of ρ_c, and C_b should not be accounted for. In fact, as
- shows, they are currently not exploited in DYN3D for SFRs applications.
- Finally, missing data-acquisition and -transfer blocks of nodal clad temperature distribution and diagrid average temperature, required for the evaluation of nodal state variables ε_a and ε_r, have to be implemented within the coupling routines.

The extension of the DYN3D/ATHLET from LWR to SFR applications was performed considering the observations listed above.

This section aims to provide further details of the modifications implemented on the existing LWR-version of DYN3D/ATHLET. The modifications implemented involved mostly the DYN3D/ATHLET coupling routines. However, minor modifications were required and, therefore, implemented also in the thermal-expansion, global-declaration and allocation/initialization modules of DYN3D standalone. All the modified routines are listed in Table 21. The table reports the name of the modified routines, their scope, and the purpose of the implemented modifications.

Table 21. Name of modified routines and purpose of the modifications

Routine name	Routine type	Purpose of the modifications
cnd_nk_mg.f	DYN3D declaration module	Declaration of DYN3D auxiliary variables driving axial thermal expansions of the fuel driven by clad, and radial diagrid expansion, respectively, TW1 and TD1
ndallocglob.f	DYN3D allocation/initialization module	Allocation and initialization of DYN3D auxiliary variables driving axial thermal expansions of the fuel driven by clad, and radial diagrid expansion, respectively, TW1 and TD1
cndintern.f	DYN3D/ATHLET coupling routine	Declaration of ATHLET auxiliary variables required for the transfer of clad nodal temperature distribution and diagrid average temperature, respectively, TCLAD1-2 and TDIAG1-2
ndallint.f	DYN3D/ATHLET coupling routine	Allocation and initialization of ATHLET auxiliary variables required for the transfer of clad nodal temperature distribution and diagrid average temperature, respectively, TCLAD1-2 and TDIAG1-2
ndthtran.f	DYN3D/ATHLET coupling routine	Allowing the transfer of the newly defined ATHLET variables to DYN3D
ndthshft.f	DYN3D/ATHLET coupling routine	Allowing the storage of the TCLAD2 and TDIAG2 in TCLAD1 and TDIAG1
ndthipol.f	DYN3D/ATHLET coupling routine	Allowing the interpolation of the newly defined ATHLET variables and its assignment to DYN3D variables
n3set_dyn_coup_080610.f	DYN3D/ATHLET coupling routine	Providing the capability of acquiring nodal clad temperature distribution and average diagrid temperature from ATHLET
ndmap_h_exp.f90	DYN3D thermal expansion module	Providing clad nodal temperature distribution from ATHLET while bypassing DYN3D clad nodal temperature distribution
readexp.f90	DYN3D thermal expansion module	Providing diagrid average temperature from ATHLET while bypassing DYN3D diagrid average temperature

2. Implementation of thermal expansions via ATHLET's GCSM

This section of the appendix aims at providing a detailed overview of how models described by Eq. 2.10 and Eq. 2.12 are implemented in ATHLET. The section shows the specific control signals used to implement the models in the ATHLET GCSM module. The control signals used for the calculation of the axial elongation of the out-of-core components are described for the strongback, CRDL, and vessel. Finally, considerations for the summation of the effects are made.

Fig. 67 shows the implementation of the axial expansion modeling of the strongback. The model requires as input the signal "SBAVT", i.e., a signal providing the average temperature of the strongback. If the component is modeled by a single heat structure, it is sufficient to provide the average temperature of the single heat structure of the strongback as "SBAVT". If instead the strongback is modeled by several heat structures, distributed radially and azimuthally across the thermal hydraulic system, an average value of the temperatures of the heat structures has to be evaluated and assigned to "SBAVT". The average temperature of the strongback should be evaluated as a mean weighted on the volume of the heat substructures constituting the whole strongback. The signal "SBAVT0" records, through the GCSM function "MEMORY", the average value of the strongback temperature at the end of the zero-transient (i.e., at time t'). In the example reported in the figure, the time corresponding to the end of the zero-transient is provided by the signal "STARTERExp". Signals "ExpSBAVT0" and "ExpSBAVT" represent the quantity evaluated through Eq. 2.6, respectively, at times t' and t. For the calculation of these last, tables where the values of ε_c are stored as a function of the temperature have to be provided by exploiting the function "FUNGEN" of the GCSM. Properties of the stainless steel 304, stored in "T.Exp304L", were considered in the example. The signal "DHSB" represents the axial elongation of the strongback calculated by Eq. 2.7. For the evaluation of "DHSB", signals "ExpSBAVT" and "ExpSBAVT0" are multiplied by their multiplication factors "A1" and "A2", respectively equal to 1 and -1 in the example, and then summed up by using the GCSM function "ADDER". The axial length of the strongback, considered at a specific reference temperature, is provided as a "GAIN" of the signal "DHSB". In the example the generic axial length of the strongback component was defined as "LASB".

Further details on the working principle of control signals of the ATHLET GCSM and functions integrated into the module (selectable under the keyword "CONTYP") can be found in the ATHLET manual (Austregesilo, et al., 2016).

```
@-----------------------------------------------------------------------
@Strongback thermal expansion
@-----------------------------------------------------------------------
S----    SBAVT @average temperature of strongback
...
-----------------------------------------------------------------------
@Strongback temperature signals
@-----------------------------------------------------------------------
S---- StrongBack temperature 0-value
@          YNAME     CONTYP     X1NAME     X2NAME     X3NAME     X4NAME
          SBAVT0     MEMORY      SBAVT STARTERExp          -          -
@           IOPT       GAIN         A1         A2         A3         A4
               1 +1.000E+00 +0.000E+00 +0.000E+00 +0.000E+00 +0.000E+00
@-----------------------------------------------------------------------
S---- StrongBack temperature 0-value expansion
@          YNAME     CONTYP     X1NAME     X2NAME     X3NAME     X4NAME
        ExpSBAVT0     FUNGEN     SBAVT0          -  T.Exp304L  T.Exp304L
@           IOPT       GAIN         A1         A2         A3         A4
               0 +1.000E+00 +0.000E+00 +0.000E+00 +0.000E+00 +0.000E+00
@-----------------------------------------------------------------------
S---- StrongBack temperature T-value expansion
@          YNAME     CONTYP     X1NAME     X2NAME     X3NAME     X4NAME
         ExpSBAVT     FUNGEN      SBAVT          -  T.Exp304L  T.Exp304L
@           IOPT       GAIN         A1         A2         A3         A4
               0 +1.000E+00 +0.000E+00 +0.000E+00 +0.000E+00 +0.000E+00
@-----------------------------------------------------------------------
S---- DH axial StrongBack expansion
@          YNAME     CONTYP     X1NAME     X2NAME     X3NAME     X4NAME
            DHSB      ADDER   ExpSBAVT  ExpSBAVT0          -          -
@           IOPT       GAIN         A1         A2         A3         A4
               0       LASB +1.000E+00 -1.000E+00 +0.000E+00 +0.000E+00
```

Fig. 67. Modeling of strongback axial expansion in ATHLET GCSM module

A procedure analogous to the modeling of the strongback axial elongation, "DHSB", is applied also for the modeling of CRDL and vessel axial expansions. However, for these two components, the axial discretization of the structures has to be considered. In particular, the axial elongations of all the levels with which the structures are axially discretized have to be evaluated. Eventually, all the obtained contributions must be summed up to obtain the total axial elongations of the CRDL and vessel. The signals' block required for the evaluations of total axial elongations of the CRDL and vessel, i.e., "DHCD" and "DHVW", are shown, respectively, in Fig. 68 and Fig. 69.

```
@-----------------------------------------------------------------------
@CRDriveline thermal expansion level #01
@-----------------------------------------------------------------------
S----    CDAVT01 @average temperature of CRDriveline in axial node #01
...
@-----------------------------------------------------------------------
S---- CRDriveline temperature 0-value Axial Lv01
@          YNAME     CONTYP     X1NAME     X2NAME     X3NAME     X4NAME
        CDAVT001     MEMORY    CDAVT01 STARTERExp          -          -
@           IOPT       GAIN         A1         A2         A3         A4
               1 +1.000E+00 +0.000E+00 +0.000E+00 +0.000E+00 +0.000E+00
@-----------------------------------------------------------------------
S---- CRDriveline temperature 0-value expansion Axial Lv01
@          YNAME     CONTYP     X1NAME     X2NAME     X3NAME     X4NAME
      ExCDAVT001     FUNGEN   CDAVT001          -  T.Exp304L  T.Exp304L
@           IOPT       GAIN         A1         A2         A3         A4
               0 +1.000E+00 +0.000E+00 +0.000E+00 +0.000E+00 +0.000E+00
@-----------------------------------------------------------------------
S---- CRDriveline temperature T-value expansion Axial Lv01
@          YNAME     CONTYP     X1NAME     X2NAME     X3NAME     X4NAME
       ExCDAVT01     FUNGEN    CDAVT01          -  T.Exp304L  T.Exp304L
@           IOPT       GAIN         A1         A2         A3         A4
               0 +1.000E+00 +0.000E+00 +0.000E+00 +0.000E+00 +0.000E+00
@-----------------------------------------------------------------------
S---- DH axial CRDriveline expansion Axial Lv01
@          YNAME     CONTYP     X1NAME     X2NAME     X3NAME     X4NAME
           DHCD01      ADDER  ExCDAVT01 ExCDAVT001          -          -
@           IOPT       GAIN         A1         A2         A3         A4
               0 LANodeLv01 +1.000E+00 -1.000E+00 +0.000E+00 +0.000E+00

...

S----    CDAVTnn @average temperature of CRDriveline in axial node #nn
...

@-----------------------------------------------------------------------
S---- CRDriveline temperature 0-value Axial Lvnn
@          YNAME     CONTYP     X1NAME     X2NAME     X3NAME     X4NAME
        CDAVT0nn     MEMORY    CDAVTnn STARTERExp          -          -
@           IOPT       GAIN         A1         A2         A3         A4
               1 +1.000E+00 +0.000E+00 +0.000E+00 +0.000E+00 +0.000E+00
@-----------------------------------------------------------------------
S---- CRDriveline temperature 0-value expansion Axial Lvnn
@          YNAME     CONTYP     X1NAME     X2NAME     X3NAME     X4NAME
      ExCDAVT0nn     FUNGEN   CDAVT0nn          -  T.Exp304L  T.Exp304L
@           IOPT       GAIN         A1         A2         A3         A4
               0 +1.000E+00 +0.000E+00 +0.000E+00 +0.000E+00 +0.000E+00
@-----------------------------------------------------------------------
S---- CRDriveline temperature T-value expansion Axial Lvnn
@          YNAME     CONTYP     X1NAME     X2NAME     X3NAME     X4NAME
       ExCDAVTnn     FUNGEN    CDAVTnn          -  T.Exp304L  T.Exp304L
@           IOPT       GAIN         A1         A2         A3         A4
               0 +1.000E+00 +0.000E+00 +0.000E+00 +0.000E+00 +0.000E+00
@-----------------------------------------------------------------------
S---- DH axial CRDriveline expansion Axial Lvnn
@          YNAME     CONTYP     X1NAME     X2NAME     X3NAME     X4NAME
           DHCDnn      ADDER  ExCDAVTnn ExCDAVT0nn          -          -
@           IOPT       GAIN         A1         A2         A3         A4
               0 LANodeLvnn +1.000E+00 -1.000E+00 +0.000E+00 +0.000E+00

...

S----    DHCDSum @sum of all DHCD: From DHCD01 to DHCDnn
...

@-----------------------------------------------------------------------
S----       DHCD
@          YNAME     CONTYP     X1NAME     X2NAME     X3NAME     X4NAME
            DHCD      ADDER    DHCDSum          -          -          -
@           IOPT       GAIN         A1         A2         A3         A4
               0 +1.000E+00 +1.000E+00 +0.000E+00 +0.000E+00 +0.000E+00
```

Fig. 68. Modeling of CRDL axial expansion in ATHLET GCSM module

```
@-----------------------------------------------------------------------
@Vessel thermal expansion level #01
@-----------------------------------------------------------------------
S----    VWAVT01 @average temperature of vessel walls in axial node #01
...
@-----------------------------------------------------------------------
S---- VesselWalls temperature 0-value Axial Lv01
@          YNAME     CONTYP     X1NAME     X2NAME     X3NAME     X4NAME
        VWAVT001     MEMORY    VWAVT01 STARTERExp          -          -
@           IOPT       GAIN         A1         A2         A3         A4
               1 +1.000E+00 +0.000E+00 +0.000E+00 +0.000E+00 +0.000E+00
@-----------------------------------------------------------------------
S---- VesselWalls temperature 0-value expansion Axial Lv01
@          YNAME     CONTYP     X1NAME     X2NAME     X3NAME     X4NAME
      ExVWAVT001     FUNGEN   VWAVT001          -  T.Exp304L  T.Exp304L
@           IOPT       GAIN         A1         A2         A3         A4
               0 +1.000E+00 +0.000E+00 +0.000E+00 +0.000E+00 +0.000E+00
@-----------------------------------------------------------------------
S---- VesselWalls temperature T-value expansion Axial Lv01
@          YNAME     CONTYP     X1NAME     X2NAME     X3NAME     X4NAME
       ExVWAVT01     FUNGEN    VWAVT01          -  T.Exp304L  T.Exp304L
@           IOPT       GAIN         A1         A2         A3         A4
               0 +1.000E+00 +0.000E+00 +0.000E+00 +0.000E+00 +0.000E+00
@-----------------------------------------------------------------------
S---- DH axial VesselWalls expansion Axial Lv01
@          YNAME     CONTYP     X1NAME     X2NAME     X3NAME     X4NAME
           DHVW01      ADDER  ExVWAVT01 ExVWAVT001          -          -
@           IOPT       GAIN         A1         A2         A3         A4
               0 LANodeLv01 +1.000E+00 -1.000E+00 +0.000E+00 +0.000E+00

...

S----    VWAVT01 @average temperature of vessel walls in axial node #nn
...

@-----------------------------------------------------------------------
S---- VesselWalls temperature 0-value Axial Lvnn
@          YNAME     CONTYP     X1NAME     X2NAME     X3NAME     X4NAME
        VWAVT0nn     MEMORY    VWAVTnn STARTERExp          -          -
@           IOPT       GAIN         A1         A2         A3         A4
               1 +1.000E+00 +0.000E+00 +0.000E+00 +0.000E+00 +0.000E+00
@-----------------------------------------------------------------------
S---- VesselWalls temperature 0-value expansion Axial Lvnn
@          YNAME     CONTYP     X1NAME     X2NAME     X3NAME     X4NAME
      ExVWAVT0nn     FUNGEN   VWAVT0nn          -  T.Exp304L  T.Exp304L
@           IOPT       GAIN         A1         A2         A3         A4
               0 +1.000E+00 +0.000E+00 +0.000E+00 +0.000E+00 +0.000E+00
@-----------------------------------------------------------------------
S---- VesselWalls temperature T-value expansion Axial Lvnn
@          YNAME     CONTYP     X1NAME     X2NAME     X3NAME     X4NAME
       ExVWAVTnn     FUNGEN    VWAVTnn          -  T.Exp304L  T.Exp304L
@           IOPT       GAIN         A1         A2         A3         A4
               0 +1.000E+00 +0.000E+00 +0.000E+00 +0.000E+00 +0.000E+00
@-----------------------------------------------------------------------
S---- DH axial VesselWalls expansion Axial Lvnn
@          YNAME     CONTYP     X1NAME     X2NAME     X3NAME     X4NAME
           DHVWnn      ADDER  ExVWAVTnn ExVWAVT0nn          -          -
@           IOPT       GAIN         A1         A2         A3         A4
               0 LANodeLvnn +1.000E+00 -1.000E+00 +0.000E+00 +0.000E+00

...

S----    DHVWSum @sum of all DHVW: From DHVW01 to DHVWnn
...

@-----------------------------------------------------------------------
S----       DHVW
@          YNAME     CONTYP     X1NAME     X2NAME     X3NAME     X4NAME
            DHVW      ADDER    DHVWSum          -          -          -
@           IOPT       GAIN         A1         A2         A3         A4
               0 +1.000E+00 +1.000E+00 +0.000E+00 +0.000E+00 +0.000E+00
```

Fig. 69. Modeling of vessel axial expansion in ATHLET GCSM module

The contributions of "DHSB", "DHCD", and "DHVW", considered together with their convention sign, have to be eventually summed up in a signal "DHEff" as shown in Fig. 70.

What was discussed up to this point, holds for the detailed methodology of out-of-core structures. For this method, in fact, detailed material properties and geometries of the structures are considered together with realistic modeling of the sodium flow paths from the core outlet to the structures.

If the simplified modeling of the out-of-core structures is performed, the strongback, CRDL, and vessel are represented by single lumped heat structures located at the inlet and outlet of the core model. That is, the heat structures of the components are not axially or radial/azimuthally discretized. This implies that the average temperature of these structures is tracked by a single temperature signal. In this case, the axial expansion CRDL and vessel are similarly evaluated as shown in Fig. 67 for the strongback but the thermal expansion model is feed by the temperature of a single heat structure. In addition, materials properties and geometries of the structures, as well as the realistic modeling of the sodium flow paths are accounted for by suitable time delay constants. The axial elongations of the effects have to be, thus, delayed with of specific times by the ATHLET GCSM function "DELAY". The generic time delays of the strongback, CRDL, and vessel are addressed as, respectively as "SBdelay", "CRDLdelay", and "VWdelay" in Fig. 71. Eventually, all the delayed contributions have to be summed up in the signal "DHEff" as in the case of detailed modeling.

```
If the detailed methodology for the modeling of out-of-core structures
is applied...
@-----------------------------------------------------------------------
S----      DHEff
@          YNAME     CONTYP     X1NAME     X2NAME     X3NAME     X4NAME
           DHEff      ADDER       DHSB       DHCD       DHVW          -
@           IOPT       GAIN         A1         A2         A3         A4
               0 +1.000E+00 -1.000E+00 -1.000E+00 +1.000E+00 +0.000E+00
```

Fig. 70. Modeling total axial expansion in ATHLET GCSM module

```
Otherwise(case simplified methodology)...
@-----------------------------------------------------------------------
S---- delayed DH axial StrongBack expansion
@          YNAME     CONTYP     X1NAME     X2NAME     X3NAME     X4NAME
         DHSBEff      DELAY       DHSB          -          -          -
@           IOPT       GAIN         A1         A2         A3         A4
               1 +1.000E+00    SBdelay +0.000E+00 +0.000E+00 +0.000E+00
@-----------------------------------------------------------------------
S---- delayed DH axial CRDriveline expansion
@          YNAME     CONTYP     X1NAME     X2NAME     X3NAME     X4NAME
         DHCDEff      DELAY       DHCD          -          -          -
@           IOPT       GAIN         A1         A2         A3         A4
               1 +1.000E+00  CRDLdelay +0.000E+00 +0.000E+00 +0.000E+00
@-----------------------------------------------------------------------
S---- delayed DH axial VesselWalls expansion
@          YNAME     CONTYP     X1NAME     X2NAME     X3NAME     X4NAME
         DHVWEff      DELAY       DHVW          -          -          -
@           IOPT       GAIN         A1         A2         A3         A4
               1 +1.000E+00    VWdelay +0.000E+00 +0.000E+00 +0.000E+00
@-----------------------------------------------------------------------
S----      DHEff
@          YNAME     CONTYP     X1NAME     X2NAME     X3NAME     X4NAME
           DHEff      ADDER    DHSBEff    DHCDEff    DHVWEff          -
@           IOPT       GAIN         A1         A2         A3         A4
               0 +1.000E+00 -1.000E+00 -1.000E+00 +1.000E+00 +0.000E+00
```

Fig. 71. Modeling total axial expansion in ATHLET GCSM module and delayed effects

3. Definition of signals dedicated to the control of CR positions

In DYN3D/ATHLET the position of CRs is driven by ATHLET through dedicated signals defined in the ATHLET input deck. For LWR applications such signals dedicated to the command of the CR position are generally exploited to simulate CR withdrawal/insertion or to keep CR initial static position otherwise. For SFR applications, the definition of ΔL_{tot}, defined as in Eq. 2.10 and Eq. 2.12, allows one to exploit the signals mentioned before also to correct dynamically the CR position according to the axial expansions of out-of-core components. In this regard, more details are provided below.

As shown in Fig. 72, the signals that drive the CR position are first declared under the keyword "HARDWARE" in the section "NEUKIN3D", dedicated to the coupling of ATHLET and DYN3D. The keyword "HARDWARE" was already available from the LWR-version of DYN3D/ATHLET.

Under "HARDWARE", one has to first specify the total number of CR banks defined in DYN3D and then declare, for each CR bank index, the name of the signal controlling the bank position. In the example, two is the number of DYN3D CR banks and "CRB01POS" and "CRB02POS" are the signals controlling, respectively, the position of the first and second banks. The signals provide the height of the CR bank from the bottom of the core.

As Shown in Fig. 73, the signals "CRB01POS" and "CRB02POS" are constituted by two parts. The first part, named "CRB01POS0" or "CRB02POS0", simulates CR withdrawal/insertion, as ordered by the reactor hardware, or their initial static position otherwise. This contribution is provided as a function of the time by using the ATHLET function "FUNGEN" and tables storing the banks' position over the time, namely, in the figure, "TabCRBP01" or "TabCRBP02". The second part is the dynamic correction "DHEff" rising from the axial expansions of out-of-core components. "DHEff" is calculated as shown in the previous section of this appendix.

```
@-----------------------------------------------------------------------
C---- NEUKIN3D
@-----------------------------------------------------------------------
----- COUPLING
...
----- CORECHAN
...
----- HARDWARE
@-----------------------------------------------------------------------
@      Tot#Banks
                2
@-----------------------------------------------------------------------
@    Dyn3DBankId    SigName
                1   CRB01POS
                2   CRB02POS
```

Fig. 72. Definition of CR banks in ATHLET input decks

```
@-----------------------------------------------------------------------
C---- GCSM
@-----------------------------------------------------------------------
...
S---- CRBack01 position
@          YNAME     CONTYP     X1NAME     X2NAME     X3NAME     X4NAME
       CRB01POS0     FUNGEN       TIME    STARTER          -  TabCRBP01
@           IOPT       GAIN         A1         A2         A3         A4
              -1         1.         0.         0.         0.         0.
S---- CRBack02 position
@          YNAME     CONTYP     X1NAME     X2NAME     X3NAME     X4NAME
       CRB02POS0     FUNGEN       TIME    STARTER          -  TabCRBP02
@           IOPT       GAIN         A1         A2         A3         A4
              -1         1.         0.         0.         0.         0.
@-----------------------------------------------------------------------
S---- CRBack01 position + dynamic correction w/ DHEff
@          YNAME     CONTYP     X1NAME     X2NAME     X3NAME     X4NAME
        CRB01POS      ADDER  CRB01POS0      DHEff          -          -
@           IOPT       GAIN         A1         A2         A3         A4
              -1         1.         1.         1.         0.         0.
S---- CRBack01 position + dynamic correction w/ DHEff
@          YNAME     CONTYP     X1NAME     X2NAME     X3NAME     X4NAME
        CRB01POS      ADDER  CRB01POS0      DHEff          -          -
@           IOPT       GAIN         A1         A2         A3         A4
              -1         1.         1.         1.         0.         0.

...
@-----------------------------------------------------------------------
C---- TABLES
@-----------------------------------------------------------------------
...
K---- TabCRBP01
      0.00000E+00  1.88680E+02
      1.00000E+06  1.88680E+02
K---- TabCRBP02
      0.00000E+00  1.88680E+02
      1.00000E+06  1.88680E+02
```

Fig. 73. Definition of signals dedicated to the command of CR banks' position in ATHLET input decks

Appendix B

1. Verification of MDT XS libraries for SPX transient analyses

To perform V&V activities of the new platform on the transient SPX start-up tests one needs to generate parametrized XS libraries. The latter were generated in the framework of the current doctoral research exploiting the SPX benchmark specifications. For verification purposes, the generated libraries are applied with DYN3D standalone to the calculations of the SPX static neutronic benchmark. Solutions obtained are then compared against DYN3D references evaluated in (Ponomarev, et al., 2021a) with non-parametrized XSs.

MDT parametrized XS libraries are generated with Serpent considering several values of the state variables, see Table 10. Considered state variables of the parametric space are temperatures of fuel and coolant as well as axial fuel and radial diagrid expansions. Values of the state variables were selected to cover the full operational range of all the SPX start-up tests starting from an isothermal core configuration at 453K.

By fixing the values of the state variables (via an internal DYN3D constant feedback option), DYN3D calculations of the SPX static neutronic benchmark are performed with the MDT parametrized XSs. Considering the applicability range covered by the XS libraries only specific benchmark cases can be selected for the verification activity. Namely, all the cases with configurations with material temperatures above 453 K: They are cases number 1, 2, 7, 8, 11, 12, and 13.

Results of calculations are compared against the DYN3D reference solutions presented in the previous section. Fig. 74 presents the deviations ΔP_{RMS} and $\Delta\rho$ evaluated against Serpent solutions for both the new DYN3D and reference ones.

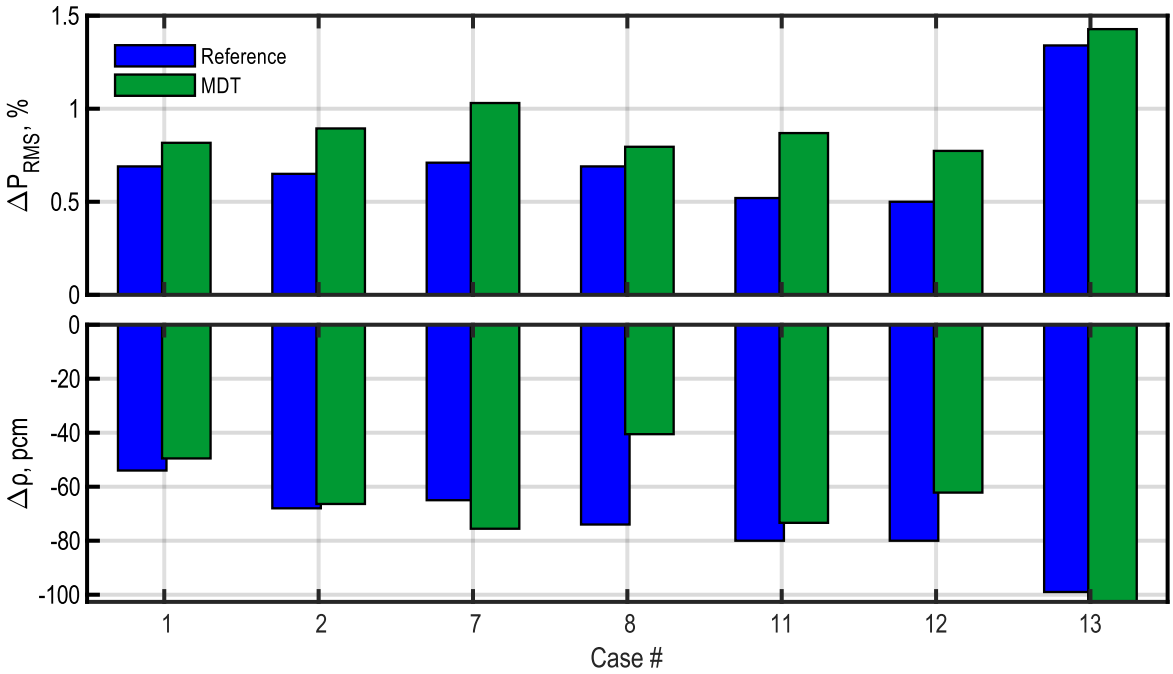

Fig. 74. Comparison on SPX static benchmark calculations: MDT XS libraries against reference

Fig. 74 shows that with both XS sets the selected benchmark cases are, with minor discrepancies, similarly predicted. Deviations of the new DYN3D results with respect to the references are in the worst case limited to 0.3% for ΔP_{RMS} and 30 pcm for $\Delta\rho$.

The verification activity showed successfully the consistency of the two XS libraries and opens up to the application of the new XS libraries to the transient analyses of SPX start-up tests.

2. Gap conductance models for SPX SST test

For the modeling of the SPX start-up tests with DYN3D/ATHLET, all the data required by the models, including the gap conductance of the fuel elements, were adopted from the benchmark specifications provided in (Ponomarev, et al., 2021b). Almost all the models allowed for a high-quality reproduction of the tests in close agreement with the available experimental trends. However, in the case of the SST, i.e., the SPX self-stabilization test, performed at hot zero-power conditions, significant deviations from the experimental trends were observed. Such deviations turned out to be due to an incorrect modeling of the gap conductance, which initial values were probably too small and, as for all the other tests, assumed to be constant during the whole transient calculations.

To improve the solutions of SST test, the ATHLET dynamic gap conductance model (Austregesilo, et al., 2016) was applied to the SPX SST model. This section provides an overview of the basic and dynamic models adopted in ATHLET for the modeling of gap conductance and of their application to the modeling of SST test. The results of the SST test calculations performed with both the models are eventually compared and briefly discussed.

As mentioned above, ATHLET offers two possible approaches for the modeling of the gap conductance "h_{gap}".

- The first approach, hereafter addressed as to the "static" approach, allows one to set an initial value of the gap conductance which is then kept constant during the whole transient calculations. The approach, summarized by Eq. B.3.1, was applied to the modeling of all the SPX start-up tests.

$$h_{gap} = h_{gap}|_0 \qquad \text{Eq. B.3.1}$$

  Relevant to this method is the choice of a suitably selected initial value of the gap conductance, "$h_{gap}|_0$", which is usually evaluated by detailed fuel performance calculations.

- The second approach, hereafter addressed as to the "dynamic" approach, consists of the dynamic evaluation of the gap conductance starting from user-set fuel gap parameters, i.e., initial gap size at room temperature and thermophysical properties of the gas in the gap. This model can be summarized by Eq. B.3.2.

$$h_{gap} = \frac{\lambda_{gap}}{\delta_{gap}} + h_{rad} \qquad \text{Eq. B.3.2}$$

In Eq. B.3.2, "λ_{gap}" is the gap gas conductivity, "δ_{gap}" is the gap size, and "h_{rad}" is the radiative heat transfer coefficient. Initial values of λ_{gap} are evaluated by ATHLET considering the gas properties of the gas gap provided by the code user. Predefined thermophysical properties are also available for several gases, e.g., Helium, Argon, Krypton, etc. Initial values of δ_{gap} are evaluated according to the temperature distribution within the fuel elements. The expansion or contraction of δ_{gap} from the room temperature value, "$\delta_{gap}|_0$", is evaluated via generic thermal expansion correlations used for fuel and clad. Values of λ_{gap}, δ_{gap}, and h_{rad} are eventually dynamically updated by ATHLET during the entire transient calculations.

Both the "static" and "dynamic" gap models were applied to the modeling of the SST test of the SPX benchmark. For the modeling of the test, Helium was assumed to fill the gap of the reactor fuel rods and room temperature gap sizes of the rods were set equal to 0.115 and 0.169 mm for fissile and fertile fuel elements respectively as proposed in (Ponomarev, et al., 2021b). For the modeling of the h_{gap} via the static approach, a fuel gap conductance of 1100 W/m^{2}K was adopted by benchmark specifications for fissile and fertile fuel rods. Calculations of the test were performed first with the static approach and then newly performed switching on the ATHLET dynamic gap conductance model.

As shown in Table 22, the application of the dynamic model introduced significant variations of the gap conductance already in steady-state calculations. The table compares conductance values and gap sizes at the end of the steady-state calculations as set/calculated by the models. The values shown in the table are considered at the core middle plane and are averaged on fissile and fertile regions.

Table 22. Static and dynamic gap models: Steady-state comparison

	Model type		
	Static	Dynamic	Difference
Fissile region $h_{gap}, \frac{W}{m^2K}$	1100	1790	+690
Fissile region δ_{gap}, mm	0.115	0.113	-0.002
Fertile region $h_{gap}, \frac{W}{m^2K}$	1100	1250	+150
Fertile region δ_{gap}, mm	0.169	0.162	-0.007

By applying the dynamic gap model, h_{gap} increases of 690 and 150 W/m^{2}K for fissile and fertile rods, respectively. Considering negligible both the difference in initial gap sizes between static and dynamic models and the radiative heat transfer coefficients, the main differences in the gap conductance values are to be attributed to the gas gap conductivity evaluated by ATHLET.

The quantities shown in Table 22 were also compared in transient calculations. Fig. 75 shows the transient evolution of the gap conductance values and gap sizes both, again, considered at the core middle plane and averaged on fissile and fertile core regions. As one might note, the most impacting contribution of the dynamic model rises not from the model dynamic part but rather from the evaluation of the initial values of h_{gap}. In fact, further dynamic effects introduced by the dynamic model are negligible on the transient calculations of the considered scenario.

By applying the dynamic gap conductance model to the calculations of the SST test, the quality of the test solutions improves thanks to a better estimated initial guess of the gap conductance, see Fig. 76. Fig. 76 shows a net improvement of the solution quality with calculated trends of power and outlet core sodium temperature, both closer to the experimental trends.

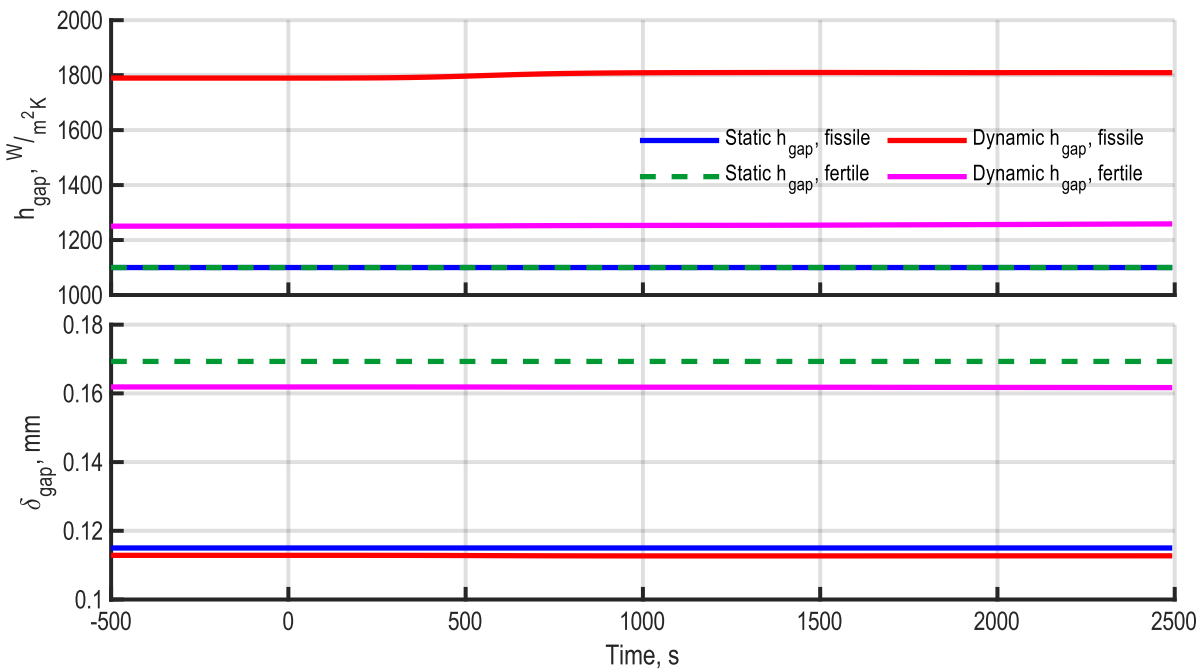

Fig. 75. Static and dynamic gap models: Transient comparison

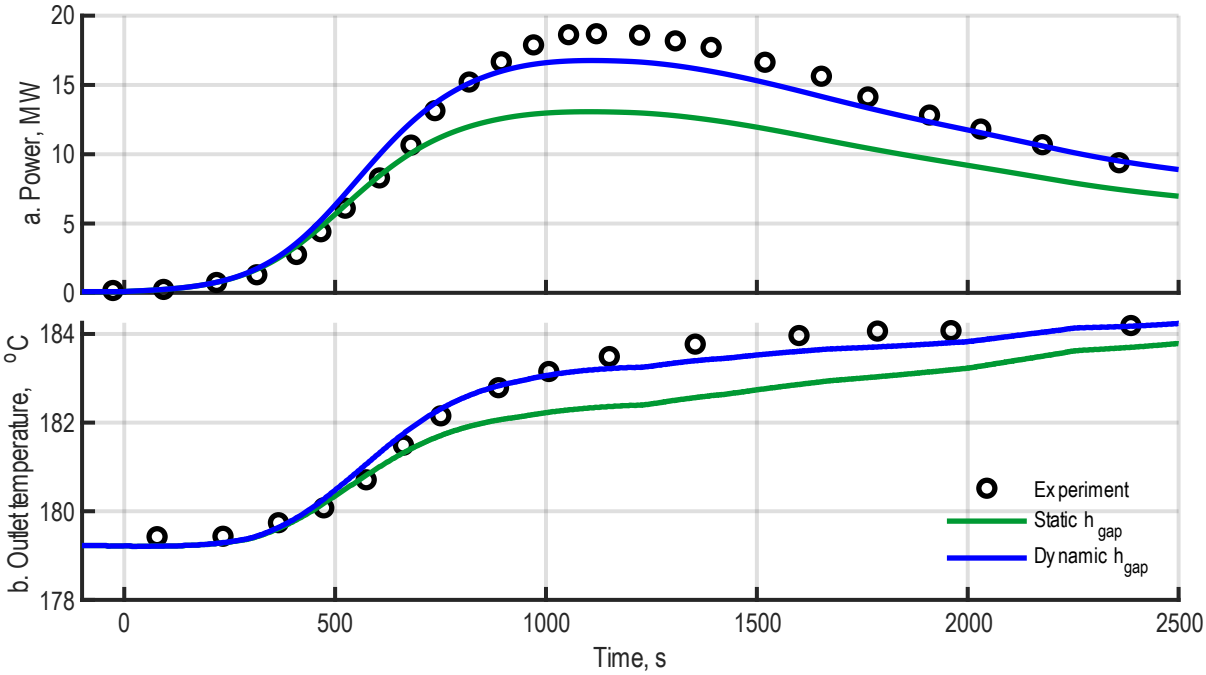

Fig. 76. SST test: Comparison of solutions with static and dynamic gap conductance

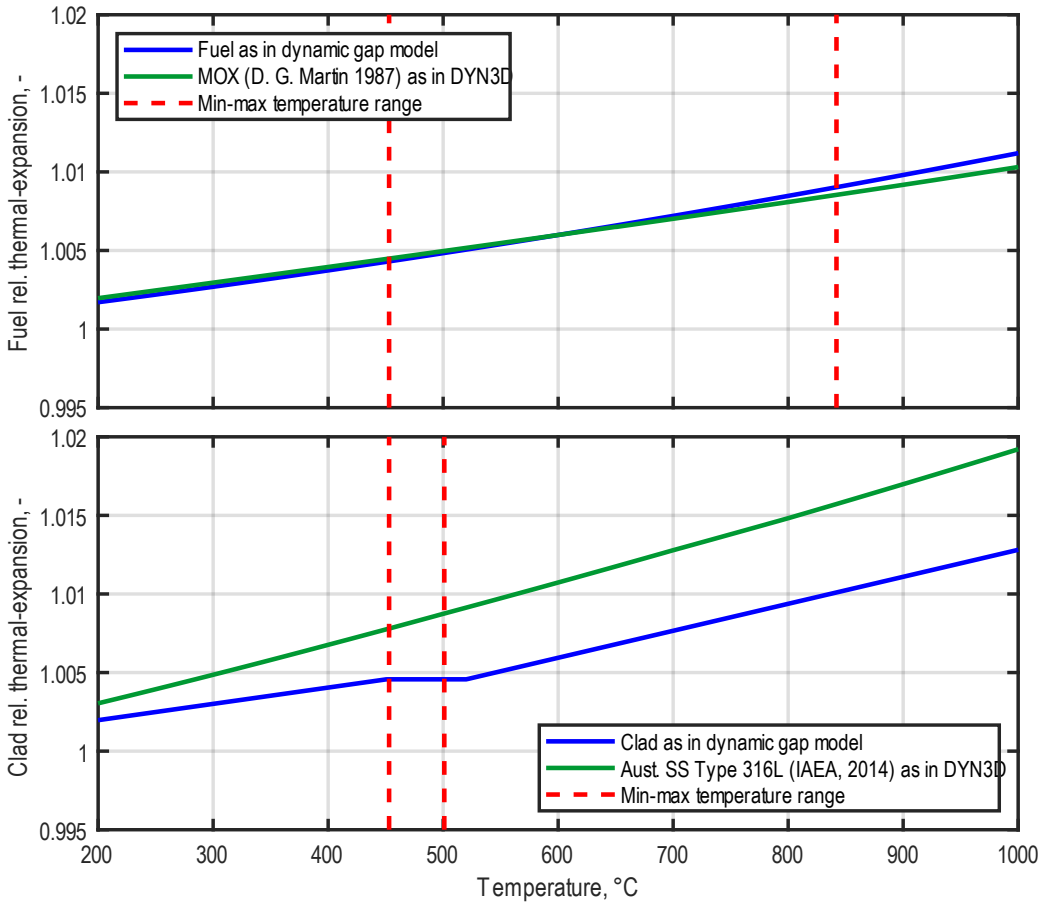

Fig. 77. Thermal expansion correlations of fuel and clad in use by the dynamic gap model against correlations of actual model materials.

Despite the significant improvements in the results, it should be mentioned that the model presents some limitations. These last are related to the dynamic evaluation of δ_{gap} that, as already mentioned above, is evaluated by considering generic fuel and clad thermal expansion correlations. Such correlations might, in fact, considerably differ from the correlations of the actual materials employed for the modeling of the fuel elements. However, such consideration is not valid for the case of the SST model presented in this section. In fact, by comparing the thermal expansion correlations used by the dynamic model and those of actually employed materials, see Fig. 77, it was observed that:

- The thermal expansion correlations of MOX fuel practically overlap.
- Even though considerable deviations found between the clad thermal expansion correlations lead to negligible discrepancies of the h_{gap} values. Such deviations were manually evaluated by applying Eq. D.2 to evaluate their effect on h_{gap}. Considering steady-state conditions and neglecting the contribution of h_{rad}, a maximum deviation of 25 W/m^2K was on h_{gap} values

To conclude this section one can state that, although the thermal expansion correlations used by the dynamic model and those of actually employed materials slightly differ, the model still allows for a more realistic determination of the h_{gap}, contributing, qualitative, to the improvement of the SST test solution.

Appendix C

1. Procedure for XS generation

For the sake of completeness, the procedure for the generation of XS libraries is described more in detail in this appendix section. It should be stressed that the procedure was not developed in the framework of the current doctoral research but was rather the outcome of several cumulative scientific work presented in (Fridman & Shwageraus, 2013; Rachamin, et al., 2013; Nikitin, et al., 2015a; 2015b).

The generation process of the XS to be employed in the DYN3D nodal diffusion analyses is carried out by the Serpent MC code. The nuclear data required by the generation process are adopted by nuclear data libraries and specifically for the present case from JEFF-3.1 (Koning, et al., 2006). The initial energy (24-) group structure considered for the generation of the few-group XSs was identified in (Fridman & Shwageraus, 2013) and was already presented in this thesis in Table 13.

Once the core configuration to be model is characterized in terms of geometries, atomic density compositions of materials in the several core regions, and respective nuclei temperatures, the XS are derived by applying the procedure described in (Nikitin, et al., 2015). The XSs' generation procedure is truthfully reported from the reference in the following:

- For the fuel subassemblies which do not face the radial reflector, the 24-group XS are generated considering a single fuel subassembly modeled in 3D geometry. Reflective radial and black axial boundary conditions are imposed on the surface of the 3D model.

- For the fuel subassemblies facing the radial reflector, the XSs are generated considering 3D geometries for fuel and reflector. A graphical view of the model is shown in Fig. 78. The XSs are finally homogenized only on those fuel subassemblies facing the radial reflector.

- For the non-multiplying regions, such as axial/radial reflectors, sodium and gas plena, empty control rods' channels, and control rods, the homogenized XS are generated considering 2D super-cell models as shown in Fig. 79. In the super-cell models, the non-multiplying (hexagonally shaped) regions are placed at the center of the cell and are surrounded by fuel regions. The XS are homogenized only over non-multiplying regions.

By applying the procedure described to this point, the DYN3D full core calculations performed with Serpent generated XSs already allow one to find generally good agreements with the full core MC

solutions. However, in presence of strong absorber regions or, in general, of regions characterized by poor neutron flux distributions and surrounded by fuel subassemblies, the quality of nodal diffusion solutions is observed to degrade. This is especially true for rodded core configurations which, respected to unrodded configurations, present somewhat larger deviations from MC full core solutions, e.g., larger deviating effective multiplication factors and power distributions.

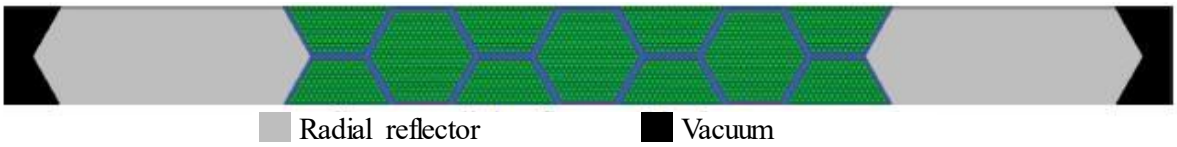

Fig. 78. View of the model used for generating XSs of fuel subassemblies facing the radial reflector. Figure from (Nikitin, et al., 2015)

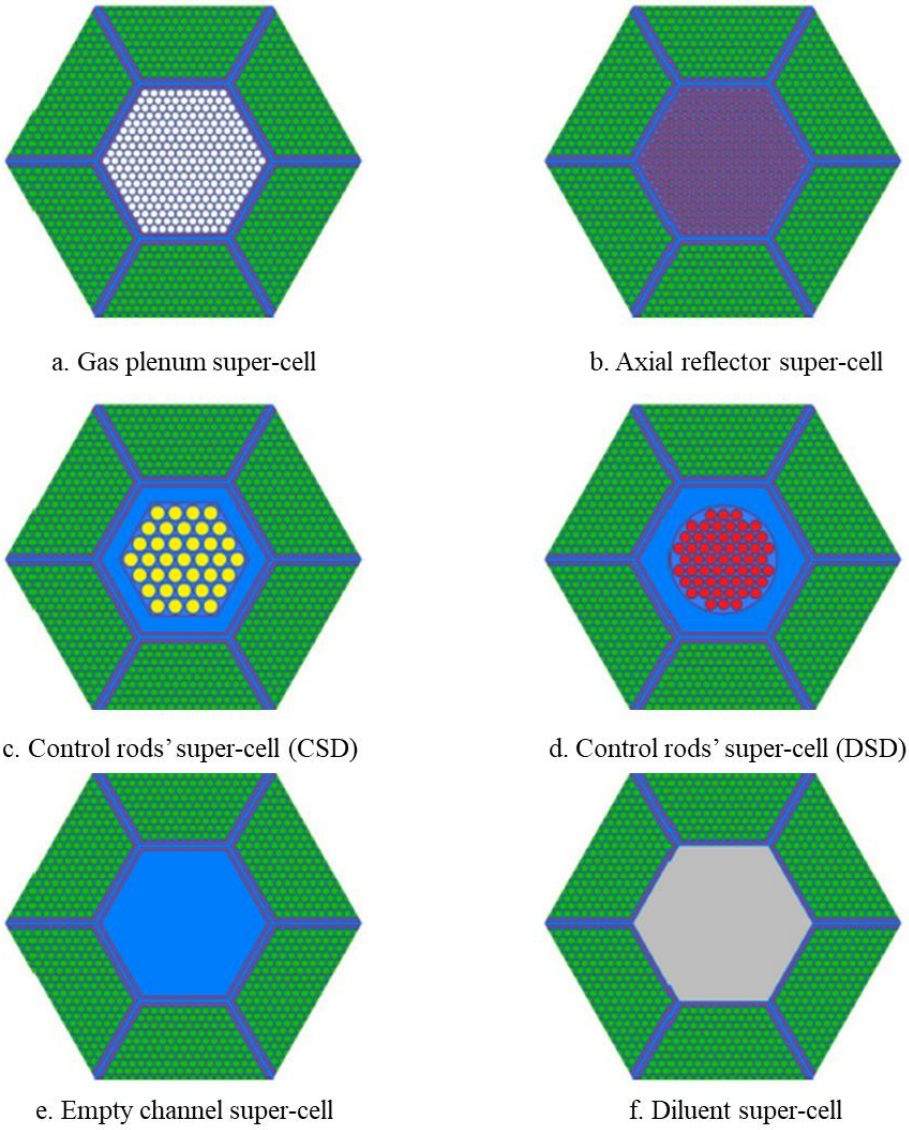

Fig. 79. Example of super-cell models for various core regions. Figure from (Nikitin, et al., 2015)

In this regard, a further step is considered in the XSs' generation process to improve the DYN3D nodal diffusion solutions. That is, the application of the Super-homogenization (SPH) method initially proposed in (Hebert, 1993; Hebert & Mathonniere, 1993) to "correct" the XSs of specific core regions. The adaptation of the method to generation of XSs in Serpent/DYN3D was developed and applied in (Nikitin, et al., 2015). The method is reported hereafter as described in the reference.

In the reference as well as in this thesis work, the SPH method was applied to correct flux-volume weighted XSs of control rods and empty control rods channels. The XSs' correction factors are evaluated by jointly use Serpent and DYN3D. The evaluation of the factors requires preliminary modeling/calculation activities, in particular:

- First, heterogeneous Serpent super-cell models of control rods and relative empty channels are employed to generate reference transport solutions, see Fig. 80a.
- Afterwards, homogeneous XSs and fluxes are evaluated in the regions of fuel and control rods (or empty channels), see Fig. 80b.
- Eventually, homogeneous super-cell models, equivalent to the Serpent super-cell models, are developed for DYN3D, see Fig. 80c.

The SPH correction factors are evaluated by applying the following iterative procedure:

- The DYN3D solutions are evaluated with the super-cell model by applying XS generated by Serpent. The neutron fluxes obtained over the fuel and non-multiplying regions of the DYN3D super-cell model[11], in Fig. 80c, are averaged for each region, "r", and energy group, "g".

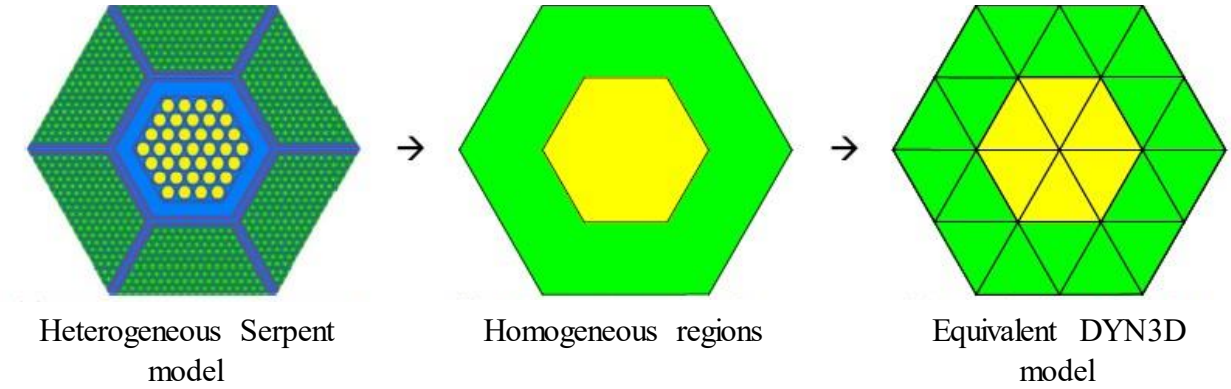

Fig. 80. Serpent and DYN3D models used to generate SPH corrected XS. Figure from (Nikitin, et al., 2015)

[11] Super-cell geometry can only be model in DYN3D by applying trigonal meshes

- SPH correction factors of region r and group g, i.e., "$\mu_{r,g}$", are obtained by applying Eq. C.1.1:

$$\mu_{r,g} = \frac{\bar{\phi}_{r,g}^{Het}}{\phi_{r,g}^{Hom}} N_g \qquad \text{Eq. C.1.1}$$

with, $\bar{\phi}_{r,g}^{Het}$ and $\phi_{r,g}^{Hom}$ the average heterogeneous and homogeneous neutron fluxes in region r and group g obtained from heterogeneous Serpent transport solution and homogeneous DYN3D diffusion solution respectively. Whereas N_g is a normalization factor calculated as in Eq. C.1.2:

$$N_g = \frac{\sum_r V_r \phi_{r,g}^{Hom}}{\sum_r V_r \bar{\phi}_{r,g}^{Het}} \qquad \text{Eq. C.1.2}$$

- Corrected XSs, $\Sigma_{r,g}^{Mod}$, are evaluated by applying Eq. E.1.3:

$$\Sigma_{r,g}^{Mod} = \mu_{r,g} \Sigma_{r,g} \qquad \text{Eq. C.1.3}$$

- Super-cell diffusion calculations are newly performed by DYN3D applying this time corrected XSs. Newly obtained homogeneous neutron fluxes are employed to evaluate the new set of the SPH factors. The procedure is repeated iteratively "n" times, until the convergence criterion of Eq. D.4 is met for each r and g.

$$\frac{\max\left|\mu_{r,g}^{n} - \mu_{r,g}^{n-1}\right|}{\mu_{r,g}^{n-1}} < 10^{-6} \qquad \text{Eq. C.1.4}$$

The whole XSs' generation procedure, including the just presented SPH correction procedure, has to be repeated considering several core configurations. These latter should be properly identified to cover the full core operational range simulated in neutron diffusion calculations. The configurations should account for different fuel and sodium temperatures, radial diagrid and axial fuel expansion, etc. Finally, the evaluated XSs have to be stored over formatted text files (XS libraries) and have to be made available for DYN3D.

The procedure exposed has been applied as described for the generation of the SPX XS libraries in the framework of the current PhD thesis.

Appendix D

1. Selection of weighting factor "wRod" in the cost function H

The performance of the modified cost function H shown in Eq. 4.3 was assessed with the help of the neutronic SPX benchmark introduced in (Ponomarev, et al., 2021a). In particular:

- Cases number 1 and 13 of the benchmark were considered as the unrodded and rodded cases for the evaluation of the $h_{unrodded}$ and h_{rodded} components respectively;
- Best-performing structures with 4, 5, and 6 energy groups were determined deterministically using the modified cost function H for three different values of w_{Rod} (i.e., 0.0, 0.5, and 1.0);
- The obtained best-performing structures were used to generate the cross-section libraries for the full SPX benchmark calculations.

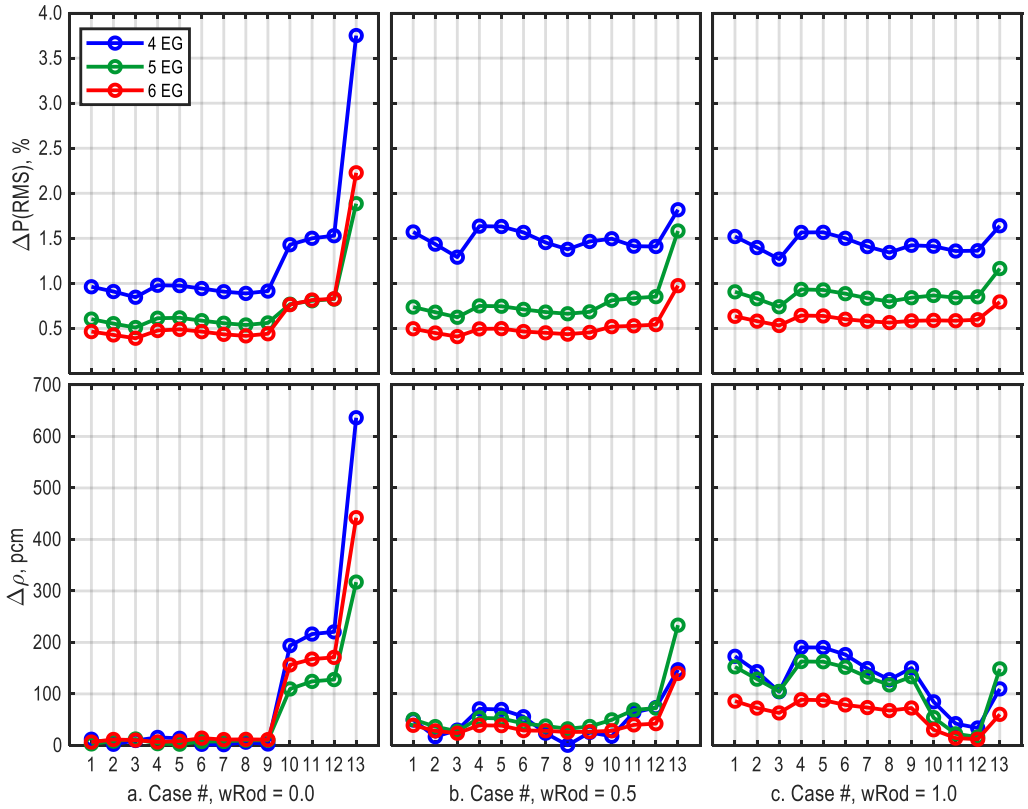

Fig. 81. Parametric study on w_{Rod}, benchmark calculation tests performed with 4, 5, and 6 EG.

The results of the parametric study are presented in Fig. 81, and lead to the following observations:

- For w_{Rod} equal to 0.0, (Fig. 81a), the function H is not representative at all for the rodded cases, i.e., from cases from number 10 to 13. That is, rodded configurations are not considered in the optimization process and the solutions coincide with the ones found by using F of Eq.

4.2 for the unrodded core configuration. Small and comparable errors are found on the unrodded configurations. In contrast, quite diverging solutions are obtained for rodded states, with error values up to ca 650 pcm $\Delta\rho$ and 4% ΔP_{RMS} in case number 13.

- For w_{Rod} equal to 0.5, (Fig. 81b), the accuracy of the unrodded solutions result slightly worsened. Nevertheless, for the rodded states, the errors in $\Delta\rho$ generally improved, and values of $\Delta\rho$ and ΔP_{RMS} of case number 13 drop below 250 pcm and 2%, respectively.

- For w_{Rod} equal to 1.0, (Fig. 81c), the components ΔP_{RMS} and $\Delta\rho$ of rodded states are further improved with respect to the results obtained for w_{Rod} equal to 0.5. However, the improvements are achieved at the expense of the accuracy in solutions of unrodded configurations. For cases from number 1 to 9 of the benchmark, one can in fact observe a slight worsening of the ΔP_{RMS} values and pronounced deviations on $\Delta\rho$ components.

Globally, acceptable compromises are found on the accuracy of the solutions by choosing w_{Rod} equal to 0.5 for the cost function H. Such a value is therefore selected to carry out further optimization analyses.

2. Selection of cooling parameters for the SA algorithm

N is the total number of iterations, T_0 is the initial temperature and r is the cooling rate. As shown in Section 4.1.2, the performance of the simulated annealing depend on the cooling schedule and are related to the parameters T_0, r, and N showed in Eq. 4.7. Suitable values of the constants were determined through parametric analyses. Eventually, the parameters T_0, r, and N were set to 1, 1000, and 1500, for the optimization of EGSs of the SPX, and to 1, 500, and 2000 for the optimization of EGSs of the Phénix. The parametric study and corresponding results are summarized in the following.

The study was performed for each optimization problem, i.e., for the optimization of the SPX and Phénix benchmarks by applying the cost function shown in Eq. 4.3. In addition, the study was initially performed also for the optimization of the SPX benchmark executed by employing the cost function in Eq. 4.2. The cost functions presented in Eq. 4.3 and Eq. 4.2 are hereafter addressed as H' and H respectively. The goal of the parametric study was to identify combinations of the input parameters that on average lead to a close agreement of the cost functions, H' and H, to their theoretical optimum values, H*, which was deterministically evaluated.

In this regard, a performance map of the SA algorithm was obtained by varying values of the input parameters T_0, r, and N. The values of the input parameters selected for the study are shown in Table

23 and were combined in 90 possible combinations. For each combination of parameters, the EGS optimization process was performed 100 times to collect statistically meaningful data.

Table 23. Input parameters and corresponding values assumed for the parametric study

Parameter	Values
T_0	1, 10, 100
r	10, 100, 300, 500, 1000, 10000
N	500, 1000,1500,2000, 2500

The results of the study were ordered by increasing values of the optimal cost, H' and H, found by performing the optimizations. Already in (Di Nora, et al., 2021a), it was shown that among 90 combinations of T_0, r, and N analysed, the first 20-30 combinations lead approximately to the similar accuracy of the SA algorithm, see trends of H in Fig. 82. Identical considerations hold for the trends of H'. Fig. 82 demonstrates deviation of optimized cost function from the theoretical minimum for different sets of SA cooling parameters, the lower part of the figure zooms into the 15 best performing sets. The cost function obtained with those 15 sets are very close to each other (and to the theoretical minimum), which means any of those sets could be used for any of considered systems. The combinations finally chosen for the optimization analyses were selected to find best compromises between number of maximum iterations required, N, and quality of optimum values, H' and H.

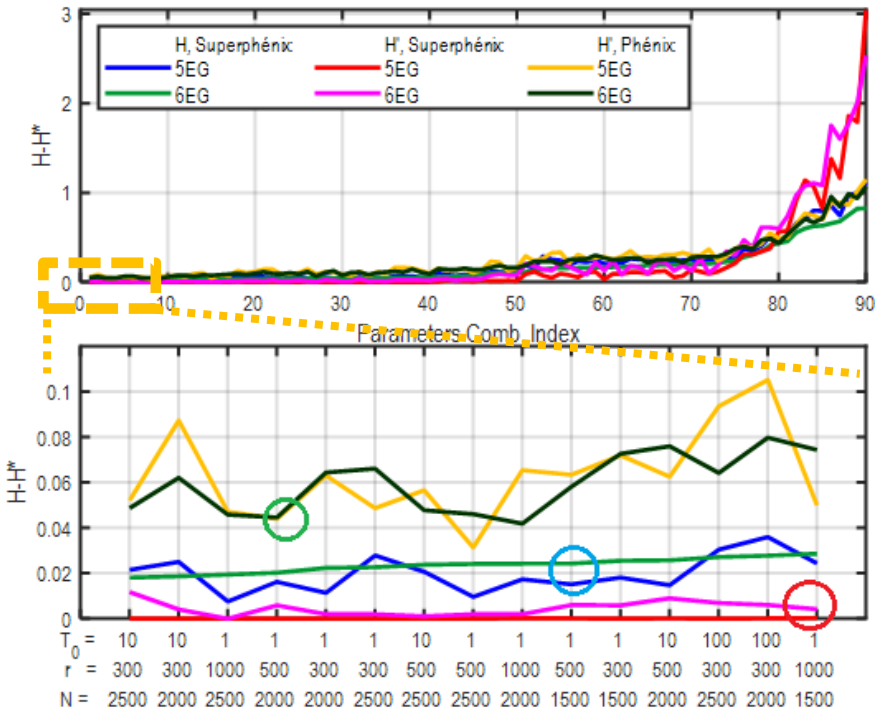

Fig. 82. parametric study on T_0, r, and N

Curriculum Vitae

PERSONAL/CONTACT INFORMATION

Name, Surname: Vincenzo Anthony, Di Nora

Email address: vincenzo.dinora@gmail.com, Phone number: (+49) 15226756172

EMPLOYMENT HISTORY

- *[Aug 2017 – Jul 2021] Scientific employee*
  Helmholtz-Zentrum Dresden-Rossendorf, Dresden, Germany
- *[Sep 2016 – Mar 2017] Intern*
  Karlsruhe Institute of Technology, Karlsruhe, Germany

EDUCATION

- *[Aug 2017 – Today] Doctor of philosophy, doctoral program in energy*
  Ecole polytechnique fédérale de Lausanne, Lausanne, Switzerland
- *[Sep 2014 – May 2017] Master degree in energy and nuclear engineering*
  Politecnico di Turin, Turin, Italy
- *[Sep 2010 – May 2014] Bachelor degree in industrial engineering*
  Università degli Studi di Catania, Catania, Italy

PROFESSIONAL QUALIFICATIONS

Certifications

- *Deterministic modeling of nuclear systems*
  Released by Chalmers university of technology, Issue date: September 2019
- *Fortran for scientific computing*
  Released by High performance computing center Stuttgart, Issue date: April 2018
- *ATHLET basic training course*
  Released by Gesellschaft für Anlagen- und Reaktorsicherheit (GRS) gGmbH, Issue date: November 2017

Workshops and schools

- *Frederic Joliot/Otto Hahn on nuclear reactors Physics, fuels, and system*
- *NRG2019, energy systems: managing the transition to renewables*
- *Liquid Metal Facilities", ENEA Casaccia, Rome*

Known codes and programming languages

- *DYN3D (neutron kinetics solver), Serpent (Monte Carlo code), ATHLET and TRACE (thermal-hydraulic codes)*
- *Python, Fortran, Matlab*

LANGUAGES SKILLS

- *Mother tongue: Italian*
- *Other languages: English, German*

PUBLICATIONS

- *Fridman, E., Nikitin, E., Ponomarev, A., Di Nora, V. A., Kliem, S., Mikityuk, K., 2023. Extension of the DYN3D/ATHLET code system to SFR applications: models description and initial validation. Annals of Nuclear Energy 182, p. 109619.*

- *Ponomarev, A., Mikityuk, K., Fridman, E., Di Nora, V. A., Bubelis, E., Schikorr, M., 2021. SPX Benchmark Part II: Transient Results. Journal of Nuclear Engineering and Radiation Science.*

- *Di Nora, V. A., Fridman, E., Nikitin, E., Bilodid, Y., Mikityuk, K., 2021. Optimization of multigroup energy structures for diffusion analyses of sodium-cooled fast reactors assisted by simulated annealing – Part I: Methodology demonstration. Annals of Nuclear Energy 155, p. 108183.*

- *Di Nora, V. A., Fridman, E., Nikitin, E., Bilodid, Y., Mikityuk, K., 2021. Optimization of multigroup energy structures for diffusion analyses of sodium-cooled fast reactors assisted by simulated annealing – Part II: Methodology application. Annals of Nuclear Energy 163, p. 108541.*

- *Di Nora, V. A., Fridman, E., Mikityuk, K., 2019. Benchmarking ATHLET against TRACE as applied to Superphénix start-up tests, in Proc.: International Congress on Advances in Nuclear Power Plants - ICAPP2019, 12.-15.05.2019, Juan-Les-Pins, France, Juan-les-Pins, France.*